UNIVERSITY OF LONDON THESIS

Degree PhD Year 2006 Name of Author JAMES
Richard William
Llewellyn

Modelling of High Resolution Liquid Crystal Devices

by

Richard William Llewellyn James

A thesis submitted for the degree of Doctor of Philosophy of
the University of London

Faculty of Engineering
Department of Electronic & Electrical Engineering
University College London

The United Kingdom

October 2006

ProQuest LLC
789 East Eisenhower Parkway
P.O. Box 1346
Ann Arbor, MI 48106-1346

Table of Contents

List of Tables

List of Figures

List of Principal Symbols

K_{11}	elastic constant associated with a splay deformation
K_{22}	elastic constant associated with a twist deformation
K_{33}	elastic constant associated with a bend deformation
q_0	chirality
ε_0	permittivity of free space
$\Delta\varepsilon$	dielectric anisotropy
$\bar{\bar{\varepsilon}}$	permittivity tensor
λ	wavelength of light
n_o	ordinary refractive index
n_e	extraordinary refractive index
Δn	birefringence
d	liquid crystal cell thickness
T	temperature
T_c	clearing point (temperature)
T^*	supercooling temperature
a, B, C	thermotropic coefficients
A	$a(T - T^*)$
S_0	equilibrium order parameter
$\mathbf{Q}$	Q-tensor representing the liquid crystal order and orientation
$\hat{n}$	liquid crystal director
$\vec{E}$	electric field vector
$\vec{H}$	magnetic field vector
u	electric potential
v	velocity
o^k	polynomial shape or basis function
$\hat{\eta}$	normal to a boundary (Γ)
$\sigma_{\alpha\beta\gamma}$	the Levi-Civita anti-symmetric tensor
$\delta_{\alpha\beta}$	the Kronecker Delta

Abbreviations

BTN	Bistable Twisted Nematic
CMOS	Complementary Metal Oxide Semiconductor
HAN	Hybrid Aligned Nematic
IPS	In-Plane Switching
ITO	Indium Tin Oxide
LdG	Landau-de Gennes
LC	Liquid Crystal
LCOS	Liquid Crystal on Silicon
PABN	Post Aligned Bistable Nematic
RGM	Reduced Grating Method
SLM	Spatial Light Modulator
VAN	Vertically Aligned Nematic
ZBD	Zenithal Bistable Device

Acknowledgements

I am grateful to my supervisors F. Aníbal Fernández and Sally E. Day for their guidance, patience and most of all making my time in the group a pleasurable one.

Philip Trwoga deserves a special mention for all the advice and support he has given me, and for all the times I have bothered him with questions about Physics. So too does my brother Gareth for helping me out so much over the last couple of years, with mathematics, programming and computer parts.

I would like thank my friends Tom Derham, Aric Whitewood and Oliver Williams for providing welcome distractions from work.

The hours spent in front of a computer have passed quickly in the company of my office mates, Mark Gardner with whom I have enjoyed many light hearted (and light centric) discussions, and Eero Willman who has proved a great source of ideas and suggestions.

I am indebted to Dr Daniel Svenšek and Chris Newton for the insightful advice and help they have provided.

At the start of my Ph.D I spent 6 weeks at the Department of Electronics and Information Systems, University of Ghent, Belgium, in order to perform experimental work. Measurements were performed on test cells kindly provided by D.K.G. de Boer, Philips, Eindhoven. I would like to thank Goran Stojmenovik, Stefaan Vermael, Chris Desimpel and Kristiaan Neyts for making me feel so welcome and for educating me on liquid crystals and Belgian beers. Additional thanks are due to Goran, who has taught me so much over the past few years.

Another collaboration which has been of great benefit has involved Rami Ghannam, Miloš Komarčević, Neil Collings and William Crossland, members of the Department of Engineering, Cambridge. Their help and suggestions have proved invaluable.

I would like to acknowledge the financial support of the EPSRC and the European network project SAMPA (Synclinic and Anticlinic Mesophases for Photonic Applications).

Finally, I would like to thank my wife Mihwa, for her patience and feigned interest in my work, and my parents for their support.

Abstract

There is much interest in the use of liquid crystals for holographic displays or light steering in telecommunication systems. These applications require a much higher resolution than conventional displays and as a consequence the pixel size and the gaps between them shrink. The impact of the fringing fields is significant and the electric field in the inter-pixel gaps can become large enough to give rise to disclinations. There is a need for modelling of these effects not only from the point of view of device optimisation but also to find ways to use them to our advantage. For instance, defects are associated with rapid changes in the refractive index which can be relocated by an applied voltage.

The first part of the work details the development of continuum theory models for liquid crystal switching. Three implementations are described; (i) a finite element discretisation of the Oseen-Frank free energy using a vector representation (constant order parameter), (ii) a constant order parameter model similar to (i), but using a tensor representation and (iii) a finite element discretisation of the Qian-Sheng equations. The implementation of (iii) includes the calculation of the flow and variations in the order parameter are allowed, which typically occur on very small scales. It also includes adaptive meshing driven by an error estimate that allows significant savings in terms of degrees of freedom and a "smart" time integrator, used to model the dynamic behaviour efficiently. In devices known to be free of disclinations the vector method is shown to exhibit better spatial convergence. However, when disclinations are present it becomes necessary to allow the order parameter to vary and to use a tensor representation to model their movement accurately.

Results produced by these models form the second part of this work. High resolution devices can be used as diffraction devices, for holographic displays or beam steering. A Spatial Light Modulator is modelled in detail in this beam steering application. Here the use of a liquid crystal device is desirable as the connectivity of the system can be electrically reconfigured. The ability of the device to steer light in a number of different directions is evaluated in terms of the diffraction efficiency, which is limited by the pixellation and the finite extent of the elastic deformation of the liquid crystal. Of particular interest are the cases where the grating angle is oblique to the pixel grid, where reorientation of the liquid crystal in the plane parallel to the electrodes is inevitable. This twisting causes the diffraction order magnitudes to depend on the polarisation state of the incident wavefront.

Choosing the surface alignment oblique to the pixel grid is found to reduce this sensitivity.

As the resolution increases further there becomes a point where the switching mechanisms used in conventional display devices become ineffectual. This limit is studied for both image display and holographic applications, by applying a chequerboard pattern of voltages to a pixel array as the pixel pitch is altered.

With Liquid Crystal On Silicon (LCOS) technology it is possible to move beyond this limit, with pixel pitches of the order of the cell thickness. However, the driving voltages tend to be limited to a few volts. Device designs are proposed that are able to use this limited voltage to reorient a thin layer of liquid crystal above the pixel grid, which in turn reorients the bulk. Under specific alignment conditions, the LC orientation can change abruptly in the inter-pixel gap. A large enough electric field can induce disclination lines, which can then be electrically repositioned so as to write high resolution into the liquid crystal. A new switching mechanism is proposed for the Zenithal Bistable Device that exploits the interaction between electrically induced disclinations and the grating surface without relying on the flexoelectric effect.

In such high intensity fields the drift of even small concentrations of ionic impurities can influence LC switching. A study of the influence of ion migration on the switching of the LC has been performed for both planar and IPS cells. By fitting experimental to simulated results the ion distributions can be characterised. Simulations show charged particles tend to accumulate above the edges of pixels. Devices with larger pixel widths are found to be less affected by the presence of a given concentration of ionic impurities.

Chapter 1

Introduction

1.1 Motivation

Increasingly liquid crystals are being used for many applications besides displays, for example in holographic projection or beam steering in telecommunication systems. For these applications performance tends to be limited by the available resolution, therefore in the drive towards higher resolution the electrode size shrinks. Even for display application the individual pixels are becoming more complex, a case in point being the in-plane switching mode, which is becoming increasingly popular, where interdigitated electrodes reorient molecules in the plane parallel to the glass substrate.

For simple display pixels, for example a twisted nematic cell, analytic expressions are available, which can be used to design fully the characteristics of the pixel. For example the optimum cell thickness can be found that maximises the transmittance. As the complexity of pixels increases such analytic expressions are no longer available. Due to the expense of fabrication, design by trial and error is undesirable. There is a need for modelling.

Modelling provides additional insight into what is happening to the molecules inside a pixel, information that is difficult to obtain from measurement. With this information it is possible to refine a design in a way that would not be possible by trial and error.

Normally the modelling requires two steps. This first step is the calculation of some quantity (usually the director) that represents the molecular orientation throughout the liquid crystal layer. The second step is to determine how light propagates through a stack that usually comprises a pair of polarisers and the liquid crystal layer.

For large simple pixels these steps are well established, a mesoscopic approach is taken, whereby the molecular orientation is represented by a unit vector, known as the director [18, 19, 20]. The director field can be obtained within the framework of continuum elastic theory. Changes in the permittivity occur on lengths scales in excess of the wavelength of light, and optical propagation is well described by the Jones Matrix method [8].

As resolution increases, two deficiencies of this approach become apparent. Fringing fields in the inter-pixel gap are strong, giving rise to a rapidly changing permittivity. As the length scale of these changes approaches the wavelength of light, diffraction occurs. The Jones Matrix method breaks down, and only by finding the solution to Maxwell's equations can the optical propagation be correctly calculated [11, 21, 22, 23]. As resolution increases, the electric field in the inter-pixel gap tends to increase too. Large electric fields tend to

induce biaxial ordering [1] of the liquid crystal and can even induce defects [24] . It becomes inaccurate to represent the molecular orientation as a simple vector.

Instead, the molecular orientation can be represented as a rank two symmetric tensor, which is capable of describing a biaxial arrangement of molecules [7, 5]. A difficulty in this approach lies in the fact that the components of the tensor vary on very short length scales in comparison to the pixel size where defects are present. From a computational point of view this means that a fine spatial discretisation is required, leading to lengthy simulation times.

An alternative approach would be a molecular dynamics calculation [25, 26, 27], in which the laws of classical mechanics are used to determine the position and orientation of each and every molecule in the device. Due to the sheer number of molecules required, this approach cannot be applied to devices with dimensions measured in microns.

The objective of this work is to study the effect of high resolution features on the liquid crystal. To this end, a model is required that is capable of resolving both length scales in a realistically sized device, with a reasonably short simulation time. Specifically, liquid crystal on silicon (LCOS) devices are considered, which are able to deliver high spatial resolution, due to the massive processing power of the electronics in the silicon backplane, with high manufacturing yields. The reduced electrode width relative to the cell thickness means that neighbouring pixels have a much stronger influence on each other than in a conventional cell. Currently the voltage that can be applied to pixels in an LCOS device is limited to a couple of volts. It is of interest to optimise the device design so that this limited voltage can be used to align the bulk of the liquid crystal. Even though the voltage is low the electric field is relatively large in the narrow inter-pixel gap. The drift of even small concentrations of ionic impurities can be significant when the electric field is large. It has been shown experimentally that under specific conditions such large fields can induce defects [24]. It is the aim of this work to find ways to use these defects to advantage, for instance by using them to write high resolution into the liquid crystal.

[1] Biaxial ordering here refers to a biaxial arrangement of uniaxial molecules, not to biaxial molecules. The large electric field causes the molecules to become ordered in two orthogonal directions

1.2 Achievements

1. A finite element discretisation of the Qian-Sheng [12] formulation has been implemented for two dimensional domains. These equation allow the orientation of the liquid crystal to be determined, taking into account the flow of the liquid crystal and changes in the order parameter. To my knowledge this is the first time that the finite element method has been applied to these equations. Complementary approaches have been used by other groups, the finite difference method [28] and the lattice Boltzmann algorithm [29, 30]. A strength of the finite element method lies in its inherent ability to model domains of arbitrary shape. In the vicinity of disclinations the order parameter varies on small scales relative to the container size. Using an adaptive meshing scheme we are able to resolve the disclination core well, yet still achieve reasonable simulation times. A fine spatial discretisation tends to constrain the time step, particularly in the case of explicit methods. An implicit time integration scheme, the Crank-Nicholson method has been used, offering improved stability, with a variable time step that is set according to the rate of change of the solution.

2. In the inter-pixel gap of high resolution devices the electric field tends to be large and the drift of ionic impurities within a cycle of an applied voltage waveform becomes significant. Experimental and theoretical studies of ion transport in planar and IPS cells have been made. Instead of measuring the effects of the ion migration only using current measurements for low applied voltages [31], the interaction between the migrating ions and reorienting liquid crystal is considered. An anisotropy in the mobilities of positive and negative ions is able to explain the measured optical response of both planar and IPS cells with high ion contents. It has been shown that IPS cells with larger electrode widths are less sensitive to movement of ionic impurities.

3. LCOS devices are well suited to beam steering and holographic applications. Previous simulations of diffraction gratings have considered the situation where the grating is conformal to the pixel grid [32, 21]. Here for the first time oblique grating angles have been considered, where the staircase like edge of the pixel grid causes diffraction in the direction perpendicular to the grating. A full range of grating orientations have been considered and the performance evaluated in terms of the diffraction efficiency and the sensitivity to the input polarisation state. Performance is limited by the finite

extent of the elastic deformation and the fringing fields at the 2π phase transition. This region is studied in 3D for the first time, and the effect of altering the pixel pitch on the diffraction efficiency is found.

4. Large electric fields in the inter-pixel gap have been shown to be able to induce disclinations in a homeotropic cell [24, 33]. Here, the effect of altering the surface alignment has been studied. A high resolution device is considered, with a thickness that exceeds the pixel pitch. Device designs are demonstrated in which a limited electrode voltage is able to switch a thin layer of liquid crystal above the electrodes, which in turn causes reorientation of the bulk. A novel switching mechanism is suggested in a bistable device, in which electrically induced disclinations are used to alternate between stable states.

1.3 Thesis outline

This thesis can be divided into three main parts. It begins with an introduction to the Physics of liquid crystals. The second part details modelling methods and the final part is a study of high resolution devices that have been simulated using these models.

1.3.1 Part I - Physics of liquid crystals

Chapter 2 discusses the properties of the liquid crystal phases and introduces the concept of an order parameter. Optical properties and methods to calculate the optical transmission are reviewed in chapter 3.

1.3.2 Part II - Modelling

Fundamental concepts of the finite element method are introduced in chapter 4. This is the principal method used to discretise equations in the chapters that follow. The first part of this chapter is a review of basic concepts, including variational forms and numerical integration. These concepts are then applied to discretise the Poisson equation. This discretisation is used to calculate the electric field in all the devices studied in this work. In Chapter 5 a finite element discretisation of the Oseen-Frank free energy formulation is developed, with the option of using a vector or tensor representation of the liquid crystal orientation, that

assumes the order parameter is constant. Chapter 6 presents the discretisation of Landau-de Gennes free energy formulation [5, 7], which allows the order parameter to vary, and is capable of describing a biaxial arrangement of molecules.

In Chapter 7 these models are extended to take into account the flow of the liquid crystal. The Ericksen-Leslie theory extends the Oseen-Frank free energy formulation, providing a way to calculate the velocity of the liquid crystal and its orientation, under the assumption that the order parameter is constant. Not only is the orientation governed by the balance of elastic and electric forces, it is affected by the velocity too. The Qian-Sheng theory extends the Landau-de Gennes free energy formulation, providing a way to calculate the velocity of the liquid crystal and its orientation, allowing for biaxial ordering and variation in the order parameter. A comparison between constant order vector and tensor implementations is made in chapter 8.

1.3.3 Part III - High resolution devices

The effect of the drift and diffusion of ionic impurities in the inter-pixel gap is studied in chapter 9, experimentally and theoretically.

In Chapter 10 a spatial light modulator has been modelled, with the assumption that the order parameter is constant. The ability of the device to steer a wavefront in a number of different directions is considered, where its performance is measured in terms of the diffraction efficiency and the sensitivity to the polarisation state of the wavefront.

Between high and low voltage electrodes the finite extent of the elastic distortion of the nematic liquid crystal and the fringing fields are the factors that most strongly determine performance. In Chapter 11 a more detailed look at this region is taken. A chequerboard voltage pattern is simulated and the diffraction efficiency is calculated as the pixel pitch is altered.

The large electric field in the inter-pixel gap is able to induce defects in the liquid crystal for certain types of alignment. Rapid changes in the permittivity will be associated with these disclinations. Devices that exhibit this behaviour are simulated in chapter 12 and possible applications are discussed.

Finally, in chapter 13 a bistable device is proposed, based on the zenithal bistable device (ZBD), which makes use of electrically induced disclinations to switch between stable states without relying on the flexoelectric effect [7].

Chapter 2

Liquid Crystal Physics

2.1 Introduction

Liquid crystals are an intermediate phase of matter existing between the crystalline solid and amorphous liquids [34, 35, 7]. They retain orientational order on melting from the solid form, but can flow readily like a liquid, and become totally disordered in the high temperature fluid phase. Liquid crystalline states arise in materials with molecules that possess geometric anisotropy or an anisotropy in the solubility properties [36]. The ordering of these molecules gives rise to anisotropy in the electric and optical properties.

2.2 Liquid Crystal Phases

Liquid crystals can be broadly categorized as either lyotropic and thermotropic [36]. Lyotropic liquid crystal molecules comprise a hydrophobic tail and a hydrophilic head and form liquid crystal phases when dissolved in a polar solvent, such as water. In such a solvent, the molecules assemble so that the tails group together, exposing the hydrophilic heads to the solvent. A wide range of phases can be formed, for example the micellar or lamellar phase (molecules form bilayers separated by solvent). Phase transitions are induced by changes to the solvent concentration or to the temperature. For very specific combinations of molecules and solvent concentrations, micelles can form that are not spherical, which can give rise to liquid crystal phases that are similar to those seen in thermotropic liquid crystals.

Thermotropic liquid crystals are typically formed from pure compounds or mixtures of rod (calamitic) or disc shaped (discotic) molecules and give rise to liquid crystal phases over a fixed temperature range. Discotic liquid crystals form nematic and columnar phases.

Broadly speaking, calamitic liquid crystals form four phases, known as the isotropic, smectic, nematic and cholesteric phases (sometimes called the chiral nematic phase). Three of these phases are sketched in Fig. 2-1. At this point it is useful to introduce the director, $\hat{n}$, which is a unit vector, which represents the preferred orientation of liquid crystal molecules averaged over a small volume.

Ordinary liquids generally possess some short-range order on a molecular scale but lack any macroscopic order. This is known as the isotropic phase. If a liquid crystal is heated sufficiently it will become isotropic. On cooling there will be a transition temperature, where various degrees of ordering of the fluid give rise to a liquid crystal phase, specifically the nematic phase. Further cooling can gives rise to another liquid crystal phase, called

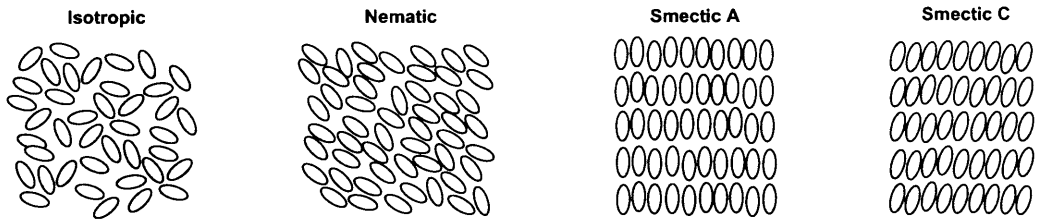

Figure 2-1: Liquid crystals phases

smectic phases, which not only posses orientational order but also a degree of positional ordering. When the temperature falls beneath the melting point the crystalline solid forms, where the molecules are rigidly bound in both position and orientation.

2.2.1 Nematic Phase

The simplest of the liquid crystal phases is the nematic phase. In this phase the molecules behave much like those of a liquid, being free to move and with no positional order, but differ in the respect that the molecules tend to align with one another. The director can change from point to point, and is a function of space. The word nematic is derived from the Greek nematos meaning thread like, referring to thread-like structures that can be observed when these materials are viewed using a polarising microscope. This phase of liquid crystal is used in virtually all commercially available liquid crystal displays. Most nematic liquid crystals are uniaxial, meaning that the major axes of the molecules tend to align with each other. Biaxial nematics also orient along a secondary axis.

2.2.2 Smectic Phases

Smectic liquid crystals are closest in structure to solid crystals and posses a high degree of order, with diffuse positional order as well as orientational order. The additional smectic order results in the formation of layered structures. There are several classes of a smectic material depending on the in-layer ordering and the angle between the layer normal and the director (labelled A, B, C, and so on, according to the chronological sequence of their detection). The most common smectic materials are smectic A, where the director is parallel to the layer normal, and smectic C, where the director is at an angle to the layer normal. There also exist phases where the molecules are ordered in a hexagonal lattice, for example the smectic B phase. Smectic materials show wax like properties, whereas nematic materials

flow more freely. More extensive descriptions of the individual classes can be found in the following references [37, 35, 7].

2.2.3 Cholesteric Phase

The chiral nematic phase replaces the nematic phase when the molecules lack inversion symmetry. The chiral component of the molecular interaction produces a helical twisted structure of pitch p, which can be as short as 100 nm [36]. The helical twist may be clockwise or anti-clockwise, depending on the molecular conformation.

The helical structure of the chiral nematic phase has the ability to selectively reflect light when the wavelength is of the order of the helical pitch length; however, in order for this to happen the material must be aligned so that the helical axis is parallel to the light propagation direction. A common commercial application for this type of phase is in thermochromic thermometer devices and other devices that change colour with temperature.

The smectic C phases can also have a chiral structure, where the director rotates about the cone between the layer normal and the tilt. In this case it is referred to as a C^* phase. Here, the asterisk denotes that the molecules are chiral, but not necessarily that the phase has a chiral structure. For instance a smectic C^* phase has both chiral molecules and chiral structure, whereas a smectic A phase formed from chiral molecules is called an A^* phase, even though it will posses no chiral structure.

Only the nematic phase is considered in this thesis.

2.3 Properties of Liquid Crystals

The anisotropy in the shape of LC molecules leads to an anisotropy in dielectric properties. Parallel to the long axis a molecule the permittivity is denoted as $\varepsilon_{\parallel}$, whereas perpendicular to this the permittivity is denoted as $\varepsilon_{\perp}$. The dielectric anisotropy ($\Delta\varepsilon$) is the difference between the parallel and perpendicular dielectric constants, and can be either positive or negative. When an electric field is applied, the induced dipole moment of the molecules creates a net torque which tends to align the molecules. For materials with a positive $\Delta\varepsilon$ the molecules tend to align parallel to the electric field [7]. Negative $\Delta\varepsilon$ materials favour perpendicular alignment.

This uniaxial symmetry also gives rise to anisotropy in the refractive index. A glass

flask filled with a nematic LC appears as an opaque fluid because light is scattered by the fluctuations in refractive index throughout the sample. The ordinary refractive index, n_o, is for light with electric field polarisation perpendicular to the director, and the extraordinary refractive index n_e, is for light with electric field polarisation parallel to the director. The birefringence is the difference between these two values [13].

The viscosity of a fluid is the internal resistance to flow, defined as the ratio of the shearing stress to the rate of shear. A flow process induces a favoured director orientation, and conversely a field-induced reorientation of the director induces a flow effect. A detailed analysis of the liquid crystal requires 5 independent viscosity coefficients, but usually the behaviour is approximated using a single rotational viscosity coefficient (γ_1).

2.4 Phase Transitions and Orientational Order

A phase transition is the transformation of a thermodynamic system from one phase to another. At the transition, a small change in a thermodynamic variable such as the temperature or pressure results in an abrupt change in one or more physical properties. An example is the transition between solid, liquid and gaseous phases. Here, the transition can be characterised by an abrupt change in density.

When a liquid crystal is cooled from the isotropic to the nematic state there is a reduction in symmetry and an associated (abrupt) increase in order at the phase transition. This transition can be characterised as first-order, as it involves a latent heat; an amount of energy is absorbed or released during the transformation between phases. First-order transitions are associated with "mixed-phase regimes" in which some parts of the system have completed the transition and others have not [38]. To quantify this behaviour it is necessary to introduce the concept of an orientational order parameter.

The orientation of the long axis of each molecule can be represented by a unit vector (ignoring its sign). In any small volume, the fluctuations of the direction of these vectors will be described by the statistical distribution $f(\theta, o)$. The mean value of this function, over the volume is a vector called the director. To characterise the orientational order, we need to examine the behaviour of this distribution. The distribution of direction vectors can now be normalised yielding the function $f'(\theta)$ where now θ represents deviations from the director orientation (this change of origin, moving the z-axis to $\hat{n}$, implies the independence from o).

A measure of the degree of order can be obtained by expanding the function in spherical harmonics, which in this case reduce to Legendre polynomials in $\cos(\theta)$. Odd order terms in this expansion are not allowed because they imply breaking the head-tail symmetry, so the first significant term is the second order term: $a_2 P_2(\cos(\theta))$. The coefficient a_2, is defined as the orientational order parameter (S) and is:

$$a_2 = 1/2 \int (f'(\theta) P_2(\cos(\theta))) d\theta \tag{2.1}$$

$$S = \frac{1}{2} \int f'(\theta)(3\cos^2\theta - 1) d\Omega. \tag{2.2}$$

This opens up the possibility of defining higher order orientational order parameters, as the coefficients of the higher order order even polynomials (4^{th}, 6^{th}, ...).

If $f'(\theta)$ is zero everywhere except at $\theta = 0$ and $\theta = \pi$ then the molecules are all aligned parallel to one another and $S = 1$, corresponding to an ordered crystalline state. If the orientation is completely random then $f'(\theta) = 1/2\pi$, and integrating equation (2.2) leads to $S = 0$; the isotropic state. In the nematic phase, the order parameter takes intermediate values that range typically from 0.4 to 0.6. It is possible for equation (2.2) to yield $S = -1/2$ if $f(\theta)$ is peaked at $\theta = \pi/2$, however this corresponds to the unlikely situation where a collection of rods favour perpendicular alignment. The order parameter can be measured in a number of ways, for example by optical birefringence measurements or by Raman scattering.

A problem with this definition is that the isotropic state is not the only molecular configuration that can give an order parameter of zero. If the molecules are arranged in a cone about the director with a specific angle, S can equal zero [39, p.17]. Additional order parameters can be defined using higher order Legendre polynomials, which can remove this ambiguity, however, for the purposes of modelling it is convenient to restrict the definition to second-order.

If we consider a smectic liquid crystal with layers normal to z, the densities of the centres of mass $\rho(z)$ can be assumed to oscillate along z from one layer to the next, in a sinusoidal

fashion. A positional order parameter can then be defined as

$$\rho(z) = \rho_0 \left(1 + \psi \cos\left(\frac{2\pi z}{d}\right)\right).$$

where ψ is the (complex) positional order parameter, d is the separation between layers and ρ_0 is the average density [36].

The majority of liquid crystal phases are uniaxial in the bulk, with a single degree of rotational symmetry about the director (the distribution function f' is independent of ϕ). The search for a nematic liquid crystal that is biaxial in the bulk has been the subject of much research, and only recently have such phases been created, made possible by molecules possessing bent cores [40].

It is possible to have a uniaxial or biaxial arrangement of biaxial molecules. Biaxial molecules can be pictured as being like a plank of wood in shape. Both short and long axes of the molecules can possess orientational order in a biaxial arrangement. It is also possible that only the long axes exhibit orientational order and the short axes are randomly oriented, or vice versa. This is a uniaxial arrangement.

Uniaxial molecules can also form uniaxial or biaxial arrangements. In the uniaxial arrangement the long axes of the molecules align with each other. The biaxial arrangement of uniaxial molecules is the most difficult configuration to picture, but it is important as it arises when defects are present. This state can be induced by an applied electric field or by constrained geometries, where there are two directions in which the long axes of the molecules tend to align.

The previous definition of the orientational order parameter was in terms of an angle, but it is useful to define an order tensor, which contains information about the orientation as well as the degree of order:

$$\mathbf{Q} = \frac{1}{2}S_1(3\hat{n} \otimes \hat{n} - I) + \frac{1}{2}S_2(3\hat{m} \otimes \hat{m} - I).$$

This definition can describe a biaxial state, where S_1 and S_2 represent the degree of order along the unit vectors $\hat{n}$ and $\hat{m}$ respectively. Using the Spectral Theorem, Q may be written in the form

$$\mathbf{Q} = \lambda_1 \hat{\mathbf{e}}_1 \otimes \hat{\mathbf{e}}_1 + \lambda_2 \hat{\mathbf{e}}_2 \otimes \hat{\mathbf{e}}_2 + \lambda_3 \hat{\mathbf{e}}_3 \otimes \hat{\mathbf{e}}_3.$$

where λ_1, λ_2 and λ_3 are the eigenvalues of Q and $\hat{\mathbf{e}}_1$, $\hat{\mathbf{e}}_2$ and $\hat{\mathbf{e}}_3$ are the corresponding eigenvectors. The eigenvalues can then be written in terms of S_1 and S_2 as

$$\begin{aligned}\lambda_1 &= S_1 - \frac{1}{2}S_2, \\ \lambda_2 &= S_2 - \frac{1}{2}S_1, \\ \lambda_3 &= -\frac{1}{2}(S_1 + S_2).\end{aligned} \tag{2.3}$$

When two eigenvalues are equal this represents a uniaxial state, corresponding to one of three possible cases; only S_1 is nonzero, only S_2 is nonzero or finally $S_1 = S_2$. When all three eigenvalues differ this represents a biaxial state. In the isotropic state all the eigenvalues are identically zero.

2.5 Theory of Phase Transitions

It is possible to explain nematic ordering using a statistical theory, such as the Onsager or Maier-Saupe Theory, or alternatively a phenomenological approach can be used to describe the general characteristics of the phase transition, for example the variation in order parameter with temperature as shown in Fig. 2-2 [36].

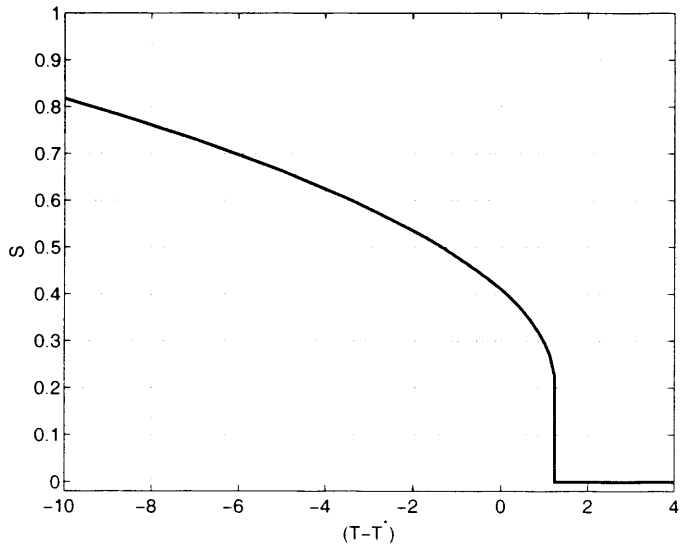

Figure 2-2: Order parameter as a function of temperature for 5CB, where T^* is the supercooling temperature, defined in Section 2.5.3. At the clearing point (when the temperature is equal to T_c) the order parameter S drops to zero. Here, $(T_c - T^*) = 1.1\,\mathrm{K}$

In the low temperature nematic phase the nematic phase is highly ordered. A flask of LC in the nematic phase appear cloudy, for reasons that will be explained in Section 2.5.3. As the temperature is increased, the order parameter drops, until at the clearing point, T_c, it falls to zero as the liquid crystal becomes isotropic. The liquid becomes transparent.

2.5.1 Onsager Theory [1]

Onsager theory is a molecular theory that tries to describe the features of the macroscopic phase from the behaviour of an individual molecule. Instead of calculating the behaviour of a huge number of molecules and how these affect the system macroscopically, it is assumed that each molecule has the same net force acting on it. Then only the forces acting on a single molecule have to be calculated, which then imply the behaviour in the bulk. An average potential is calculated for the individual molecule which then can be used to determine the forces and torques acting on the molecule.

In Onsager theory the molecules are assumed to be hard rods, with a length far greater than diameter. The only forces considered as important in this model are repulsive forces. Consider a single rod as it approaches another. The rods cannot interpenetrate each other, corresponding to a potential that is infinite when one molecule intersects another and zero otherwise. The equilibrium configuration is the state that minimises this thermodynamic potential. When the rods are parallel they can be positioned in close proximity to each other, but when they are at some angle to one another there is a large volume which the approaching cylinder cannot encroach. This angular arrangement sees a decrease in the number of positions available to the rod: the positional entropy has decreased.

A parallel arrangement of rods leads to an increase in positional entropy, but a decrease in orientational entropy. Thus, under certain circumstances the parallel arrangement will be entropically favourable, whereas in other cases the angular arrangement is favourable. This model correctly predicts a phase transition, but makes several assumptions which lead to an overly abrupt picture of the phase transition than is observed experimentally, from a strongly ordered nematic phase to a highly disordered isotropic phase. Additionally the model incorrectly predicts a transition density that is independent of temperature and an overly high value of order at the transition temperature of $S(T_c) \sim 0.84$.

2.5.2 Maier-Saupe Theory [2, 3, 4]

Onsager theory predicts a phase transition, but the many assumptions give an inaccurate picture of the transition. In Maier-Saupe theory the potential is assumed to be attractive, corresponding to van der Waals forces, and this anisotropic attraction stabilizes parallel alignment of molecules. The steric repulsions that were considered in Onsager theory may not be negligible as was assumed in the original presentation of this theory. The value of order at the transition temperature given by this theory is $S(T_c) \sim 0.44$, which is in much better agreement with experiment.

2.5.3 Landau-de Gennes Theory [5, 6, 7]

Both Onsager and Maier-Saupe theories are statistical models that fail to fully capture the features of the transitions due to the assumptions they make or through neglect of fluctuations. Landau-de Gennes theory is a phenomenological model that seeks to describe the features of the phase transition observed experimentally, without calculating inter-molecular interactions.

There are two regimes that can be distinguished. Below T_c the fluctuations in the order parameter are small, but the fluctuations in orientation are significant and can be described within the framework of the continuum elastic theory, which will be discussed in Section 2.6. These fluctuations in orientation and the resulting difference in birefringence between domains give rise to the cloudy appearance the bulk nematic phase. Assuming the discontinuities at T_c are small, then the Landau theory holds for a limited range below T_c.

Above T_c there are fluctuations in both order and orientation [7, 41]. At high temperatures the order parameter is zero. This is a long range measure, however, on short length and time scales order can be present without affecting significantly the value of S. As the temperature falls close to T_c, the free energy of the nematic states approaches that of the isotropic state. The energy barrier for the spontaneous creation of nematic "swarms" is reduced and as a result both the size and longevity of the swarms increase. The orientation of each swarm is uncorrelated and experimentally their influence can be seen in light scattering experiments.

Assuming the order parameter is small near the transition temperature, the difference

in the free energy density of the two phases can be expanded in powers of the order tensor:

$$f_B(\mathbf{Q}) := F_0 + \frac{1}{2}A(T)\,\mathrm{tr}(\mathbf{Q}^2) + \frac{1}{3}B(T)\,\mathrm{tr}(\mathbf{Q}^3) + \frac{1}{4}C(T)\,\mathrm{tr}(\mathbf{Q}^2)^2 + O(\mathbf{Q}^5). \tag{2.4}$$

in the absence of electric fields, magnetic field and elastic distortion [5, 7].

Since Q is traceless, there is no linear invariant appearing in this expression. This ensures that the isotropic state is a local minimum of the free energy. It is assumed that $A(T)$ depends linearly on the temperature, $A(T) \simeq a(T - T^*)$, and that the higher order coefficients are independent of temperature, in agreement with molecular theories. From Monte-Carlo simulations (calculating the equilibrium configuration for a large sample of molecules), it can be shown that just above T_c, B and C are not strictly independent of temperature and their values should be adjusted taking into account Gaussian fluctuations. However, for this work the former assumption is made for simplicity.

It is possible to write (2.4) in terms of S_1 and S_2 using

$$\mathrm{tr}(\mathbf{Q}^n) = \sum_{i=1}^{3} \lambda_i^n,$$

where the eigenvalues are given by (2.3). Assuming that the LC is uniaxial ($S_2 = 0$) this yields [7]:

$$f_B(S_1) := F_0 + \frac{3}{4}A(T)S_1^2 + \frac{1}{4}B(T)S_1^3 + \frac{9}{16}C(T)S_1^4 + O(S_1^5). \tag{2.5}$$

The equilibrium value of the order parameter, S_0, is given by finding the stationary values of (2.5). The first root is $S_1 = 0$, which corresponds to the isotropic phase, and the remaining two roots are given by:

$$S_0 = (-B \pm \sqrt{B^2 - 24AC})/(6C).$$

There are two (real) solutions to this equation when $B^2 > 24AC$ (when the nematic phase is stable or metastable), one negative and one positive. As described earlier (section 2.4) the negative root is unlikely to occur on physical grounds and the positive root corresponds to the equilibrium order parameter in the nematic phase.

Figure 2-3 shows the free energy, plotted as a function of order parameter for a range

of temperatures for 5CB. At high temperatures only the isotropic state is stable. As the

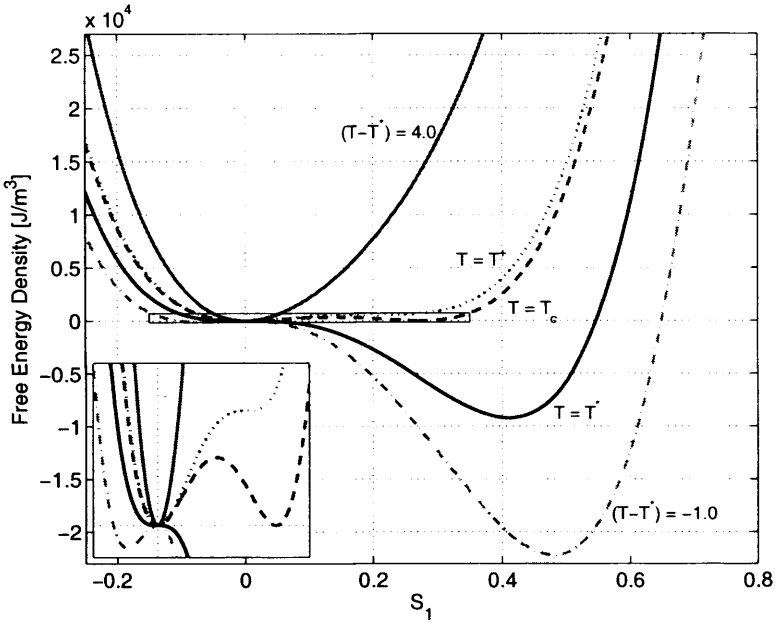

Figure 2-3: Free energy as a function of temperature for 5CB

temperature falls to T^+ the nematic state becomes metastable. In the temperate range $T_c < T < T^+$ the isotropic state remains the global minimum, but the nematic state is metastable. At the clearing point, $T = T_c$, both isotropic and nematic phases are stable and equal in energy. For this reason the T_c is sometimes written as T_{NI}. Between $T^* < T < T_c$ the isotropic state becomes metastable and the nematic state becomes the minimum energy state. Below $T < T^*$ the isotropic state becomes unstable and the nematic state is the global minimum.

$$T^+ = T^* + \frac{B^2}{24aC}. \qquad T_c = T^* + \frac{B^2}{27aC}.$$

The order parameter can be determined from measurements of the macroscopic properties of a liquid crystal, such as the optical birefringence, nuclear magnetic resonance (NMR) [42] or Raman scattering [36, p.3]. By Measuring the latent heat and the order parameter (as a function of temperature) the values of a, B and C can be found [36, p.250] (by curve fitting). In [43, Appendix], three independent measurements are taken to obtain these coefficients: the jump in order parameter at the transition, the difference in temperatures T_c and T^* and the latent heat of the transition.

2.6 Elasticity

Liquid crystals exhibit curvature elasticity like most solids: they deform under stress, and return to their initial state when the stress is removed. It is possible to treat the liquid crystal as a continuum, thereby ignoring molecular details. This approach was initiated by Oseen [18], Zocher [19] and Frank [20], based on the minimisation of an energy constituted by elastic and electric terms. The elastic constants of a liquid crystal determine the restoring torques that arise when the system is perturbed from its equilibrium configuration. These deformations can be divided into three basic types; splay, twist and bend.

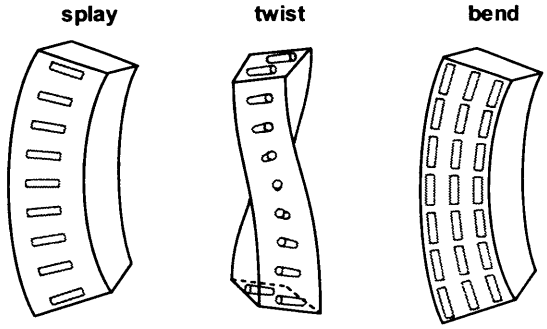

Figure 2-4: Types of deformation in liquid crystals, after [13, p.14]

The elastic energy density can be written as a Taylor expansion in the gradients of the director field [39]:

$$f_D(\hat{n}, \nabla\hat{n}) = k(\hat{n}) + \mathbf{K}(\hat{n}) \cdot \nabla\hat{n} + \nabla\hat{n} \cdot \mathbb{K}(\hat{n}) \cdot \nabla\hat{n},$$

where $\mathbf{K}$ is a second-order tensor and $\mathbb{K}(\hat{n})$ is a fourth-order tensor. Simplification is possible by taking into account the material symmetries of LCs. Firstly, the free energy, $\mathcal{F}$, should be frame-indifferent. In other words the free energy should be the same in any two rigid frames, implying that:

$$f_D(O\hat{n}, O\nabla\hat{n}O^T) = f_D(\hat{n}, \nabla\hat{n}),$$

where O is a proper orthogonal tensor, i.e. $OO^T = I$, $\det(O) = 1$ [39]. The second

requirement is evenness

$$f_D(-\hat{n}, -\nabla\hat{n}) = f_D(\hat{n}, \nabla\hat{n}),$$

and finally $|\hat{n}| = 1$. Taking into account the restrictions given above, f_D takes the form:

$$\begin{aligned} f_D = \; & \frac{1}{2}K_{11}\,(\nabla \cdot \hat{n})^2 + \frac{1}{2}K_{22}\,(\hat{n} \cdot \nabla \times \hat{n} + q_0)^2 + \frac{1}{2}K_{33}\,|\hat{n} \times \nabla \times \hat{n}|^2 + \\ & \frac{1}{2}(K_{22} + K_{24})[\mathrm{tr}(\nabla\hat{n})^2 - (\nabla \cdot \hat{n})^2], \end{aligned} \tag{2.6}$$

where K_{11}, K_{22} and K_{33} are elastic constants associated with splay, twist and bend deformations and the final $K_{22} + K_{24}$ term is often referred to as the saddle-splay modulus. The chirality parameter q_0 is equal to $2\pi/p$, where p is the pitch of the LC.

When an electric field is applied to switch the liquid crystal it is the balance between the electric torque and the elastic restoring torques that determines the resulting director profile. The total free energy can be written

$$\begin{aligned} \mathcal{F} &:= \mathcal{F}_D - \mathcal{F}_E + \mathcal{F}_S \\ &= \int_\Omega \{f_D - f_E\} + \int_\Gamma \{f_S\}, \end{aligned} \tag{2.7}$$

where f_S is a surface term arising from the anchoring at the alignment layers and f_E is the electrostatic energy density,

$$f_E := \frac{1}{2}\varepsilon_0(\vec{E} \cdot \bar{\bar{\varepsilon}} \cdot \vec{E}),$$

which is a function of the electric field, $\vec{E}$, and the permittivity tensor $\varepsilon_{\alpha\beta} = \varepsilon_\perp\delta_{\alpha\beta} + \Delta\varepsilon n_\alpha n_\beta$. A similar expression can be written in terms of the magnetic field.

In a liquid crystal with a positive dielectric anisotropy the molecules tend to align parallel with an applied electric field. For a negative dielectric material the molecules favour perpendicular alignment. An LC cell comprises an LC layer sandwiched between glass substrates. By design, the molecules have a preferred alignment at these substrates, giving rise to an elastic force that opposes the response to the electric field. Removing the applied field thus restores the starting molecular configuration.

As a result of these opposing forces, reorientation of the liquid crystal is a threshold

phenomenon. There is no elastic distortion until a voltage threshold is overcome at the Fréedericksz transition (assuming zero pre-tilt at the surfaces). This threshold voltage for a planar aligned cell is [44]:

$$V_{th} = \pi \sqrt{\frac{K_{11}}{\varepsilon_0 |\Delta\varepsilon|}}.$$

When the applied voltage exceeds V_{th}, the Fréedericksz threshold, a region of elastic distortion arises between the surfaces and the bulk. This region is of finite extent and is defined as the electric coherence length. Using a one elastic constant approximation it may be written as

$$\xi_e = \frac{1}{|E|} \sqrt{\frac{K_{11}}{\varepsilon_0 |\Delta\varepsilon|}}.$$

2.7 Defects

In Section 2.2.1 it was stated that nematics were so named due to the filaments that can be observed when viewed by a polarising microscope [7, 45, 46]. Such structures correspond to discontinuities in the director (as first suggested by [47]) and are referred to as disclinations [48]. In a display pixel, rubbing or photo-alignment are used at the alignment layers to ensure that the director field is uniform. Without this alignment, many nematic domains form and at the interface between these domains the director field is often discontinuous. This pattern of defects when observed between crossed polarisers is known as a '*Schlieren* texture' [49].

The director can be discontinuous at a point, along a line or a surface. Point and line disclinations are stable, but sheet disclinations are unstable and spontaneously smear. In the absence of an applied field the region of distortion will completely disappear. However, in the presence of an applied field a sheet disclination will smear out to occupy a region of finite extent, the thickness of which is defined as the electric or magnetic coherence length. Such structures are referred to as [domain] walls. There is no discontinuity in the director, which varies continuously in the wall, either by bending, splaying, twisting or by some combination of the three deformations.

Fig. 2-5 shows some common disclination types, which are classified by their strength: the number of times the director field rotates by 2π about the disclination core. Disclinations

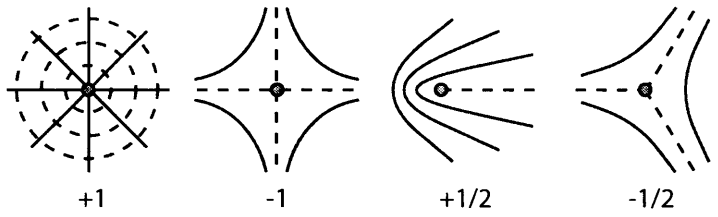

Figure 2-5: Example of line disclinations that arise in liquid crystals, after [7]

of half-integral index are associated with lines, whereas integral index disclinations can be associated with either lines or points. Point disclinations have a high distortion energy and are only stable in confined geometries. Any disclination points or lines with strength greater than 1/2 are metastable and tend to split into a number of 1/2 disclination lines that then move apart, reducing the free energy [50]. For example, a +1 disclination will split into two +1/2 disclinations.

For the purposes of modelling, the discontinuity in the director field at the disclination core can present a problem in a continuum theory. If the order is not allowed to vary, the free energy density tends to infinity here and the Euler-Lagrange equations become ill-conditioned. In order to model disclination dynamics it is possible to introduce cuts to exclude this singularity [51], or to make use of Landau theory, whereby the order parameter changes to accommodate the disclinations whilst the Q-tensor components vary smoothly.

2.8 Modelling Methods

Molecular and mesoscopic simulations gain the most attention, but recently there has been renewed interest in all-atom simulations [52, 53, 54]. Currently, all-atom simulations are feasible over short time scales (tens of nanoseconds) and are limited to a few hundred molecules.

Molecular simulations seek the position and orientations of a set of interacting molecules [27]. There are two main methods by which these quantities are found, Molecular Dynamics (MD) and Monte Carlo (MC). In Molecular Dynamics the laws of classical mechanics are used to determine the force and torque acting on each molecule, which in turn are calculated from an interaction potential. This represents the potential energy of a particular arrangement of molecules, and are usually based on pairwise interactions. In the Monte

Carlo approach molecules are displaced or rotated by a random amount, and the changes are accepted or rejected according to a rule. For instance a change will be accepted if it lowers the potential energy.

The problem is reduced to that of finding a potential function that describes the behaviour of the material. A Hamiltonian may be written, taking into account interaction between nuclei and electrons. The potential can be then found (rigourously) by solving the Schrödinger equation. This is feasible, but computationally expensive and so more commonly an analytic form is selected that approximates the true potential.

For liquid crystals the most commonly used potential is the Gay-Berne potential [55, 56]. It is an extension of the Lennard-Jones potential to anisotropic pair interaction.

Molecular simulations have been shown able to reproduce the various liquid crystal phases, using samples of a few thousand molecules [25, 26]. Such simulations are performed on relatively short length and time scales. To simulate real devices the length scales are in the order of microns and the time scale milliseconds. The sheer number of molecules precludes feasible simulation times. Mesoscopic approaches are an ideal means to tackle such calculations. Instead of modelling each individual molecule or atom the orientation of the liquid crystal is considered a smoothly varying function of time and space. The continuum theory provides a means to find this function. For example the orientation of the liquid crystal is given by the function that minimises the functional $\mathcal{F}$ in Section 2.6, subject to certain boundary conditions. Typically, analytic solutions to such boundary value problems are available only for a limited set of conditions. In general, a numerical approach, such as the finite difference or finite element method to name but two, are required to solve such problems.

Chapter 3

Optical Modelling

3.1 Introduction

Materials that form liquid crystal phases have rod or disc like molecules. This anisotropy in shape leads to an anisotropy in electric, magnetic and optical properties. A flask of liquid crystal in the isotropic phase will appear clear, as the molecules are randomly oriented so that on average there is no change in the refractive index. On cooling below the cooling point, many nematic domains form, and from one domain to the next the average molecular orientation is uncorrelated. At the domain boundaries the change in refractive index scatters light, leading to a milky appearance. In a large sample, fluctuations in orientation contribute further to this scattering.

Most nematic liquid crystals have uniaxial optical symmetry with two refractive indices n_o and n_e. Incident light with a polarisation state perpendicular to the director sees a refractive index of n_o, whereas the parallel state sees a refractive index of n_e. The birefringence is defined as $\Delta n = n_e - n_o$, and tends to be positive for most liquid crystals.

Commonly the Jones [8] or Berreman [9] methods are used, in conjunction with ray-tracing techniques to determine the optical transmission of a liquid crystal cell from a given director field. An advantage of the Berreman method over that Jones method is that it takes into account reflections between adjacent layers, which can be significant, particularly when a device contains absorbing layers.

When modelling display pixels (such as planar or IPS cells) the director orientation varies on large length scales relative to the wavelength of light. As the resolution increases, the director orientation can vary on the same scale as the wavelength of light, particularly in the inter-pixel gaps. In this case, the lateral variation in the permittivity can cause light to diffract and the Jones and Berreman methods break down.

Instead the full solution to Maxwell's Equations must be sought. There are several ways commonly used to discretise these equations, the finite-difference time-domain (FDTD) method [21], the beam propagation method [22] and the coupled wave method [23]. In the coupled wave or grating method (GM) the cell is regarded as the fundamental unit of a periodic structure in the transverse plane (normally the plane parallel to the alignment surfaces), composed of several layers. Each layer has it own constant dielectric tensor.

The grating method is well suited to the study of periodic structures. The structure is divided into a number of layers and in each layer the permittivity is assumed periodic and

is described as a Fourier series. As in the Berreman method a transfer matrix is formed for each layer and the product of all the transfer matrix can be used to fully characterize optical propagation through the LC medium.

In this work both the Jones method and the grating method have been used. Two GM implementations were available, the first written by Chris Desimpel and Hans Desmet from the Liquid Crystals & Photonics Group at Ghent University, Belgium. The second is a reduced order implementation, as detailed in [11]. This chapter details these two methods.

3.2 Plane waves and Polarisation states

Light incident on an LC cell can be represented as electromagnetic waves; specifically plane waves. The electric field oscillates in the direction perpendicular to the propagation vector. The direction of these transverse oscillations in light emerging from a lamp or laser will be uncorrelated from one wave to the next. The light is said to be unpolarised. In an isotropic medium a wave propagates at the same speed regardless of the direction of the wave in this plane. In a liquid crystal this is no longer the case and the propagation speed changes with the angle of oscillation. Using the principle of superposition, incoming waves can be decomposed into two independent directions of vibration. The polarisation state can be characterized by the magnitude of these two components. The two components of the electric field may be written as

$$E_x = A_x \cos(\omega t - kz + \delta_x)$$
$$E_y = A_y \cos(\omega t - kz + \delta_y).$$

where k is the wave number, ω is the angular frequency, A_x and A_y are amplitude coefficients and δ_x and δ_y represent the phase. If $\delta_y - \delta_x = 0$ or π then the light is said to be linearly polarised (along $A_x x = A_y y$.)

When $\delta_y - \delta_x$ is non-zero the electric field vector rotates in the xy-plane and its endpoint traces an ellipse. In the special case when $\delta_y - \delta_x = \pm\pi/2$ and $A_x = A_y$ then the light is circularly polarised. The endpoint of the electric field vector traces a circular path.

The polarisation state of an arbitrary wavefront may be represented by a Jones vector,

$$J = \begin{pmatrix} A_x \exp(i\delta_x) \\ A_y \exp(i\delta_y) \end{pmatrix}$$

which contains the complex amplitude coefficients of the electric field components. Usually we are interested only in the polarisation state, in which case a normalised Jones vector may be used.

In display devices LC cells are usually placed between a pair of polarisers. The first polariser allows the beams entering the LC medium to vibrate in one direction only. The emerging light is said to be linearly polarised. As light propagates through the LC, the polarisation state of the light changes and the transmission depends on the orientation of the output polariser and the polarisation state of the light exiting the LC. By changing the applied voltage the intensity of the transmitted light can be controlled.

There are many possible configurations of LC cell in terms of electrode patterns, and rubbing directions that are used in displays. The planar, twisted and IPS cells are examples of commonly used cell types. There are two mechanisms that can be exploited to change the polarisation state of the outgoing wavefront. The first mechanism is exploited in the planar cell. The polariser is oriented at 45° to the rubbing direction. Light propagating through the LC layer can be considered as the superposition of two components, one perpendicular, the other parallel to the director, each of which propagate at different speeds. At the exit of the cell a phase difference will exist between the two components. If this optical path length is set correctly, the phase difference will be π; effectively the polarisation state will have undergone a 90° rotation. Applying a voltage tilts the director and reduces the phase difference. The wavelength of light that maximises the transmittance will therefore depend on the voltage and so planar cells appear coloured. For this reason they are unpopular for display applications.

The twisted cell operates using a second mechanism; guiding. The upper alignment layer is rubbed at 90° relative to the lower alignment surface. The molecules are twisted in the bulk of the LC and if the cell is sufficiently thick, then the polarisation state of the propagating light will follow this twist. Such cells operate almost independently of the wavelength. It is possible to exploit both effects to maximise the transmittance for thin cells, as in the MTN mode [57].

3.3 Jones Method [8]

In the previous section it was shown how the polarisation state of a plane-wave can be described by a Jones vector. For a layer of material we can write the incoming Jones vector as $[Ex, Ey]^T$ and the outgoing vector as $[Ex', Ey']^T$. A Jones matrix maps the incoming to the outgoing Jones vector:

$$\begin{pmatrix} Ex' \\ Ey' \end{pmatrix} = \mathbf{M} \begin{pmatrix} Ex \\ Ey \end{pmatrix}.$$

The Jones matrix, M, of a uniaxial layer with its optic axis aligned along x may be written as

$$\mathbf{M} = \begin{pmatrix} \exp(-in_{eff}\frac{2\pi}{\lambda}d) & 0 \\ 0 & \exp(-in_o\frac{2\pi}{\lambda}d) \end{pmatrix},$$

where λ is the wavelength and d is the layer thickness. The relative phase difference between the two propagating components after the layer is $\delta = 2\pi\Delta nd/\lambda$. The effective refractive index, n_{eff}, accounts for the effective reduction in birefringence caused by the tilt angle of the director, which can be calculated by:

$$\frac{1}{n_{eff}^2(\theta)} = \frac{\sin^2(\theta)}{n_o^2} + \frac{\cos^2(\theta)}{n_e^2}$$

When the fast axis is not aligned along x the Jones matrix may be written as

$$\mathbf{M}' = \mathbf{R}(-\chi)\mathbf{M}\mathbf{R}(\chi),$$

where $\mathbf{R}$ is a rotation matrix and χ is angle between the slow-fast axis of the layer and the xy-axis [13]. The rotation matrix on the right hand side decomposes the light onto the slow and fast axis of the medium. Finally the rotation matrix on the left hand side transform the polarisation state back to the xy-coordinates. $\mathbf{R}$ is defined as

$$\mathbf{R}(\chi) = \begin{pmatrix} \cos(\chi) & \sin(\chi) \\ -\sin(\chi) & \cos(\chi) \end{pmatrix}.$$

In a liquid crystal cell the orientation of the director can vary throughout the structure. The LC layer may be divided into a number of layers and a Jones matrix can be written for each layer. Taking the product of each Jones matrix then relates the polarisation state of the incident wave to that of the transmitted wave for the whole device.

The strength of the Jones method lies in its simplicity and speed. The original formulation assumes normal incidence, but the extended Jones Method was developed to allow oblique incidence [58, 59].

3.4 Maxwell's Equations

In order to calculate the propagation of light through an LC medium one needs to find the solution to Maxwell's equations. The Jones method that was previously introduced is itself a solution to these equations, making a number of simplifying assumption. The phasor form of these can be written:

$$\nabla \times \vec{E} = -i\omega\mu_0\vec{H} \tag{3.1}$$

$$\nabla \times \vec{H} = i\omega\varepsilon_0\bar{\bar{\varepsilon}}\vec{E}, \tag{3.2}$$

where μ_0 is the permeability of free space. These equations can be written in tensor notation as

$$\begin{aligned} \sigma_{ijk}\partial_j E_k &= -i\omega\mu_0 H_i \\ \sigma_{ijk}\partial_j H_k &= i\omega\varepsilon_0\varepsilon_{ij}E_j \end{aligned} \tag{3.3}$$

For both the Berreman and grating methods, the structure is divided into layers, as shown in Fig. 3-1. This significantly reduces the order of the problem as the equations can be solved locally within each layer. In the Berreman method the permittivity is assumed to a be function of z only, whereas in the grating method the permittivity may vary along x and y, therefore diffractive effects are taken into account. Complementary methods, such as finite element or finite difference methods do not divide the structure in this fashion, integration is performed on a global basis.

It is convenient to rearrange (3.1) and (3.2) (following [11]) so that they depend only on transverse components of the magnetic and electric fields, and can be solved within each

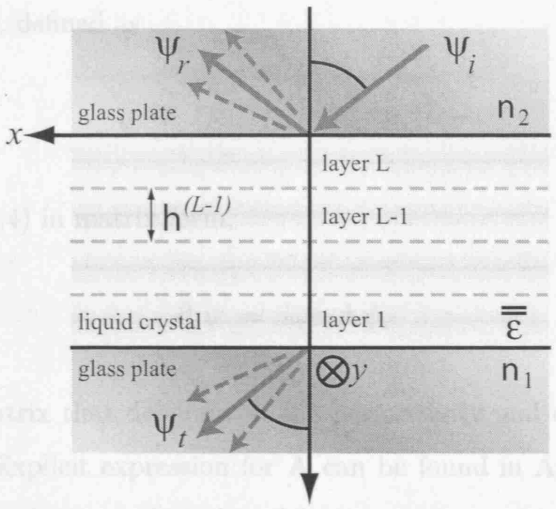

Figure 3-1: For the grating and Berreman methods the LC layer is divided into a number of layers. ψ is a vector that contains the transverse components of the electric and magnetic field. ψ_i is the incident, ψ_r the reflected and ψ_t the transmitted vector

layer. Setting $i = z$ in 3.3 gives the longitudinal equations:

$$\sigma_{z\gamma\lambda}\partial_\gamma E_\lambda = -i\omega\mu_0 H_z$$

$$\sigma_{z\gamma\lambda}\partial_\gamma H_\lambda = i\omega\varepsilon_0\varepsilon_{z\gamma}E_\gamma + i\omega\varepsilon_0\varepsilon_{zz}E_z,$$

which can be rearranged to give expressions for E_z and H_z in terms of the transverse field components.

From (3.1) and (3.2) the transverse equations can be obtained by setting $i = \alpha = \{x, y\}$:

$$\sigma_{\alpha\beta z}\partial_\beta E_z + \sigma_{\alpha z\beta}\partial_z E_\beta = -i\omega\mu_0 H_\alpha$$

$$\sigma_{\alpha\beta z}\partial_\beta H_z + \sigma_{\alpha z\beta}\partial_z H_\beta = i\omega\varepsilon_0\varepsilon_{\alpha\beta}E_\beta + i\omega\varepsilon_0\varepsilon_{\alpha z}E_z$$

Substituting the expressions for E_z and H_z yields the following equations that contain only transverse field components, the Marcuvitz-Schwinger equations:

$$\sigma_{\alpha\beta z}\partial_\beta \frac{1}{i\omega\varepsilon_0\varepsilon_{zz}}\left(\sigma_{z\gamma\lambda}\partial_\gamma H_\lambda - i\omega\varepsilon_0\varepsilon_{z\gamma}E_\gamma\right) + \sigma_{\alpha z\beta}\partial_z E_\beta = -i\omega\mu_0 H_\alpha$$

$$\sigma_{\alpha\beta z}\partial_\beta\left(\frac{-1}{i\omega\mu_0}\sigma_{z\gamma\lambda}\partial_\gamma E_\lambda\right) + \sigma_{\alpha z\beta}\partial_z H_\beta = i\omega\varepsilon_0\varepsilon_{\alpha\beta}E_\beta + \frac{i\omega\varepsilon_0\varepsilon_{\alpha z}}{i\omega\varepsilon_0\varepsilon_{zz}}\left(\sigma_{z\gamma\lambda}\partial_\gamma H_\lambda - i\omega\varepsilon_0\varepsilon_{z\gamma}E_\gamma\right). \tag{3.4}$$

Introducing a vector ψ, defined as

$$\psi = [E_x, E_y, H_x, H_y]^T,$$

it is possible to cast (3.4) in matrix form:

$$\partial_z \psi = i\omega\varepsilon_0 \mathbf{A}\psi, \tag{3.5}$$

where $\mathbf{A}$ is a 4×4 matrix that depends on the permittivity and contains the differential operators ∂_x and ∂_y. Explicit expression for $\mathbf{A}$ can be found in Appendix A.1. It can be demonstrated that the solution to (3.5) has the form

$$\psi(z_0 + h) = \exp(ik_0 A h)\psi(z_0) \quad \text{or} \quad \psi(z_0 + h) = \mathbf{T}^{(l)}\psi(z_0)$$

and the propagation though each layer can be described by a transfer matrix, $\mathbf{T}^{(l)}$. For the whole stack of layers comprising the LC the global transfer matrix is given by the product of the individual transfer matrices.

$$\mathbf{T} = \prod_{l=1}^{L} \mathbf{T}^{(l)}, \qquad \mathbf{T}^{(l)} = \exp(ik_0 \mathbf{A} h^{(l)})$$

The difficulty lies in calculating the exponential of a matrix to determine the transfer matrix of each layer. This can be calculated using the Maclaurin series:

$$\exp(\mathbf{M}) = 1 + \mathbf{M} + \frac{\mathbf{M}^2}{2!} + \frac{\mathbf{M}^3}{3!} + ...$$

where $\mathbf{M} = ik_0 A h^{(l)}$. However, this sequence is slowly converging. $\mathbf{T}^{(l)}$ can be calculated more efficiently from the eigenvectors and eigenvalues of $\mathbf{M}$:

$$\mathbf{T}^{(l)} = V \exp(\lambda) V^{-1} \tag{3.6}$$

Here, V is the eigenvector matrix of $\mathbf{M}$ and λ is a matrix whose diagonal entries are the eigenvalues of $\mathbf{M}$.

3.4.1 Berreman Method [9]

In the Berreman method it is assumed that the permittivity tensor does not vary along x nor y. Then the spatial derivatives in the x and y direction reduce to $\partial/\partial x_\alpha = -ik_\alpha$ [9], where k_α is the wavenumber in the α direction.

After assembling the **T** matrix for the whole stack of layers comprising the LC, the incident, transmitted and reflected field vectors satisfy

$$\psi_t = \mathbf{T}(\psi_i + \psi_r).$$

Since the tangential components of the electric and magnetic fields are continuous across the LC-glass interface, it is possible to rearrange this equation to give the reflection and transmission coefficients for transverse electric (TE) and transverse magnetic (TM) polarisations.

3.4.2 Grating Method [10, 11]

In the grating method the permittivity tensor is assumed to vary laterally as well. The permittivity is assumed to be a periodic function of x and y so that it may expressed in terms of a Fourier series as

$$\varepsilon_{ij}(x, y, z) = \sum_{m,n=-\infty}^{\infty} \tilde{\varepsilon}_{ij}^{(m,n)}(z) \exp(-ik_{x,m}x - ik_{y,n}y),$$

where $k_{x,m} = 2\pi n/d_x$, $k_{y,m} = 2\pi n/d_y$ and d_α is the length of the structure along α [10, 11].

According to the Bloch-Floquet theorm the electromagnetic field inside and outside the grating can be expressed by the Fourier series

$$\upsilon(x, y, z) = \sum_{m,n=-\infty}^{\infty} \tilde{\upsilon}^{(m,n)}(z) \exp(-i\alpha_m x - i\beta_n y),$$

with

$$\alpha_n = k_{x,inc} + k_{x,n} = k_0 \sin(\theta)\cos(o) + 2\pi n/d_x$$

$$\beta_n = k_{y,inc} + k_{y,n} = k_0 \sin(\theta)\sin(o) + 2\pi n/d_y.$$

When these two series are substituted into (3.5), products of the electromagnetic field and the permittivity in the time domain arise. A product in the time domain corresponds to a (discrete) convolution in the frequency domain. This is known as Laurent's rule or the Convolution theorem:

$$(F * G)_n = \sum_{m=-\infty}^{\infty} F_{n-m} G_m$$

The product of the permittivity and the field vector ψ becomes

$$(\varepsilon_{ij} * \psi)_{p,q} = \sum_{m,n=-\infty}^{\infty} \tilde{\varepsilon}_{ij}^{(p-m,q-n)} \exp(-ik_{x,p-m}x - ik_{y,q-n}y)\tilde{\psi}^{(m,n)} \exp(-i\alpha_m x - i\beta_n y).$$

A differential equation may then be written in terms of the Fourier coefficients:

$$\partial_z \tilde{\psi} = i\omega\varepsilon_0 \tilde{\mathbf{A}} \tilde{\psi}. \tag{3.7}$$

This equation can be solved using numerical integration, but a very fine spatial discretisation is required to avoid numerical dissipation. For this reason the method outlined at the end of section 3.4 is used instead.

The first block of $\mathbf{A}$, a_{11}, is equal to $i/k_0\,(\partial_x \varepsilon'_{zx} + \varepsilon'_{zx}\partial_x)$, where $\varepsilon'_{zx} = \varepsilon_{zx}/\varepsilon_{zz}$ and can be calculated as

$$\begin{aligned} k_0 \tilde{a}_{11} \tilde{E}_x^{(m,n)} &= i(\partial_x \tilde{\varepsilon}_{zx}^{\prime(p-m,q-n)} \tilde{E}_x^{(m,n)} + \tilde{\varepsilon}_{zx}^{\prime(p-m,q-n)} \partial_x \tilde{E}_x^{(m)}) \\ &= i(-ik_{x,p-m} \tilde{\varepsilon}_{zx}^{\prime(p-m,q-n)} \tilde{E}_x^{(m,n)} - i\alpha_m \tilde{\varepsilon}_{zx}^{\prime(p-m,q-n)} \tilde{E}_x^{(m,n)}) \\ &= \alpha_p \tilde{\varepsilon}_{zx}^{\prime(p-m,q-n)} \tilde{E}_x^{(m,n)}. \end{aligned}$$

If the region is homogeneous, then equations (3.1) and (3.2) reduce to a Helmholtz equation for the transverse field components with solution:

$$u_{m,n}(z) = A_{m,n}^{(L)} \exp(-i\gamma_{m,n}^{(L)} z) + B_{m,n}^{(L)} \exp(i\gamma_{m,n}^{(L)} z),$$

where

$$\alpha_m^2 + \beta_n^2 + \gamma_{m,n}^2 = k = \varepsilon k_0^2. \tag{3.8}$$

Here, ε is the permittivity of the (ambient) medium from where the wave is incident. The value of $\gamma_{m,n}$ is calculated from (3.8) and requires special treatment when the refractive index is complex [10]. The total field is given by:

$$u(x,y,z) = \sum_{m,n=-\infty}^{\infty} A_{m,n}^{(L)} \exp(-i\alpha_m x - i\beta_n y - i\gamma_{m,n}^{(L)} z) + B_{m,n}^{(L)} \exp(-i\alpha_m x - i\beta_n y + i\gamma_{m,n}^{(L)} z).$$

The first term comprises a finite number of incident propagating plane waves and an infinite number of evanescent plane waves. Evanescent waves are formed due to total internal reflection at an interface and decay exponentially with distance from this interface. The second term comprises a finite number of outgoing propagating plane waves and an infinite number of evanescent waves. For a unique solution to exist, the input incident field must be known. With a single incident beam this equation takes the form of a Raleigh expansion at the entrance of to medium:

$$u(x,y,z) = A_{0,0}^{(L)} \exp(-i\alpha_0 x - i\beta_0 y - i\gamma_{0,0}^{(L)} z) + \sum_{m,n=-\infty}^{\infty} B_{m,n}^{(L)} \exp(-i\alpha_m x - i\beta_n y + i\gamma_{m,n}^{(L)} z).$$

It is assumed that no waves are incident from the substrate side, and so the Raleigh expansion of the transmitted field in the substrate simplifies to:

$$u(x,y,z) = \sum_{m,n=-\infty}^{\infty} A_{m,n}^{(1)} \exp(-i\alpha_m x - i\beta_n y - i\gamma_{m,n}^{(1)} z).$$

3.4.3 Single Layer

The differential equations contain at most second order derivatives and there are several numerical algorithms that can be used to find the solution provided that the field and its first derivative are known at the interfaces. For this problem, however, the amplitudes of the reflected and transmitted waves are not known and a different method must be used.

The shooting method provides a means to find the solution to this boundary-value problem. A brief overview of the method will be given here, but a complete description can be found in [10]. First of all a set of particular solutions are constructed that correspond to a transmitted wave of unit amplitude. The transmitted wave can be written as the sum of two independent polarisation states, the transverse magnetic and transverse electric fields. For normal incidence these components can be considered as propagating independently

within the LC layers, but this is no longer the case for conical diffraction.

By solving (3.7) using integration or by directly computing $\exp(i\omega\varepsilon_0\tilde{\mathbf{A}})$ a set of input vectors is obtained, each corresponding to one of the particular solutions.

The tangential components of the electric and magnetic field are continuous across the interface between the top layer of the stack and the superstrate (as they are across all interfaces). These Fourier components obtained from the shooting method can be matched to the Rayleigh expansions at the top of layer. By solving the system of equations the Rayleigh coefficients can be fully determined. The reflected and transmitted waves are then known.

3.4.4 Stack of Layers

The simplest way to deal with a stack of gratings is to form the **T** matrix for the whole of the LC layer as was done in the Berreman method and perform matching with the Rayleigh expansion as outlined above. When the Rayleigh coefficients are known, the transmitted and reflected wave can be directly found from the Rayleigh expansion for any incident field.

Another method is to assume that separating each layer of the stack is an infinitely thin layer of the superstrate in which the Rayleigh expansion is valid. The problem can be written in matrix form, where the matrix relates the Rayleigh coefficients of the up-going and down-going waves. This is known as the **T** matrix propagation algorithm [10].

$$\begin{pmatrix} A^{(L)}_{m,n}\exp(i\gamma^{(L)}_{m,n}z_{L-1}) \\ B^{(L)}_{m,n}\exp(-i\gamma^{(L)}_{m,n}z_{L-1}) \end{pmatrix} = \begin{pmatrix} \mathbf{T}_{11} & \mathbf{T}_{12} \\ \mathbf{T}_{21} & \mathbf{T}_{22} \end{pmatrix} \begin{pmatrix} A^{(1)}_{m,n}\exp(i\gamma^{(1)}_{m,n}z_0) \\ B^{(1)}_{m,n}\exp(-i\gamma^{(1)}_{m,n}z_0) \end{pmatrix}.$$

where in fact there are two sets of $A_{m,n}$ and $B_{m,n}$ coefficients corresponding the transverse electric and magnetic fields.

A problem with the **T**-matrix approach becomes apparent when a large number of beams (Fourier components) are used. The **T**-matrix links evanescent waves in one layer to the next, and as the number of layers increases, these terms can grow exponentially [60]. Due to the finite precision of floating point arithmetic this results in numerical contamination. In LC regions such waves can be neglected, but this is no longer the case for regions with complex refractive index or finite conductivity, such ITO layers or polarisers.

This numerical contamination can be avoided using the **S**-Matrix propagation algorithm [10, 61, 60]. The **S**-Matrix can be calculated recursively from the **T**-matrices of each layer

and can be interpreted as reflection and transmission matrices, which remain bounded.

$$\begin{pmatrix} B_{m,n}^{(L)} \exp(-i\gamma_{m,n}^{(L)} z_{L-1}) \\ A_{m,n}^{(1)} \exp(i\gamma_{m,n}^{(1)} z_0) \end{pmatrix} = \begin{pmatrix} \mathbf{S}_{11} & \mathbf{S}_{12} \\ \mathbf{S}_{21} & \mathbf{S}_{22} \end{pmatrix} \begin{pmatrix} B_{m,n}^{(1)} \exp(-i\gamma_{m,n}^{(1)} z_0) \\ A_{m,n}^{(L)} \exp(i\gamma_{m,n}^{(L)} z_{L-1}) \end{pmatrix}$$

3.4.5 Reduced Grating Method [11]

For 3D problems, the size of the system matrix, $\tilde{\mathbf{A}}$, becomes very large. The Reduced [Order] Grating Method (RGM) [11] reduces the order of the calculation by projecting the system matrix onto a Krylov subspace.

Initially, it is assumed that ψ_r is zero, so that the Rayleigh coefficients at the entrance to the stack are known. Using this assumption it is possible to project the system matrix onto a subspace calculated from ψ_i. In order to take into account the reflections between the stack and the glass substrate, iterations are required to make corrections to the Rayleigh coefficients at the entrance to the stack. In each iteration the propagation through the entire stack has to be calculated. Typically convergence is achieved within two or three iterations.

The starting point for the RGM is to notice that solution to (3.7) can be written as a Maclaurin series:

$$\tilde{\upsilon}(z_0 + h) = \tilde{\upsilon}(z_0) + ik_0 h\tilde{\mathbf{A}} \cdot \tilde{\upsilon}(z_0) + \frac{(ik_0 h\tilde{\mathbf{A}})^2}{2!} \cdot \tilde{\upsilon}(z_0) + \ldots$$

A large number of Krylov vectors, $r_k = \tilde{\mathbf{A}}^k \tilde{\upsilon}(z_0)$, are required to calculate accurately $\tilde{\upsilon}(z_0 + h)$. The Krylov vectors are linearly dependent and so only a few (Q) well chosen orthogonal vectors are required to represent $\tilde{\upsilon}(z_0 + h)$ accurately. A Lanczos procedure can be used to calculate this basis and then a much reduced system matrix can be written in terms of this basis. The solution to (3.7) is then obtained by taking the exponential of this $Q \times Q$ reduced system matrix, which can be quickly calculated using equation (3.6). Another advantage of this method is that the system matrix does not have to be stored in full, instead only the first Krylov vector needs to be saved.

A disadvantage of this approach is that numerical contamination occurs if real polarisers or a large number of beams are used. Unfortunately an algorithm similar to the **S**-matrix propagation algorithm is yet to be developed in conjunction with a reduced order approach.

Chapter 4

The Finite Element Method

4.1 Introduction

Differential equations can be formulated for many of the fundamental laws of physics, biology and chemistry. For instance the electric potential in a medium can be found by solving one such equation, the Laplace equation. There are several types of differential equation, two of which are considered here. An ordinary differential equation (ODE) contains functions of one independent variable, and derivatives in that variable. A partial differential equation (PDE) contains functions of multiple independent variables and their partial derivatives.

In some cases the fundamental laws are better formulated as integral equations. Sometimes a problem can be formulated in either way, for example Maxwell's equations.

On its own a differential or an integral equation has many possible solutions. If some additional information is known, such at the value of the function at a certain position, then it is often possible restrict the number of solutions.

If the equation is dependent on both space and time, the function could be given at a given time for all space. By solving the equation it is possible to determine how the function evolves in time from the starting configuration. This is known as an initial value problem (IVP).

Another class of problems that commonly arise in engineering and physics are boundary value problems (BVPs). Here the value of the function is specified and constant at a number of points in space. An example of such a problem would be finding the electric potential in the dielectric region of a capacitor with a fixed voltage applied to the electrodes.

For a large class of initial value problems the solution can be shown to exist and to be unique. Boundary value problems may have a unique, a finite number, or maybe infinitely many solutions. A solution may not exist at all. When there are multiple possible solutions it is necessary to take a guess at the solution in order to find a solution to the differential equation.

The finite element method is a numerical technique widely used to find the numerical solution to initial and boundary value problems. It is based on a discretisation of the domain into smaller regions, or elements, where the solution sought is approximated by simpler functions. The overall solution is then constructed by the juxtaposition of these functions. This process converts a problem based on differential or integral equations (or a combination of both) into an algebraic problem, well suited for computer solution. One

important advantage of the method is that it is "exact in the limit", that is, the solution will monotonically improved when the mesh is refined.

This technique is well suited to modelling complex geometries such as liquid crystal microlenses or colloid particles immersed in a LC. For the majority of the work presented in this thesis the finite element method has been employed, and this chapter briefly describes the foundations of this method.

To begin, a description of the weighted residual approach is given, followed by a brief introduction to variational forms. Finally a finite element discretisation of the Poisson equation in an anisotropic medium is described, which is used to calculate the electric potential in the liquid crystal for all simulations presented in this thesis.

4.2 Weighted Residuals

Weighted residuals is a method for obtaining the approximate solutions to differential equations. Consider a differential equation written in the general form:

$$\mathcal{L}u = g,$$

over a domain Ω with boundary, where $\mathcal{L}$ is a linear operator and g is the excitation function. The system can be solved to find the unknown function u. In some cases a closed form solution can be obtained, but for many problems in particular for those of practical interest a closed form is unavailable and a numerical method is required. To make the numerical method manageable some approximations have to be made: the solution is approximated by

$$u(x) = \sum_{j=1}^{N} u^j b^j(x). \tag{4.1}$$

b^j are known basis functions over the domain Ω, which can be for example polynomials or sinusoids and u^j are amplitude coefficients, where the superscript represents the element number. The search for a solution in an infinite dimensional space (finding the exact function u) has been replaced with the simpler task of calculating the coefficients u^j in

a finite dimensional space. To help find these coefficients we define an error residual.

$$R(x) = \mathcal{L}u^j b^j(x) - g(x).$$

Here, the sum is omitted for simplicity. If the precise solution were known then this residual would be zero; however, since u is represented only approximately we can only hope to make R as small as possible. To determine the values of the coefficients it is necessary to obtain a system of N equations, one for each coefficient. This can be achieved by introducing another set of basis functions, w^i, the weighting functions over Ω and each of which are orthogonal to $R(x)$. The system of equations is obtained by taking the inner product of $R(x)$ and w^i:

$$\left\langle \mathcal{L}u^j b^j(x) - g(x),\ w^i(x) \right\rangle = 0.$$

where both i and j range from one to N. This is known as the weak form and can be written in matrix form as $a_{ij}u^j = c^i$, where $a_{ij} =< \mathcal{L}b^j(x),\ w^i(x) >$ and $c^i =< g(x),\ w^i(x) >$, where summation is implied over the repeated indices.

The choice of $w^i(x)$ can be from a different set of function from the basis functions. In the Galerkin approach, the weight functions are chosen identical to the basis functions: $w^i(x) = b^i(x)$.

Another approach, which is perhaps more intuitive is to minimise $< R(x), R(x) >$, which is known as a least-squares approach. This method has the advantage that it can be applied to any boundary value problem the operator, and results in a functional that is self-adjoint. However, the functional contains higher order derivatives than the Galerkin form. Additional boundary constraints are required in terms of the higher order derivatives at the boundaries. If these are not well known, or worse still unspecified, spurious solutions will result. Furthermore, the continuity requirements of the basis functions is higher.

4.3 Variational Method

In the previous section we saw that the weighed residual approach could be used to find the solution $u(x)$ for a general BVP. In the variational method a functional is defined (a mapping from $u(x)$ to a scalar), which is stationary with respect to small changes (δu) about the

desired solution $u(x)$. In other words the desired solution minimises the functional. Often, when the operator $\mathcal{L}$ is self-adjoint, the Galerkin and variational approaches coincide.

Starting with a functional of the form $\Pi = \int_\Omega \{f(u, u', x)\}$, taking the first variation from u to $u + \delta u$ gives [62, 63, 64]

$$\delta\Pi = \int_\Omega \left\{ \frac{\partial f}{\partial u}(\delta u) + \frac{\partial f}{\partial(\partial u/\partial x_\alpha)} \frac{\partial}{\partial x_\alpha}(\delta u) + \ldots \right\},$$

where u must be an admissible function That is to say it is sufficiently differentiable and satisfies the assigned values on the boundary. Integrating the second term by parts yields

$$\delta\Pi = \int_\Omega \left\{ \frac{\partial f}{\partial u}(\delta u) - \frac{\partial}{\partial x_\alpha}\left[\frac{\partial f}{\partial(\partial u/\partial x_\alpha)}\right](\delta u) + \ldots \right\} + \int_\Gamma \left\{ \eta_\alpha \left[\frac{\partial f}{\partial(\partial u/\partial x_\alpha)}\right](\delta u) + \ldots \right\},$$

where $\hat{\eta}$ is the normal to the boundary. Since δu is arbitrary this corresponds to

$$\begin{aligned} \frac{\partial f}{\partial u} - \frac{\partial}{\partial x_\alpha}\left[\frac{\partial f}{\partial(\partial u/\partial x_\alpha)}\right] &= 0 \quad \text{for } x \in \Omega, \\ \eta_\alpha \frac{\partial f}{\partial(\partial u/\partial x_\alpha)} &= 0 \quad \text{for } x \in \Gamma. \end{aligned}$$

These are the Euler-Lagrange equations, sometimes referred to as the 'strong form'. Note that the first equation is satisfied over Ω and the final term on the boundary (often called the natural boundary condition). A variational approach is convenient because a suitable choice of functional can be used to solve any initial or boundary value problem, by ensuring simultaneously that the PDE and the boundary conditions are (weakly) enforced.

When the solution vector is known, the functional can be easily evaluated giving a single parameter that is often of interest, such as the total energy.

How is the variational expression obtained? For the study of liquid crystals the functional is taken to be the free energy, but for other problems a stored energy or power flow can be used. It is also possible to obtain the variational directly from the equations which you want to solve, by multiplying them by δu and then integrating by parts.

Once a variational expression is obtained, how can a solution be methodically found? One way to is obtain a perturbation formula, but perhaps the most straightforward approach is known as the Rayleigh-Ritz method.

The first step of this method is to substitute the basis or shape functions (4.1) into the variational form. The aim of the method is to find the values of the amplitude coefficients u^k

that minimise the variational form. To find the best combination of amplitude coefficients we differentiate the variational from with respect to each coefficient in turn:

$$\frac{\partial \Pi}{\partial u^k} = 0.$$

This gives a set of N equations, which can be solved to find all the coefficients.

4.3.1 Constraints

Sometimes we wish to find the solution to a PDE subject to some constraint. For example, in the incompressible Navier-Stokes equation we seek the velocity, $\vec{v}$, subject to the constraint that $\nabla \cdot \vec{v} = 0$. This is commonly achieved by introducing a Lagrange multiplier or by using a penalty method [64]. A more complicated approach is to calculate the shape functions such that they satisfy the constraint (i.e. projecting the equations onto a divergence free subspace).

Lagrange Multipliers [64]

If the constraint is a differential equation of the form $C(u) = 0 \in \Omega$, it can be satisfied by supplementing the variational form as follows:

$$\overline{\Pi} = \Pi + \int_{\Omega} \{\lambda^T C(u)\},$$

where λ is a Lagrange multiplier (a vector in the discretised form). This can be written in matrix form as

$$\begin{pmatrix} \mathbf{K} & \mathbf{C} \\ \mathbf{C}^T & 0 \end{pmatrix} \begin{pmatrix} \mathbf{u} \\ \lambda \end{pmatrix} = \begin{pmatrix} \mathbf{f}_1 \\ \mathbf{f}_2 \end{pmatrix}.$$

A disadvantage of this approach is that the solution vector is extended by the number of Lagrange multipliers and the zero in the diagonal tends to increase the condition number of the matrix.

Penalty Method [64]

In the penalty method the variational form is supplemented by

$$\overline{\Pi} = \Pi + \alpha \int_{\Omega} \{C^T(u)C(u)\}.$$

where the penalty factor α is a positive number. The larger this value, the more strongly the constraint is enforced, however, very large values can give rise to numerical contamination. The solution vector is not expanded in this approach.

4.4 Finite Element Method

Previously the concept of basis functions was introduced where the solution is represented as in equation (4.1), where the solution should approach the physical solution as N tends to infinity. In the finite element method the domain of interest is divided into a number of elements. Within each element an expansion in terms of some basis function is made. The total field is then the sum of the expansions in each element. In the finite element method the basis shape functions are interpolation polynomials, the order of which depends on the variational form and is typically of first or second order. These polynomial shape functions b^k are denoted by ϕ^k. In this way the integrals that appear in the weak form can be evaluated as the product of simple functions in each element, even if the geometry of the computational domain is of complex shape. The weak form can be obtained by applying the Galerkin or Rayleigh-Ritz methods.

4.4.1 Boundary conditions

Boundary conditions can be divided into two main types, enforced and natural. Enforced boundaries correspond to Dirichlet constraints, for example the fixed voltage on an electrode surface. The admissible basis functions should be chosen such that they satisfy these constraints. Natural boundary conditions are those that arise from the weak form and apply on open boundaries. In general, it is possible to modify the weak form to obtain any desired open boundary condition. In a variational approach this boundary condition is given by the term over Γ given by the first variation. Typically, the natural boundary that arises will be a Neumann type.

When studying liquid crystals many structures of interest tend to be periodic. To satisfy this condition it is possible to supplement the weak form with the following surface integral on the periodic boundary Γ_P

$$\int_{\Gamma_P} \{\phi^i(u - \tilde{u})\}$$

where $\tilde{u}$ is the value of u on the corresponding boundary, which weakly enforces $u = \tilde{u}$. A similar integral needs to be applied on the corresponding boundary $\tilde{\Gamma}_P$. An alternative approach is to strongly enforce periodicity. Nodes on the boundary $\tilde{\Gamma}_P$ can be eliminated in terms of the nodes on the corresponding boundary Γ_P. An advantage of this approach is that the number of degrees of freedom is reduced, and is the one implemented.

4.4.2 Shape Functions

In the finite element method the shape functions are interpolation polynomials. The order of these polynomials is set by the continuity requirements of the weak form. For example if the weak form is first order, linear P1 shape functions can be used.

Higher order elements lead to a more complex implementation but offer better accuracy for a given number of unknowns (i.e. convergence is improved). Fig. 4-1 shows the node placement for linear and quadratic elements in a two-dimensional domain.

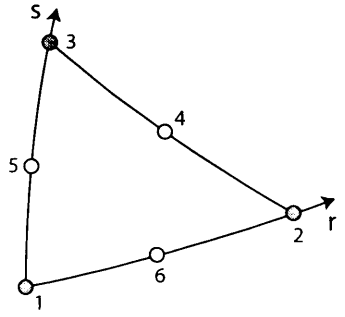

Figure 4-1: A triangle defined by nodes $\{1, 2, 3\}$ is a first order (P1) element, whereas a triangle defined by nodes $\{1, 2, 3, 4, 5, 6\}$ is a second order polynomial (P2) element

For linear triangular (P1) elements the shape functions can be defined as

$$\begin{aligned} \phi^1 &= 1 - r - s \\ \phi^2 &= r \\ \phi^3 &= s, \end{aligned} \tag{4.2}$$

and for quadratic (P2) triangular elements as

$$\begin{aligned} \phi^1 &= 1 - 3r - 3s + 2r^2 + 2s^2 + 4rs \\ \phi^2 &= -r + 2r^2 \\ \phi^3 &= -s + 2s^2 \\ \phi^4 &= 4rs \\ \phi^5 &= 4s - 4rs - 4s^2 \\ \phi^6 &= 4r - 4rs - 4r^2, \end{aligned}$$

where r and s are local area coordinates that lie in $[0, 1]$. For the unit triangle with vertices $(x, y) = (0, 0)$, $(1, 0)$ and $(0, 1)$, the condition holds that $(x, y) = (r, s)$.

4.4.3 Analytic and Numerical Integration

After discretisation the matrix entries will depend on the integral of products of shape functions and their derivatives. For example, the product of two first order shape functions $M_{ij} = \int_\Omega \{\phi^i \phi^j\}$, defined by (4.2), can be integrated analytically as follows: When $i = j$

$$2A \int_0^1 \int_0^{1-r} r^2 ds dr = 2A \int_0^1 (1 - r) r^2 dr = \frac{A}{6},$$

otherwise $(i \neq j)$

$$2A \int_0^1 \int_0^{1-r} rs ds dr = 2A \int_0^1 \frac{1}{2} r(1 - r)^2 dr = \frac{A}{12},$$

or more concisely, $M^{ij} = \frac{A}{12}(1 + \delta_{ij})$, where A is the element area.

It is often necessary to integrate the product of a number of shape functions and their derivatives. When an equation has a large number of terms and or when high order shape

functions are used, analytic integration leads a complex implementation. Extensive re-arrangement of the equations is necessary so as to collect terms with the same number of shape functions and shape function derivatives. Typically a table of integrals is formed that stores the integral of every combination of shape functions and their derivatives that appear in the weak form.

Using numerical integration these complications can be avoided. Instead of analytically integrating a function (a product of shape functions), the weighted sum of the function is calculated at specific sample points in an element. Provided there are enough sample points to capture the behaviour of the function, there is no loss of precision. The use of a numerical scheme opens up the possibility to use iso-parametric elements, which are better able to conform to curved boundaries.

First we introduce the use of numerical integration in 1D and then extend this idea to 2D. The integral of a function can be evaluated as the weighted sum of the function sampled at the Gauss points:

$$\int_0^1 f(r)dr \approx \sum_{i=1}^{M} w_i f(r_i).$$

For the example of $f(r)$ being a linear function over the interval (0,1), a single sample point is sufficient to perform the integration, located at $r_i = 1/2$ and with a weight $w_i = 1$. In 2D, it is convenient to work entirely in local coordinates. The value of the integral becomes:

$$\int_0^1 \int_0^1 f(r,s)|J|drds \approx \sum_{i=1}^{M} w_i f(r_i,s_i)|J|.$$

The Jacobian, J, must be recalculated in each element and the procedure is as follows. Firstly, the x and y coordinates can be written in local coordinates by interpolating the coordinates of the element nodes x_i, y_i:

$$x(r,s) = \sum_{j=1}^{N} x^j o^j(r,s).$$

$$y(r,s) = \sum_{j=1}^{N} y^j o^j(r,s).$$

The Jacobian can then be evaluated in terms of derivatives of the shape functions with

respect to r and s:

$$J = \begin{bmatrix} \frac{\partial x}{\partial r} & \frac{\partial y}{\partial r} \\ \frac{\partial x}{\partial s} & \frac{\partial y}{\partial s} \end{bmatrix}$$

For straight edged elements the Jacobian is constant within the element. For iso-parametric elements the Jacobian must be reevaluated at each sample point.

Similarly spatial derivatives can be evaluated as:

$$\begin{bmatrix} \frac{\partial \phi^j}{\partial x} \\ \frac{\partial \phi^j}{\partial y} \end{bmatrix} = J^{-1} \begin{bmatrix} \frac{\partial \phi^j}{\partial r} \\ \frac{\partial \phi^j}{\partial s} \end{bmatrix}$$

There are number of numerical integration schemes available, each using different sample points and weights. Gaussian quadrature is the most widely used method for integrating polynomials because they are guaranteed to be exact for polynomials less than a specified degree [14, 65]. Fig. 4-2 shows the location of the Gauss points for integrating a 4^{th} order polynomial. If the function is discontinuous then Gaussian quadrature will be inaccurate as low order polynomials tend to oscillate wildly about discontinuities. A disadvantage of Gaussian quadrature is that the sample points for second order function are distinct from those for a third order function. Usually the maximum order function appearing in the weak form is identified, and used to determine the number of Gauss points needed. All functions, even the low order ones, are evaluated at each point. This is wasteful, and can be avoided by using a different set of Gauss points for the lower order functions.

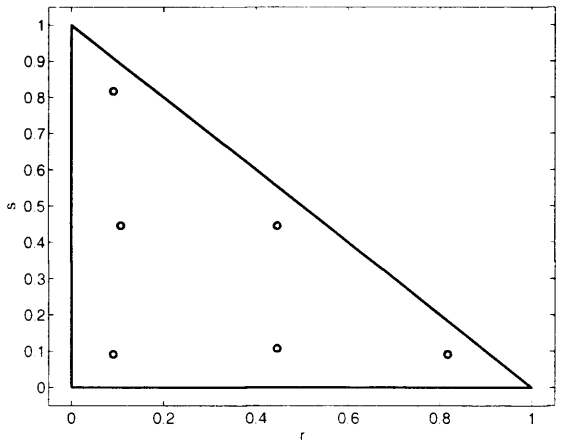

Figure 4-2: Gauss points: 4^{th} order integration [14]

An alternative way to solve this problem is to use Clenshaw-Curtis integration [66]. Given the sample points to integrate a second order function, a third order function can be integrated by adding additional sample points. For a given weak form, this means that lower order functions only have to be evaluated for the first few sample points. A disadvantage is that more sample points are required to integrate a given order function in comparison to Gaussian quadrature. Furthermore, the implementation is more complex.

In this thesis analytic integration is used for first order shape functions and Gaussian quadrature for second order shape functions.

4.5 Newton's method

After applying the Rayleigh-Ritz method there are two types of matrix problems to solve: a linear system of equations or an eigenvalue problem. The first of these is dealt with in this section. Eigenvalue problems do not arise in this thesis, hence their description is omitted.

When the weak form contains terms higher than second order, it is no longer possible to obtain the solution by solving a single systems of equations. An iterative method is required. For a matrix problem of the form $\mathbf{A}(u)u = \mathbf{b}$, the left hand side, $\mathbf{F}(u) = \mathbf{A}(u)u$, can be approximated by a Taylor series:

$$\mathbf{F}(u) \approx \mathbf{F}(u^m) + \mathbf{F}'(u^m)\Delta u + \frac{1}{2}\mathbf{F}''(u^m)\Delta u^2 + ...,$$

where m denotes the iteration number and $\Delta u = u^{m+1} - u^m$. Keeping first order terms this gives

$$\mathbf{F}'(u^m)\Delta u = \mathbf{b} - \mathbf{F}(u^m).$$

After each iteration u^{m+1} is updated by $u^{m+1} = u^m + \Delta u$ and $\mathbf{F}'(u^m)$ and $\mathbf{F}(u^m)$ are reevaluated.

Convergence is only achieved using Newton's method provided the choice of initial condition is sufficiently "near to" the final solution. If the solution is known to lie in some interval and $F' \neq 0$ on that interval, then the Newton iteration will converge to the solution. When there are zeros of the derivative nearby, Newton's method can display highly erratic behaviour and may or may not converge.

Normally quadratic convergence is achieved using Newton's method, but if $F' = 0$ at the solution, the convergence rate deteriorates to linear. For highly non-linear problems convergence can be improved by using a line search algorithm; the right hand side of equation (6.9) is scaled by a damping factor, which can be optimally chosen by a strategy such as the Armijo-Goldstein method [67, 68].

4.6 Time Integration

The moment of inertial density is usually negligible for LCs. With this simplification the LC orientation satisfies a parabolic differential equation (depending on $\frac{\partial u}{\partial t}$). A finite difference in the time domain method that calculates the time evolution of the function $u(x)$ is presented in this section.

One method is to discretise this term using a forward difference at time t_n. This is an explicit method, meaning that substitution is required at each time step, as opposed to solving a system of equations. Although this method is fast, it is not unconditionally stable. The maximum stable time step is limited by the spatial discretisation. Time integration is performed with first order accuracy.

Alternatively a backward difference can be used at time t_n. Now the method is implicit and unconditionally stable. However, a system of equations must be solved at each time step. The accuracy is also of first order.

The final method we consider is the Crank-Nicholson method (sometimes referred to as the trapezoid rule). Here a central difference approximation is made for the time derivative, which improves the accuracy of the time integration to second order. This method is implicit, therefore a relatively large time step may be used. If higher order accuracy is required then there are alternative time integration techniques that may be used, such as the Runge-Kutta methods.

In this thesis only two of these methods are used: the forward difference approximation for its simplicity and the Crank-Nicholson method for is accuracy and stability. Proofs of the stability and convergence of the various schemes can be found in any standard text, for example [69]

The Crank-Nicholson method is demonstrated below for a heat transfer problem, fol-

lowing [70]. The governing equation is

$$\frac{\partial T}{\partial t} + \nabla \cdot (\vec{v}T) = k\nabla^2 T + S, \tag{4.3}$$

where S represents the heat source and sinks and $\vec{v}$ is the known velocity field. This can be generalised to the non-linear case and expressed in matrix form as

$$\mathbf{M}\dot{T} + (\mathbf{N}(T) + \mathbf{K})T = f, \tag{4.4}$$

Substituting $\mathbf{A}$ for $\mathbf{N}(T) + \mathbf{K}$ and evaluating the time derivative between time steps at $t_{n+1/2}$ gives:

$$\mathbf{M}\dot{T} + \frac{1}{2}(\mathbf{A}T_{n+1} + \mathbf{A}T_n) = \frac{1}{2}(f_{n+1} + f_n). \tag{4.5}$$

The time derivative may then be replaced with its central difference approximation $\dot{T}|_{n+1/2} = \frac{1}{\Delta T}(T_{n+1} - T_n)$:

$$\left[\frac{2}{\Delta t}\mathbf{M} + \mathbf{A}\right] T_{n+1} = \left[\frac{2}{\Delta t}\mathbf{M} - \mathbf{A}\right] T_n + f_{n+1} + f_n, \tag{4.6}$$

Since $f_n - \mathbf{A}T_n = \mathbf{M}\dot{T}$, the solution stored from the previous time step can be used to simplify this expression

$$\left[\frac{2}{\Delta t}\mathbf{M} + \mathbf{A}\right] T_{n+1} = \mathbf{M}\left[\frac{2}{\Delta t}T_n + \dot{T}_n\right] + f_{n+1}. \tag{4.7}$$

If the equation is non-linear then Newton iterations (see section 4.5) are required within each time step. The final matrix form of the equation becomes

$$\begin{aligned}\left[\frac{2}{\Delta t}\mathbf{M} + \mathbf{K} + \mathbf{N}'(T^m_{n+1})\right](T^{m+1}_{n+1} - T^m_{n+1}) &= \mathbf{M}\left[\frac{2}{\Delta t}T_n + \dot{T}_n\right] \\ &+ f_{n+1} - \left[\frac{2}{\Delta t}\mathbf{M} + \mathbf{K} + \mathbf{N}(T^m_{n+1})\right]T^m_{n+1},\end{aligned} \tag{4.8}$$

where m denotes the iteration number and $\mathbf{N}'(T^m_{n+1}) = \left[\mathbf{N}(T^m_{n+1})T^m_{n+1}\right]'$.

4.7 Example - Poisson Equation

If voltages are applied at the electrodes, a potential distribution is established within a liquid crystal cell, given by the solution to the Poisson equation:

$$\mathcal{L}u = -\rho \tag{4.9}$$

where $\mathcal{L} = \nabla \cdot \varepsilon_o \bar{\bar{\varepsilon}} \cdot \nabla$ and ρ is the charge density.

If Green's theorem is applied to the integral $\int_\Omega v\mathcal{L}udx$, then we obtain

$$\int_\Omega v\mathcal{L}udV = \int_\Omega u\mathcal{L}^* vdV + \int_\Gamma F(u,v)ds$$

where $\mathcal{L}^*$ is the formal adjoint of $\mathcal{L}$. If $\mathcal{L}^* = \mathcal{L}$, the operator $\mathcal{L}$ is said to be formally self-adjoint [71, p.280]. In the case of the Poisson equation, two successive applications of Green's theorem (neglecting the right hand side of (4.9)) yield

$$\begin{aligned} -\int_\Omega v(\nabla_\alpha \varepsilon_{\alpha\beta}\nabla_\beta u)d\Omega &= \int_\Omega (\nabla_\alpha v\varepsilon_{\alpha\beta}\nabla_\beta u)d\Omega - \int_\Gamma v(\varepsilon_{\alpha\beta}\nabla_\beta u)\eta_\alpha d\Gamma \\ &= -\int_\Omega u(\nabla_\beta \varepsilon_{\alpha\beta}\nabla_\alpha v)d\Omega - \int_\Gamma \{v(\varepsilon_{\alpha\beta}\nabla_\beta u)\eta_\alpha - u(\varepsilon_{\alpha\beta}\nabla_\alpha v)\eta_\beta\}\, d\Gamma. \end{aligned}$$

By summing over α and β we find that

$$\begin{aligned} \mathcal{L}^* v &= \int_\Omega (\nabla_\alpha \varepsilon_{\beta\alpha}\nabla_\beta v)d\Omega, \\ F(u,v) &= -\int_\Gamma \{\varepsilon_{\alpha\beta}(v\nabla_\beta u\eta_\alpha - u\nabla_\alpha v\eta_\beta)\}\, d\Gamma, \end{aligned}$$

so the operator $\mathcal{L}$ is formally self-adjoint [71] if $\varepsilon_{\beta\alpha} = \varepsilon_{\alpha\beta}$, as is true for liquid crystal materials.

With the self-adjoint property of the operator satisfied, we can proceed in forming a variational expression in the following way:

$$\Pi = \frac{1}{2} < \mathcal{L}u, u > + < \rho, u >. \tag{4.10}$$

$$\Pi = -\frac{1}{2}\int_\Omega \left\{\nabla u \cdot \varepsilon_0 \bar{\bar{\varepsilon}} \cdot \nabla u\right\} + \int_\Omega \{\rho u\}. \tag{4.11}$$

Integrating by parts and making the first variation vanish gives

$$\delta\mathbf{\Pi} = \int_{\Omega} \left\{\delta u(\nabla \cdot \varepsilon_0 \bar{\bar{\varepsilon}} \cdot \nabla u)\right\} + \int_{\Omega} \{\rho \delta u\} - \int_{\Gamma} \left\{\delta u(\varepsilon_0 \bar{\bar{\varepsilon}} \cdot \nabla u) \cdot \hat{\eta}\right\} = 0 \qquad (4.12)$$

which, since δu is arbitrary, leads to the Euler-Lagrange equations $\nabla \cdot \varepsilon_0 \bar{\bar{\varepsilon}} \cdot \nabla u = -\rho$ over Ω and $(\bar{\bar{\varepsilon}} \cdot \nabla u) \cdot \hat{\eta} = 0$ over Γ. In fact, the condition over Γ is weakly enforced across the sides/faces of each and every element in the mesh. In an LC cell we consider both the permittivity and potential to be continuous across the element boundaries (as is enforced by our choice of shape functions) and thus the effect of this boundary term can be neglected on internal boundaries. Only when there is an abrupt change in the permittivity, for instance at the boundary between two different dielectrics, is it necessary to calculate this boundary integral.

Consider what this boundary condition means for a simple planar aligned cell, where the LC is sandwiched between two sheet electrodes and is assumed to extend indefinitely in a plane parallel to the electrodes. To model this structure, the modelling window must be of finite extent, and on open boundaries Γ_N the natural boundary conditions applies. Here, the presence of the permittivity term in $(\bar{\bar{\varepsilon}} \cdot \nabla u) \cdot \hat{\eta} = 0$ results in a deflection of the electric field at the boundary if the director is tilted. This deflection is unwanted; ideally the natural boundary condition would be that of $\nabla u \cdot \hat{\eta} = 0$.

It is possible to devise an operator that satisfies the desired Euler-Lagrange equations over both Ω and Γ, but this operator turns out to be non-self-adjoint. Variational formulations can be constructed for such operators by introducing an auxiliary problem, the adjoint problem [72]. This leads to a doubling of the number of unknowns.

A more straightforward path to a solution, and the one taken here, is given by the Galerkin approach. The strong form is multiplied by an arbitrary test function o and integrated over the domain.

$$\int_{\Omega} \left\{o(\nabla \cdot \bar{\bar{\varepsilon}} \cdot \nabla u)\right\} + \int_{\Gamma_N} \{o(\nabla u) \cdot \hat{\eta}\} = -\frac{1}{\varepsilon_0} \int_{\Omega} \{\rho o\} \qquad (4.13)$$

Here, the desired Neumann boundary condition over the open boundary Γ_N has been included in the weak form. Applying Green's Theorem yields

$$-\int_{\Omega} \nabla o \cdot \bar{\bar{\varepsilon}} \cdot \nabla u d\Omega + \int_{\Gamma} o(\bar{\bar{\varepsilon}} \cdot \nabla u) \cdot \hat{\eta} d\Gamma + \int_{\Gamma_N} o(\nabla u) \cdot \hat{\eta} d\Gamma = -\frac{1}{\varepsilon_0} \int_{\Omega} \rho o d\Omega. \qquad (4.14)$$

The surface integral over Γ can be neglected due to the continuity of u everywhere except the open boundaries, where Γ coincides with Γ_N:

$$-\int_\Omega \nabla\phi\cdot\bar{\bar{\varepsilon}}\cdot\nabla u d\Omega+\int_{\Gamma_N}\phi[(I+\bar{\bar{\varepsilon}})\cdot\nabla u]\cdot\hat{\eta}d\Gamma=-\frac{1}{\varepsilon_0}\int_\Omega\rho\phi d\Omega. \tag{4.15}$$

Now we have in the bulk $\nabla\cdot\varepsilon_0\bar{\bar{\varepsilon}}\cdot\nabla u=-\rho$ as before, and on the open boundaries $\nabla u\cdot\hat{\eta}=0$ as required.

With the weak form defined, the next step is to substitute u by the discrete form $u^k\phi^k$. The permittivity may be be written in discrete form as $\varepsilon_{\alpha\beta}\Rightarrow\varepsilon_\perp\delta_{\alpha\beta}+\Delta\varepsilon n^k_\alpha n^l_\beta\phi^k\phi^l$, where $\hat{n}$ is the LC director. However, after discretisation this substitution breaks the head tail symmetry of the director. If a 180° rotation of the director occurs within an element this will result in an unwanted change in the energy Π. Instead the permittivity tensor should be discretised as $\varepsilon_{\alpha\beta}\Rightarrow\varepsilon^k_{\alpha\beta}\phi^k$.

The surface integral can be simplified by introducing a modified permittivity: $\varepsilon'_{\alpha\beta}=\varepsilon_{\alpha\beta}+\delta_{\alpha\beta}$

$$-\varepsilon^k_{\alpha\beta}u^j\int_\Omega\frac{\partial\phi^i}{\partial x_\alpha}\frac{\partial\phi^j}{\partial x_\beta}\phi^k d\Omega+n_\alpha\varepsilon'^k_{\alpha\beta}u^j\int_\Gamma\phi^i\frac{\partial\phi^j}{\partial x_\beta}\phi^k d\Gamma=-\frac{1}{\varepsilon_0}\rho^k\int_\Omega\phi^i\phi^k d\Omega, \tag{4.16}$$

This expression can be written in matrix form as

$$\mathbf{Au}=\mathbf{b}, \tag{4.17}$$

where the contributions from the surface integral render the sparse matrix $\mathbf{A}$ asymmetric. The maximum order of the derivatives appearing is first order, and therefore it is possible to use first order (P1) shape functions.

Chapter 5

Constant Order Parameter Formulation

5.1 Introduction

In this chapter a finite element discretisation of the Oseen-Frank free energy functional is described under the assumption that the order parameter is constant. This assumption is valid when modelling most commercially produced devices and remains so unless the electric field is particularly high, or unless geometrical features give rise to disclinations. If disclination lines are present in a device, they correspond to singularities in the free energy density when the order parameter is held constant. In certain numerical methods, such as the finite difference method, these singularities require special treatment because the Euler-Lagrange equations become ill-conditioned. This problem may be overcome by excluding the disclination core by an appropriate cut [73]. In a finite element approach one may use singular shape functions.

Although a solution can be obtained using these methods, they neglect the biaxial ordering of the liquid crystal induced by large electric fields and in proximity to disclinations. Therefore, this formulation is only strictly valid when the director field is a smoothly varying function. Explicit time integration is used to determine the dynamic evolution of the director field, and the implementation is well suited to model large areas such as a display pixel, where the mesh requires many elements.

Two models are developed to obtain the director field, the first that minimises the free energy written in terms of a director field $\hat{n}$, as in (2.6), and the second in terms of a tensor field Q, with the order parameter S_0 held constant. An advantage of the tensorial representation is that it correctly maintains the nematic head-tail symmetry after discretisation, whereas the vector method does not. A clash of heads or tails gives rise to an un-physical region of high energy when a vectorial representation is used.

5.2 Energy balance

The free energy functional (2.7) has contributions from elastic, electrostatic and surface energies

$$\begin{aligned} \mathcal{F} &:= \mathcal{F}_D - \mathcal{F}_E + \mathcal{F}_S \\ &= \int_\Omega \{f_D - f_E\} + \int_\Gamma \{f_S\}. \end{aligned} \tag{5.1}$$

Two forms of the distortion energy, $\mathcal{F}_D$, are considered; one using a vector and the other using a tensor representation. In the tensor method the spatial derivatives should be calculated in terms of Q, after which Q can be substituted by $S_0(3\hat{n}\otimes\hat{n}-I)/2$ to obtain an equation in terms of $\hat{n}$. The electrostatic energy is quadratic in $\hat{n}$ and is written is terms of the electric field $\vec{E}$ and the permittivity tensor $\varepsilon_{\alpha\beta}=\varepsilon_\perp\delta_{\alpha\beta}+\Delta\varepsilon n_\alpha n_\beta$:

$$\begin{aligned} f_E &:= \frac{1}{2}\varepsilon_0(\vec{E}\cdot\bar{\bar{\varepsilon}}\cdot\vec{E}) \\ &= \frac{1}{2}\varepsilon_0\varepsilon_\perp(u_{,\alpha}u_{,\alpha})+\frac{1}{2}\varepsilon_0\Delta\varepsilon(u_{,\alpha}n_\alpha n_\beta u_{,\beta}), \end{aligned}$$

where $\alpha,\beta\in\{x,y,z\}$ and $u_{,\alpha}=\frac{\partial u}{\partial x_\alpha}$. To enforce the constraint that $\hat{n}\cdot\hat{n}=1$ the energy functional is supplemented by the following term:

$$\int_\Omega\left\{\lambda[\hat{n}\cdot\hat{n}-1]\right\},$$

where λ is a Lagrange multiplier.

A solution can be found numerically by applying the Rayleigh-Ritz method. Firstly, the director and potential are discretised using $n_\alpha\approx n_\alpha^i\phi^i$ and $u\approx u^i\phi^i$, where ϕ^i are the shape functions. Then the steady-state solution is given by the stationary value of the free energy:

$$\frac{\partial\mathcal{F}}{\partial n_\delta^p}=0, \qquad \frac{\partial\mathcal{F}}{\partial\lambda^p}=0.$$

Note that one must solve for both the nodal values of the directors, n_δ^p, and the Lagrange multipliers. A method to obtain the steady-state solution is given in Appendix A.

Often we want to learn how the director field evolves with time into the equilibrium state. In order to calculate the dynamic behaviour of the LC the free energy should be minimised according to a dissipation principle:

$$\begin{aligned} \frac{\partial}{\partial\dot{n}_\delta^p}\int_\Omega\left\{\frac{\gamma_1}{2}\dot{n}_\mu^a\dot{n}_\mu^b o^a o^b\right\} &= -\frac{\partial\mathcal{F}}{\partial n_\delta^p}, \\ \gamma_1\dot{n}_\mu^i\delta_{\mu\delta}\int_\Omega\left\{o^p o^i\right\} &= -\frac{\partial\mathcal{F}}{\partial n_\delta^p}. \end{aligned}$$

Here, the flow of the LC has been neglected. In Section 7 the dissipation is modified to account for the reorientation of the LC induced by its flow. Using a forward difference

approximation for the time derivative yields the matrix form:

$$\frac{\gamma 1}{\Delta t} M^{pi}_{\delta\mu}(n^i_\mu(t+\Delta t) - n^i_\mu(t)) = -R^p_\delta(t). \tag{5.2}$$

where $M^{pi}_{\delta\mu} = \delta_{\mu\delta} \int_\Omega \{\phi^p \phi^i\}$ and depends only on the mesh connectivity. The right hand side vector $R^p_\delta = \frac{\partial \mathcal{F}}{\partial n^p_\delta}$ is the sum of all contributions from each and every element of the mesh. It may be written as $G^{pi}_{\delta\mu} n^i_\mu$, but it is more efficient to assemble the vector directly.

The time step is severely restricted when using explicit methods such as this, but there are several advantages. If Gaussian elimination is used to solve the resulting system of equations, the pivots and factors of the matrix **M** need only be calculated once, after which a solution can be sought by substitution, a fast procedure. Furthermore, the Lagrange multiplier may be dropped and the unitary length of the director maintained by renormalisation each iteration, provided the time step is small enough.

If an implicit method is used for time integration, such as the Crank Nicholson method, then terms in $\frac{\partial}{\partial n^i_\mu} R^p_\delta$ will contribute to the left hand side of (5.2) and the Lagrange multiplier must be calculated. Although this method is more accurate and stable, the pivots and factors of the matrix must be calculated every few time steps, which is a time consuming procedure. Therefore only the explicit method is considered here.

It is possible to make the matrix **M** diagonal using a technique known as mass lumping [74], so that it may be trivially inverted. Most simply a lumped mass matrix may be formed using quadrature, where the sample points coincide with the nodes of the element. This technique would substantially speed up the first iteration, and furthermore would simplify parallelisation. Of course any such approximation reduces the accuracy of the calculated solution.

The contribution to the right hand side of (5.2) from the electric term is the same for both the vector and tensor methods and can be written as

$$\frac{\partial \mathcal{F}_E}{\partial n^p_\delta} = \varepsilon_0 \Delta\varepsilon u^a o^a_{.\mu} n^p_\mu o^p u^b o^b_{.\delta}.$$

5.3 Vector Method

The distortion energy density using a vector representation of the LC orientation is given by [18, 19, 20]

$$f_D = \frac{1}{2}K_{11}\left(\nabla\cdot\hat{n}\right)^2 + \frac{1}{2}K_{22}\left(\hat{n}\cdot\nabla\times\hat{n}+q_0\right)^2 + \frac{1}{2}K_{33}\left|\hat{n}\times\nabla\times\hat{n}\right|^2 + \frac{1}{2}(K_{22}+K_{24})[\mathrm{tr}(\nabla\hat{n})^2 - (\nabla\cdot\hat{n})^2]. \tag{5.3}$$

Before launching into the discretisation it is advantageous to rearrange this equation by grouping the terms that are higher than second order in $\hat{n}$:

$$f_D = \frac{1}{2}K_{11}\left(\nabla\cdot\hat{n}\right)^2 + K_{22}q_0(\hat{n}\cdot\nabla\times\hat{n}) + \frac{1}{2}K_{22}q_0^2 + \frac{1}{2}(K_{33}-K_{22})\left|\hat{n}\times\nabla\times\hat{n}\right|^2 + \frac{1}{2}K_{22}\left[(\hat{n}\cdot\nabla\times\hat{n})^2 + |\hat{n}\times\nabla\times\hat{n}|^2\right] + \frac{1}{2}(K_{22}+K_{24})[\mathrm{tr}(\nabla\hat{n})^2 - (\nabla\cdot\hat{n})^2].$$

The final term can be written in the following form [39, p.159]

$$\frac{1}{2}(K_{22}+K_{24})[\mathrm{tr}(\nabla\hat{n})^2 - (\nabla\cdot\hat{n})^2] = \frac{1}{2}(K_{22}+K_{24})\nabla\cdot[(\nabla\hat{n})\cdot\hat{n} - (\nabla\cdot\hat{n})\hat{n}],$$

and in this form the Divergence Theorem may be applied.

$$\int_\Omega\left\{\frac{1}{2}(K_{22}+K_{24})\nabla\cdot[(\nabla\hat{n})\hat{n} - (\nabla\cdot\hat{n})\hat{n}]\right\} = \int_\Gamma\left\{\frac{1}{2}(K_{22}+K_{24})[(\nabla\hat{n})\cdot\hat{n} - (\nabla\cdot\hat{n})\hat{n}]\cdot\hat{\eta}\right\}.$$

When the boundary (which is normal to $\hat{\eta}$) is subject to strong anchoring this term contributes the same amount for all director fields [39], i.e. it is a *null Lagrangian*. However, if the boundary is left free then this term will then have an effect on the calculated director field.

The constant term $K_{22}q_0^2$ can be dropped and $(K_{22}+K_{24})$ may be expanded to give

$$f_D = \frac{1}{2}(K_{11}-K_{22}-K_{24})\left(\nabla\cdot\hat{n}\right)^2 + K_{22}q_0(\hat{n}\cdot\nabla\times\hat{n}) + \frac{1}{2}(K_{33}-K_{22})\left|\hat{n}\times\nabla\times\hat{n}\right|^2 + \frac{1}{2}K_{22}\left[(\hat{n}\cdot\nabla\times\hat{n})^2 + |\hat{n}\times\nabla\times\hat{n}|^2 + \mathrm{tr}(\nabla\hat{n})^2\right] + \frac{1}{2}K_{24}\,\mathrm{tr}(\nabla\hat{n})^2.$$

Further simplification is possible using the following identities, which assume $\hat{n}\cdot\hat{n}=1$ [39,

p.115]. The K_{22} term can be simplified using

$$\begin{aligned}(\hat{n}\cdot\nabla\times\hat{n})^2+|\hat{n}\times\nabla\times\hat{n}|^2 &= |\nabla\times\hat{n}|^2,\\ \mathrm{tr}(\nabla\hat{n})^2+|\nabla\times\hat{n}|^2 &= \nabla\hat{n}\cdot\nabla\hat{n},\end{aligned}$$

and the $K_{33}-K_{22}$ term can be simplified using

$$2(\hat{n}\times\nabla\times\hat{n}) = \nabla(\hat{n}\cdot\hat{n}) - 2(\hat{n}\cdot\nabla)\hat{n},$$

where the term $\nabla(\hat{n}\cdot\hat{n})$ is zero due to the unit length of the director. This gives

$$\begin{aligned}f_D = \ & \frac{1}{2}(K_{11}-K_{22}-K_{24})\,(\nabla\cdot\hat{n})^2 + q_0K_{22}(\hat{n}\cdot\nabla\times\hat{n}) + \frac{1}{2}K_{22}\,(\nabla\hat{n}\cdot\nabla\hat{n})\\ & + \frac{1}{2}(K_{33}-K_{22})\,|(\hat{n}\cdot\nabla)\hat{n}|^2 + \frac{1}{2}K_{24}\,\mathrm{tr}(\nabla\hat{n})^2.\end{aligned}$$

The reduction in the number of curl operators leads to a simplified implementation (in agreement with [75]) and furthermore the order of the equations drops to second order when $K_{22}=K_{33}$. Alternatively this equation can be written using tensor notation as

$$\begin{aligned}f_D = \ & \frac{1}{2}(K_{11}-K_{22}-K_{24})n_{\mu,\mu}n_{\nu,\nu} + \frac{1}{2}K_{22}n_{\mu,\nu}n_{\mu,\nu} + q_0K_{22}\sigma_{\mu\nu\lambda}n_\mu n_{\lambda,\nu}\\ & + \frac{1}{2}(K_{33}-K_{22})n_\mu n_{\alpha,\mu}n_\nu n_{\alpha,\nu} + \frac{1}{2}K_{24}n_{\mu,\nu}n_{\nu,\mu}.\end{aligned}$$

where $\sigma_{\alpha\mu\nu}$ is the Levi-Civita anti-symmetric tensor. The next step is the discretisation of the free energy in terms of the shape functions and the nodal values of the director, which gives

$$\begin{aligned}f_D = \ & \frac{1}{2}(K_{11}-K_{22}-K_{24})n^a_\mu n^b_\nu o^a_{,\mu}o^b_{,\nu} + \frac{1}{2}K_{22}n^a_\mu n^b_\mu o^a_{,\nu}o^b_{,\nu} + q_0K_{22}\sigma_{\mu\nu\lambda}n^a_\mu n^b_\lambda o^a o^b_{,\nu}\\ & + \frac{1}{2}(K_{33}-K_{22})n^a_\mu n^b_\alpha n^c_\nu n^d_\alpha o^a o^b_{,\mu} o^c o^d_{,\nu} + \frac{1}{2}K_{24}n^a_\mu n^b_\nu o^a_{,\nu}o^b_{,\mu}.\end{aligned}$$

The contribution to the right hand side of (5.2) from the elastic terms, $R^p_\delta = \frac{\partial \mathcal{F}_D}{\partial n^p_\delta}$, can be

written as

$$R^p_\delta = \int_\Omega \Big\{ (K_{11} - K_{22} - K_{24}) n^a_\mu \phi^a_{.\mu} \phi^p_{.\delta} + K_{22} n^a_\delta \phi^a_{.\mu} \phi^p_{.\mu} + q_0 K_{22} \sigma_{\delta\mu\nu} (\phi^a \phi^p_{.\nu} - \phi^p \phi^a_{.\nu}) n^a_\mu \\ + (K_{33} - K_{22}) \left(n^d_\mu \phi^p \phi^a_{.\delta} + n^d_\delta \phi^a \phi^p_{.\mu} \right) n^a_\mu n^c_\nu \phi^c \phi^d_{.\nu} + K_{24} n^a_\mu \phi^a_{.\delta} \phi^p_{.\mu} \Big\}.$$

5.4 Tensor Method

In Section 2.6 the method to obtain the distortion energy in terms of the director was summarised. Similarly, the free energy density can be written as a Taylor expansion in the gradients of the Q tensor field [76, 77], giving

$$f_D = \frac{1}{2} L_1 Q_{jk,l} Q_{jk,l} + \frac{1}{2} L_2 Q_{jk,k} Q_{jl,l} + \frac{1}{2} L_4 \sigma_{jkl} Q_{jm} Q_{km,l} + \frac{1}{2} L_6 Q_{jk} Q_{lm,j} Q_{lm,k}. \quad (5.4)$$

Here the K_{24} term has been neglected. The coefficients L_1 to L_6 can be related to K_{11}, K_{22} and K_{33} as detailed in [77], and depend on the definition of the Q tensor that is used. With $Q = S_0(3\hat{n} \otimes \hat{n} - I)/2$ they can be related by

$$\begin{aligned} L_1 &= \frac{2}{27 S_0^2} (K_{33} - K_{11} + 3K_{22}), \\ L_2 &= \frac{4}{9 S_0^2} (K_{11} - K_{22}), \\ L_4 &= \frac{8}{9 S_0^2} (q_0 K_{22}), \\ L_6 &= \frac{4}{27 S_0^3} (K_{33} - K_{11}). \end{aligned} \quad (5.5)$$

The weak form in terms of Q can be obtained by replacing Q with $Q^k_{\alpha 3} o^k$. Then the stationary value can be found as

$$\frac{\partial \mathcal{F}_D}{\partial Q^p_{jk}} = \int_\Omega \Big\{ L_1 o^p_{.l} Q^b_{jk} o^b_{.l} + L_2 o^p_{.k} Q^b_{jl} o^b_{.l} + \frac{1}{2} L_4 \sigma_{jlm} Q^a_{mk} \left(o^a o^p_{.l} - o^p o^a_{.l} \right) \\ + \frac{1}{2} L_6 \left(o^p Q^b_{lm} o^b_{.j} Q^c_{lm} o^c_{.k} + 2 Q^a_{lm} o^a o^p_{.l} Q^c_{jk} o^c_{.m} \right) \Big\}.$$

In order to convert this equation from a tensorial to a vectorial form the chain rule may be applied

$$\begin{aligned} R^p_\delta &= \frac{\partial \mathcal{F}_D}{\partial Q^p_{jk}} \frac{\partial Q^p_{jk}}{\partial n^p_\delta}. \\ &= \frac{\partial \mathcal{F}_D}{\partial Q^p_{jk}} \frac{3S_0}{2} \left(n^p_j \delta_{k\delta} + n^p_k \delta_{j\delta} \right). \end{aligned}$$

$$\begin{aligned} R^p_\delta = \frac{3S_0}{2} \int_\Omega \Big\{ & 2L_1 n^p_k \phi^p_{,l} Q^b_{k\delta} \phi^b_{,l} + L_2 n^p_k \left(\phi^p_{,\delta} Q^b_{kl} + \phi^p_{,k} Q^b_{\delta l} \right) \phi^b_{,l} \\ & + \frac{1}{2} L_4 \left(\sigma_{klm} Q^a_{m\delta} + \sigma_{\delta lm} Q^a_{mk} \right) n^p_k \left(\phi^a \phi^p_{,l} - \phi^p \phi^a_{,l} \right) \\ & + L_6 \left(n^p_k \phi^p Q^b_{lm} \phi^b_{,k} Q^c_{lm} \phi^c_{,\delta} + 2 n^p_k Q^a_{lm} \phi^a \phi^p_{,l} Q^c_{k\delta} \phi^c_{,m} \right) \Big\}. \end{aligned}$$

All that remains is to substitute the director for the remaining Q tensors. The spatial derivatives of $Q_{\alpha 3}$ can be replaced by $n_\alpha n_3$, however more care must be taken where $Q_{\alpha 3}$ appears, specifically in the L_4 and L_6 terms. For the final L_6 term, the isotropic part $-\delta_{lm}$ simplifies to the same form as the L_1 term. Due to the presence of the σ in the L_4 term, the isotopic parts $-\delta_{m\delta}$ and $-\delta_{mk}$ cancel. This gives finally:

$$\begin{aligned} R^p_\delta = \frac{9S_0^2}{4} \int_\Omega \Big\{ & (2L_1 - S_0 L_6) n^p_k \phi^p_{,l} n^b_k n^b_\delta \phi^b_{,l} + L_2 n^p_k \left(\phi^p_{,\delta} n^b_k n^b_l + \phi^p_{,k} n^b_\delta n^b_l \right) \phi^b_{,l} \\ & + \frac{1}{2} L_4 \left(\sigma_{klm} n^a_m n^a_\delta + \sigma_{\delta lm} n^a_m n^a_k \right) n^p_k \left(\phi^a \phi^p_{,l} - \phi^p \phi^a_{,l} \right) \\ & + \frac{3S_0}{2} L_6 \left(n^p_k \phi^p n^b_l n^b_m \phi^b_{,k} n^c_l n^c_m \phi^c_{,\delta} + 2 n^p_k n^a_l n^a_m \phi^a \phi^p_{,l} n^c_k n^c_\delta \phi^c_{,m} \right) \Big\}. \end{aligned}$$

which is the elastic contribution to the right hand side of (5.2).

5.5 Weak Anchoring

The most commonly used expression to describe the interaction between the liquid crystal and the alignment surface was proposed by Rapini-Papoular [78]. A generalized form of this expression can be written as

$$f_S(\theta, \varphi) = A_1 \sin^2(\theta - \theta_0) + A_2 \sin^2(\varphi - \varphi_0).$$

where A_1 and A_2 are anchoring coefficients, θ_0 is the pre-tilt and φ_0 is the pre-twist. The values of the coefficients depend on the surface treatment.

An alternative expression for the surface free energy density can be written in terms of $\hat{n}$ as [79]

$$f_S(\hat{n}) = W_\xi(\hat{n}\cdot\hat{\xi})^2 + W_\zeta(\hat{n}\cdot\hat{\zeta})^2,$$

and in terms of $\mathbf{Q}$ as

$$f_S(\mathbf{Q}) = W_\xi(\hat{\xi}\cdot\mathbf{Q}\cdot\hat{\xi}) + W_\zeta(\hat{\zeta}\cdot\mathbf{Q}\cdot\hat{\zeta}),$$

where W_ξ and W_ζ are anchoring coefficients [80]. $\hat{\xi}$ and $\hat{\zeta}$ are unit vectors that are orthogonal to each other and the easy direction too. This form is obtained by expressing the surface free energy as a spherical harmonic expansion, truncated to include at most second order terms. The presence of the two anchoring coefficients allows a different penalty to be associated with azimuthal and zenithal perturbations from the easy direction. Furthermore, planar degenerate anchoring may be achieved by setting one of the coefficients to zero.

The anchoring coefficients W_ξ and W_ζ may be related to A_1 and A_2 by the following expressions.

$$W_\xi = \frac{1}{2}\left(A_1 - \frac{5}{8}A_2\right) \quad \text{and} \quad W_\zeta = \frac{1}{2}\left(A_1 + \frac{5}{8}A_2\right).$$

5.6 Conclusions

Finite element discretisations of the Oseen-Frank free energy functional have been developed. There are two different implementations, one using a vectorial and the other using a tensorial representation of the LC orientation. The tensor method correctly maintains the nematic head-tail symmetry, but the equations are of higher order in $\hat{n}$, which places a further constraint on the maximum time step. A detailed comparison of the vector and tensor methods will be made in chapter 8.

Chapter 6

Variable Order Parameter Formulation

6.1 Introduction

For most applications the distance over which there is significant variation of the director is large in comparison to the size of a molecule, and as a result the LC orientation may be described by a vector field under the assumption that the order parameter is constant. This approach was initiated by Oseen [18], Zocher [19] and Frank [20], based on the minimisation of an energy contributed to by elastic and electric terms.

However, when disclinations are present the Euler-Lagrange equations become numerically ill conditioned, i.e. the free energy density contains singularities. Disclinations can arise about geometrical feature or can be induced by large electric fields and this theory is incapable of describing their motion.

A generalisation of this theory to use the tensor order parameter is described by Landau-de Gennes [7, 5, 81]. In this theory the equilibrium state of the liquid crystal is determined by the balance of elastic, electric and thermotropic energies. This approach prevents singularities from arising at the disclination core, by allowing the order parameter to relax. In such regions the liquid crystal tends to be biaxial, and by solving in terms of individual components of the Q tensor, such regions are properly described.

There is much speculation on the ability of mesoscopic approaches to describe appropriately the physical situation on length scales in the order of the molecular length. Evidence suggests that mesoscopic models are capable of quantitatively describing the response of the LC even on length scales approaching the molecular length [82, 83]. Were this not the case one would have to resort to molecular or atomistic simulations.

A fine mesh is required to account for steep gradients of the order parameter in the proximity of disclinations, which severely limits the time step particularly in the case of explicit methods. An implicit time integration scheme is used here to alleviate this problem. Using finite elements with an adaptive meshing scheme the mesh density can be concentrated about disclinations, affording significant savings in terms of number of degrees of freedom compared to traditional finite difference methods.

In this section, a finite element implementation of the Landau-de Gennes free energy functional is detailed. An approach to obtain the steady state Q-tensor field is described and then generalised for the dynamic case. Details of the adaptive meshing scheme are then given. Finally, the model is validated by comparison with some previously published

results: specifically, the order parameter variation about a $+1/2$ disclination line.

6.2 Q-Tensor Statics

In this section a formulation for the steady state Q-tensor field is presented, detailing the steps taken to obtain a matrix form of the problem from the governing equations. The Landau-de Gennes free energy functional (LdG) [7, 5] is defined as

$$\begin{aligned}\mathcal{F}(\mathbf{Q}) &:= \mathcal{F}_D(\partial\mathbf{Q}) + \mathcal{F}_B(\mathbf{Q}) - \mathcal{F}_E(\mathbf{Q}) + \mathcal{F}_S(\mathbf{Q}) \\ &= \int_\Omega \{f_D(\partial\mathbf{Q}) + f_B(\mathbf{Q}) - f_E(\mathbf{Q})\} + \int_\Gamma \{f_S(\mathbf{Q})\},\end{aligned} \tag{6.1}$$

where Ω is an open bounded subset of $\mathbb{R}^3$ with boundary Γ and $\mathbf{Q}$ is as in [12, 77]. The free-energy densities, $f_B(\mathbf{Q})$ and $f_D(\partial\mathbf{Q})$, are due to bulk and elastic contributions respectively and $f_S(\mathbf{Q})$ is the surface free-energy density. Reorientation of the LC is induced by an applied electric field and thus, $f_E(\mathbf{Q})$, the electrostatic energy density is also included.

The bulk free-energy density determines the state of the LC, be it uniaxial or biaxial nematic or isotropic. It can be written as an expansion in the scalar invariants of the Q-tensor about the nematic-isotropic transition, truncated to include at most fourth order terms:

$$f_B(\mathbf{Q}) := \frac{1}{2}A\,\mathrm{tr}(\mathbf{Q}^2) + \frac{1}{3}B\,\mathrm{tr}(\mathbf{Q}^3) + \frac{1}{4}C\,\mathrm{tr}(\mathbf{Q}^2)^2, \tag{6.2}$$

where A, B and C are the material bulk constants [7]. The truncation used is sufficient to describe the Q-tensor field due to a disclination: a biaxial arrangement of uniaxial molecules lying in a ring about the disclination core [73]. The inclusion of higher order terms allows such states as the bulk biaxial phase [7].

The distortion energy density is quadratic in the gradients of the Q-tensor:

$$f_D(\partial\mathbf{Q}) := \frac{1}{2}L_1 Q_{\alpha\beta,\gamma}Q_{\alpha\beta,\gamma} + \frac{1}{2}L_2 Q_{\alpha\beta,\beta}Q_{\alpha\gamma,\gamma} + \frac{1}{2}L_4\sigma_{\alpha\beta\lambda}Q_{\alpha\gamma}Q_{\beta\gamma,\lambda} + \frac{1}{2}L_6 Q_{\alpha\beta}Q_{\gamma\lambda,\alpha}Q_{\gamma\lambda,\beta}. \tag{6.3}$$

The mappings between the elastic constants and $\{L_1 ... L_6\}$ are as in (5.5). For simplicity of presentation the splay-bend anisotropy (L_6) and chiral terms (L_4) have been omitted from

derivation that follows.

To describe weak surface anchoring a simple penalty-like method can be used to enforce alignment

$$f_S(\mathbf{Q}) := \frac{1}{2} W \operatorname{tr}\left((\mathbf{Q} - \mathbf{Q}_0)^2\right),$$

where $\mathbf{Q}_0$ is the prescribed Q-tensor on the boundary and W is the anchoring strength. A more advanced form is used in our model, with a different penalty associated with azimuthal and zenithal deformations, given by an expansion in the components of the Q-tensor [80].

The electrostatic energy is linear in the components of the Q-tensor and is written in terms of the electric field $\vec{E}$.

$$f_E(\mathbf{Q}) := \frac{1}{2}\varepsilon_0(\vec{E} \cdot \bar{\bar{\varepsilon}} \cdot \vec{E}).$$

The electric field is calculated from the electric potential which is found using the approach shown in Section 4.7. An estimation of the permittivity of the LC medium is required in terms of $\mathbf{Q}$:

$$\varepsilon_{\alpha\beta} = \varepsilon_\perp \delta_{\alpha\beta} + \Delta\varepsilon \left(\frac{2}{3S_0} Q_{\alpha\beta} + \frac{1}{3}\delta_{\alpha\beta} \right).$$

$\Delta\varepsilon$ is the dielectric anisotropy and $\varepsilon_\perp$ is the permittivity in the direction perpendicular to the long axis of the molecule. In the uniaxial state $\mathbf{Q}$ is defined as $S_0\left(3\hat{n}\hat{n} - I\right)/2$, where $\hat{n}$ is the director and S_0 is the equilibrium value of the order parameter, which can be found from the stationary value of f_B, giving $S_0 = \left(-B + \sqrt{B^2 - 24AC}\right)/(6C)$. The polarizability of the LC is neglected in this description, however the inclusion complicates the model only slightly and it has been included in the final implementation.

In order to solve these equations the symmetry and zero-trace of the Q-tensor should be maintained. There are several possible ways to do this. All 9 components of the Q-tensor can be solved for, and the constraints can be imposed using Lagrange multipliers or a penalty method. Most efficiently the constraints can be imposed strongly by using on five degrees of freedom. In other words $\mathbf{Q}$ is written in terms of a five dimensional subspace,

defined by an orthonormal basis [84]

$$\mathbf{Q} = q_i \mathbf{T}_i. \tag{6.4}$$

There are many possible choices for the basis tensors $\mathbf{T}_i$; we use one from [84]. This choice maintains the symmetry and the zero trace of the Q-tensor and enables us to calculate steady state or dynamic solutions.

$$\begin{aligned}
\mathbf{T}_1 &= (3\hat{\mathbf{e}}_z \otimes \hat{\mathbf{e}}_z - \mathbf{I})/\sqrt{6}, \\
\mathbf{T}_2 &= (\hat{\mathbf{e}}_x \otimes \hat{\mathbf{e}}_x - \hat{\mathbf{e}}_y \otimes \hat{\mathbf{e}}_y)/\sqrt{2}, \\
\mathbf{T}_3 &= (\hat{\mathbf{e}}_x \otimes \hat{\mathbf{e}}_y + \hat{\mathbf{e}}_y \otimes \hat{\mathbf{e}}_x)/\sqrt{2}, \\
\mathbf{T}_4 &= (\hat{\mathbf{e}}_x \otimes \hat{\mathbf{e}}_z + \hat{\mathbf{e}}_z \otimes \hat{\mathbf{e}}_x)/\sqrt{2}, \\
\mathbf{T}_5 &= (\hat{\mathbf{e}}_y \otimes \hat{\mathbf{e}}_z + \hat{\mathbf{e}}_z \otimes \hat{\mathbf{e}}_y)/\sqrt{2},
\end{aligned}$$

where $\hat{\mathbf{e}}_x$, $\hat{\mathbf{e}}_y$ and $\hat{\mathbf{e}}_z$ are unit vectors along x, y and z. $\mathbf{T}_1$ describes changes in the order parameter; $\mathbf{T}_2$, changes in the biaxiality and $\mathbf{T}_3$, $\mathbf{T}_4$ and $\mathbf{T}_5$ correspond to rotations [50]. Defined in this way, the basis tensors satisfy the orthogonality condition: $\mathrm{tr}(\mathbf{T}_i \mathbf{T}_j) = \delta_{ij}$.

From (6.2) and (6.4) the bulk free energy density becomes

$$\begin{aligned}
f_B =& \frac{A}{2} q_k q_k + \frac{C}{4} (q_k q_k)^2 + \frac{B}{2\sqrt{2}} \left[q_2 (q_4^2 - q_5^2) + 2 q_3 q_4 q_5 \right] \\
&+ \frac{B}{6\sqrt{6}} q_1 \left[2 q_1^2 + 3 (q_4^2 + q_5^2 - 2 q_2^2 - 2 q_3^2) \right].
\end{aligned} \tag{6.5}$$

From (6.3) and (6.4) and considering, for brevity, a two dimensional problem oriented in the x-z plane, the elastic and electric energies can written respectively as

$$\begin{aligned}
f_D =& \frac{L_1}{2} q_{k,\alpha} q_{k,\alpha} + \frac{L_2}{4} \left[q_{2,x}^2 + q_{3,x}^2 + q_{4,x}^2 + q_{4,z}^2 + q_{5,z}^2 \right] \\
&+ \frac{L_2}{12} \left[q_{1,x}^2 + 4 q_{1,z}^2 + 6 q_{2,x} q_{4,z} + 6 q_{3,x} q_{5,z} \right] \\
&+ \frac{L_2}{2\sqrt{3}} \left[2 q_{1,z} q_{4,x} - q_{1,x} (q_{2,x} + q_{4,z}) \right].
\end{aligned} \tag{6.6}$$

$$f_E = \frac{\varepsilon_0 \Delta\varepsilon}{3 S_0} \left(\frac{1}{\sqrt{6}} q_1 u_{,x}^2 - \frac{1}{\sqrt{2}} q_2 u_{,x}^2 - \sqrt{2} q_4 u_{,x} u_{,z} - \frac{2}{\sqrt{6}} q_1 u_{,z}^2 \right). \tag{6.7}$$

The final step in the procedure is to represent the Q-tensor components, q_k, and the potential, u ($\vec{E} = -\nabla u$), as a linear combination of the finite element shape functions (interpolation functions, piecewise polynomials) with amplitude coefficients chosen to approximate q_k and u. It is advantageous to use second order shape functions in both cases. The asymptotic error is of fourth order as opposed to second order for first order elements, giving better accuracy for the same number of nodes (the trade-off is a decrease in sparsity). An extensive convergence analysis of these equations is given in [85]. In each element the discretised form of q_k and u can be written

$$q_k \approx \sum_{i=1}^{N} q_k^i \phi^i, \qquad u \approx \sum_{i=1}^{N} u^i \phi^i,$$

where N is the number of nodes in the element, ϕ^i are shape functions and q_k^i and u^i are the amplitude coefficients to be found. The *LdG* free-energy functional is minimised according to:

$$\frac{\partial \mathcal{F}}{\partial q_k^i} = 0. \tag{6.8}$$

In order to determine the matrix form, a solution vector $\mathbf{q} = \{q_k^i\}$ is introduced containing the values of all five Q-tensor components at each node. The non-linear system (6.8) takes the form $[\mathbf{K} + \mathbf{B}(\mathbf{q})]\,\mathbf{q} = \mathbf{g}$, which can be solved using the Newton-Raphson method for $\Delta\mathbf{q} = \mathbf{q}^{m+1} - \mathbf{q}^m$, where m denotes the iteration number, leading to

$$[\mathbf{K} + \mathbf{J}(\mathbf{q}^m)]\,\Delta\mathbf{q} = \mathbf{g} - [\mathbf{K} + \mathbf{B}(\mathbf{q}^m)]\,\mathbf{q}^m. \tag{6.9}$$

Detailed expressions for $\mathbf{K}$, $\mathbf{B}$ and $\mathbf{g}$ have been found using Maple, starting from

$$\mathbf{Kq} = \frac{\partial \mathcal{F}_D}{\partial q_k^i}, \qquad \mathbf{Bq} = \frac{\partial \mathcal{F}_B}{\partial q_k^i}, \qquad \mathbf{g} = \frac{\partial \mathcal{F}_E}{\partial q_k^i},$$

and can be found in Appendix A.2. Here, $\mathbf{K}$ contains terms independent of $\mathbf{q}$ arising from the distortion and surface energies while the terms depending on $\mathbf{q}$ from the bulk energy are grouped in the matrix $\mathbf{B}$. When the L_6 term is included in the distortion energy, since it is non-linear, it contributes to $\mathbf{B}$. The vector $\mathbf{g}$ comes from the electrostatic energy density. At each iteration there is an overhead associated with the assembly of the Jacobian matrix

J which is defined as

$$J_{ij} = \frac{\partial(B_{ik}q_k)}{\partial q_j}.$$

Iterations are performed until $\|\Delta\mathbf{q}\| < \zeta$ for a given tolerance ζ.

6.3 Q-Tensor Dynamics

The Q-tensor field varies with time according to a dissipation principe. Neglecting translational flow of the LC the dissipation, $\mathcal{D}$, can be written as

$$\mathcal{D} = \int_\Omega \left\{ \frac{1}{2}\mu_1 \dot{Q}_{\alpha\beta}\dot{Q}_{\alpha\beta} \right\},$$

where μ_1 can be related to the rotational viscosity using $\mu_1 = \frac{2}{9S_0^2}\gamma_1$, leading the dynamic equilibrium equation:

$$\frac{\partial \mathcal{F}}{\partial Q^i_{\alpha\beta}} + \frac{\partial \mathcal{D}}{\partial \dot{Q}^i_{\alpha\beta}} = 0. \tag{6.10}$$

To obtain the weak form in terms of q, (6.10) can be written as

$$\frac{\partial \mathcal{F}}{\partial q^i_k} + \frac{\partial \mathcal{D}}{\partial \dot{q}^i_k} = 0.$$

Numerical integration in time is performed using the Crank-Nicholson method. Due to the non-linearity of the governing equations, Newton iterations are performed within each time step. Using n to denote the time step and m for the iteration number, the matrix form can be written as

$$\begin{aligned}\left[\frac{2\mu_1}{\Delta t}\mathbf{M} + \mathbf{K} + \mathbf{J}(\mathbf{q}^m_{n+1})\right]\Delta\mathbf{q}_{n+1} &= \mu_1\mathbf{M}\left[\frac{2}{\Delta t}\mathbf{q}_n + \dot{\mathbf{q}}_n\right] \\ &+ g_{n+1} - \left[\frac{2\mu_1}{\Delta t}\mathbf{M} + \mathbf{K} + \mathbf{B}(\mathbf{q}^m_{n+1})\right]\mathbf{q}^m_{n+1}.\end{aligned} \tag{6.11}$$

The right hand side is written in terms of the solution at the last time step. $\dot{\mathbf{q}} = \frac{\partial \mathbf{q}}{\partial t}$, and this form provides damping of roundoff errors [70]. The matrix M^{ij}_{kl} arises from $\mathcal{D}$ and is $\delta_{kl}\int_\Omega\{o^i o^j\}$.

6.4 Adaptive Meshing

A fine discretisation of the disclination core is required to determine the motion of the disclinations accurately, yet the container size can be large. It is inefficient to use a fine mesh everywhere, and thus there is a need to concentrate the mesh nodes where the Q-tensor varies rapidly.

The most common method of mesh adaption is refinement. An error estimate is calculated and if a specific error limit is exceeded in an element, the element is divided. This process is repeated until the error is below the limit throughout the whole of the computational domain. If a dynamic solution is required, regions where the solution varies rapidly are not fixed in space, and so it is necessary to unrefine (or merge) elements that are too small, in order to limit the number of elements in the mesh. Unrefinement is more complicated than refinement. A procedure known as decimation can be used to combine elements according to some criteria, in this case the error estimate, to create polygonal patches. These patches can then be meshed by Delaunay triangulation. Unrefinement could be avoided by refining each time starting from the initial triangulation instead of the previous triangulation.

Remeshing is chosen here, as opposed to refinement [86], as this tends to give rise to better quality meshes. Generation of triangular meshes tends to be a quick process, but for 3D problems it can be slow in comparison to refinement. An alternative approach that is perhaps better suited to 3D is a moving mesh, where the topology of the triangulation is maintained, but the nodes of the mesh are, on occasion, repositioned.

In this section the algorithm used to calculate the error estimate and the steps taken to then create the mesh are detailed. These steps are very much dependent on the mesh generator chosen. There are many commercially and freely available mesh generators [87, 88], but it is difficult to control these from within another program.

For mesh generation we choose DISTMESH [89] for several reasons. It is written in *MATLAB* (the same language that we have used to solve the Qian and Sheng equations), it produces high quality meshes, it is simple to use and understand and, most importantly, it allows the mesh density function to be specified (defined at the nodes of a grid).

The mesh density is determined from the error estimate, which in turn is calculated from the gradient of the Q-tensor field. Since the error estimate should be defined on a

grid, the first step is to interpolate to find the Q-tensor components on the grid.

6.4.1 Overview

An outline of the remeshing algorithm is given below. Each one of the steps is elaborated in the following sections. Typically remeshing is performed every 10-20 time steps.

1. use previous mesh density to calculate node spacing for regular mesh
2. distribute regular grid points
3. interpolate Q-tensor from FE mesh onto grid
4. calculate error estimate
5. calculate new mesh density function from error estimate
6. limit the gradient of the mesh density to improve mesh quality
7. generate mesh
8. interpolate values of the Q-tensor, the flow components and the potential from the old to the new mesh

6.4.2 Calculate Node Spacing for Error Estimate Grid

The calculated error estimate is required on a grid, so it may be used to calculate the mesh density function in an efficient manner. The mesh density function gives the desired element edge length throughout the computational domain. It is inefficient to use a uniform mesh, as rapid variations in the error will only occur in the proximity of disclinations. A method of choosing the nodal spacing of the non-uniform grid is required. Since the mesh density function, $h(x, y)$, from the last iteration is available and assuming the solution has not changed extensively since the last iteration, this spacing can be calculated. For the first iteration a uniform density function is used. Taking the minimum value over the rows and columns of $h(x, y)$ gives the mesh density for the grid along x and y respectively:

$$h_x = \min(h(x, :)), \qquad h_y = \min(h(:, y)).$$

The previous mesh density used to create the FE mesh may be very fine, and using this form directly would give a very fine grid, resulting in a slow calculation of the error estimate. Integrating the inverse of the mesh density gives an estimate of the number of node spanning the axis. The equations below give the mesh density scaled to give approximately N nodes in the x-direction and M nodes in the y-direction.

$$h_x^s(x) = h_x(x)\frac{\int_0^{l_x} h_x^{-1}(x)dx}{N-1},$$
$$h_y^s(y) = h_y(y)\frac{\int_0^{l_y} h_y^{-1}(y)dy}{M-1},$$

where l_x and l_y are the dimensions of the structure in the x and y directions respectively.

6.4.3 Distribute Regular Grid Points

Using the scaled mesh density calculated above a distribution of nodes can be found that gives an M by N grid concentrated in regions where the Q-tensor is varying rapidly. In the x-direction nodes are distributed according to $\{x_1 = x_0 + h_x^s(0),\ x_2 = x_1 + h_x^s(x_1),\ ...,\ x_n = x_{n-1} + h_x^s(x_{n-1}),\ ...,\ x_{N-1} = x_{N-2} + h_x^s(x_{N-2}),\ x_N = l_x\}$. Special treatment of the end point is necessary to ensure it coincides with the boundary. Using the same approach nodes can be placed in the y-direction.

6.4.4 Interpolate Q-tensor from Mesh to Grid

The *MATLAB PDE toolbox* contains the routine *tri2grid* which interpolates a linear function defined at the nodes of a mesh onto a grid which need not necessarily be uniform. The routine returns for each point on the grid the triangle that contains it, and the local coordinates of the point within that triangle. Subsequent calls to *tri2grid* can be accelerated using this information. Since our code uses second order elements, we use this information and the second order shape functions to interpolate from the FE mesh to the regular grid.

6.4.5 Calculate Error Estimate

There are a number of ways to estimate the error in a numerical solution. Three methods are described here: an a posteriori error estimate, an empirical error estimate and finally an

estimate found by a technique known as patch recovery. The error estimate is defined as

$$\|e\| = \|q - q_h\|. \tag{6.12}$$

where q_h is either the known solution or an approximate solution that is of higher accuracy than q. For instance q_h could be the solution calculated on a finer mesh than the original solution. The value of $\|e\|$ can be evaluated over subdomains or even individual elements (defined as Ω_i)

$$\|e\|^2 = \sum_{i=1}^{m} \|e\|_i^2$$
$$\xi_i = \|e\|_i / \overline{e}_m.$$

This allows the error to be estimated in the individual elements (ξ_i), where $\overline{e}_m$ is the permitted error in any element. This value should be chosen so that the disclination core is properly resolved.

The value of ξ_i is an ideal measure to drive a mesh refinement algorithm. If it exceeds a certain threshold ($\xi_i > 1$) the element is refined. Elements are divided and then divided again until all elements are beneath the threshold and this repeated division tends to give rise to a smoothly graded mesh. If the error is below a certain threshold then the element can be unrefined; however, this process is more involved than refinement.

A Posteriori Error Estimate

An a posteriori error analysis of a differential equation allows an error estimator to be accurately constructed using a given solution. For a Euler-Lagrange equation of the form

$$\mathbf{K}(q) \cdot q + \nabla \cdot \mathbb{K}(q)[\nabla q] = g$$

we can take advantage of the extensive work that has been carried out for the Laplace problem, which can be generalised [90] to give the following estimate:

$$\|e\| = \alpha \|h(g - \mathbf{K}(q) \cdot q)\| + \beta \left(\frac{1}{2} \sum_{\Gamma \in \partial\Omega} h_\Gamma^2 (\hat{\eta} \cdot \mathbb{K}(q)[\nabla q])^2 \right)^{\frac{1}{2}}.$$

where α and β are constants. The first term is a volume term, which corresponds to the norm of the residual. The second term corresponds to the jump in the flux of q across the element boundaries (∇q). Here, h_Γ represents the side length of the elements and $\hat{\eta}$ is te normal to these sides.

Patch Recovery [64]

Patch recovery is a popular technique because it is applicable to a wide range of problems regardless of the underlying PDE [91]. Here a more accurate vector q_h is calculated from the solution vector. This is possible because there exist certain 'super-convergent' points within an element, where the solution is more accurate than at the nodes. These points turn out to be the Gauss integration points. By considering the patch of elements connected to a node it is possible to construct a polynomial which passes through these points using a least-squares approach with an order of accuracy one higher than the solution vector. This polynomial then gives q_h at the nodes and then (6.12) gives the error.

Empirical Error Estimate

When the accuracy of the error estimate is not so important, an empirical estimate that is quick to calculate can often suffice. For elasticity problems, an energy norm can be written for the error [64, 86].

$$\|e\|^2 = \int_\Omega \left\{ (Q_{\alpha\beta,\gamma} Q_{\alpha\beta,\gamma})^2 \right\}.$$

Since the error estimate is used to drive a mesh generator, it is the speed at which the estimate may be calculated that is important, not so much the accuracy. An empirical error estimate (this energy norm) is the method implemented.

6.4.6 Calculate Mesh Density Function

After the error estimate is calculated, a mesh density function then needs to be found. It can be calculated as

$$h = \xi_i^{-1/p} h_i. \tag{6.13}$$

where p is the polynomial order of the shape functions [64]. The Q-tensor components are smoothly varying, although the spatial gradients can be steep. For other problems, where singularities exist, then p should be modified to a value of 0.5 to 1.0 depending on the type of singularity [64].

This form seems to be directly taken from a mesh refinement point of view; if the error in an element is too large then divide the element. The factor of p then controls the growth rate.

However, the error estimate is required on a regular grid. Consider two uniform meshes that are adequately fine to represent the changes in the Q-tensor that occur on the FE mesh. For each mesh equation (6.13) yields a different h. Undesirably, the size function depends on the discretisation of the regular grid.

To overcome this problem we use a modified form that gives rise to an element size that depends only on the spatial derivatives of the Q-tensor

$$h \propto (Q_{\alpha\beta,\gamma} Q_{\alpha\beta,\gamma})^{-1}. \tag{6.14}$$

A scaling factor is chosen that limits the smallest element size so that the disclination core is properly resolved, i.e. there are a few nodes per correlation length in proximity to disclinations. The maximum value must also be limited so that nodes coincide with the features of the boundary. When calculating the gradient of the Q-tensor field the *MATLAB* *gradient* function cannot be applied due to the non-uniformity of the grid. A modified procedure is required that maintains second order accuracy on an non-uniform mesh. Fig. 6-1 shows the mesh density function calculated prior to the annihilation of $+1/2$ and $-1/2$ disclination lines, as described in [28].

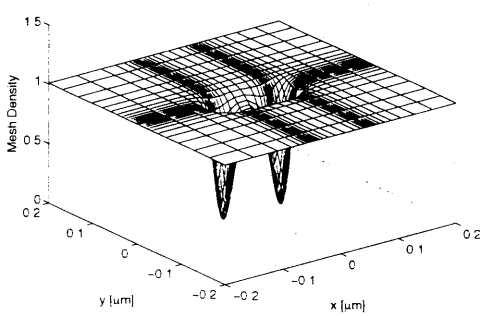

Figure 6-1: Mesh density calculated directly from the error estimate

Calculating the mesh size function in this way works well provided the solution does not change dramatically between remeshings.

6.4.7 Limit the Gradient of the Mesh Density

Sharp changes of the mesh density are not only problematic for the mesh generator, but give rise to stretched elements and a poor quality mesh. Furthermore error estimates tend to be guaranteed only for triangles that are nearly equilateral. Using the calculated size function directly can give rise to such sharp changes in mesh density, particularly at the edge of electrodes.

To overcome this problem we seek the steady-state solution to the *Gradient Limiting Equation* [92], with starting a configuration given by (6.14)

$$\frac{\partial h}{\partial t} = \min(|\nabla h|, g) - |\nabla h|.$$

This equation can be discretised using an implicit or an explicit method, however, more efficiently a Fast-Marching Algorithm can be used [92]. Starting with the node with the smallest mesh density, we check that its neighbours do not exceed the gradient limit g by calculating the forward difference, $|\nabla h| > g$. If any neighbour exceeds this value it is updated according to

$$\begin{aligned} g = \big[&\max(D^{-x}h_{jk}, 0)^2 + \min(D^{+x}h_{jk}, 0)^2 + \\ &\max(D^{-y}h_{jk}, 0)^2 + \min(D^{+y}h_{jk}, 0)^2 \big]^{1/2}. \end{aligned} \tag{6.15}$$

This equation can be rearranged to give a quadratic equation for h_{jk} in terms of the surrounding nodes. The procedure is then repeated for the next smallest node, until all nodes have been checked and updated if necessary. Fig. 6-2 shows the mesh density function after gradient limiting.

Although the Fast-Marching Algorithm is fast compared to directly solving the PDE, it can be time consuming to search for the node with the minimum value of h. Data structures such as the minheap or Fibonacci heap can be used to reduce the search time. The later has the advantage of having the function for the promotion of keys in the heap built into the specifications.

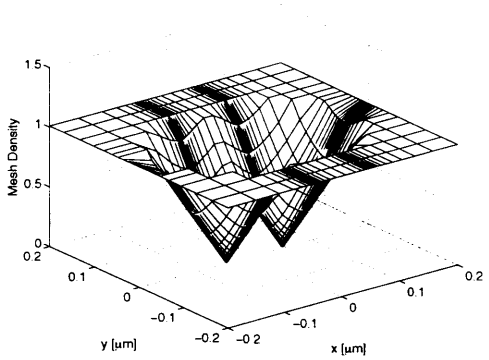

Figure 6-2: Mesh density after gradient limiting applied

6.4.8 Generate the Mesh

The mesh generator *DISTMESH* [89] requires two input arguments; a mesh density (referred to as a distance function in *DISTMESH*) that describes the geometry and the mesh density. A large number of nodes are initially positioned randomly throughout the computational domain and then some are rejected with a probability determined by the density function. The triangulation is then performed and, finally, a force-based spring method is used to reposition the nodes to improve the mesh quality. This method of initialing the nodes of the mesh is simple and works well provided that there are not large changes in the mesh density. Unfortunately the mesh adaption ratio tends to be of the order 100 : 1 when disclinations are present in the modelling window. Vast regions of the modelling window become nodeless after the rejection rule is applied and the initial triangulation fails. It becomes necessary to position the nodes in a more precise fashion, using Delaunay triangulation and refinement so that the initial mesh satisfies the density function. *DISTMESH* is then used to improve the mesh quality.

Some slight modifications to *DISTMESH* are necessary to meet our needs. Firstly the program was modified to allow a functional description of the geometry function and a discrete description of the mesh density function. The *hmatrix.m* function then creates a continuous function from the discrete mesh density using the *MATLAB* function *interp2*. A slight modification is required: the default *'linear'* argument *interp2* should be omitted, as it is only suitable for mesh density functions defined on uniform meshes. Fig. 6-3 shows the mesh generated for the two disclination problem.

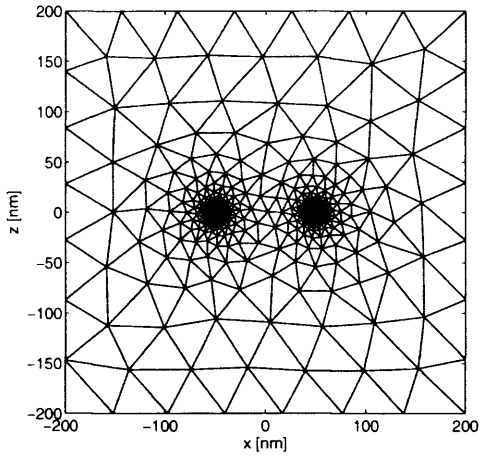

Figure 6-3: Mesh generated by *DISTMESH* using the gradient limited density function. Ratio between the longest and shortest triangle edge is approximately 100 : 1.

6.4.9 Interpolate from the Old to the New Mesh

The final procedure is to interpolate values of the Q-tensor, the flow components and the potential onto the new mesh. Unfortunately no variant of *tri2grid* is available in *MATLAB* that provides this facility. Each node of the new mesh is considered in turn. Elements of the old mesh that are in the neighbourhood of the new node are checked to see if they contain the node. In the containing element, using second order shape functions the solution vector at the new node is then found by interpolation.

6.5 Validation

In this section, results of validation tests are compared to some previously published results [73, 93], performed using a single elastic constant approximation ($L_2 = 0$) and the material parameters of MBBA [94, 7] [1]:

$a = 8.67 \times 10^4\,\mathrm{N/m^2K}$, $(T - T^*) = -4\,\mathrm{K}$, $A = a(T - T^*)$,

$B = -2.12 \times 10^6\,\mathrm{N/m^2}$, $C = 1.74 \times 10^6\,\mathrm{N/m^2}$,

$\gamma_1 = 0.076\,\mathrm{Pa{\cdot}s}$ and $k = 6\,\mathrm{pN}$.

The Q-tensor formulation was tested for two simple cases: a planar and a twisted cell. Both static and dynamic director profiles were found to agree well with a previously verified constant-order-parameter model, based on a vectorial representation of the director [95].

[1] There is a wide variation in the published values of the elastic constants for MBBA. An averaged value is used here

To verify that the model can simulate variations of the order parameter appropriately it is insightful to study disclinations. A starting director configuration with a $+1/2$ disclination at the centre of the modelling window was chosen and iterations performed using the steady-state Q-tensor formulation. Such disclinations have been extensively studied, see for example [73, 93]. Fig. 6-4 shows the variation in the two order parameters as a function of the distance from the disclination core. At the disclination core ($r = 0$) the

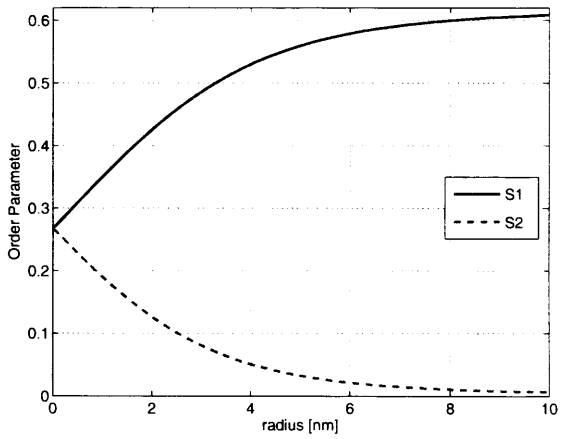

Figure 6-4: Order Parameters $S1$ and $S2$ as a function of radius from the core of a $+1/2$ disclination.

two order parameters are equal, and the LC is in the uniaxial nematic state. Encircling the disclination core is a ring of maximal biaxiality at approximately $r \approx 1$nm. For large values of r the LC is again uniaxial. This behaviour is in agreement with [73, 93].

6.6 Conclusions

A finite element model of the Landau-de Gennes free energy functional has been presented and validated. The ability to adapt the mesh allows the study of realistically sized devices with proper consideration of small scale features and disclinations, providing significant savings in terms of the number of degrees of freedom and computation cost in comparison to traditional finite difference methods. Time integration is performed using an implicit method, thus additional savings are available through the use of a variable time step in accord with the rate of change of the LC orientation. More detail on the specific implementation details will be given in the next chapter.

An adaptive meshing scheme and error estimate have been presented that allow the

mesh density to be concentrated where needs be, for instance near disclination lines. The error estimate is quick to calculate and the reduction in the number of elements affords a welcome reduction to the simulation time. Although the results presented in here are for the 2D case, extending the method to 3D is straightforward.

Chapter 7

Hydrodynamics

7.1 Introduction

A nematic LC flows much like a conventional liquid, and in most cases the flow disturbs the alignment [96]. Conversely a change in alignment will often induce a flow. In common liquid crystal (LC) structures relaxation dynamics can be greatly affected by the flow of the LC. In fact, (back)flow immediately after a holding voltage is removed can cause molecules to tilt further and accelerates the subsequent relaxation to a homogeneous state [97]. Ericksen-Leslie theory [98, 99] has been applied to the study of backflow with much success. In this theory the orientation of the LC is represented by a director field and thus the equations are restricted to a uniaxial state with a constant degree of order.

However, when high holding voltages are applied, the order parameter drops and the biaxial ordering increases near the alignment layers [12]. Similarly, these effects occur in the vicinity of disclinations, and since the order parameter cannot relax in the Ericksen-Leslie theory, the equations become numerically ill conditioned. The Qian and Sheng formulation [12] is a generalisation of the Ericksen-Leslie theory that allows a reduction of the order parameter and biaxiality. Instead of representing the molecular orientation by directors, the Q-tensor, a rank-two symmetric tensor is used. The Beris-Edwards equations [100] are a similar generalisation, but consider only two viscosity coefficients. Furthermore the viscosity coefficients in the Qian and Sheng equations can be obtained directly from the Ericksen-Leslie coefficients, the standard means to characterise LCs.

The effect of hydrodynamics on the movement of topological disclinations has been investigated by Tóth *et al.* [101] and Svenšek and Žumer [28]. Tóth *et al.* use a lattice Boltzmann algorithm to approximate the Berris Edwards equations. In this technique the momentum space is reduced to a few discrete points, giving sets of local equations that can be solved individually. The density flowing into a point is redistributed to lattice neighbours using a set of collision rules. All computations are performed locally at each lattice point and so there is intrinsic parallelism. Svenšek and Žumer use a finite difference discretisation of the Qian and Sheng equations. Similar discretisations of these governing equations can be found in [29, 30, 102, 103].

To begin, a form of the (incompressible) Navier-Stokes equations is described, which is generalised to take into account the anisotropy of the liquid crystal. This same form is used to calculate the velocity field for both Ericksen-Leslie and Qian and Sheng equations.

although there is a difference in some of the stress tensor terms. Firstly the Ericksen-Leslie theory will be introduced, starting with the calculation of the director dynamics. Finally a more detailed look at an implementation of the Qian-Sheng equations is given, taking a finite element approach. An implicit time integration scheme is used with an adaptive time step. Finally, the model is validated by looking at the pair-annihilation of $\pm 1/2$ disclinations.

7.2 Navier-Stokes Equations

In this section a finite element discretisation of the velocity-pressure form of the incompressible Navier-Stokes equations is described [104, 105]. The momentum equation, written in terms of a generalised stress tensor σ is

$$\rho \frac{dv_\alpha}{dt} = \partial_\beta \left(-p\delta_{\beta\alpha} + \sigma^d_{\beta\alpha} + \sigma^e_{\beta\alpha} + \sigma^v_{\beta\alpha} \right), \tag{7.1}$$

where the total time derivative operator $\frac{d}{dt}$ is defined as $\left(\frac{\partial}{\partial t} + \vec{v} \cdot \nabla\right)$. There are several contributions to the overall stress tensor; $\sigma^v_{\alpha\beta}$, the viscous stress, $\sigma^e_{\alpha\beta}$, the electric field-induced stress and $\sigma^d_{\alpha\beta}$, the distortion stress. For finite element analysis it is desirable to convert these strong equations into more amenable weak forms. A Lagrangian that satisfies the Euler-Lagrange equation above does not exist unless the non-linear advective term can be neglected, in other words $(\vec{v} \cdot \nabla)\vec{v} = 0$. If these non-linear terms are included then no variational form exists, in which case the Weighted-Residual Method can be used, as is common in the field of fluid dynamics.

The pressure field, p, is such that it satisfies the continuity equation, acting as a Lagrange multiplier to enforce the incompressibility of the fluid:

$$\partial_\mu v_\mu = 0.$$

The expression for the electric field-induced stress tensor is simplified assuming that the LC is incompressible:

$$\sigma^e_{\alpha\beta} = D_\alpha E_\beta - \frac{1}{2} D_\mu E_\mu \delta_{\alpha\beta},$$

where $\vec{D}$ is the electric displacement.

The viscous stress $\sigma^v_{\alpha\beta}$ and the distortion stress $\sigma^d_{\alpha\beta}$ are different in the case of the Ericksen-Leslie and the Qian & Sheng equations. These will be detailed individually in the following sections.

7.3 Ericksen-Leslie theory

There are two formulations of the equations of hydrodynamics of nematic LCs, the Ericksen-Leslie-Parodi (ELP) [98, 99, 7] and the Harvard [106] formalism. The ELP equations are most widely used and are described in this section.

In order to calculate the velocity field we require the distortion stress and the viscous stress. To calculate the director field a modified form of the dissipation must be found that takes into account the reorientation of the liquid crystal induced by its flow. These three terms can be found from the Rayleigh dissipation function (energy density) of an anisotropic fluid is [105, 15]:

$$\begin{aligned} d = & \frac{1}{2}\eta(v_{\beta,\alpha}v_{\beta,\alpha} + v_{\beta,\alpha}v_{\alpha,\beta}) \\ & + \frac{1}{2}\xi_1(n_\alpha v_{\mu,\alpha} - \dot{n}_\mu)(n_\beta v_{\mu,\beta} - \dot{n}_\mu) \\ & + \frac{1}{2}\xi_2(n_\alpha v_{\alpha,\mu} - \dot{n}_\mu)(n_\beta v_{\beta,\mu} - \dot{n}_\mu) \\ & + \xi_3(n_\alpha v_{\mu,\alpha} - \dot{n}_\mu)(n_\beta v_{\beta,\mu} - \dot{n}_\mu) \\ & + \frac{1}{2}\xi_4 n_\alpha n_\beta n_\mu n_\nu v_{\beta,\alpha} v_{\nu,\mu} \end{aligned} \tag{7.2}$$

First of all we deal with the calculation of the director field. The dissipated energy is $\mathcal{D} = \int_\Omega \{d\}$. The rate of change of the free energy is equal to the rate of change of the dissipated energy. Taking a finite element approach, an equation for the dynamic behaviour of $\hat{n}$ can be written as

$$\frac{\partial \mathcal{F}}{\partial n^i_\alpha} + \frac{\partial \mathcal{D}}{\partial \dot{n}^i_\alpha} = 0,$$

with $\mathcal{F}$ defined as in (5.1). After some manipulation, the dissipation can be written in terms of the standard Leslie coefficients. The rate of change of the dissipated energy with respect

to $\dot{n}$ is then simply

$$\frac{\partial \mathcal{D}}{\partial \dot{n}_\alpha^i} = \int_\Omega \left\{ \left(\gamma_1 N_\alpha + \gamma_2 A_{\alpha\mu} n_\mu \right) \phi^i \right\}.$$

where

$$N_\alpha = \frac{dn_\alpha}{dt} + W_{\alpha\mu} n_\mu$$

and μ_1 and μ_2 are viscosity coefficients. The symmetric part of the velocity gradient is defined as $A_{\alpha\beta} = \frac{1}{2}(\partial_\alpha v_\beta + \partial_\beta v_\alpha)$ and the vorticity tensor is $W_{\alpha\beta} = \frac{1}{2}(\partial_\alpha v_\beta - \partial_\beta v_\alpha)$.

The dynamics of the director are fully determined. Finally, it is possible to calculate the viscous stress from the Rayleigh dissipation function as follows:

$$\sigma_{\alpha\beta}^v = \frac{\partial d}{\partial v_{\beta,\alpha}}. \tag{7.3}$$

Once again, after some simplification, the viscous stress tensor can be written in terms of the Leslie coefficients as

$$\begin{aligned} \sigma_{\alpha\beta}^v = {} & \alpha_1 n_\alpha n_\beta n_\mu A_{\mu\nu} n_\nu + \alpha_2 n_\alpha N_\beta + \alpha_3 N_\alpha n_\beta \\ & + \alpha_4 A_{\alpha\beta} + \alpha_5 n_\alpha A_{\beta\mu} n_\mu + \alpha_6 A_{\alpha\mu} n_\mu n_\beta. \end{aligned}$$

And finally, the distortion stress is given by

$$\sigma_{\alpha\beta}^d = -\frac{\partial f_D}{\partial n_{\mu,\alpha}} n_{\mu,\beta}.$$

7.4 Qian-Sheng Equations [12]

To calculate hydrodynamics whilst taking into account variations in the order parameter one must rewrite the Rayleigh dissipation function in terms of Q. The dissipation function should now be formed from the invariants containing $\mathbf{Q}$, $\dot{\mathbf{Q}}$ and A, where A is defined as before as $A_{\alpha\beta} = \frac{1}{2}(\partial_\alpha v_\beta + \partial_\beta v_\alpha)$. There are several forms of the dissipation function that, under the assumption that the order parameter is constant, reduce to the Ericksen-Leslie theory. It has been shown that the Beris-Edwards [100] and the Qian-Sheng [12] equations are two such forms, with different terms appearing in the dissipation function

[107, 108]. Qualitatively the flow field about annihilating disclination lines agrees well using both theories [101, 28]. The effect of the difference in dissipation function is most evident in the viscous stress; it is 4^{th} order in Q for the Beris-Edwards equations and 2^{nd} order for the Qian-Sheng equations.

We have chosen to implement the Qian-Sheng equations as the viscosity coefficients correspond directly to the Leslie coefficients and discretisation is more straightforward. Here, the dissipation function is written such that any terms in $\mathbf{Q}$ or $\dot{\mathbf{Q}}$ are second order, that is, they depend on S^2. Most of the terms appearing in (7.2) can be straightforwardly substituted to give a dissipation function in terms of $\mathbf{Q}$, but the procedure for the terms in $n_\alpha \dot{n}_\mu$ is a little more complicated. The following substitution is used:

$$n_\alpha \dot{n}_\mu = \frac{4}{9S_0^2}\left(Q_{\alpha\lambda} + \frac{1}{2}S_0\delta_{\alpha\lambda}\right)\dot{Q}_{\mu\lambda},$$

the proof of which is

$$\begin{aligned}
\frac{4}{9S_0^2}\left(Q_{\alpha\lambda} + \frac{1}{2}S_0\delta_{\alpha\lambda}\right)\dot{Q}_{\mu\lambda} &= n_\alpha n_\lambda \frac{\partial}{\partial t}(n_\mu n_\lambda) \\
&= n_\alpha n_\lambda(\dot{n}_\mu n_\lambda + n_\mu \dot{n}_\lambda) \\
&= n_\alpha (n_\lambda n_\lambda)\dot{n}_\mu + \frac{1}{2}n_\alpha n_\mu \frac{\partial}{\partial t}(n_\lambda n_\lambda) \\
&= n_\alpha \dot{n}_\mu.
\end{aligned}$$

The terms in the dissipation should be bilinear in $\dot{Q}$ and A, but can contain Q many times:

$$\begin{aligned}
d = {} & \frac{1}{18}(9\eta + \xi_1 + \xi_2)\, v_{\beta,\alpha} v_{\beta,\alpha} + \frac{1}{18}(9\eta + 2\xi_3)\, v_{\beta,\alpha} v_{\alpha,\beta} + \frac{1}{18}\xi_4 v_{\alpha,\alpha} v_{\beta,\beta} \\
& + \frac{2}{9S_0^2}(\xi_1 + \xi_2 + 2\xi_3)\, \dot{Q}_{\alpha\beta}\dot{Q}_{\alpha\beta} \\
& + \frac{1}{2}\xi_1\left(\frac{4}{9S_0^2}Q_{\alpha\nu}Q_{\beta\nu}v_{\mu,\alpha}v_{\mu,\beta} + \frac{4}{9S_0}Q_{\alpha\beta}v_{\mu,\alpha}v_{\mu,\beta} - \frac{8}{9S_0^2}Q_{\alpha\nu}\dot{Q}_{\mu\nu}v_{\mu,\alpha} - \frac{4}{9S_0}\dot{Q}_{\mu\alpha}v_{\mu,\alpha}\right) \\
& + \frac{1}{2}\xi_2\left(\frac{4}{9S_0^2}Q_{\alpha\nu}Q_{\beta\nu}v_{\alpha,\mu}v_{\beta,\mu} + \frac{4}{9S_0}Q_{\alpha\beta}v_{\alpha,\mu}v_{\beta,\mu} + \frac{8}{9S_0^2}Q_{\alpha\nu}\dot{Q}_{\mu\nu}v_{\alpha,\mu} + \frac{4}{9S_0}\dot{Q}_{\mu\alpha}v_{\alpha,\mu}\right) \\
& + \xi_3\left(\frac{4}{9S_0^2}Q_{\alpha\nu}Q_{\beta\nu}v_{\mu,\alpha}v_{\beta,\mu} + \frac{4}{9S_0}Q_{\alpha\beta}v_{\mu,\alpha}v_{\beta,\mu}\right) \\
& + \xi_3\left(\frac{4}{9S_0^2}Q_{\alpha\nu}\dot{Q}_{\mu\nu}v_{\mu,\alpha} + \frac{4}{9S_0^2}Q_{\alpha\nu}\dot{Q}_{\mu\nu}v_{\alpha,\mu} + \frac{4}{9S_0}\dot{Q}_{\mu\alpha}v_{\mu,\alpha}\right) \\
& + \frac{1}{2}\xi_4\left(\frac{4}{9S_0^2}Q_{\alpha\beta}Q_{\mu\nu}v_{\beta,\alpha}v_{\nu,\mu} + \frac{4}{9S_0}Q_{\alpha\beta}v_{\beta,\alpha}v_{\mu,\mu}\right)
\end{aligned} \tag{7.4}$$

Once again, the rate of change of the free energy is equal to the rate of change of the dissipated energy. The dynamic evolution of the Q-tensor is given by this solution to

$$\frac{\partial \mathcal{F}}{\partial Q^i_{\alpha\beta}} + \frac{\partial \mathcal{D}}{\partial \dot{Q}^i_{\alpha\beta}} = 0,$$

with $\mathcal{F}$ is defined as in (6.1). The rate of change of the dissipated energy with respect to $\dot{\mathbf{Q}}$ is then

$$\frac{\partial \mathcal{D}}{\partial \dot{Q}^i_{\alpha\beta}} = \int_\Omega \left\{ \left(\frac{1}{2}\mu_2 A_{\alpha\beta} + \mu_1 N_{\alpha\beta} \right) \phi^i \right\},$$

where

$$N_{\alpha\beta} = \frac{dQ_{\alpha\beta}}{dt} + W_{\alpha\mu}Q_{\mu\beta} - Q_{\alpha\mu}W_{\mu\beta}.$$

The vorticity tensor is defined identically to the ELP theory as $W_{\alpha\beta} = \frac{1}{2}(\partial_\alpha v_\beta - \partial_\beta v_\alpha)$.

The viscous stress is obtained using (7.3), with d defined as in (7.4), in terms of Q.

$$\begin{aligned}\sigma^v_{\alpha\beta} =& \beta_1 Q_{\alpha\beta}Q_{\mu\nu}A_{\mu\nu} + \beta_4 A_{\alpha\beta} + \beta_5 Q_{\alpha\mu}A_{\mu\beta} + \beta_6 Q_{\beta\mu}A_{\mu\alpha} \\ &+ \frac{1}{2}\mu_2 N_{\alpha\beta} - \mu_1 Q_{\alpha\mu}N_{\mu\beta} + \mu_1 Q_{\beta\mu}N_{\mu\alpha}.\end{aligned}$$

where the viscosity coefficients $\{\mu_1, \mu_2, \beta_1, \beta_4, \beta_5, \beta_6\}$ can be obtained from the Ericksen-Leslie coefficients $\{\alpha_1, \alpha_2, ..., \alpha_6\}$ using the mappings given in [77, 12].

$$\mu_1 = \frac{2}{9S_0^2}\gamma_1. \qquad \mu_2 = \frac{2}{3S_0}\gamma_2. \qquad \beta_1 = \frac{4}{9S_0^2}\alpha_1. \qquad \beta_5 = \frac{2}{3S_0}\alpha_5. \qquad \beta_6 = \frac{2}{3S_0}\alpha_6.$$

$$\beta_4 = \alpha_4 + \frac{S_0}{2}(\beta_5 + \beta_6).$$

The distortion stress is given by

$$\begin{aligned}\sigma^d_{\alpha\beta} =& -\frac{\partial f_D}{\partial(Q_{\mu\nu,\alpha})}Q_{\mu\nu,\beta}. \\ =& -L_1 Q_{\mu\nu,\alpha}Q_{\mu\nu,\beta} - L_2 Q_{\mu\nu,\nu}Q_{\mu\alpha,\beta} - L_4 \sigma_{\gamma\mu\alpha}Q_{\gamma\nu}Q_{\mu\nu,\beta} - L_6 Q_{\alpha\gamma}Q_{\mu\nu,\gamma}Q_{\mu\nu,\beta}\end{aligned}$$

7.4.1 Q-Tensor Implementation

The dynamic evolution of the Q-tensor can be written in terms of q_k as

$$\frac{\partial \mathcal{F}}{\partial q_k^i} + \frac{\partial \mathcal{D}}{\partial \dot{q}_k^i} = 0.$$

where the rate of change of the dissipated energy with respect to $\dot{q}$ is

$$\frac{\partial \mathcal{D}}{\partial \dot{q}_k^i} = \int_\Omega \left\{ \mathrm{tr}\left(\frac{1}{2}\mu_2 A \mathbf{T}_k + \mu_1 N \mathbf{T}_k \right) \phi^i \right\}. \tag{7.5}$$

The tensors **A**, **W** and **N** are as defined in Section 7.4. The expanded form of this expression is given in Appendix A.2.

Using the Crank-Nicholson method for time integration the matrix equation for the Q-tensor becomes

$$\begin{aligned} \left[\frac{2\mu_1}{\Delta t}\mathbf{M} + \overline{\mathbf{K}} + \mathbf{J}(\mathbf{q}_{n+1}^m) \right] \Delta \mathbf{q}_{n+1} &= \mu_1 \mathbf{M} \left[\frac{2}{\Delta t}\mathbf{q}_n + \dot{\mathbf{q}}_n \right] \\ &+ \overline{\mathbf{g}}_{n+1} - \left[\frac{2\mu_1}{\Delta t}\mathbf{M} + \overline{\mathbf{K}} + \mathbf{B}(\mathbf{q}_{n+1}^m) \right] \mathbf{q}_{n+1}^m. \end{aligned} \tag{7.6}$$

The right hand side is written in terms of the solution at the last time step, $\dot{\mathbf{q}} = \frac{\partial \mathbf{q}}{\partial t}$. This form provides damping of roundoff errors [70]. The matrix M_{kl}^{ij} is formed by $\delta_{kl} \int_\Omega \{\phi^i \phi^j\}$. $\overline{\mathbf{g}}$ is made up of $\mathbf{g}$ and velocity terms from **A**, $\overline{\mathbf{K}}$ comprises $\mathbf{K}$ and velocity terms from **W** (which renders $\overline{\mathbf{K}}$ asymmetric). Here, $\mathbf{g}$, $\mathbf{K}$ and $\mathbf{B}$ are as used in Section 6.2.

7.4.2 Navier-Stokes Discretisation

The weak form is obtained taking a Galerkin approach, giving a set of three coupled equations for the x, y, and z components of the velocity:

$$\int_\Omega \left\{ \rho \phi^i \frac{dv_\alpha}{dt} \right\} = \int_\Omega \left\{ \phi^i \partial_\beta \left(-p\delta_{\beta\alpha} + \sigma_{\beta\alpha}^d + \sigma_{\beta\alpha}^e + \sigma_{\beta\alpha}^v \right) \right\}.$$

The shape functions here are the same second order functions used to represent the Q-tensor components. Similarly for the pressure

$$\int_\Omega \{ \psi^i \partial_\mu v_\mu \} = 0.$$

A different set of shape functions, ψ, of lower order are used for the pressure. If they are of the same order as those for the velocity too many constraints are placed upon the velocity, leading to oscillatory solutions for the pressure [70]. An alternative to this mixed interpolation procedure is using a formulation stabilized by the inclusion of damping terms [70].

The momentum equation is integrated by parts, yielding

$$\int_\Omega \left\{ \rho \phi^i \frac{dv_\alpha}{dt} \right\} = - \int_\Omega \left\{ \phi^i_{,\beta} \left(-p\delta_{\beta\alpha} + \sigma^d_{\beta\alpha} + \sigma^e_{\beta\alpha} + \sigma^v_{\beta\alpha} \right) \right\}.$$

The surface terms that arise from the integration are set to zero, leading to the natural boundary condition

$$\eta_\beta \left(-p\delta_{\beta\alpha} + \sigma^d_{\beta\alpha} + \sigma^e_{\beta\alpha} + \sigma^v_{\beta\alpha} \right) = 0,$$

for the velocity components. For non-slip or periodic boundaries this surface term can indeed be neglected, but if any part of the boundary remains free then this boundary integral should be modified appropriately. No pressure boundary condition is implied in the above formulation, the pressure at the boundary merely satisfies the incompressibility condition as required.

The use of a numerical integration scheme allows some simplification of these expressions. The weak form of the momentum equation can be rearranged as

$$\int_\Omega \left\{ \rho \phi^i \frac{dv_\alpha}{dt} - p\phi^i_{,\alpha} + \phi^i_{,\beta} (v_{\mu,\nu} G^{\alpha\mu}_{\beta\nu} + v_\mu U^{\alpha\mu}_\beta + V^\alpha_\beta) \right\} = 0,$$

where $G^{\alpha\mu}_{\beta\nu}$ contains the material viscosity coefficients and the components of the Q-tensor, q_k, and $U^{\alpha\mu}_\beta$ is made up of gradients in q_k. V^α_β contains the driving stress components due to the reorientation of the LC, the distortion stress and the field induced stress. Maple has been used to obtain expressions for $G^{\alpha\mu}_{\beta\nu}$, $U^{\alpha\mu}_\beta$ and V^α_β.

For elasticity driven dynamics of LCs the low-Reynolds number approximation can be made, whereby the non-linear advective term, $(\vec{v}\cdot\nabla)\vec{v}$, arising from the total time derivative is neglected. An unsteadyness parameter can be defined as the ratio of the characteristic times of the Q-tensor and the velocity fields (τ and τ_0) respectively [28]. The characteristic

times are defined as:

$$\tau \approx \mu_1 \frac{\xi^2}{L_1}, \qquad \tau_0 = \frac{\rho L^2}{\alpha_4},$$

where L is the container size and ξ is the characteristic length for order parameter variations, also referred to as the correlation length [12, 109], which is typically a few nanometres:

$$\xi = \sqrt{\frac{27CL_1}{B^2}}.$$

The characteristic time of the Q-tensor field, τ, is typically tens of nanoseconds. When studying disclination dynamics the velocity field adapts quickly to a given Q-tensor field. A small unsteadyness parameter results and the partial time derivative can be neglected from (7.1). Typically these two approximations are valid in the case of conventional cell dynamics (in the absence of disclinations). However, in extreme cases, with large electric fields and large container sizes, this unsteadyness parameter is no longer small. Here, the electric (or magnetic) coherence length should be used to determine the characteristic time of the Q-tensor field instead of the correlation length:

$$\xi_e = \frac{1}{|E|}\sqrt{\frac{K_{11}}{\varepsilon_0|\Delta\varepsilon|}}.$$

Then a time stepping procedure, such as (7.6), may be used to calculate the velocity field with the pressure assumed steady within each time step so that the incompressibility condition holds for all time.

After discretising the velocity and pressure using $v_\alpha = v_\alpha^i \phi^i$ and $p = p^i \psi^i$, the system of equations may be written in matrix form as

$$\begin{pmatrix} \mathbf{D} & \mathbf{C} \\ \mathbf{C}^T & 0 \end{pmatrix} \begin{pmatrix} \mathbf{v} \\ \mathbf{p} \end{pmatrix} = \begin{pmatrix} \mathbf{f}_1 \\ \mathbf{f}_2 \end{pmatrix}. \tag{7.7}$$

assuming both the advective term and the partial time derivative can be dropped. The sub-matrices $\mathbf{D}$ and $\mathbf{C}$ arise from the terms in $\vec{v}$ and p respectively. The vectors $\mathbf{f}_1$ and $\mathbf{f}_2$ arise from V_β^α and the Dirichlet boundary conditions applied to the velocity and pressure solutions and $\mathbf{v} = \{v_\alpha^i\}$. A scaled pressure vector $\mathbf{p}$ is introduced to improve the condition

number of the system matrix. In the above formulation the choice was made to integrate the pressure term by parts, but this operation is not essential. It has the advantage that the resultant system matrix is symmetric, but the real difference is seen on open boundaries. This procedure modifies the natural boundary condition so that it is well-posed on open boundaries. The resulting weak form contains no derivatives of the pressure, introducing the possibility to represent the pressure by a function that is not C^0 continuous. Improved convergence is reported in [70] using these functions, which allow the continuity equation to be satisfied on an element by element basis.

Two element types have been tested, firstly, the P2P1 Taylor-Hood [110] element with second order functions for the velocity components and continuous linear functions for the pressure and, secondly, the P2(P1+P0) (as used to solve the Ericksen-Leslie equations in [111]) with second order functions for the velocity components and a discontinuous linear approximation for the pressure. Here, the pressure is defined as $p = p_o + p^i\psi^i$. The implementation of the later is more complicated, and the solution vector is extended by the number of elements in the mesh. More complicated elements, using bubble functions, are common in the field of computational fluid dynamics, but these lead to a much expanded solution vector and a more complex implementation. The P2P1 element was found to give a solution vector ($\mathbf{v}$) differing by $\|\mathbf{v} - \mathbf{v}'\|_\infty \approx 10^{-5}$ compared to the P2(P1+P0) element ($\mathbf{v}'$). This difference is not substantial, therefore the simpler P2P1 element is used.

7.5 Algorithm Details

The equations are put into dimensionless form in terms of length and time scales ξ and τ. To summarize the discussions made in the previous sections, second order polynomials are chosen as the shape functions for q_k, u and $\vec{v}$, and first order functions for the pressure. Integration is performed numerically using Gauss quadrature, opening up the possibility to use iso-parametric elements, which are better able to conform to curved boundaries. For the Q-tensor problem in 2D, 16 Gauss points are chosen to avoid integration loss, giving 8^{th} order accuracy. The system of three coupled equations (4.17), (7.6) and (7.7) is solved using algorithm 1. A time stepping procedure for the Q-tensor forms the basis for the algorithm and within each time step Newton iterations are performed to deal with the non-linear terms, using $\zeta \approx 10^{-6}$. In each time step the flow and the potential solutions are assumed steady.

The most time consuming part of the procedure is the dynamic calculation of the Q-tensor.

Algorithm 1 Time Stepping

$\dot{\mathbf{q}}_n \leftarrow 0$, $\Delta t_n \leftarrow \tau$
while $t < t_{max}$ **do**
  $\dot{\mathbf{q}}_{n+1} \leftarrow 2\dot{\mathbf{q}}_n - \dot{\mathbf{q}}_{n-1}$
  $\mathbf{q}^p_{n+1} \leftarrow \mathbf{q}_n + \Delta t_n \dot{\mathbf{q}}_n$ {predictor}
  $\mathbf{q}_{n+1} \leftarrow \mathbf{q}^p_{n+1}$
  repeat {Iterative Loop}
    {Pseudo-steady-state solutions for $\mathbf{u}$ and $\mathbf{v}$}
    compute $\mathbf{u}_{n+1}(\mathbf{q}_{n+1})$
    compute $\mathbf{v}_{n+1}(\mathbf{q}_{n+1}, \dot{\mathbf{q}}_{n+1}, \mathbf{u}_{n+1})$
    {Newton iteration for Q-tensor}
    compute $\Delta\mathbf{q}_{n+1}(\mathbf{q}_{n+1}, \mathbf{q}_n, \dot{\mathbf{q}}_n, \mathbf{u}_{n+1}, \mathbf{v}_{n+1})$
    $\mathbf{q}_{n+1} \leftarrow \mathbf{q}_{n+1} + \Delta\mathbf{q}_{n+1}$
    $\dot{\mathbf{q}}_{n+1} \leftarrow (\mathbf{q}_{n+1} - \mathbf{q}_n)/\Delta t_n$
  until $\|\Delta\mathbf{q}_{n+1}\| < \zeta$
  $t \leftarrow t + \Delta t_n$
  $\mathbf{d}_n \leftarrow (\mathbf{q}_{n+1} - \mathbf{q}^p_{n+1})/(3(1 + \Delta t_{n-1}/\Delta t_n))$
  $\Delta t_{n+1} \leftarrow \Delta t_n (\nu/\|\mathbf{d}_n\|)^{1/3}$
  $n \leftarrow n + 1$
end while

An *Incomplete LU Factorisation* is used for preconditioning, and the resultant system of equations is solved using a *Generalized Minimum Residual Method* [112, 113]. The execution time for the iterative method is almost independent of the matrix bandwidth; however, this is not the case for the calculation of the preconditioner. Savings are achieved by applying a bandwidth reduction technique such as a *Symmetric Reverse Cuthill-McKee Permutation* [114]. Furthermore, the preconditioner can be kept constant during the Newton iterations for the Q-tensor, with no significant loss of precision.

The Q-tensor is a function of the velocity and potential at step $n+1$. Strictly speaking two loops are required, one to ensure consistency and the other to deal with the non-linear terms. In practice, since the calculation of the Q-tensor is the bottleneck, it is preferable to update the pseudo steady-state values of the velocity and potential fields during the Newton iterations for the Q-tensor field.

Time integration is performed by an implicit method, therefore a large time step may be used. However, due to the non-linearity of the equations some limit is imposed. When a voltage is applied the Q-tensor changes rapidly and a small time step should be used to capture the transient behavior. After some time, as steady-state is approached, a much

larger time step may be used. A variable time stepping procedure [70, vol. II, p.798] provides an effective means to calculate the dynamic behavior. In algorithm 1the time integration error is maintained below a threshold, ν, by changes to the time step, Δt_n. We have found $\nu \approx 10^{-4}$ is a good compromise between computation time and accuracy.

Changes to the order parameter not only occur on small time scales, but small length scales too. Such changes occur in proximity to disclinations, where it is important to use a fine mesh in order to calculate accurately the induced flow. Adaptive meshing is used solve this problem efficiently, particularly when calculating the motion of disclinations over large distances. The mesh density is calculated from an error estimate of a given solution, as described in Section 6.4. Strictly speaking, an error estimate should be obtained for both Q-tensor and velocity solutions, and the two should then be combined in some way. However, it turns out that two estimates are in fact very similar, since the major force driving the flow tends to be the distortion stress. Regions of rapid variation in the Q-tensor, such as in proximity to disclinations, coincide with regions of high velocity. For simplicity then, it is sufficient to use the single error estimate based on the Q-tensor solution.

The nodes of the mesh are rearranged so that LC nodes are at the start of the solution vector, followed by the dielectric nodes. This avoids having to remove zero rows and columns from the Q-tensor matrix that correspond to dielectric regions. Another complication arises due to the pressure which is discretised at the P1 nodes. It is convenient to place the P1 nodes at the start of the solution vector. The final arrangement of nodes is given below:

{LC P1, LC P2, Dielectric P1, Dielectric P2}.

The solution vectors for the Q-tensor components, the flow and the potential are defined as:

$\{q_1, q_2, q_3, q_4, q_5\}$ length {LC P1&P2, LC P1&P2, LC P1&P2, LC P1&P2, LC P1&P2},

$\{v_x, v_y, v_z, p\}$ length {LC P1&P2, LC P1&P2, LC P1&P2, LC P1},

$\{u\}$ length {LC&Dielectric P1&P2}.

Although this arrangement is convenient for assembly, it has the disadvantage that bandwidth of the matrices becomes quite large. A large bandwidth can severely slow some methods of solving systems of equations. Interleaving components of q_k and v in the solution vector reduces the bandwidth, but complicates the implementation. At all times the simplest implementation has been chosen to minimize the chance of programming error. It becomes increasingly important that a bandwidth reduction technique is employed if the

solution method is iterative, however this has the disadvantage that the diagonal dominance of the matrix may be lost.

7.6 Validation

In this section, results of validation tests are compared to some previously published results [28], performed using a single elastic constant approximation ($L_2 = 0$) and the material parameters of MBBA [94, 7]:

$a = 8.67 \times 10^4\,\mathrm{N/m^2K}$, $(T - T^*) = -4\,\mathrm{K}$, $A = a(T - T^*)$,

$B = -2.12 \times 10^6\,\mathrm{N/m^2}$, $C = 1.74 \times 10^6\,\mathrm{N/m^2}$,

$\gamma_1 = 0.0763\,\mathrm{Pa{\cdot}s}$, $\gamma_2 = -0.0787\,\mathrm{Pa{\cdot}s}$,

$\alpha_1 = 0.0065\,\mathrm{Pa{\cdot}s}$, $\alpha_4 = 0.0832\,\mathrm{Pa{\cdot}s}$,

$\alpha_5 = 0.0463\,\mathrm{Pa{\cdot}s}$, $\alpha_6 = -0.0344\,\mathrm{Pa{\cdot}s}$,

$k = 6\,\mathrm{pN}$ and $\rho = 10^3\,\mathrm{kg/m^3}$.

The flow solver is first tested individually and then in combination with the Q-tensor solver.

7.6.1 Flow Formulation Validation

The flow around a cylinder [115] and the driven cavity problem [116] have been used to test the flow formulation. Such tests are normally performed using high Reynolds numbers where the advective term is important, or when the flow can no longer be assumed steady. Complications arise due to non-linearities that in general can be neglected in the case of LC flow. For the study of flow around a cylinder the dimensions are set according to [115], with a container size of 2.5 m by 0.41 m. At the point (0.5, 0.2) m a cylinder of radius 0.1 m is centred [1]. An isotropic liquid is considered in this benchmark test, and so all viscosity coefficients are set to zero except for $\beta_4 = 4 \cdot 10^{-4}\,\mathrm{Pa{\cdot}s}$. Non-slip conditions are applied to all boundaries with the exception of the inflow and outflow. At the inflow boundary the incoming velocity is assumed to take a quadratic form $v_x = 0.3 \cdot 4y(0.41 - y)/0.41^2$ and at the outflow boundary the velocity is left free and the pressure is set to zero. A mass density of $\rho = 1.0\,\mathrm{kg/m^3}$ is assumed. Convergence was achieved with Reynolds numbers in

[1] This is a standard benchmark used to test Navier-Stokes solvers, with a container size many times larger than a typical LC cell

the region of 100 [2] and the magnitude of the resulting flow is shown in Fig. 7-1. For higher Reynolds numbers the velocity field can no longer be assumed steady.

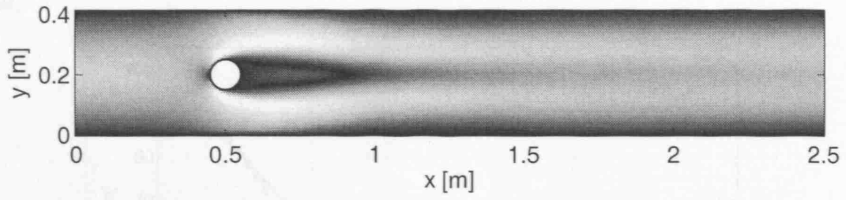

Figure 7-1: Magnitude of the flow past a cylinder with a Reynolds no. of 100.

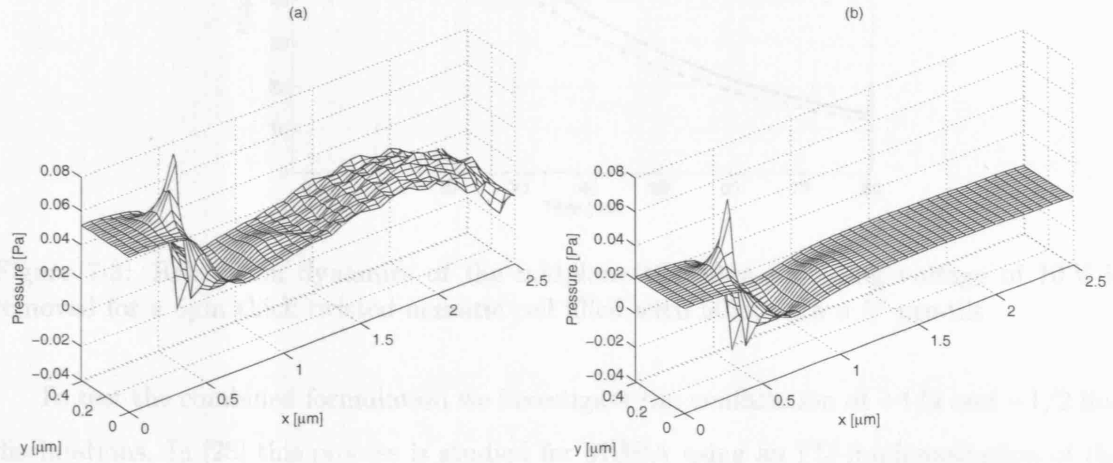

Figure 7-2: Pressure field for flow past a cylinder for Reynold's number of 100 after 9 iterations (a) equal (2^{nd}) order interpolation for the pressure and velocity and (b) mixed interpolation (2^{nd} order for the velocity and 1^{st} order for the pressure)

Fig. 7-2 shows the pressure calculated with and without mixed interpolation for a Reynold's number of 100. With mixed interpolation convergence to an error of 10^{-9} is achieved after 9 iterations. Without mixed interpolation convergence is not achieved with such a high Reynold's number, and the calculated pressure is oscillatory. Here, the pressure is plotted after 9 iterations.

7.6.2 Validation of the Combined Formulation

When a large holding voltage is removed from a twisted cell, the LC rapidly relaxes near the alignment layers. This induces flow, which is maximum at the mid-plane. Reorientation

[2] In an LC cell the Reynolds number is much smaller than is used here. Such a larger number is chosen to test the implementation of the non-linear advective terms

of the LC is induced by this flow; the mid-plane directors actually over-tilt before relaxing to the starting twisted state. Fig. 7-3 shows the value of the mid-plane tilt both with and without flow.

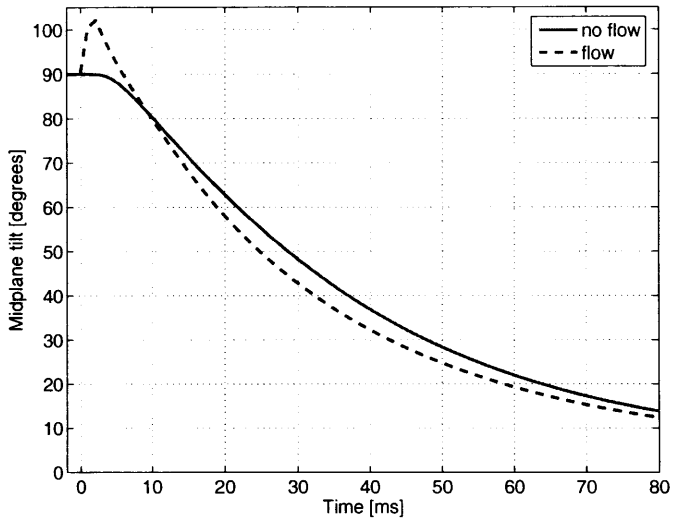

Figure 7-3: Relaxation dynamics of the midplane tilt after a holding voltage of 10 V is removed for a 5μm thick twisted nematic cell filled with 5CB, with a 5° pre-tilt

To test the combined formulation we investigate the annihilation of $+1/2$ and $-1/2$ line disclinations. In [28] this process is studied for MBBA using an FD implementation of the Qian and Sheng equations.

Disclinations are positioned along the x-axis, separated by a distance of 100nm. Much larger disclination separations can be modelled by refining the mesh only in the vicinity of disclinations, as shown in Fig. 6-3. A large time step can be used when the disclinations are widely separated and slowly moving. However, when the disclinations are close they move rapidly and small time steps are necessary to follow the variations in the order parameter and flow. Therefore, a variable time stepping procedure [70] provides an effective means to calculate the dynamic behaviour.

There are two possible starting configurations depending on the placement of the two disclinations: (a) and (b) as shown in Fig. 7-4. In (a) the initial tilt is set to $\theta_a = \frac{\pi}{2} + \tan^{-1}\left(\frac{z}{x-a}\right) - \tan^{-1}\left(\frac{z}{x+a}\right)$, where the initial disclination separation is $2a$, and in (b) it is set to $\theta_b = \theta_a - \frac{\pi}{2}$. The same boundary conditions are applied to all sides of the modelling window. For the Q-tensor Neumann boundary conditions are applied – the natural boundary condition when using a single elastic constant formulation. For the velocity components,

the non-slip condition is assumed to match the state in the bulk of the LC. No boundary condition is required for the pressure. Starting with $v = 0$ the steady state flow arising from

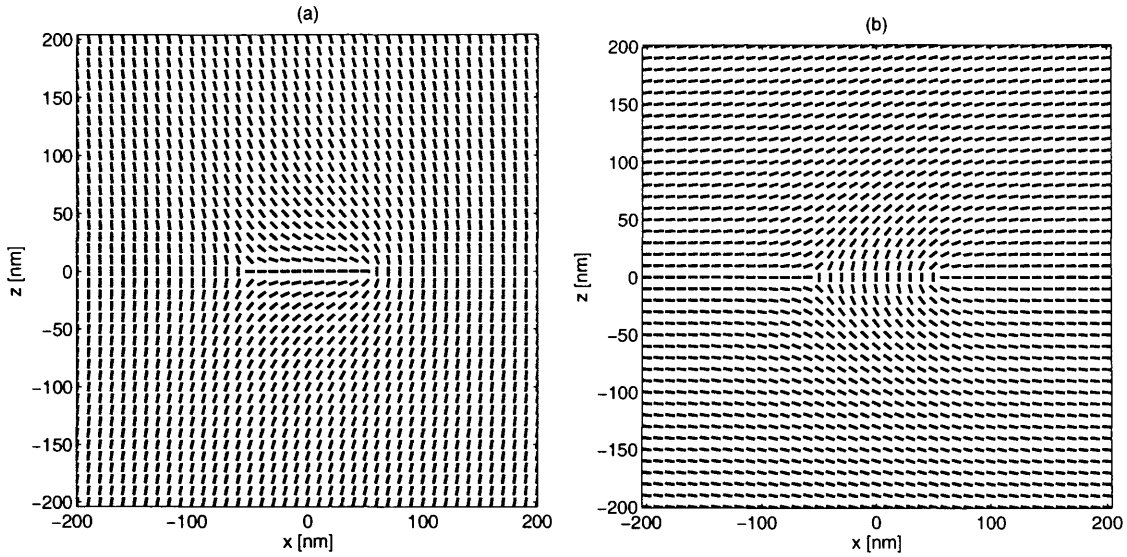

Figure 7-4: Representation of the director profiles for configurations (a) and (b) given by the eigenvector associated with the largest eigenvalue of Q.

the individual components of the stress tensor were calculated and the results agree well with those in [28]. Fig. 7-5 shows the flow field for the complete stress tensor, for comparison with Fig. 4(a) of [28]. This field is highly sensitive to the disclination separation.

Tóth *et al.* employ periodic boundary conditions on the left and right hand boundaries of the modelling window, which causes an increase of the horizontal flow in the central channel and accentuates the vortices above and below each disclination.

To further verify the finite element implementation a finite difference discretisation was created, using a staggered grid, as detailed in Section C.2. Both finite element and finite difference implementations were found to give rise to the same pressure field for each component of the driving stress tensor. In addition the motion of the disclinations was checked in the absence of flow for both implementations. The same annihilation time and disclination velocity was found for both finite element and finite difference implementations.

Fig. 7-6 shows the disclination position versus time for the two configurations with and without flow. This can be compared with Fig. 2 of [28]. The flow field serves to speed up preferentially the $+1/2$ disclination, an effect that has recently been observed experimentally [117]. It can be noted that for both configuration (a) and (b) the disclination path coincides in the absence of flow, coinciding with the results in [28, 101]

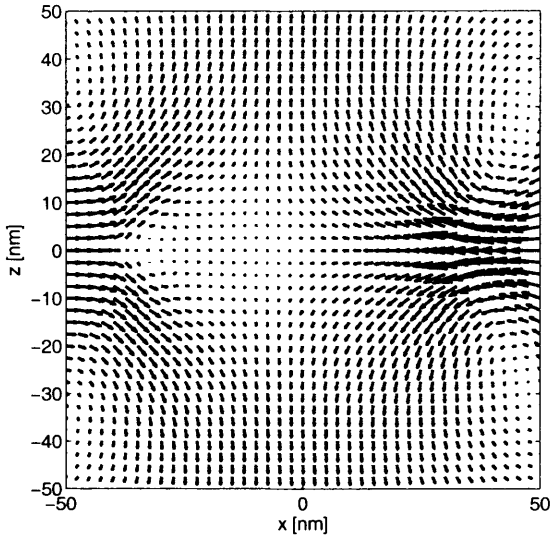

Figure 7-5: Velocity field due to the stress tensor for a disclination separation of 75nm, assuming an isotropic fluid.

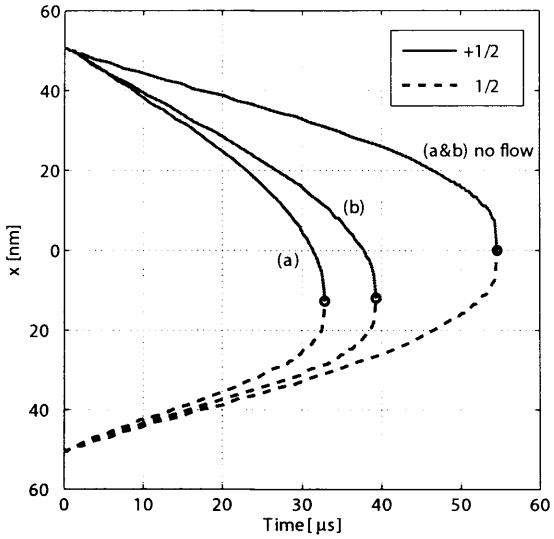

Figure 7-6: Disclination position versus time for configurations (a) and (b) with and without flow.

7.7 Conclusions

A finite element model of the Qian and Sheng formulation, a generalisation of the Ericksen-Leslie theory, allowing for changes in the order of the LC, has been presented and validated. The ability to adapt the mesh allows the study realistically sized devices with proper consideration of small scale features and disclinations, providing significant savings in terms of the number of degrees of freedom and computation cost in comparison to traditional finite difference methods. Time integration is performed using an implicit method, thus additional savings are available through the use of a variable time step in accord with the rate of change of the LC orientation.

When studying interfacial properties (for example at the interface between a nematic and an isotropic liquid crystal), even the small density changes between the two regions that result can have a large effect on the velocity [82]. In this case the compressible Navier-Stokes equations should be solved. However, for the most part the assumption of incompressibility (as implemented) is valid for a wide range of applications.

For the problem of disclination pair annihilation this model agrees well with previously published results, and the demonstrated doubling in speed of the $+1/2$ disclination shows the importance of the flow of the LC when studying dynamic variations in the Q-tensor field.

Chapter 8

Vector Tensor Comparision

8.1 Introduction

In Chapter 5 two constant order parameter models were developed, one using a vectorial, the other a tensorial representation of the liquid crystal orientation. The purpose of this section is to compare the two representations. Each has its advantages and disadvantages, and this section aims to aid in the choice of method for a particular structure. This discussion also provides a justification for the methods chosen in the subsequent Results section.

A comparison of these methods was made by Anderson *et al.* [118], wherein one dimensional simulations were performed for a number of simple cell types. They concluded that the vector method was in all cases superior to the tensor method. The reason given was that the tensor method allows walls to slip between mesh points (if too poor a discretisation is used). This chapter will test this conclusion more extensively.

In [118] the π-cell forms the basis of the comparison. This section begins in the same way, but with a more complete description of the π-cell, in terms of the stable states and the possible means to switch between them. Then, the constant order vector and tensor implementations are used to simulate the π cell, and the results compared. Finally, more complicated structures are considered, which require two or three dimensional modelling in order to test whether or not the vector method should indeed be the most adequate representation.

When the applied voltage is large, transitions between topologically distinct states can occur, through an intermediate biaxial phase [16, 119] and this was not considered in [118]. A brief discussion of this process is given here. However, since the aim of this section is to compare constant order parameter implementations, only the low voltage cases have been simulated.

8.2 Discretisation error

Before running any numerical simulation the computational domain must first be meshed. The mesh must be "fine enough" to resolve the fastest variations in the solution, but how fine exactly is "fine enough"? The maximum element size is chosen such that the change in the director orientation is limited between the nodes of the mesh. It turns out that this limit differs according to representation of the LC orientation that is used. A large change in orientation between nodes will not only lead to a significant increase in the error,

but can also lead to unexpected and un-physical solutions that are an artefact of the poor discretisation. This in fact constitutes an improper use of the numerical method.

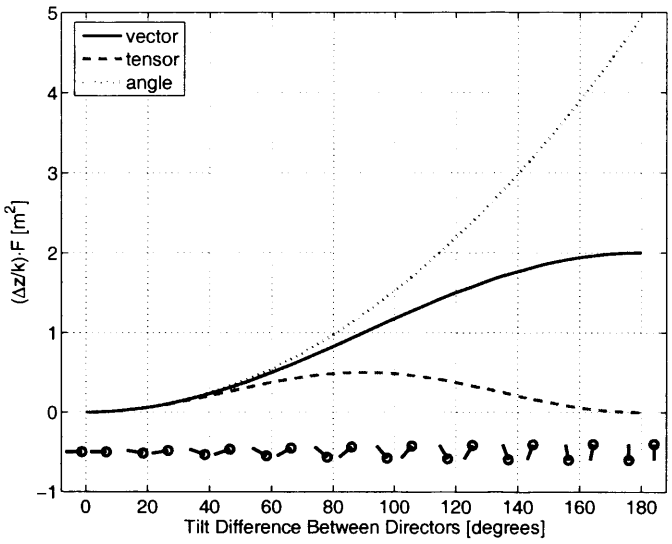

Figure 8-1: Free energy between two directors as tilt angle between them is increased in opposite directions. The lower portion of the figure is a sketch of the orientation of the two directors at certain angles. The energy has been calculated (considering a single elastic constant formulations) using three representations of the LC orientation; vector, tensor and angular

In Fig. 8-1 the free energy between two directors is calculated as the angle between them is varied. Three representations are considered: vector, tensor and angular. For the vector method the free energy density is given by equation (5.3) and for the tensor method equation (5.4). With an angular representation the free energy density may be written $f = \frac{1}{2}K_{22}\left(\frac{\partial\theta}{\partial z}\right)^2$. In practice an angular representation is seldom used for complicated structures because the twist becomes degenerate when the director lies vertically, leading to a singular system of equations without a unique solution.

With an angular representation the calculated energy assumes that the tilt varies linearly between the two nodes. The vector and tensor methods consider the components of the director as varying linearly between the two nodes. To see why this is a problem, consider the calculated energy when the tilt difference between the two director is 180°. The linear variation implies that $n_x = 0$ and that n_z varies between $+1$ and -1, passing through 0 at the midpoint between the two nodes. Although the unitary length of the director is satisfied at the nodes, in between them it is not. For this reason the vector method, and even more so the tensor method, underestimate the energy.

If additional nodes are added to span the angle variation, then the calculated energies for the tensor and vector representations approach that of angular representation.

In the tensor method, when the angle between the two directors is 80°, the energy is half of what it should be. Unlike the vector and angular representations there is a low energy penalty associated with any further tilt. If the angle increases beyond 90°, there is no longer any energy penalty inhibiting further tilt. Worse still, it is energetically favourable for the two directors to tilt further until they lie parallel, pointing in opposite directions. In a two or three dimensional simulation this transition would be one between topologically distinct states.

Such a transition is extremely unlikely in the vector method, as it is energetically unfavourable. However, when the angle between the two directors is high, the energy is still less than it should be, and like the tensor method the error is high.

The situation when the tilt difference between the two directors is between 120° and 180° can be avoided in most structures by using a fine enough mesh and by careful choice of the starting director configuration. In certain structures disclinations arise, and clashes between the head and tail of directors cannot be avoided. The tensor method will correctly consider these as low energy regions, but the vector method will consider the energy to be large.

In summary, if the mesh to not fine enough, the unitary length of the director is not adequately maintained using the vector or tensor representations. For a given mesh the error in the solution will be higher for the tensor than the vector method.

8.3 Implications for modelling practical devices

When using the tensor method, a coarse mesh can allow transitions between topologically distinct states, as was discussed in the previous section. A fine enough discretisation will not allow such a transitions, but in 2D and 3D simulations such a fine mesh can lead to long simulation times. In this section several practical devices are modelled using relatively coarse meshes with both the vector and tensor methods

First of all a π-cell is simulated. A π-cell has two topologically distinct states, each of which can be simulated using a one dimensional model. A summary of how the π cell behaves in theory and practice is detailed, and then the structure is modelled using both

the constant order vector and tensor methods.

Finally, devices are considered where clashes in the head and tail of the director occur. In particular two cases are considered, a structure with multiple domains and then the director field about a cylindrical spacer.

8.3.1 The π-cell

For normal display applications the surface alignment is chosen such that there is a single stable state in the absence of an applied voltage. An applied voltage induces reorientation of the liquid crystal. Both switched and un-switched states are topologically equivalent.

The π-cell is a simple geometry in which the alignment layers are rubbed in a parallel fashion, to yield a splayed director field in the absence of an applied voltage. A simple structure with sheet electrodes is considered here, nevertheless, the cell exhibits a complex switching behaviour that stems from the fact that there are two stable states. This complex behaviour is ideal to highlight differences between tensor and vector representations. In this section a qualitative description of the switching mechanism will be described, with the use of simulated results that have been produced using the material properties of ZLI4792 from Merck [120].

$K_{11} = 13.2\,\text{pN}$, $K_{22} = 6.5\,\text{pN}$, $K_{33} = 18.3\,\text{pN}$, $\gamma_1 = 0.1232$ Pa·s,

$\varepsilon_\perp = 3.1$, $\Delta\varepsilon = 5.2$,

$n_o = 1.4794$, $n_e = 1.5763$

A cell thickness of $d = 2.84\,\mu\text{m}$ is chosen so that the cell acts as a half-wave plate at a wavelength of $\lambda = 0.55\,\mu\text{m}$ (the tilt of the LC has been neglected in this calculation). At the upper and lower alignment surfaces the pre-tilt is $\theta_U = 10.0°$ and $\theta_L = -10.0°$ respectively. A pre-twist of $\varphi_U = 1°$ is set at the upper alignment layer with respect to the lower alignment layer. Without an offset in twist the calculated director profile is constrained to lie in the $x-z$ plane. 1° may seem a little high, but this value was chosen so that the effects are seen over a reasonable time scale (of the order of 10 ms).

In the π-cell there are two topologically distinct states, referred to as the horizontal (H) and the vertical (V) or bend state, as sketched in Fig. 8-2. These states are separated by an energy barrier, which is sufficient to prevent a spontaneous transition between the two states. In the absence of an applied voltage and for pre-tilts less than 45° the H state has the lowest energy.

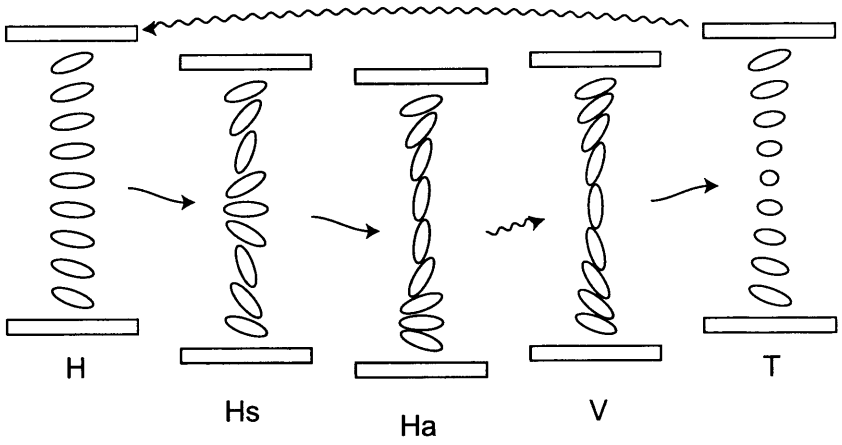

Figure 8-2: Stable states of the π-cell, after [15, 16], where wavy lines represent a nucleation process. H-horizontal, Hs-symmetric horizontal, Ha-asymmetric horizontal, V-vertical and T-twisted states

H state

Applying a voltage to the H state gives rise, initially, to the symmetric horizontal state (Hs). At the centre of the cell is a region of splay, essentially a bend-splay wall, the thickness of which is twice the electric coherence length. In the ideal case, where the upper and lower surface alignments are exactly opposite, the Hs state is stable. In reality these two alignments will differ, resulting in the displacement of the central splayed region towards one of the alignment layers, giving rise to the asymmetric Horizontal state (Ha). This switching process is shown in Fig. 8-3. The Hs state forms within a few milliseconds, but Ha takes approximately 150 ms to form with 7 V applied.

Fig. 8-4 (a) shows the corresponding transmittance for this director field, as well as for 5 V and 6 V. Simulations have been performed using two different pulse lengths, a long pulse of 140 ms represented by the solid lines and a shorter pulse of 40 ms represented by the dotted lines. At the end of the long pulse, there is a relaxation from the Ha $\rightarrow$ H state, whereas at the end of the short pulse relaxation occurs from the Hs $\rightarrow$ H state, which, due presence of the central splayed region is a faster process. For a full study of the relaxation dynamics, including flow, see [15]. For display applications the fast relaxation of Hs is desirable, however, a means to prolong the lifetime of this state is required if it is to be used in a real device. The figure indicates that one way to increase the lifetime of Hs, albeit an undesirable means from a practical point of view, is to increase the applied voltage.

Fig. 8-4 (b) shows the effect of changing the asymmetry of the surface tilt on the

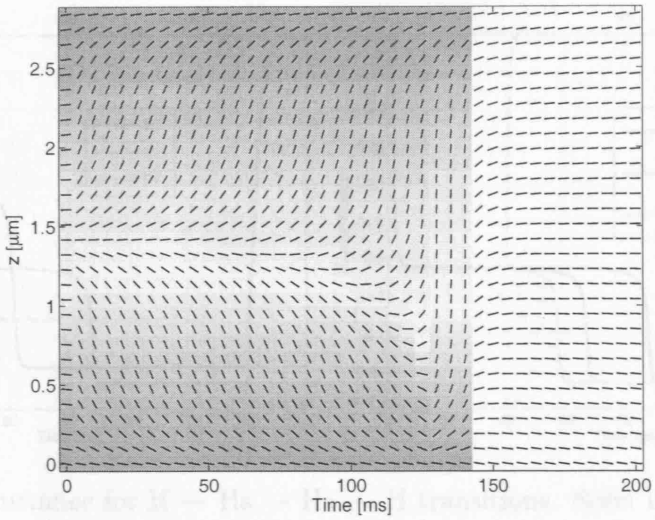

Figure 8-3: Director and potential fields for H $\xrightarrow{7V}$ Hs $\xrightarrow{7V}$ Ha $\xrightarrow{0V}$ H transitions, induced by applying 7 V for 140 ms and then 0 V. $\theta_U = 10.1°$, $\theta_L = -10.0°$ with a discretisation of 101 points (reduced for display purposes). With these parameters both tensor and vector methods yield identical results.

transmittance. It would appear that the onset of the Ha state is a direct consequence of the surface tilt asymmetry. To achieve reasonable lifetimes of the Hs state, the tilt asymmetry needs to be very low, and the alignment must be as uniform as possible across the whole of the device. Furthermore, the Hs state lifetime can be prolonged by increasing the surface tilt at both upper and lower alignment layers. This brings the energy of the Hs and Ha states closer together, slowing the transition from the Hs to the Ha state.

H to V transition

As the voltage rises there is a point, called the critical voltage (V_c), at which the Ha state is no longer the minimum energy state and the V state becomes energetically favourable. Fig. 8-5 shows the free energy for both H and V states as a function of voltage, with $V_c = 2.4\,\mathrm{V}$. Increasing the pre-tilt has the effect of reducing the value of V_c.

As the H and V states are topologically different, increasing the voltage above V_c does not switch between the two states. Before discussing a mechanism by which this transition can occur, it is worth describing the V state.

The V state is the most commonly used mode of the π-cell. The applied voltage tunes the birefringence of the device and it has the advantage that it automatically compensates for the viewing angle. In [17] the relaxation from a high to a low voltage bend state is studied

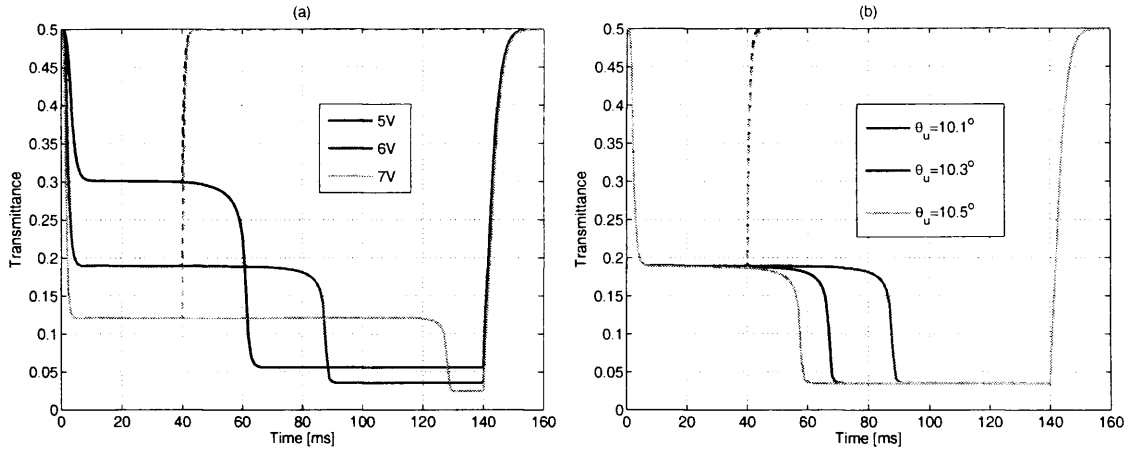

Figure 8-4: Transmittance for H → Hs → Ha → H transitions. Solid lines are for a pulse length of 140 ms (Ha → H relation), dashed lines for 40 ms (Hs → H relation). (a) shows the effect of changing the magnitude of the voltage pulse, to the values indicated in the legend. $\theta_U = 10.1°$, $\theta_L = -10.0°$. (b) shows the influence of the surface tilt asymmetry on the transmittance. θ_U as in legend, $\theta_L = -10.0°$ with 6 V applied

including flow. In Fig. 8-5, when the voltage falls below 1.8 V, the bend state transforms into a 180° twisted state, which is topologically equivalent. The elastic constants and pretilt determine the voltage below which the T state forms, or indeed whether or not it forms at all.

Now the mechanisms for the transition between states will be discussed. Experimental observations using a polarizing microscope were made of a π-cell with square electrodes of area 1 cm^2 that partially spanned the LC layer. It was found that an applied voltage of $\sim 2V_c$ was required to form the V state. This a nucleation process; to begin with localised regions of the device undergo the transition. The change in these regions could be induced by electrode edge effects, the presence of spacers, imperfections in alignment or by the sides of the cell.

Regions of H and V state will coexist, separated by disclination lines. For voltages above V_c, the V domains have the lowest energy and thus grow at the expense of the H domain [119, 121]. The growth rate, v, is proportional to $(\mathcal{F}_V - \mathcal{F}_H)d/\gamma_1$ [122], where d is the thickness of the LC layer. $\mathcal{F}_H$ is the free energy of the horizontal state and $\mathcal{F}_V$ is the free energy of the vertical or twisted state. Depending on the sign of v, the domains will grow or shrink. In fact, by holding the voltage at V_c the different domains happily coexist and are stationary.

Assuming a voltage above V_c is applied, after a few seconds, the LC between the elec-

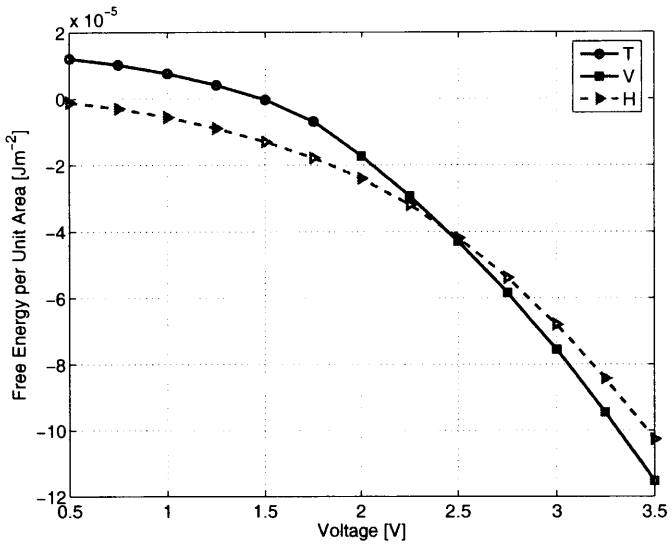

Figure 8-5: Free energy per unit area (of the electrodes) as a function of applied voltage for horizontal and vertical states, after [17]. The energy of the V and H states are equal when the applied voltage is V_c

trodes in its entirety will be in the V state. How is it possible to now return to the H state? Once again this is most straightforwardly achieved by a nucleation process. It was found experimentally that when the applied voltage was reduced below V_c, the field of view began to fill with H domains. Why is a voltage twice that of V_c required to give rise to the V state, but a voltage just below V_c gives the H state? When in the V state the LC beyond the electrode edge will remain in the H state. As soon as the voltage falls below V_c these H domains will grow, extending beneath the electrodes.

This domain growth is a slow process that can take seconds, too slow for display applications. One method to enable spontaneous switching between topologically distinct state is breaking of the surface anchoring under a large electric field, but this requires special surface treatment [123]. Another means to achieve this switching is by applying a very high voltage to the H state. The idea is to compress the region of splay at the centre of the cell so that its size becomes comparable with the correlation length. If the voltage is high enough, two of the eigenvalues of the Q-tensor at the centre of the cell are exchanged, resulting in a $\pi/2$ change in the director [16]. The intermediate step involves biaxial ordering at the centre of the cell. First of all there is a decrease in S_1 and an increase in S_2. When these two values are equal then a melting process follows: the long axis of the Q-tensor changes by $\pi/2$ to lie vertically. The order parameter S_1 is now associated with this vertical

axis. Finally follows an order reconstruction; S_1 increases to the bulk equilibrium value and S_2 decreases to zero, giving the V state. This process is very fast, taking a fraction of a millisecond (so fast that Ha does not have time to form). The voltage threshold, which is temperature dependent, is high $5 - 10\,\mathrm{V/\mu m}$ [16], requiring a thin cell ($d \approx 1\mu\mathrm{m}$) to be a feasible switching mechanism for display applications. The Landau-de Gennes theory can model this behaviour, but tends to overestimate the value of this threshold voltage. In [16] the reason given is that the theory does not fully describe the intermediate biaxial phase (when representing the orientation in terms of a spherical harmonic expansion, it may be necessary to include fourth order terms too [34]). The reverse process, a transition between V and H states without domain growth, would require the application of a large lateral field. Using a constant order parameter model, no matter how large the applied voltage, such transitions between topologically distinct states would not occur.

Constant order vector and tensor modelling of the π-cell

In the previous section the results (for example Fig. 8-3) were performed on a mesh with 100 nodes. Using this fine mesh, both tensor and vector methods were found to give identical results. However, when the number of points is reduced there becomes a point where the two methods can give different results [118].

To illustrate this point, the switching from the H to Hs state is simulated using both vector and tensor methods using a comparatively coarse mesh with 30 nodes. For this mesh density and an applied voltage of 7 V the central splayed region is described by approximately 3 nodes. Using the vector method the result is very similar to that achieved previously using 100 nodes. Even with a very coarse mesh the result is similar, but the accuracy with which the wall width can be determined decreases. The constant order tensor method, however, does not share this property. The dynamics of the director given by the constant order tensor method with 30 nodes is shown in Fig. 8-6.

During the first stages of switching the result corresponds well with those from the fine mesh, but at around 10 ms the angle between the two central directors suddenly increases above $\pi/2$ and then continues towards π, giving the V state. When the voltage is removed at 140 ms there is a relaxation to the T state. Using a coarse mesh, the tensor method allows a transition between topologically distinct states. This transition can be avoided by increasing the mesh density, but as the applied voltage increases the splayed region shrinks

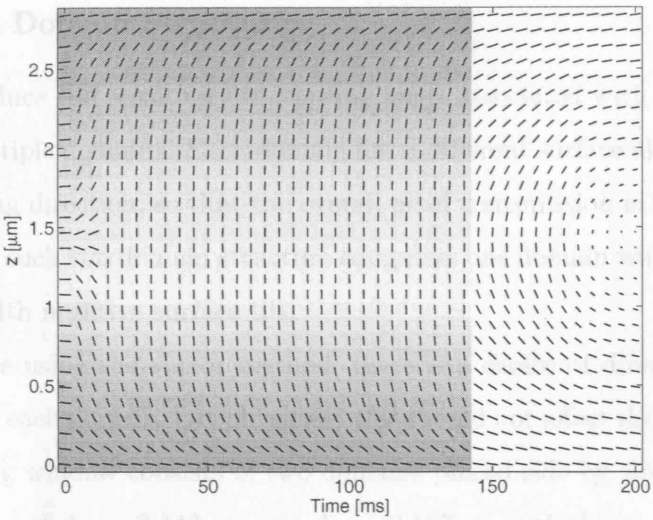

Figure 8-6: Director field produced by the tensor method as a function of time, for an applied voltage of 7 V. The mesh has 30 points vertically (as displayed). The background colour represents the potential.

and an increasingly fine mesh is required to avoid loosing the splayed region between mesh points.

The tensor method allows walls to disappear between mesh points when too coarse a mesh is used for a given applied voltage, whereas the vector method does not, regardless of the discretisation used. Since these walls can move, the tensor method requires a uniform fine mesh to maintain the walls, the density of which can be calculated directly from the electric coherence length. For three-dimensional problems this constraint on the mesh size gives rise to a large number of degrees of freedom. Only by using an adaptive meshing scheme can the number of degrees of freedom be reduced to a manageable level whilst still resolving the walls.

Provided that the assumption of a constant order parameter is valid, the vector method gives a lower error than the tensor method and does not allow walls to disappear between mesh points. In this case the vector method preferable. This conclusion is in agreement with [118]. Whether or not the vector method superior for more complicated 2D and 3D structures is investigated in following sections.

If the order parameter cannot be assumed constant, for instance if the electric field is in excess of 5 V/µm or disclinations are present, then a variable order tensor model should be used.

8.3.2 Multiple Domain Structure

An approach to reduce the sensitivity to viewing angle associated with a planar cell is the introduction of multiple domains. Each domain has a different surface alignment, optimised for a specific viewing direction, so that the overall pixel transmission is less sensitive to the viewing angle. One such two domain structure comprises one domain with a positive surface tilt, and another with negative surface tilt.

In this structure using the vector method, there is a choice of directions in which the vectors can point in each domain, but physically this should not affect the calculated director field. The modelling window consists of two domains placed side by side with a horizontal spatial discretisation of $\Delta x = 0.143\,\mu\text{m}$ and $\Delta z = 0.167\mu\text{m}$, a thickness $5\,\mu\text{m}$, and material constants of ZLI4792. In the left hand domain a pre-tilt of $-2°$ is chosen on both upper and lower alignment surfaces. In the right hand domain a $2°$ pre-tilt is chosen as well as a slight offset in twist ($1°$).

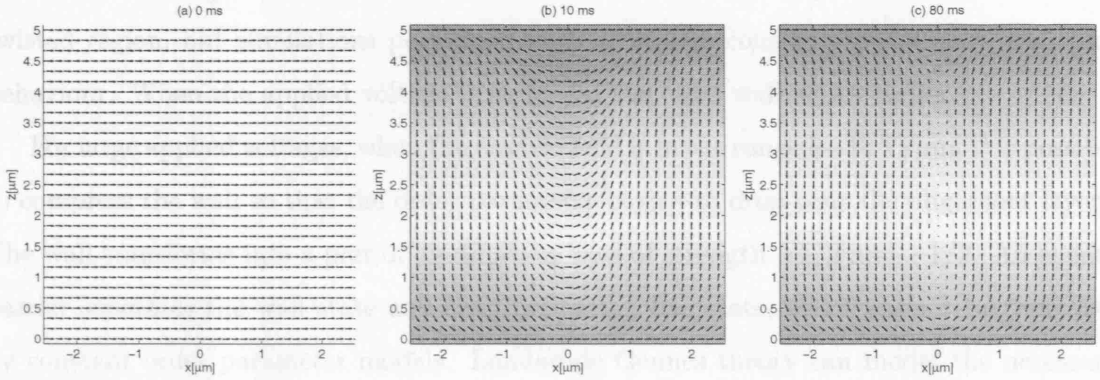

Figure 8-7: Director field produced by the vector method at the interface between two domains of opposite surface tilt. The background colour represents the potential. In both domains the director points in the positive x-direction ($\searrow\!\!\nearrow$). At $t = 0$, 8 V is applied.

Fig. 8-7 (a) shows the initial director profile for the vector method after relaxation from a starting configuration in which vectors point in the same direction in both domains. At the boundary between the two domains the director tilt is the mean of the two domains, zero, and at the extremes of the modelling window the tilt is $\pm 2°$. Subsequently, when 8 V is applied, the torque on the director is lowest at the centre of the cell (along $x = 0$); switching spreads inwards from the edges of the structure towards the centre where a bend-splay wall forms, as shown in (b) after 10 ms. Much like the π-cell the central directors along the line $x = 0$ cannot rotate in the $x - z$ plane (in a constant order parameter model) as this would

correspond to a transition between topologically distinct states. For applied voltages in excess of twice the Fréedericksz threshold the central directors begin to twist, undergoing a rotation of π, until the state shown in (c) is reached after 80 ms. The twisted region occupies a smaller region of space than did the region of bend and thus minimises the free energy. This twist-bend wall has been observed experimentally [7, p.189] [124, 125] and predicted theoretically [126, 127]. Since there are two ways in which the LC can twist, in and out of the page, experimentally kinks in the wall are observed when the twist changes direction. The width of this wall is independent of the mesh density and is approximately twice the electric coherence length and thus decreases as the applied voltage increases.

When the pre-twist is changed to 0.1° in the right hand domain, the twist wall still forms, but at a slower rate. Experimentally there will always be some difference in twist between the two domains, and although this may be very small, it is incorrect to neglect it in simulations, as this prevents the formation of the twist wall; the bend-splay wall persists. A low value of K_{22} relative to the other elastic constants encourages the formation of this twisted region, but simulations performed with all elastic constants equal show the same behaviour. When the applied voltage is increased the twist wall arises earlier.

For large applied voltages, when the electric field is in the range $5-10\,\mathrm{V/\mu m}$, it is possible to compress the wall so that the order parameter begins to drop near the alignment layers. The wall transforms into a pair of disclination lines of strength $+1/2$ and $-1/2$. An energy barrier separates the wall state and the disclination line state, which cannot be overcome by constant order parameter models. Landau-de Gennes theory can model the necessary order parameter changes that allow this transition, but tends to overestimate the voltage threshold.

Fig. 8-8 shows the director profile obtained by the constant order tensor method using an identical starting director configuration to the vector method. After the initial relaxation, the director profile (at $t = 0$) is identical to that produced by the vector method (Fig. 8-7). After 10 ms of applying 8 V a bend-splay wall forms at the centre of the cell, which then transforms into a twist wall. Up until 30 ms the director field corresponds well with the vector method, but at 40 ms the twist wall is lost between the central mesh points. In fact this gives rise to the disclination line state, a topologically different state. As was discovered with the π-cell, the tensor method requires a finer mesh. Increasing the horizontal mesh density was found to maintain the region of bend-splay wall between the two domains and

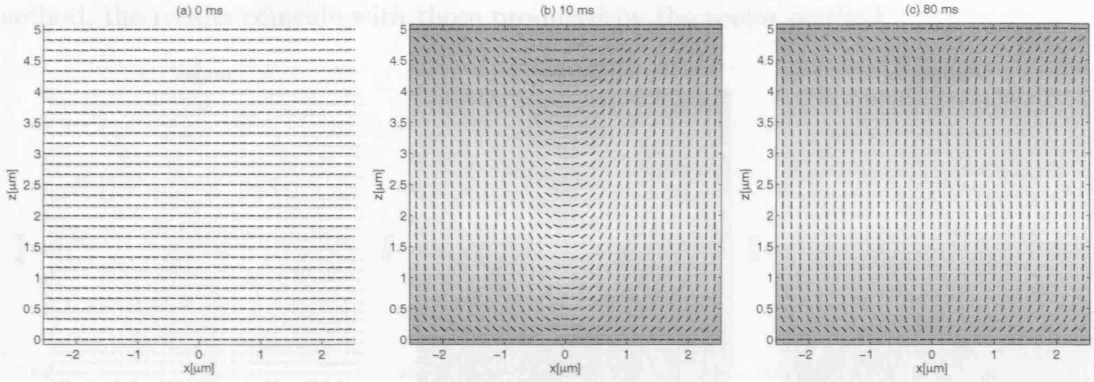

Figure 8-8: Director field produced by the tensor method at the interface between two domains of opposite surface tilt ($\searrow\nearrow$). At $t = 0$, 8V is applied.

gives identical results to the vector method.

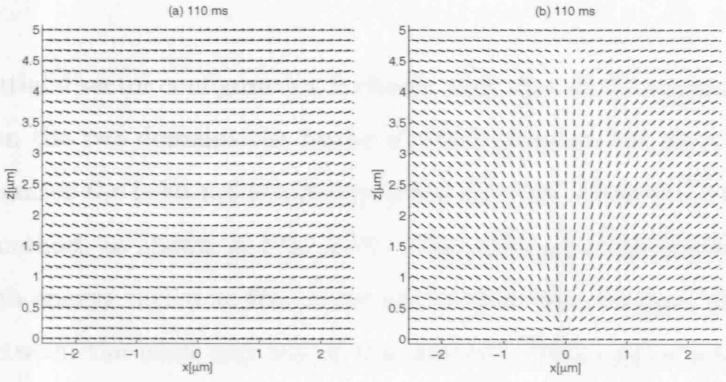

Figure 8-9: Director field 30 ms after removing 8 V. (a) is the result produced by the vector method after relaxation from Fig. 8-7, (b) is the result produced by the tensor method after relaxation from Fig. 8-8

The director field 30 ms after removing 8 V is shown in Fig. 8-9. The vector method, (a), shows a quick relaxation, which is fastest at the centre of the cell due to the rapid spreading of the twist wall. This is the behaviour that would be observed experimentally, provided the applied voltage was not sufficient to give rise to disclinations. Relaxation at the centre of the cell is much slower with the tensor method, due to the loss of the wall between mesh points during switching. The elastic distortion is low at the interface between then two domains, and the directors at $x = 0$ slowly relax until they point into the page; the disclination lines have transformed into twist disclinations. Elsewhere the directors point in the positive x-direction. The disclination lines attract each other and annihilate, but this is a slow process for such a large cell thickness. When a finer mesh is used for the tensor

method, the results coincide with those produced by the vector method.

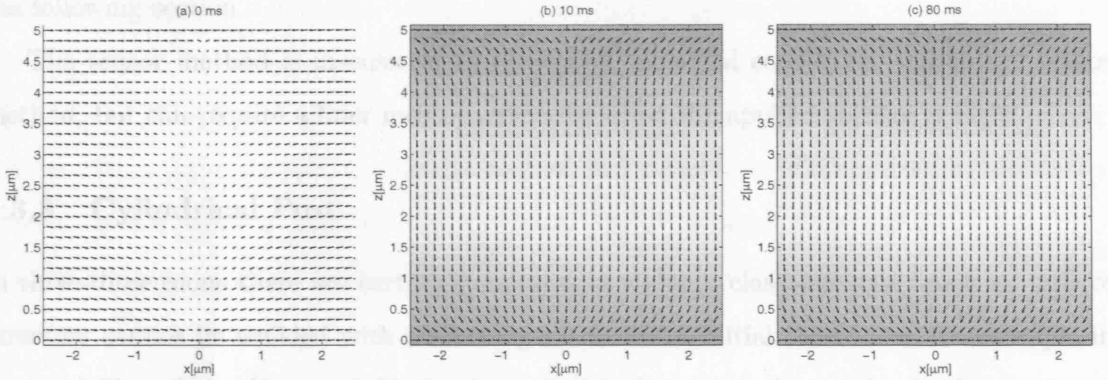

Figure 8-10: Director field produced by the vector method at the interface between two domains of opposite surface tilt. In the left hand domain the director points in the positive x-direction and in the right hand domain in the negative x-direction ($\searrow\swarrow$). At $t = 0$, 8 V is applied.

When the initial director configuration is chosen such that all directors point towards the interface between the two domains the tensor method produces the same result as before; it correctly recognizes the head-tail symmetry of the director. However, this is not the case for the vector method, as shown in Fig. 8-10. This starting configuration gives rise to a non-physical high energy region at the centre of the structure, because the vector method distinguishes between the head and tail of the director. This causes azimuthal (into the page) deflection of the directors with no voltage applied, as shown in (a). A pair of $\pm 1/2$ twist disclination lines are present at the top and bottom alignment layers at $x = 0$. Now the only clashes between director heads and tails occur near the disclination core, and the energy is overestimated in this region. Therefore, if the heads of two adjacent directors point towards each other, a continuous rotation of π is implied between them, in either bend, twist or splay. At $t = 0$, 8 V is applied to the cell and within a few milliseconds the director switches vertically at the centre of the cell. Switching spreads out from the centre of the cell, so after only 10 ms the cell is almost fully switched. The final state shows the presence of two line disclinations, identical to the tensor method when too coarse a mesh is used, but this state has been reached much more rapidly. Once again this method cannot accurately model disclination dynamics. Although in this example it appears obvious that a bad choice of starting configuration has been contrived, it illustrates what happens when clashes between the heads or two tails cannot be avoided, which is often the case for more

complex three-dimensional structures. An example of one such structure will be shown in the following section.

The tensor method is insensitive to the choice of initial conditions, unlike the vector method, but can require a finer mesh particulary when the applied voltage is high.

8.3.3 Cylindrical Post

In three-dimensions there are certain structures in which a clash between heads or tails of directors cannot be avoided with an intelligent choice of initial conditions, for example in the modelling of the director field about a cylindrical post. In this section both tensor and vector methods are used to model the director field about such a post, in the absence of an applied voltage.

The upper and lower alignment layers are aligned similarly with a pre-tilt of 2° and planar degenerate anchoring is assumed over the surface of the cylindrical post. The starting conditions are chosen such that all directors lie in the positive y-director except around the post, where the directors follow the surface in a counter-clockwise fashion.

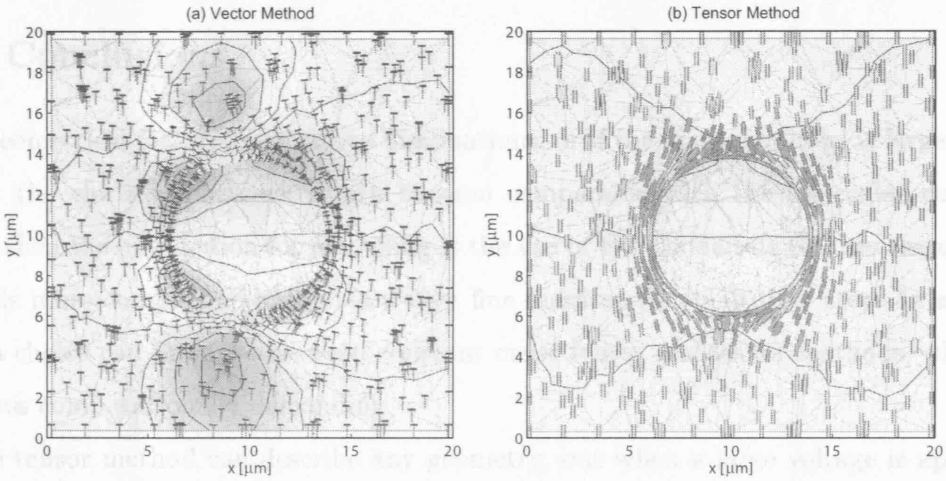

Figure 8-11: Director field across a slice though a cylindrical post, positioned in the middle of the LC layer. Planar degenerate anchoring is assumed on the surface of the post. (a) shows the field produced by the vector method and (b) by the tensor method with 0 V applied. The background colour highlights regions where the director field is distorted and is the potential field for a small applied voltage.

First of all the relaxation process from the initial director configuration will be examined using the vector method. On the right side the post, the surface directors point in the same direction as those in the LC bulk. However, on the left side of the post the surface directors

point in the opposite direction to those in the bulk. This clash gives rise to a (spurious) large free energy in this region when using the vector method, which in turn causes the surface directors to rotate, in the plane parallel to the post. After a rotation of π, the directors on this section of the post point in the same direction as the bulk. This process creates two regions of splay on the post surface that then diverge. Fig. 8-11 (a) shows the director profile across a slice half-way though the LC layer after relaxation.

When using the tensor method, because the head tail symmetry is maintained, the initial director configuration does not give rise to a high energy region on the left side of the post. After relaxation the director profile shown in Fig. 8-11 (b) is obtained. The directors remain in a circular arrangement about the post, and the resulting director profile corresponds to the minimum energy state. At the top and bottom of the post $-1/2$ defects are present

For this structure and many other three-dimensional structures the vector method gives rise to non-physical regions of high energy that prevents the method from describing the actual stable states of the system. In these cases the tensor method should be used, and preferably the order parameter should be allowed to vary.

8.4 Conclusions

If the geometrical features give rise to disclinations, or if the applied voltage is large enough so that the electric coherence length become comparable with the molecular coherence length, then the only option for modelling is the use of the Landau-de Gennes theory. This theory is more complex and requires a very fine mesh and a small time step. In all other cases, a choice can be made between constant order tensor and vector methods, which are much less computationally demanding.

The tensor method can describe any geometry, but when a large voltage is applied, a fine discretisation is required (of the order of the electric coherence length) to prevent walls from being lost between mesh points. The vector method does not suffer this problem, a coarse mesh suffices, but for certain structures it is not possible to choose a starting director configuration that avoids clashes between heads or tails of directors. It has the further advantage that it is simpler to implement if is computationally faster. Therefore its use is preferred where possible.

Since the problem with the tensor method only appears when high voltages are applied

then this gives a simple method to test which method is best to apply, that can be performed with a coarse mesh. Before a voltage is applied to any starting director configuration the director should first be allowed to relax. If the same relaxed director configuration is obtained by both vector and tensor methods, then the most appropriate method when a voltage is applied is the vector method. If these configurations differ then at some point or points in the structure two heads or two tails of directors clash giving rise to a non-physical region of high energy. The tensor method must be used, with an adaptive meshing scheme, or a discretisation on the order of the electric coherence length.

Chapter 9

Ion Transport in Liquid Crystal Cells

9.1 Introduction

Ion migration in a liquid crystal (LC) cell can have a significant influence on the electric field and this in turn on the liquid crystal director orientation, even when the ion concentration is low. On application of a voltage, charges migrate towards the electrodes and accumulate at the alignment layers, effectively reducing the applied potential across the cell and therefore reducing the director tilt reached. The relaxation time of the cell can be significantly increased due to the long diffusion time of the ions. In some cases an image from one displayed frame persists to the next; an effect known as image sticking. Although the ion content of LC cells is generally low, it tends to increase with the device age. A square wave voltage excitation is normally applied to overcome these problems, but as DC offsets remain the study of this effect is important.

Previous publications have considered the movement of ions through a cell with low applied voltages, where the reorientation of the liquid crystal can be neglected [31]. The purpose of this chapter is to demonstrate the effect of the movement of ions on LC switching and relaxation. Here, switching refers to the reorientation of the LC in response to an electric field. The movement of ions will influence the electric field and the LC orientation in turn. Reorientation of the LC will affect the ion migration in two ways. Firstly, the change in permittivity influences the electric field and the ion drift. Secondly, the molecular orientation will affect the ease with which ions can diffuse.

To this end, ion migration in two common cell types, the planar and the IPS cell, is considered. The IPS cell is becoming more common in display applications. Interdigitated electrodes promote lateral switching of the LC, resulting in a transmittance that is less sensitive to viewing angle than in the planar cell. The electrode area is typically a quarter of that of the planar cell and as a result an applied voltage is effectively screened by a lower charge density.

This chapter describes experimental work of the author performed in the laboratories of the Liquid Crystals and Photonics Group in the University of Ghent, Belgium and the corresponding modelling. A test device constructed by Philips has been filled with a mixture of different LC materials in an effort to achieve a high ion content. On the same substrate one planar cell and a number of IPS cells with differing electrode widths and gap, are present. Alignment surfaces were rubbed in an anti-parallel fashion, yielding a uniform

director field in the absence of an applied voltage with a 2° pre-tilt. A model that takes into account reorientation of the LC director and the drift and diffusion of ions is used to gain insight into the mechanisms governing the measured optical and electrical behaviour. All measurements were made at room temperature, with the LC in the nematic phase.

As a starting point for the work, the transient current response of the planar cell is used to calculate the ion concentration and the mobilities of the ions present within the test device. Elastic and optical properties representative of the LC mixture in the test device are then found by applying a square wave voltage to the planar cell (minimizing the net drift of ionic impurities). Afterwards, a step voltage is applied to the planar cell, and the optical transmittance is measured to show the influence of the ion migration on the LC orientation. By fitting experimental and simulated results it is possible to refine the estimation of the ion mobility. Finally, optical measurements of IPS cells are compared to simulations to gain insight into the effect of the electrode width and gap on ion migration.

9.2 Calculation of director profile and ion migration

In this section the model used to calculate the reorientation of the LC, the drift and diffusion of ions and the potential distribution is summarized. Reorientation of the director influences the electric field and the movement of the ions. On the other hand, the movement of the ions themselves change the electric field and thus influence the orientation of the director. Three coupled differential equations, the first for the director distribution, the second for ion migration and the third for the potential distribution, must be solved. For the time evolution of the director ($\hat{n}$) a single elastic constant formulation is given by Kilian and Hess [76].

An algorithm developed at the University of Ghent [128] calculates the migration of ionic impurities through the liquid crystal. A Monte-Carlo approach is used to calculate drift and diffusion of the migrating ions, whereby representative lumped charges are used to model the actual charge distribution present within the cell. Using this approach the positions of the representative charges need to be updated relatively infrequently in comparison to the director field.

The electric field can be assumed quasi-stationary with respect to the reorientating directors and migrating ions. When a square wave is applied the charges move back and

forth. Here, the model fully resolves all dynamic behaviour using a time step in the order of a few microseconds. Ions are defined by a mobility and concentration and their trajectory is fully determined. The amount of charge separation that can occur in a cycle of the waveform is plainly frequency dependent. As the ions move backwards and forwards the effective permittivity of the cell can be considered as changing. Taking a long term view, the permittivity can be considered as complex, i.e. there is an ion conductivity. In our model, from the charge density and the electric field, this complex permittivity can be calculated.

From an experimental point of view this complex permittivity is a useful parameter. In [129] a novel approach is introduced where it is used to characterize the ion kinds in a cell. Here, it is assumed that the voltage is below the Fréedericksz threshold for a cell without passivation layers. To characterize representative ion kinds we use a complementary approach in terms of ion transit times when a step voltage is applied. To simplify matters, only two kinds are considered, however, many more representative ion kinds could be found by curve fitting if desired.

For low voltages this complex permittivity can fully describe the behaviour of migrating ions. However, for higher voltages the director, electric field and ion density are coupled and all dynamics must be resolved to properly model ion migration. It is this regime that is studied in this chapter.

The current flow, required for experimental comparison, can be determined from the charge accumulation on the electrodes. This charge is

$$Q = \int_0^{l_x} \rho_s dx, \tag{9.1}$$

where the electrode of length l_x is aligned along the $\hat{x}$ direction and is normal to $\hat{\eta}$. The surface charge density is given by

$$\rho_s = -\left(\varepsilon_o \bar{\bar{\varepsilon}} \cdot \nabla u\right) \cdot \hat{\eta}. \tag{9.2}$$

Special treatment of the charge density is required at the electrode edges where the distribution becomes asymptotic [130].

To calculate the simulated transmittance the director field is first calculated as described earlier, taking into account ion migration. From the director field and polarizer orientations the optical transmittance is then found using the Jones Method [8].

9.3 Estimation of Ion Content

It is possible to estimate both charge density and mobility, from the induced current flow in a planar cell when a step voltage is applied.

9.3.1 Theory

There are two contributions to the measured current, the switching current due to the change in permittivity caused by reorientation of the liquid crystal and the ion current due to the drift and diffusion of ions.

If the applied voltage is below the Fréedericksz threshold only the contribution due to ion migration is measured. If the ion concentration is 'low' the influence of ion migration on the electric field can be neglected. This assumption also implies that the applied voltage (U_0) is sufficient to separate fully the charge content of the cell, without switching the LC. The ion concentration can be determined by integrating the current flow in time:

$$n_0 = \frac{1}{\alpha e S d} \int_0^{t_{tr}} I(t) dt, \tag{9.3}$$

where e is the electron charge, S is the area of the cell, T is the time at which the charges have fully separated, and d is the cell thickness. The term α represents the drop in potential across the alignment layers and is the ratio of the total cell capacitance including both alignment layers and the capacitance of the LC layer only ($\alpha = C_{tot}/C_{LC}$). The capacitance of the liquid crystal and the alignment layers is given by

$$C_{LC} = \varepsilon_o \varepsilon_{LC} \frac{S}{d_{LC}}.$$
$$C_{AL} = \varepsilon_o \varepsilon_{AL} \frac{S}{d_{AL}}.$$

where d_{LC} and d_{AL} is the thickness of the LC and the alignment layer and ε_{LC} and ε_{AL} are the relative permittivities. The total series capacitance can be written

$$C_{tot} = \frac{C_{AL} C_{LC}}{C_{AL} + 2C_{LC}}.$$

A simple model can be used to describe the current flow, as detailed in [131]. Two charge distributions of equal concentration (n_0) but opposite sign are assumed to exist

within the cell. The mobilities of the positive and negative ions (μ_1, μ_2) are assumed to be single valued, but not necessarily equal. Many charge distributions with differing mobilities may exist in the cell, but it is instructive to fit to a model using two representative charge distributions.

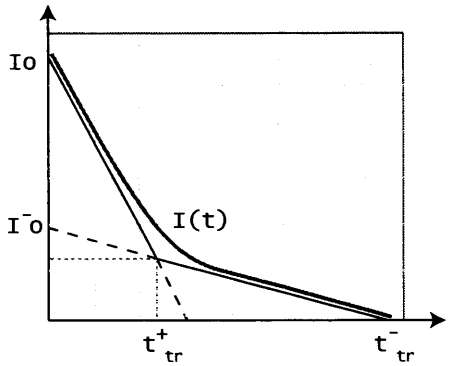

Figure 9-1: 'Triangle' method for predicting current flow

Initially, the current declines linearly due to the movement of the faster of the ion distributions. Extrapolating this decline, a time is reached t_{tr}^{+} when the faster ions have drifted to an alignment layer and no longer contribute to the induced current. Subsequently, the current is dominated by the migration of the slower ion distribution. The current diminishes linearly once again, but with a lower gradient, until the slower ions have accumulated at the opposite alignment layer, at a time t_{tr}^{-}. If the two ion distributions are of equal mobility then a single linear decline of the current is observed.

For higher charge densities, partial screening of the applied voltage can no longer be neglected, and a larger voltage is required to separate both ion distributions fully. In such situations the current flow no longer decays linearly, but as shown in Fig. 9-2(a) instead. Even with this higher charge density, the proposed simple model remains valid near $t = 0$. The initial current, I_0, is proportional to the applied voltage and provides a means to estimate the sum of the ion mobilities:

$$I_0 = \frac{eSn_0(\mu_1 + \mu_2)\alpha^2 U_0}{d}. \tag{9.4}$$

For applied voltages above the Fréedericksz threshold a switching current is induced. The switching current dominates for low ion concentrations, as plotted in Fig. 9-2(b). For high ion concentrations the ion current is dominant, accentuated by the partial screening

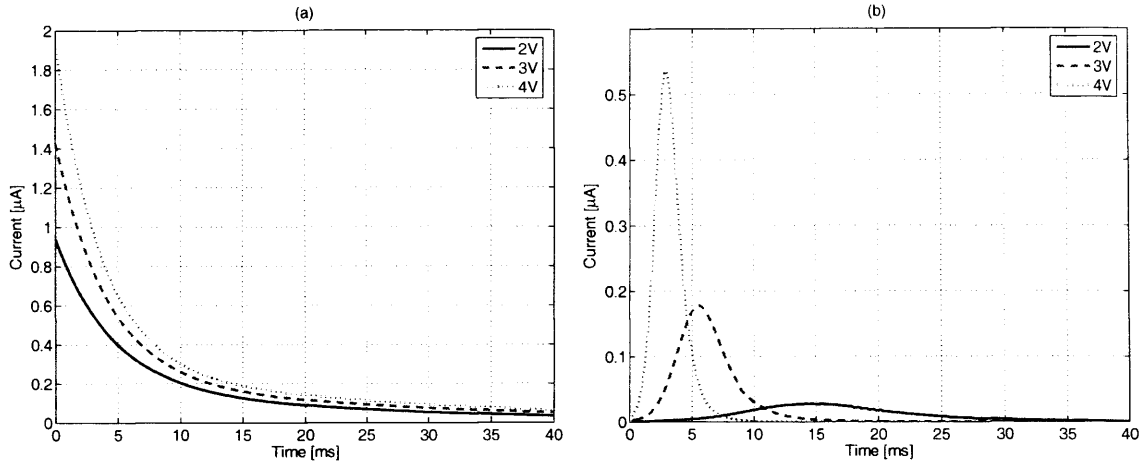

Figure 9-2: Calculated current when a step voltage is applied due to (a) ion migration only ($\Delta\epsilon = 0$), (b) director reorientation only ($n_0 = 0$)

of the applied field by ion separation. For intermediate concentrations the effects of both the ion and switching current are evident in the measured current.

9.3.2 Current Measurements

Measurements of the current flow for the planar cell were made for step voltages ranging from 1 V to 8 V, the upper limit set to avoid electrolysis of the LC. Prior to all experiments the cell was short-circuited for 10 s to ensure that the ions were homogeneously distributed. Fig. 9-3 shows the transient current flow, which is in the order of a few μA, measured by a sensitive current-voltage amplifier.

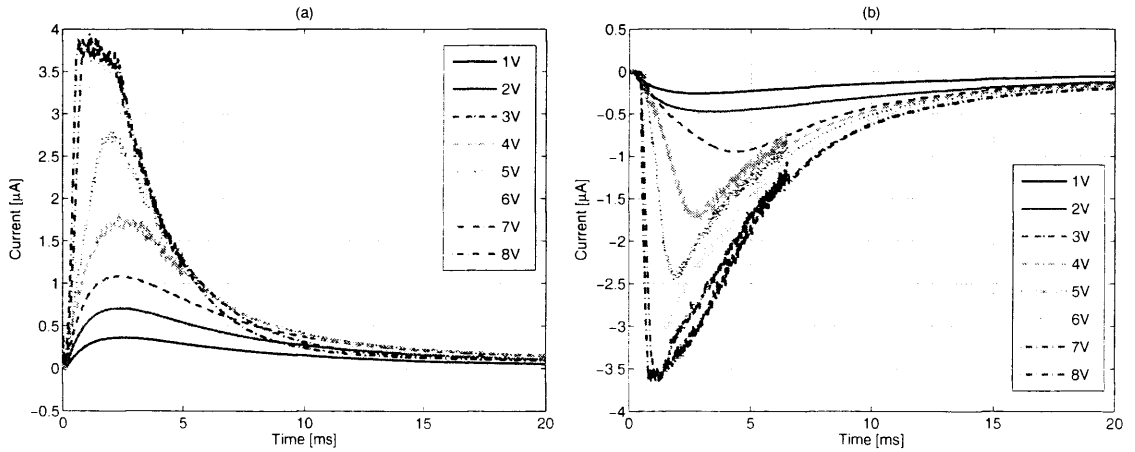

Figure 9-3: Measured transient current flow for a planar cell (a) when a step voltage is applied and (b) when the cell is subsequently short-circuited

The experimental apparatus included components to remove transient peaks from the measured current, the consequence of which is clear below 2 ms, and conclusions should not be drawn from the behaviour before this time. Below 4V the magnitude of the current is proportional to the applied voltage and is therefore representative of the ion current. For higher voltages this proportionality is lost as the switching current begins to contribute.

Partial separation of the ion content is sufficient to screen the applied field for low applied voltages, and equation (9.3) is no longer representative of the total charge content. A high voltage must be applied to ensure complete charge separation occurs, but not so high that the switching current becomes a significant contribution. Before performing any calculations some specifications of the cell are required. The cell is 4.8 µm thick with an electrode area of 25 mm^2 and an alignment layer thickness of 100 ± 50 nm. Calculating the charge density from the data shown in Fig. 9-3 as a function of voltage, gives an ion concentration that tends to $n_0 \approx 1060\,\mu m^{-3}$ as the voltage increases, assuming an 100 nm thick alignment layer.

Equation (9.4) can be used to estimate the sum of the ion mobilities. After extrapolating the 1 V and 2 V curves linearly to $t = 0$ to find I_0, equation (9.4) gives on average $(\mu_1 + \mu_2) = 563\,\mu m^2/Vs$.

9.4 Calculation of Optical and Electrical Properties of the LC Mixture

By applying a square wave voltage of sufficiently high frequency compared to the ion mobility, the influence of ion migration on LC switching can be minimized. The planar cell was placed between crossed polarizers positioned at ±45° to the optic axis, and the optical transmittance measured by a photodiode, using a HeNe laser source.

Fig. 9-4 shows the optical transmittance as a function of time. From the electro-optic curve the Fréedericksz threshold was determined as $V_{th} \approx 1.2$ V. From the relationship

$$\varepsilon_0 \Delta\varepsilon V_{th}^2 = K_{11}\pi^2.$$

K_{11} is found approximately equal to $10^{-12}\Delta\varepsilon$. Gauging this threshold optically is not very accurate, but other methods, such as capacitive measurements are also difficult when the

ion content is this high.

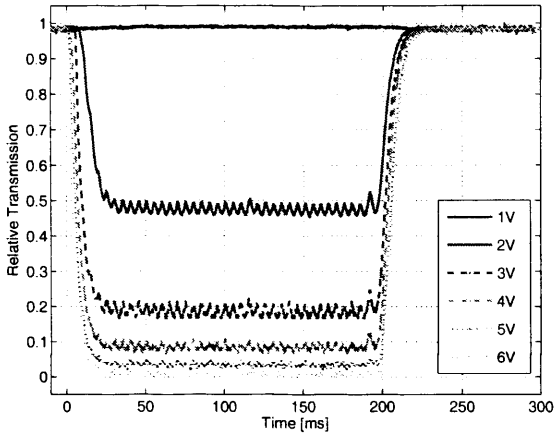

Figure 9-4: Experimental planar cell transmittance with (1kHz) square wave voltages applied

To begin, it is necessary to calculate the optical birefringence of the LC. When this is known, it is possible to estimate the other unknown properties of the LC by curve fitting. In Fig. 9-4, the transmittance is monotonically decreasing for each voltage pulse applied. Therefore, the optical path length must be such that the phase difference between the two propagating modes through the LC is always less than π. That is

$$\Delta n \leq \frac{\lambda}{2d},$$

giving $\Delta n \leq 0.067$. The upper limit of this is taken as the birefringence for the simulations that follow.

The alignment surfaces were rubbed to achieve a planar alignment with a 2° pre-tilt. Using this information and the dimensions of the cell given in the previous section it is now possible to simulate the dynamic variation of the director field for a range of different elastic constants and viscosities. By fitting experimental to simulated switching curves (obtained by calculating the transmittance from the director profile using the Jones Method [8]), the remaining unknown properties of the LC were found. Fig. 9-5 compares the experimental and simulated switching curves for an applied voltage of 2 V.

Table 9.1 summarizes the material properties of the liquid crystal, where ε_{LC} is the permittivity perpendicular to the long axis of the molecule and ε_{AL} is the permittivity of the alignment layers.

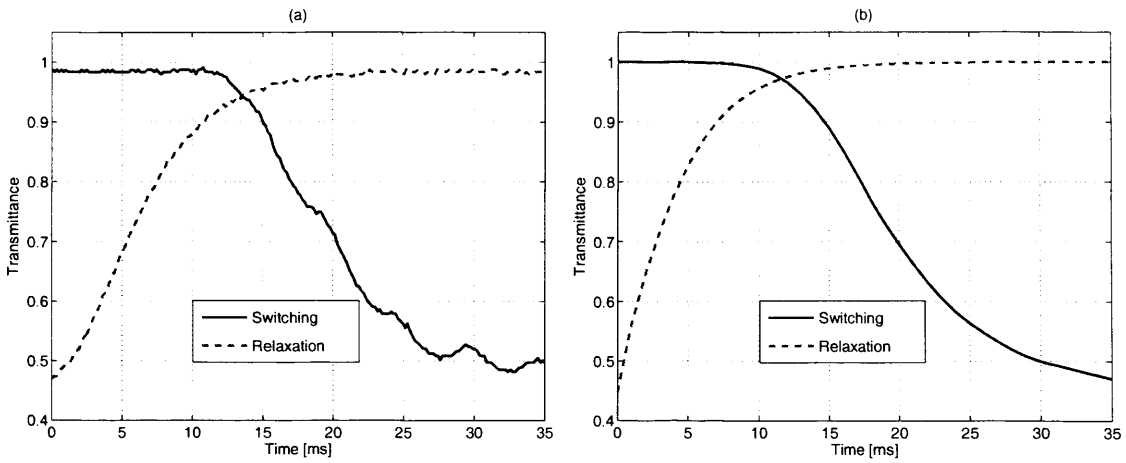

Figure 9-5: (a) Experimental and (b) simulated switching curves with an alternating voltage of 2 V applied. The undulations in the measured transmittance are due to charge separation within each cycle of the applied voltage waveform

Table 9.1: Fitted Material Properties

K_{11} [pN]	ε_{LC}	$\Delta\varepsilon$	γ [Pa·s]	Δn	ε_{AL}
12.0	5.0	12.0	0.065	0.067	4.0

9.5 Influence of ion migration on planar cell switching

Applying a step voltage to the planar cell shows the influence of the screening of the electric field on the orientation of the liquid crystal. A step voltage was applied for 200 ms and the cell subsequently short-circuited. The transmittance was measured using the optical setup described in Section 9.4 for a range of applied voltages, as shown in Fig. 9-6. Initially, at $t = 0$, the applied voltage causes switching of the LC, and simultaneously the charges within the LC begin to separate. For applied voltages below 4 V enough charge separation has occurred after 200 ms to screen the applied voltage below the switching threshold, and the LC relaxes to its initial state. Above 4 V the charge separation partially screens the applied voltage and reduces the director tilt, but at 200 ms charge separation is incomplete. Fig. 9-7 (a) is a sketch of the potential and the charge density soon after applying the step voltage, and (b) at 200 ms.

When the cell is short-circuited at 200 ms the charge built up at the alignment layers induces an electric field, which will be referred to as the charge separation field (sketched in Fig. 9-7 (a)). This charge separation field is sufficient to tilt the LC director further. Mutual repulsion of ions at the alignment layers gives rise to a potential barrier over which

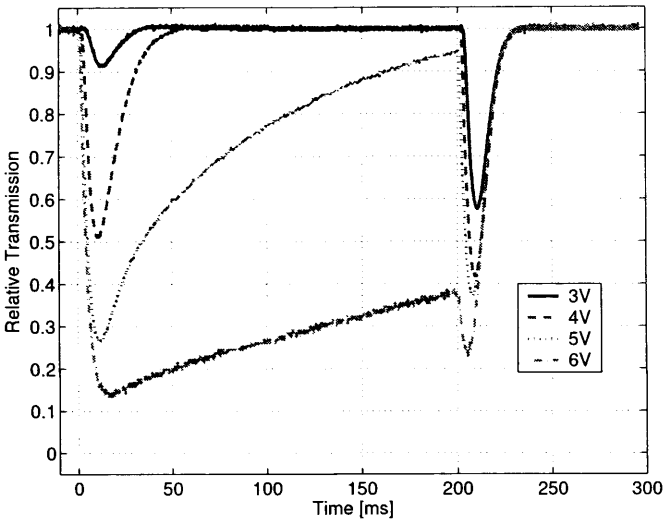

Figure 9-6: Measured planar cell transmittance. Step voltage applied at $t = 0$. At $t = 200$ ms the cell is short-circuited

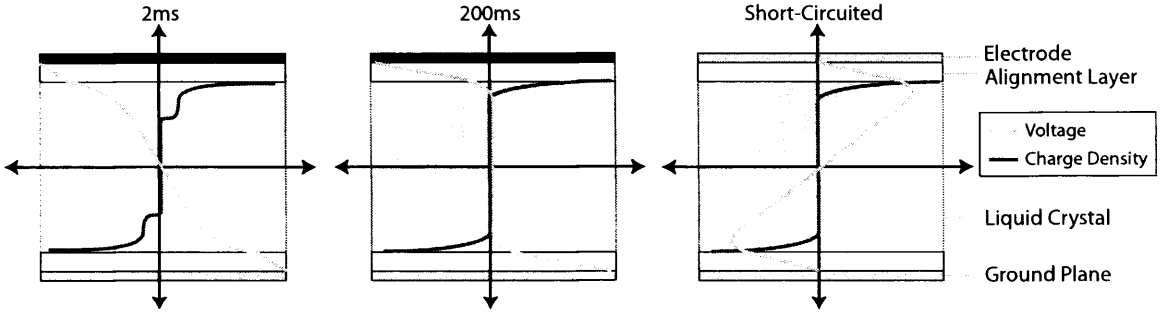

Figure 9-7: Potential and charge distributions when (a) voltage initially applied, (b) complete charge separation has occurred and (c) when cell short-circuited

ions must first diffuse, before drifting towards the cell centre under the influence of the charge separation field. This process causes the charge separation field to diminish, and finally it falls below the switching threshold and the LC returns to a homogeneous state. The two troughs in transmittance were expected to be symmetric, but the first trough is significantly elongated. A possible cause for this asymmetry could be ion generation within the LC layer.

Long-term DC leakage current measurements have shown that ions are generated in the liquid crystal bulk [132]. A neutral molecule has a broad slowly decaying distribution of decay time, and so ion generation has a dispersive nature. Generated ions give rise to a current that decays more slowly than exponentially. The generation rate tends to increase with the age of a cell and has been found to be weakly dependant on the temperature

and the applied field. A very high generation rate is required to achieve a match with experiment, with a doubling of the charge density every 200 ms. Over the considered time scales, this behaviour can probably be attributed to a difference in the mobility of positive and negative ions.

When the voltage is removed at 200 ms the director tilt is limited to $\pi/4$ (even for the 6 V case) due to the partial screening of the applied voltage by the separated charge. Consequently backflow effects are not evident immediately after short-circuiting the cell, nor are they seen later when the charge separation field reorients the director to lie perpendicular to the alignment layers. The presence of the slowly diminishing charge separation field inhibits backflow, as confirmed by the presence of a single not a double minimum in the measured transmittance after 200 ms. Flow of the LC only serves to accelerate the dynamic behaviour.

Table 9.2: Estimated Ion Concentration and Mobility

d_{AL} [nm]	n_0 [μm^{-3}]	μ_1 [$\mu m^2/Vs$]	μ_2 [$\mu m^2/Vs$]
100	1060	431	132
150	1086	531	46

Fitting simulated and experimental current and optical measurements allows estimation of the mobilities of the two charge distributions, as shown in Table 9.2 for two possible alignment layer thicknesses. The value of α depends on the alignment layer thickness, d_{AL}, and so the concentration and mobility are different in each case. Even small changes in the alignment layer thickness have a profound influence in the presence of ionic impurities. A cell with a 200 nm alignment layer will be screened by half the charge density required to screen a cell with a 100 nm alignment layer. With an 150 nm thick alignment layer the charge content is able to screen the applied voltage with ease. A large difference in positive and negative ion mobility is required to reproduce the gradual screening seen experimentally.

Fig. 9-8 shows the calculated director profile and potential distribution that results using an 150 nm alignment layer and an applied voltage of 4 V. For the sake of illustration the positive ions are chosen to be faster than the negative. When a voltage is applied the faster ions migrate (towards the lower ground electrode) more rapidly than slower ions rise, causing a large drop in potential near the upper electrode that promotes reorientation of the liquid crystal. As this switched region increases in size the transmittance falls. The slower

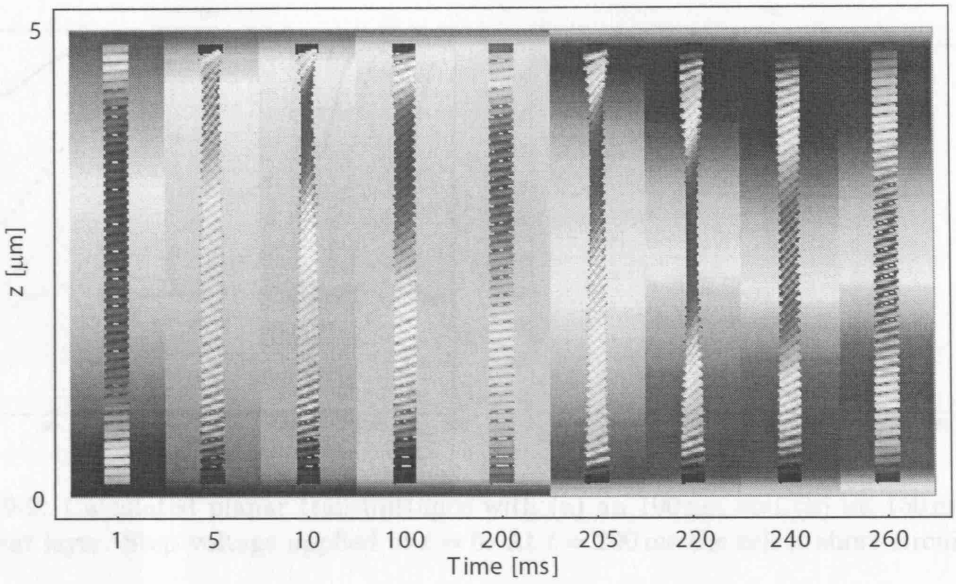

Figure 9-8: Dynamic evolution of the director with different positive and negative ion mobilities. Background colour represents the potential. Step voltage applied at $t = 0$. At $t = 200\,\text{ms}$ the cell is short-circuited

ions eventually migrate to the upper electrode and the applied field is screened, causing a slower relaxation of the liquid crystal.

Rapid reorientation of the liquid crystal occurs when the cell is short-circuited due to the charge separation field. The faster ions built up near the ground plane diffuse across the potential barrier and then drift to the centre of the cell, and unseparated slower ions drift towards them. The slower ions accumulated near the electrode diffuse across the potential barrier, then drift to the centre whilst unseparated faster ions drift towards them. As a result a much more rapid response is observed when the cell is short-circuited, provided that a proportion of the charges remain unseparated prior to short-circuiting the cell. The time taken for the charges to reach a homogenous state is not strongly dependent on the difference between positive and negative ion mobility, in contrast to the ion separation time when a voltage is applied.

The simulated optical transmittance with a 100 nm alignment layer is shown in Fig. 9-9(a), calculated as detailed in 9.2. A long response time is seen when a voltage is applied, in agreement with experiment (see Fig. 9-6), but the second trough that arises when the cell is short-circuited is elongated in comparison. By 200 ms, a high degree of charge separation has occurred. There are few unseparated charges that can drift towards the alignment layers

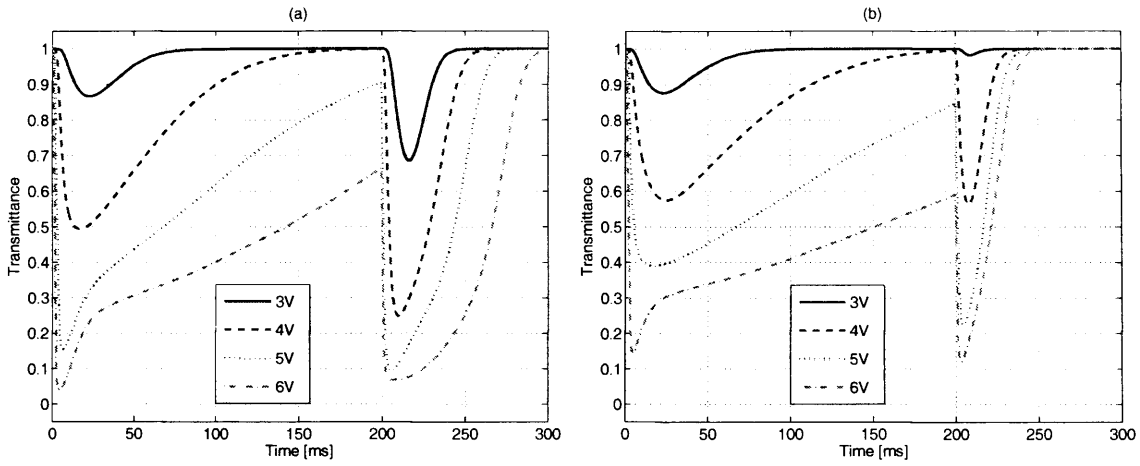

Figure 9-9: Calculated planar transmittance with (a) an 100 nm and (b) an 150 nm thick alignment layer. Step voltage applied at $t = 0$. At $t = 200$ ms the cell is short-circuited

to diminish the charge separation field when the cell is short-circuited. The diffusion of ions across the potential barrier is the principal mechanism that reduces the charge separation field. The long diffusion time of the ions is responsible for the elongated second trough.

Increasing the alignment layer thickness to 150 nm yields Fig. 9-9(b). A greater proportion of unseparated charges remain at 200 ms, due to the increased ease with which the applied field is screened. When the cell is short-circuited, these unseparated charges drift towards the alignment layers, and the charge separation field rapidly diminishes, as indicated by the narrow second trough that is observed.

9.6 Influence of ion migration on IPS switching

A number of IPS cells with differing electrode widths and pitches were available on the same pixel array as the planar cell. Three of these are used here, labelled IPS6, IPS7 and IPS9, as detailed in Table 9.3. It is of interest to study the influence of the electrode width and gap on the sensitivity to ion migration. The same optical setup as introduced in 9.4 was used to measure the optical transmittance, with the exception of the crossed polarizers, which were rotated to lie parallel and perpendicular to the optic axis. The optical transmission was measured when a step voltage was applied and then after 200 ms the cell was short-circuited. A 10° rubbing direction relative to the electrode edges ensures consistent switching of the liquid crystal.

The interdigitated electrodes of an IPS cell have a width and gap in the order of the

Table 9.3: IPS Electrode Dimensions

cell	width [μm]	gap [μm]
IPS6	4	4
IPS7	6	6
IPS9	12	18

cell thickness. Leakage current is significant, thus agreement between simulated and experimental current flows is not easy to achieve. The IPS cell electrode surface area is relatively small in comparison to the planar cell, and as a result it is more sensitive to the presence of ionic impurities.

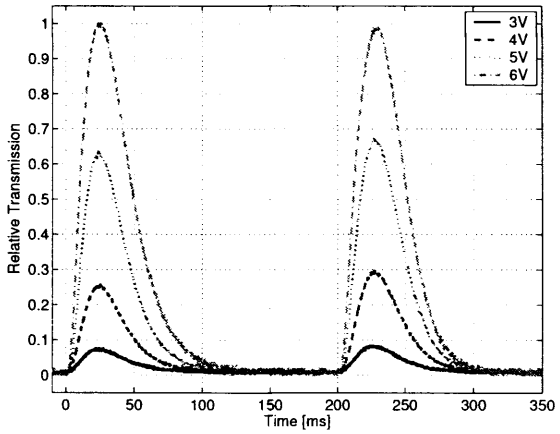

Figure 9-10: Measured transmittance for IPS7. Step voltage applied at $t = 0$. At $t = 200$ ms the cell is short-circuited

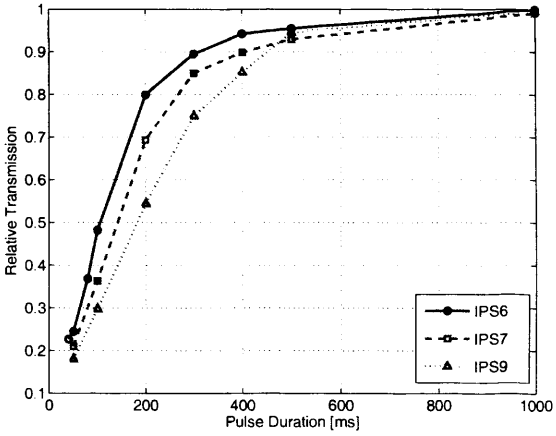

Figure 9-11: peak magnitude of the transmittance after removing 4 V voltage pulses of varying durations

Fig. 9-10 shows the measured optical response of IPS7. For 2 V and below there is negligible change in the transmittance. Backflow effects are not evident in the measured transmittance for the same reasons given for the planar cell. A much more symmetric response is observed than in the planar cell, which is perhaps surprising considering a larger proportion of ions remain unseparated for a given voltage after 200 ms. In the planar cell this situation would serve to shorten the second transmittance peak relative to the first, however, ions move quite differently in an IPS cell.

When a step voltage is applied to an IPS cell there is large potential drop across the electrode gaps, and ions migrate laterally towards the electrodes. Charges tend to accumulate at the alignment layers directly beneath the electrode edges, as sketched in Fig. 9-12. These charges both diffuse and repel each other, resulting in a slow migration towards the

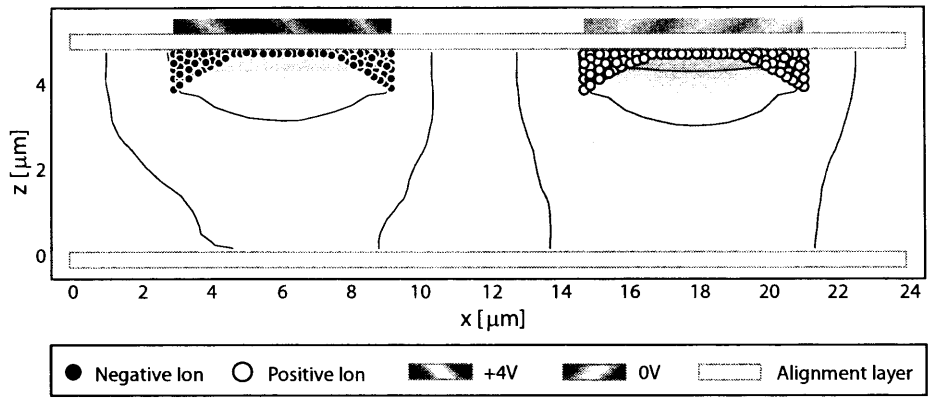

Figure 9-12: Sketch of ion and potential distribution in an IPS cell

centre of the electrodes. Partial screening of the applied field results in an increase in the electric field component perpendicular to the electrodes and ions begin to drift upwards, further screening the applied voltage. Eventually charges evenly distribute along the alignment layer beneath the electrodes. With a small electrode width this process can occur more rapidly and the applied voltage is quickly screened.

When the cell is short-circuited a charge separation field is induced. The separated charge beneath the electrodes can migrate in two ways. In both cases the mutual repulsion of ions gives rise to a potential barrier over which the ions must diffuse before drifting. These ions can either move downwards or laterally. The electric field is larger between the electrodes than beneath the electrode centre and so the majority of the ions overcome the potential barrier beneath the electrode edges and then drift under the influence of the charge separation field. As a result, the charge density beneath the electrode edges drops relative to the centre. Ions remaining beneath the electrodes repel each other and diffuse, moving to the electrode edge to replace the escaping ions. It is the speed of this lateral movement that governs the duration of the observed peaks in transmittance.

The discussion so far has neglected any unseparated charges that exist when the IPS cell is short-circuited. Since the IPS cell has a lower electrode area than the planar cell, there will be a greater proportion of unseparated charge. There are again two ways these ions can move, upwards or laterally. The electric field is largest in the inter-electrode gap, so lateral movement is favoured towards the electrode edges. These charges can then move across the potential barrier and then migrate along the alignment layer beneath the electrodes. The movement of both separated and unseparated ions is limited by the speed at which they

can move beneath the alignment layer; which depends on the diffusion time of the ions.

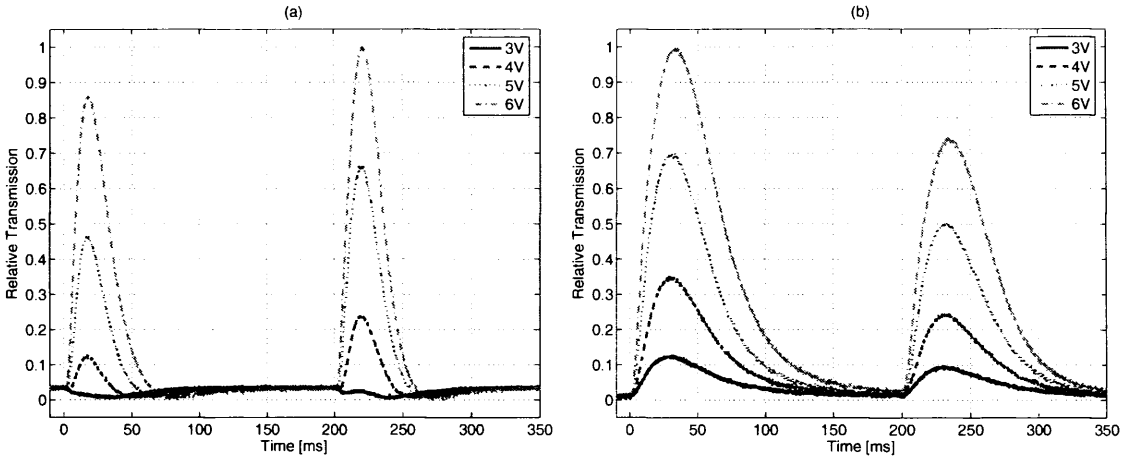

Figure 9-13: Measured transmittance for (a) IPS6 and (b) IPS9. Step voltage applied at $t = 0$. At $t = 200$ ms the cell is short-circuited

Fig. 9-13 (a) shows the transmittance measured for IPS6. Both IPS6 and IP7 have the same electrode area, but IPS6 has 4 µm gap between electrodes. For a given applied voltage the electric field is larger than IPS7 and so it could be predicted that switching would be accelerated, but in fact the transmittance peaks are shorter. Instead, ions are able to very quickly distribute evenly along the alignment layer beneath the shorter electrodes and screen the applied voltage. When the cell is short-circuited at 200 ms more charge separation has occurred relative to IPS7. The second transmittance peak is larger than the first due to this large quantity of separated charge.

IPS9 has a lower electrode surface area than IPS7, and so the ion content should be more able to screen a given applied potential, however it exhibits a greater degree of switching, as shown in Fig. 9-13(b). It is the larger 12 µm electrode width that dominates the behaviour; ions accumulate at the alignment layers beneath the electrode edges and take a longer time to distribute evenly, giving rise to a long transmittance peak. Less ion separation has occurred by 200 ms compared to IPS7, giving rise to a lower charge separation field when the cell is short-circuited, and the LC reorients to a lesser extent.

Fig. 9-11 shows the peak magnitude of the second transmittance peak after removing 4 V pulses of different durations. This magnitude is proportional to the quantity of separated charge. The plot shows clearly that the shorter the electrode width, the more rapidly charge separates to screen the applied voltage.

Simulations were performed using the material and ion parameters found for the planar

cell, with an alignment layer thickness of 100 nm. The IPS cell electrode area is approximately a quarter that of the planar cell, and so relatively the ion content is much larger. It was found necessary to triple the number of representative charges used in the Monte-Carlo simulations in comparison to the planar cell to obtain convergence within each time step.

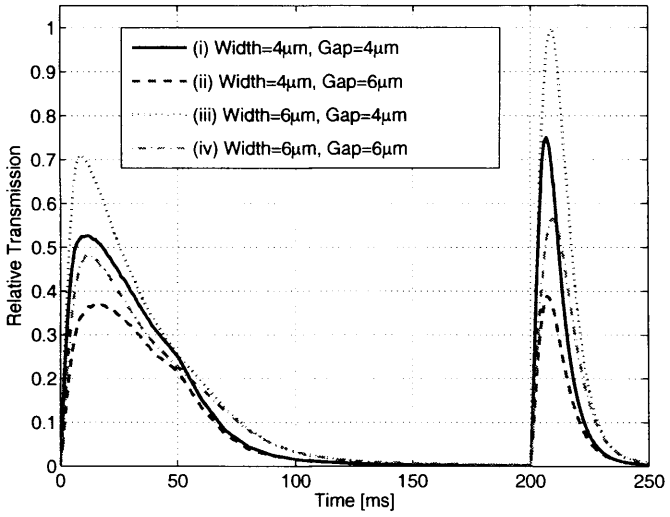

Figure 9-14: Calculated transmittance as the electrode width and gap is altered. Step voltage of 4 V applied at $t = 0$. At $t = 200$ ms the cell is short-circuited

Fig. 9-14 shows the simulated transmittance (normalised for clarity) as the electrode width and gap is altered. A step voltage of 4 V is applied at $t = 0$. At $t = 200$ ms the cell is short-circuited. The increase in the electric field component perpendicular to the electrodes leads to an increase in the director tilt. The two peaks are more symmetric compared to the planar cell, in agreement with experiment. When a voltage is applied the faster ions are able to screen one of the electrodes within a few milliseconds. As a result the migration of the slower ions dominates the optical behaviour over the time scales shown here.

Comparing (i) and (iv) in Fig. 9-14 we see that due to the higher field in (i) the liquid crystal switches more rapidly. An electrode of narrow width is screened in a short time, thus the transmittance diminishes more rapidly with a 4 μm electrode width. The height of the second peak also increases as the electrode width is reduced because a greater quantity of charge can separate in a 200 ms interval. The electrode area is larger in case (iii) than (i), and so the charge density is less able to screen the applied field, resulting in a higher transmittance. However, due to the larger electrode width, screening is slowed, lengthening the transmittance peaks in comparison to (i). Again because the electrode width is nar-

rower in (ii) than (iv), the duration of the transmittance peaks is reduced and since the effective electrode area is lower, the charge content screens the applied voltage more quickly. The IPS simulations show the same dependence on the electrode widths and gaps as seen experimentally.

In summary, increasing the electrode width increases the resilience to ion migration due to the accumulation of ions beneath the edges of electrodes. It is the physical length of the electrode which is important not the ratio to the electrode gap. In addition, increasing the electrode width whilst maintaining the gap increases the electrode area, which decreases the ability of the ions to screen a given applied voltage. In the IPS mode used for displays, the electrode width is usually set smaller than the gap to reduce the dead zone beneath the electrodes [133]. It is desirable to keep the gap small to achieve a fast switching speed. A narrow electrode width will give a good contrast ratio but will compromise the resilience to ion migration.

9.7 Simulation at the IPS Electrode End

Simulations at the end of an electrode of IPS7 have been performed, using the modelling window shown in Fig. 9-15, with and without ionic impurities. The Neumann boundary condition ensures $\nabla u \cdot \hat{\eta} = 0$ and $\nabla \hat{n} \cdot \hat{\eta} = 0$, where $\hat{\eta}$ is the normal to the boundary.

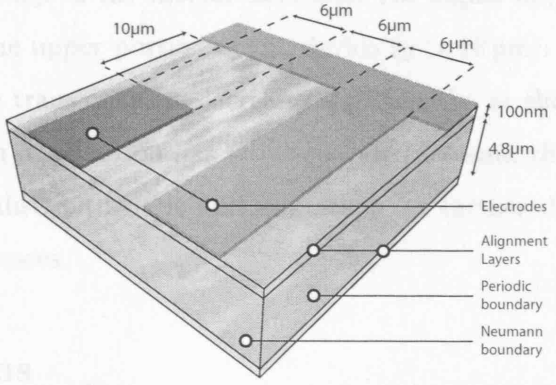

Figure 9-15: 3D IPS electrode end modelling window

Extensions to the models introduced in Section 9.2 are used to calculate the director field and ion migration in three-dimensions. A three-dimensional model of ion migration that employs a mesh hopping routine over the nodes of a tetrahedral mesh has been developed [134]. A finite element vector model with three elastic constants has been used for the

director calculation [95].

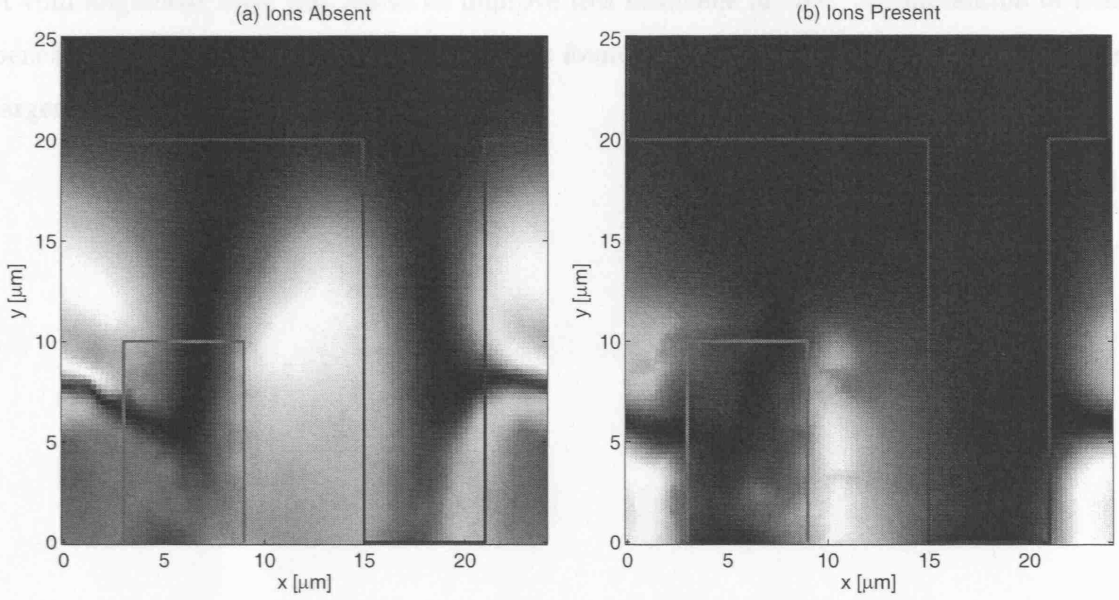

Figure 9-16: Calculated transmittance for IPS7, 15 ms after applying a step voltage of 8 V. (a) Ions absent and (b) ions present. Electrode outlines are overlayed

Fig. 9-16(a) shows the calculated transmittance between crossed polarizers (aligned as in 9.6), 15 ms after the application of 8 V and neglecting ion migration. Switching is most prominent for $y < 10\,\mu m$, where the electric field is highest, and a bend-splay wall forms beneath the left hand edge of the shorter electrode. For higher applied voltages, switching extends further into the upper portion of the device ($y > 10\,\mu m$). When ion migration is taken into account the transmittance decreases significantly, as shown in Fig. 9-16(b). At this time the faster ion distribution has fully separated beneath the ground electrode, but the slower of the ion distributions is still migrating. A further drop in transmittance is observed as time progresses.

9.8 Conclusions

Even low ion concentrations can have an influence on the dynamic behaviour of a liquid crystal cell. Modelling just two ion distributions equal in density but opposite in sign, each with a different mobility, has been found adequate to reproduce the complex interaction seen experimentally in both optical measurements and current transients, between ion migration and director switching in planar and IPS cells. Planar cells, by virtue of a large electrode

surface area relative to IPS cells, were found to be most resilient to the migration of ions. A thin alignment layer was found to improve this resilience further. Accumulation of ions beneath the electrode edges of IPS cells was found to slow ion migration, particularly for larger electrode widths.

Chapter 10

Spatial Light Modulators

10.1 Introduction

A Spatial Light Modulator is a device comprising an array of optical elements with a prescribed spatial pattern, configured electrically or optically and used to modulate light intensity and or phase. Liquid crystals are the common medium for SLMs [135, 136, 137], as the birefringence can be tuned by an electric field in order to modulate the incident light, providing a means to reconfigure the connectivity of a system. A programmable high-resolution SLM is considered here to provide beam steering with the specific application to a telecommunications switch [138, 139]. A reflective SLM is chosen, providing a fully programmable array of phase levels implemented using an array of nematic liquid crystal pixels.

A linear optical phase variation across the device and an abrupt 2π phase transition (flyback) are desired so as to form a blazed grating. To achieve high resolution, pixel dimensions are comparable to the cell thickness and thus the voltage applied to each pixel in order to achieve different phase levels will have a significant effect on its neighbours, particularly at the flyback. These fringing fields not only elongate the flyback (in conjunction with the finite extent of the elastic deformation) but can reorient the LC in the plane parallel to the electrodes (i.e. induce twist), which affects the polarisation state of the outgoing light. These twisted regions cause the diffraction order magnitudes to depend on the input polarisation state, which is undesirable in telecommunications applications.

Previous studies of LC diffraction gratings or phase holograms have considered the case where both the surface alignment and the grating are conformal to the pixel grid [140, 32, 21]. In that case, a simple 2D model will suffice to calculate the LC orientation. In general, however, one may wish to steer an incoming wavefront in a number of different azimuthal directions relative the pixel grid. The surface alignment may be at some angle to the grating and the grating may even be oblique to the pixel grid. An oblique grating will have a rather ragged (staircase-like) edge due to the pixelation that will diffract light in the direction perpendicular to the grating. In this chapter we consider the ability of the device to provide steering in a number of different directions, considering both the cases when the grating is conformal to the pixel grid and when it is oblique, where the LC orientation can only be obtained by full 3D modelling and twist cannot be neglected.

This chapter is arranged as follows. Firstly, the electrode voltages required to give

a linear variation in phase are calculated. Modelling of the liquid crystal orientation is performed for two configurations which differ in their electrode placement relative to a fixed QWP. Two different surface alignments are considered, conformal and at 45° to the pixel grid. Secondly, a grating conformal and oblique to the pixel grid are considered individually in detail, for a wavefront of a single polarisation state. Finally, the far-field diffraction patterns are calculated for the complete set of input polarisation states and a range of steering directions, taking into account both conformal and oblique gratings relative to the pixel grid. The sensitivity of the diffraction orders to the polarisation state of the incoming wavefront and the diffraction efficiency are used to determine the optimum surface alignment and to compare the two configurations. The results are not only important for this specific application; they provide a means to estimate the performance for more general voltage patterns, such as those used in holographic applications, which can be considered as a superposition of a number of gratings in different orientations.

10.2 Computational Method

The modelling comprises two steps; the calculation of the orientation of the liquid crystal with an applied voltage, followed by the calculation of light propagation through this anisotropic medium. The LC orientation is calculated using the constant order vector method detailed in chapter 5. There is rapid lateral variation of the director relative to the wavelength of light. A Reduced [Order] Grating Method (RGM) is used for the optical calculations presented in this section [11].

10.3 Device Geometry

The device geometry is shown in Fig. 10-1, it is a reconfigurable phase modulating LCOS device, for application in a telecommunication system as a beam steering device. By changing the applied electrode voltages the LC can be tuned and the network connectivity can be reconfigured. Since reconfiguration is performed infrequently, the response time is not critical. A device filled with a ferroelectric material [7] would not adequately confine light to a single diffraction order, being able to support only two phase levels. A nematic material is better suited to reproduce the linear phase variation required for beam steering. E7 (Merck) has been chosen for the purposes of simulation, with material properties detailed

in Table 10.1 [1] [141].

Table 10.1: Material Properties (E7)

Symbol	Quantity	Symbol	Quantity
K_{11}	11.1 pN	$\varepsilon_{\perp}$	5.2
K_{22}	10.0 pN	$\Delta\varepsilon$	13.8
K_{33}	17.1 pN	n_o	1.5
λ	1.55 µm	n_e	1.689

Outgoing light from an optical fibre is of unknown polarisation state, thus an optical arrangement is needed that lacks polarisers. Furthermore, the performance of the device should be independent of the polarisation state of the incident light.

Strong anchoring is chosen on the alignment surfaces such that the director field is uniform with neither twist nor splay in the absence of an applied voltage. A pre-tilt of 2° is assumed in the positive z direction, where tilt is defined as the angle between the director and the xy plane.

Incident linearly polarised light parallel to the director will see a refractive index of n_e when entering the device. An applied voltage changes the tilt of the director, so as the light propagates further a reduced refractive index is seen. Therefore the applied voltage can control the phase of the outgoing wavefront. Light polarised perpendicular will however only ever see a refractive index of n_o regardless of the tilt of the director. The phase of the outgoing wavefront will be independent of the applied voltage. Intermediate polarisation states will allow the phase to be modulated by an amount that depends on how 'close' the polarisation state is to the alignment direction. Furthermore, because the director is at some angle to the polarisation state, there will be some conversion of the polarisation state. If a transmissive configuration is used the achievable optical phase excursion and the diffraction efficiency in turn are dependent on the polarisation state of the incident wavefront.

Operating in the reflective mode and positioning a quarter wave plate (QWP) between the LC and the reflector (oriented at 45° to the surface alignment) reduces this dependency [138]. This can be explained by considering the effect of the QWP and the second pass through the LC layer on the individual polarisation states considered earlier. On the first

[1] These material parameters are temperature dependent, however, for the purposes of simulation they are assumed constant. It is possible to use simulations to gauge the sensitivity of the diffraction orders to variations in each of these parameters. This information could then be used to compensate for any such changes

pass through the LC layer the phase of the parallel polarised light was fully tunable by the applied voltage. The QWP then rotates the polarisation state perpendicular to the alignment (a 90^o total rotation from both passes). On the second pass through the LC layer a constant refractive index of n_o is seen regardless of the director tilt and no further phase modulation is possible. Previously the perpendicularly polarised light was unaffected by its first pass through the LC. The effect of the QWP is to rotate the polarisation state parallel to the director, so that on the second pass through the LC the director tilt can modulate the phase. Therefore this arrangement provides polarisation independent operation for not only these two polarisation states, but the intermediate ones too. The polarisation insensitivity provided by the QWP comes at the cost of halving the phase excursion normally provided by the reflective mode. The QWP is chosen to be 3 µm thick and it is assumed for the purposes of simulation that it is ideal, with no variation in thickness. If the thickness deviates from the ideal then the rotation due to the QWP will differ from 90^o and some sensitivity to the polarisation will be introduced A similar effect is seen when there is twist of the LC. On the first pass though the LC the twist not only reduces the effective phase modulation but causes some rotation of the polarisation state too. The QWP is aligned for a particular polarisation state, therefore the further rotation due to the twist reduces the effectiveness of the QWP.

An optical phase excursion of 2π is desirable, giving a high diffraction efficiency without the need for a complex optical configuration. In other words, the cell must act as a waveplate and hence should be at least 8.21 µm thick for operation at the near infrared wavelength of 1.55 µm for E7. The actual cell thickness must be in excess of this due to the reduction in phase excursion caused by the splay deformation of the LC near the alignment layers, the extent of which is defined as the electric coherence length. A 10 µm thick LC layer is chosen, thick enough to achieve the full phase excursion without the need to apply large voltages to the electrodes.

Electrodes lie in the xy plane, with a pitch set to match the cell gap and an inter-pixel gap of 0.5 µm. To ensure sufficient electrodes are available to give a linear phase variation, a relatively large grating period of 100 µm is chosen. The deflection angle, θ_m, can be found using the grating equation:

$$p(\sin\theta_m - \sin\theta_i) = m\lambda, \tag{10.1}$$

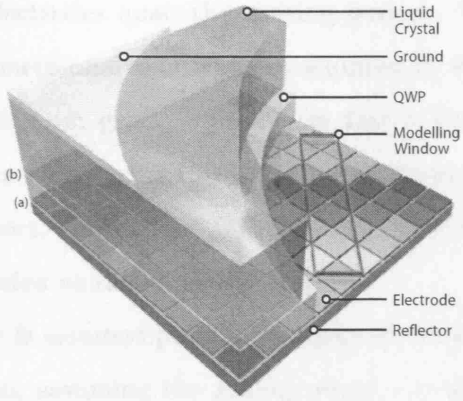

Figure 10-1: SLM Configurations (a) with the electrodes forming the reflector, and (b) with electrodes positioned between the LC and the QWP. Electrode colour represents the voltage for a grating oblique to the pixel grid

where θ_i is the angle of incidence and m is an integer denoting the diffraction order. This gives the deflection angle associated with the first diffraction order as approximately 0.9°. With a suitable arrangement of a number of SLMs, as in [137], or by using a lens, this angle can be increased. Alternatively, the grating period can be reduced by using fewer electrodes per period, but the flyback region will obscure a larger portion of the grating, decreasing the diffraction efficiency. Additionally, the jump in phase between neighbouring electrodes will increase causing a reduction in the linearity of the phase profile [32, 142].

The ability of the device to steer a wavefront in a number of directions is tested by eight specific voltage patterns applied to the pixel grid, as shown in Fig. 10-2. The title that accompanies each pattern is referred to as the grating angle and is the angle of the grating relative to x. Two possible [surface] alignments are considered at each grating angle; (i) parallel to x (ii) at 45° to the pixel grid. These alignment directions relative to the pixel grid are indicated by the arrows in the figure caption.

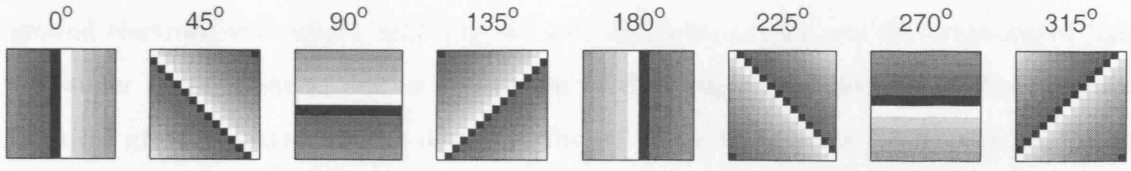

Figure 10-2: Pixel array voltage pattern at each grating angle. Two possible alignments are considered, (i) $\longrightarrow$ conformal (along $\hat{x}$) and (ii) $\nearrow$ at 45° (along $(\hat{x}+\hat{y})/\sqrt{2}$) to the pixel grid

When the grating angle is along $\hat{x}$ (or $\hat{y}$) the solution to a two-dimensional problem

is sought in which ten electrodes span the grating period. When the grating is at 45° to the pixel grid three-dimensional modelling is required in which a grid of 14x14 pixels is required to achieve a 100 µm grating period (in fact a 99 µm period is given by this arrangement). Modelling a 140^2 µm^2 x 10 µm volume that resolves properly the inter-pixel gaps is a daunting prospect. Fortunately, the volume of the modelling window can be minimised when it is oriented as shown in Fig. 10-1.

The modelling window is assumed periodic for both the director and optical calculation. For the optical calculation, assuming the grating repeats indefinitely means the power is concentrated in distinct orders. In reality the aperture will be of finite extent and to obtain the actual far-field response one must convolve the near-field response of the grating with that of the aperture [139, 137].

Two device configurations are analysed, configuration (a) where electrodes form the reflector, and configuration (b) which is more complex from a manufacturing point of view, where transparent electrodes are positioned between the LC and QWP.

For display applications indium tin oxide (ITO) is usually used as the material for transparent electrodes as it exhibits a low absorption in the visible spectrum. At infra-red wavelengths this material becomes very lossy and reflects strongly [143, 144]. The optical constants of ITO are strongly dependent on the material on which it is deposited, the thickness and the post-treatment. At the wavelength of 1.55 µm the refractive index and the extinction coefficient take a wide range of values [143, 145]. There are other conductive materials that are more transparent at this wavelength, such as indium-oxide doped with zinc [146] or cadmium [144]. With careful design of electrode material, thickness, and matching layers the transmission can be maximised [147]. The details of the optical properties of the ITO must be taken into account in the final optimisation, but are not dealt with in this chapter. In a real device, if these layers are not carefully designed the ground electrode will reflect light into the zero diffraction order and the transmitted light will suffer an attenuation due to absorption of the transparent electrode. The reflection from the ground electrode alone decreases the +1 order by between 0.3 dB and 2.1 dB and increases the zero order by as much as 11 dB for an 100 nm thick ITO layer with the material constants published in [143, 145]. In configuration (b) a fraction of the light will reflect from the additional transparent electrode that is present without passing through the QWP, increasing the dependence of the diffraction orders on the input polarisation state.

A linear 2π variation in the phase of the outgoing wavefront is required and the electrode voltages are carefully chosen to achieve this. Using a one-dimensional model, the phase of the dominant component of the outgoing light is calculated as the voltage is varied. To exploit the electro-optic curve fully, the minimum electrode voltage is set to 0 V. Electrode voltages are chosen so that the corresponding phase levels are equally spaced to give the desired grating period, and are arranged to position the flyback at the centre of the modelling window. For configuration (a) a maximum electrode voltage is calculated as 6.45 V to achieve a 2π optical phase. Configuration (b) exhibits a reduced maximum voltage of 3.04 V and an associated decrease in power consumption. It is possible to maximise the

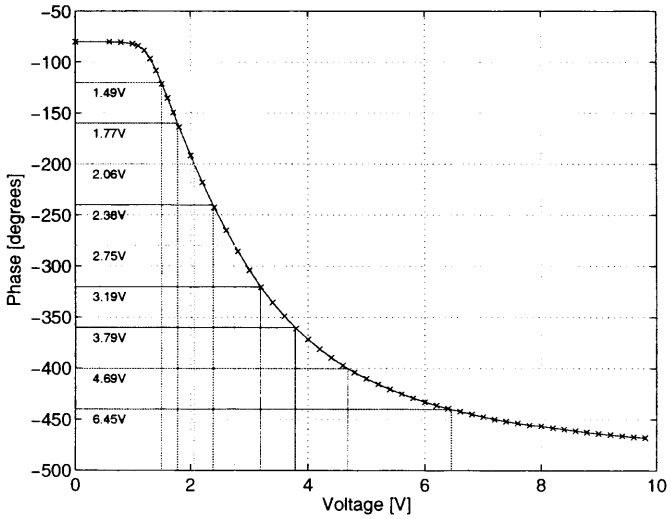

Figure 10-3: Phase of the dominant component of the outgoing wavefront as a function of voltage

diffraction efficiency by optimising the electrode voltages for a specific grating angle [148]. Such a procedure could be applied for all possible grating angles, but the calculation is time consuming particularly in case of oblique grating angles. The aim of this chapter is to compare the two device configurations and two surface alignments. Keeping the electrode voltages the same at each and every grating angle serves this purpose.

10.4 Grating and alignment conformal to the pixel grid

The simplest case to analyse is a grating angle and surface alignment conformal to each other and to the pixel grid. By comparing the diffraction pattern to that of an ideal grating it is possible to determine how various factors, such as pixelation or the finite extent of the

LC deformation, affect performance. Fig. 10-4 shows the voltage distributions on the top of the alignment layer for configurations (a) and (b) when the grating angle is conformal to the pixel grid. For configuration (a) the QWP has a smoothing effect on the electrode voltages, which aids in the formation of a linear phase profile, but extends the flyback region and reduces the effective applied potential.

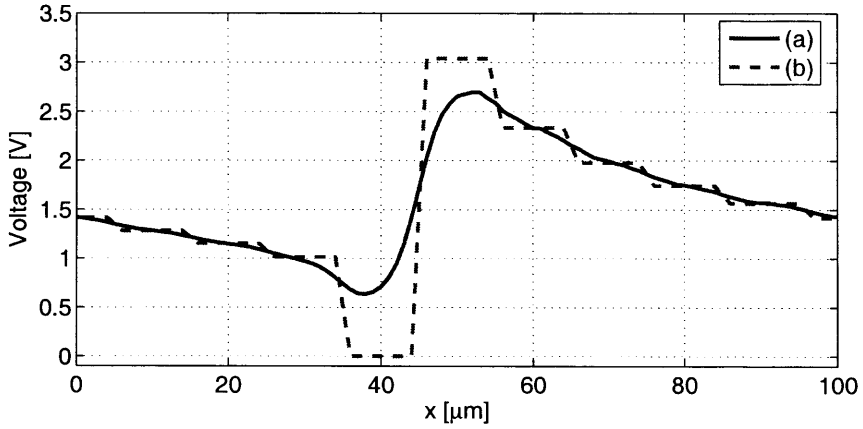

Figure 10-4: Voltage distribution on the alignment layer surface ($z = 0\,\mu\text{m}$)

It was found necessary to apply a bias voltage (5 V for 15 ms) to all electrodes prior to the calculated voltage values to prevent the formation of a bend-splay wall that later transforms into a twist wall above the centre of the highest voltage electrode. Then, after applying the calculated voltages shown in Fig. 10-4, the director profile shown in Fig. 10-5 is obtained at steady-state for configuration (b) with a 0° alignment. Fringing fields have a much stronger influence on the LC for this configuration than for (a). This causes the LC to splay even more strongly between high and low voltage electrodes, so much so that the director in fact changes direction, and an abrupt flyback results.

From the director field, the phase of the dominant component of the outgoing wavefront can be calculated, as shown in Fig. 10-6 for both configurations (which serves to deflect light into the +1 diffraction order). A linear phase response is achieved, but the phase response differs from the ideal one in several respects. Elastic forces within the LC reduce the largest phase modulation from the desired 2π, and also elongate the flyback region. The stepped voltage profile shown in Fig. 10-4 for configuration (b) introduces oscillations in the phase profile. It is important to consider the effect these differences have on the diffraction pattern.

To achieve this, the diffraction pattern for an ideal (blazed) phase grating has been

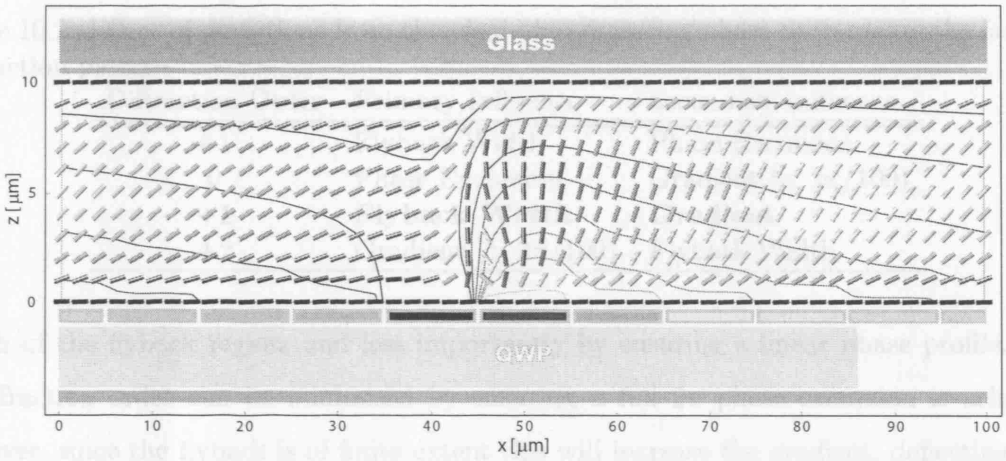

Figure 10-5: Director profile and equipotential contours with a grating angle of 0° and a 0° alignment for configuration (b), where the director colour represents the tilt

calculated. Changes were then made to the phase profile, for example by increasing the phase gradient from the ideal $2\pi/100\,[\text{rad}\cdot\mu\text{m}^{-1}]$, and the new diffraction pattern compared to the ideal. Three factors have been considered; the extent of the flyback region, the phase excursion and finally the gradient.

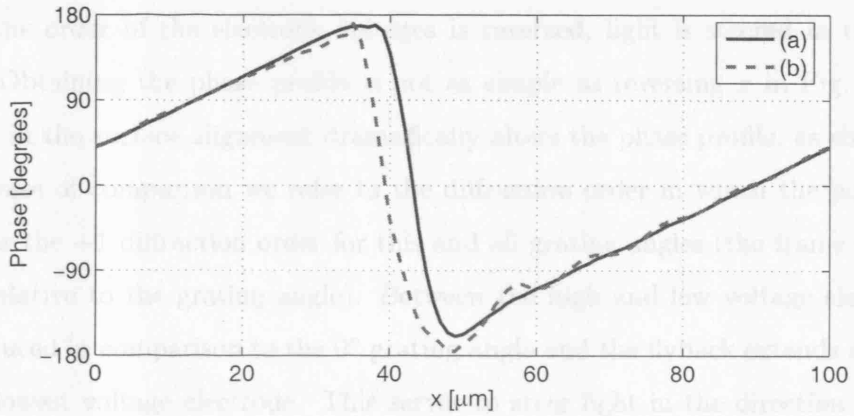

Figure 10-6: Optical phase of the dominant component of the outgoing wavefront with a grating angle of 0°

Table 10.2 summarises how these factors influence the diffraction orders. Only orders close to the main diffracted beam are considered, because it is in these orders in which power is concentrated. Furthermore, light diffracted into the remaining orders is deflected away from regions of interest.

The table indicates that the +1 diffraction order can be maximized by reducing the

Table 10.2: Effect of deviations from the ideal blazed grating phase response on the far field diffraction pattern

Diffraction Order	Primary Influence	Secondary Influence
-1	Flyback Width	Phase Excursion
0	Phase Excursion	Gradient ($< 2\pi/100$)
+1	**Flyback Width**	**Gradient**
+2	Gradient ($> 2\pi/100$)	Flyback Width

width of the flyback region, and less importantly by ensuring a linear phase profile. The 0 diffraction order can be minimised by ensuring a full 2π phase excursion is achieved; however, since the flyback is of finite extent this will increase the gradient, deflecting light into the +2 order. Increasing the extent of the flyback causes diffraction into the negative orders, reducing the magnitude of the +1 order.

In Fig. 10-6 a similar phase response is seen for both configuration (a) and (b), but both differ from the ideal in several respects. Most notably the flyback is of finite extent, which causes a decrease in the +1 order. A phase excursion close to 2π is achieved, thus a low zero diffraction order results. The stepped applied voltage in configuration (b) superimposes on the phase profile an undulation that deflects light into the higher diffraction orders.

When the order of the electrode voltages is reversed, light is steered in the opposite direction. Obtaining the phase profile is not as simple as reversing x in Fig. 10-6. The asymmetry in the surface alignment dramatically alters the phase profile, as shown in Fig. 10-7. For ease of comparison we refer to the diffraction order in which the power is concentrated as the +1 diffraction order for this and all grating angles (the frame of reference is chosen relative to the grating angle). Between the high and low voltage electrodes the splay is reduced in comparison to the 0° grating angle and the flyback extends significantly above the lowest voltage electrode. This serves to steer light in the direction opposite to that desired, in other words into the negative diffraction orders, as well as decreasing the +1 order. Due to the effective reduction in applied potential in configuration (a), caused by the smoothing effect of the QWP, the flyback is less abrupt than in (b). An increase in gradient from the ideal phase profile, a problem that particulary afflicts configuration (b), causes deflection into the +2 diffraction order. Above the highest and the lowest voltage electrodes, the turning points in phase (at $-x = 30$ and $-x = 55$) have a low curvature, deflecting light into the 0 order.

For the two cases shown here, where both the grating angle and alignment are conformal

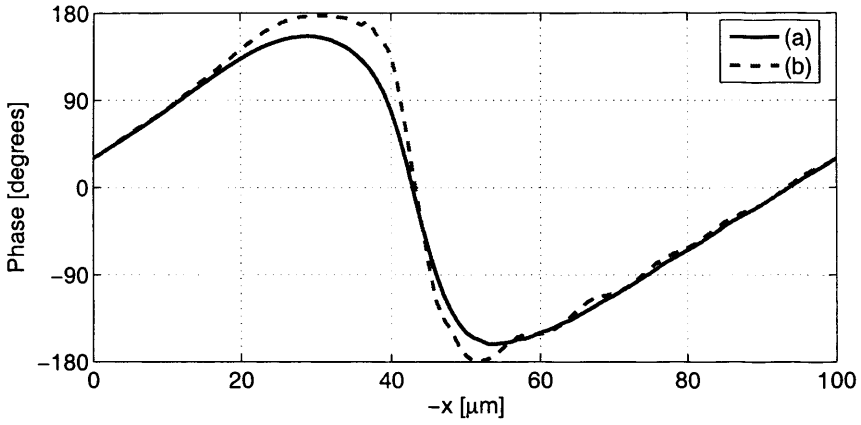

Figure 10-7: Optical phase of the dominant component of the outgoing wavefront with a grating angle of 180°

to the pixel grid, there is negligible twisting of the LC. The QWP is found to provide operation independent of the polarisation state of the incoming wavefront. In other words an almost identical far field diffraction pattern is achieved for all possible input polarisations.

A 45° alignment and or a 90° grating angle give rise to regions of twist within the LC layer, concentrated in the flyback region, which reduce the effectiveness of the QWP and thus introduce a sensitivity to the input polarisation. This effect has been predicted theoretically and measured experimentally [149, 150]. A sinusoidal relationship between the input polarisation and the magnitude of the diffraction orders results [149], with a modulation that depends on both the size of the flyback region and the amount of twist within the LC layer. Clearly, if the grating angle is restricted to those conformal to the pixel grid (0°, 90° and 180°), a 0° alignment will minimise the twist and is preferred.

10.5 Grating oblique to the pixel grid

When the grating is oblique to the pixel grid then the preferred alignment direction is not so clear. To analyse this problem a grating angle of 45° is considered, where twisting of the director can no longer be avoided for any choice of surface alignment. To show where the LC twists the optical reflectance has been calculated, with a polariser added in front of the device, aligned parallel to the alignment direction. This is plotted in Fig. 10-1. The polarisation state of the light passing through the LC layer is unaffected where the directors are well aligned with the polariser. The QWP, oriented at 45° to the rubbing direction,

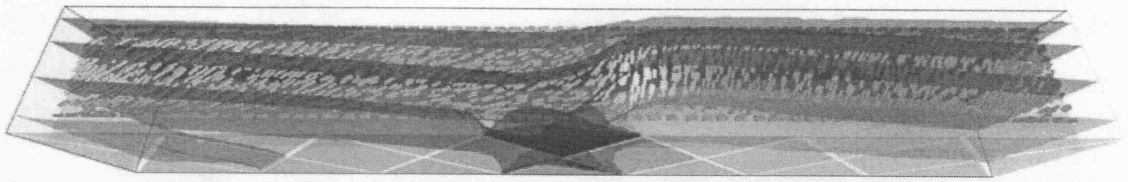

Figure 10-8: Equi-potential surfaces and director field with a grating angle of 45° and 45° alignment for configuration (a). Director colour represents the twist

rotates the polarisation by 90°, so that in such regions the light is blocked by the polariser on exiting the device. Over most of the device the directors appear to be well aligned and the reflectance is zero. At the flyback, in particular, fringing fields induce twist which will cause further rotation of the polarisation state. The angle of this unwanted second rotation depends on the incident polarisation state. Light exiting the LC tends to be elliptically polarised where there is twist and can even become circularly polarised at the flyback. In other words some portion of the light leaks into the orthogonal polarisation state and can pass through the polariser. This leakage effects the phase response and the diffraction orders in turn.

Alignment conformal to the pixel grid, orients some directors parallel and others perpendicular to the electrode edges, resulting in a large amount of twist. With an alignment of 45° the angle between the director and the electrode edges varies much less, and a reduced antisymmetric twisting of the liquid crystal results.

If performance is measured solely in terms of polarisation insensitivity then these arguments suggest that a 0° alignment is favoured for grating angles conformal to the pixel grid and a 45° alignment is favoured for the oblique angles. If arbitrary steering is required then the full range of grating angles must be taken into consideration.

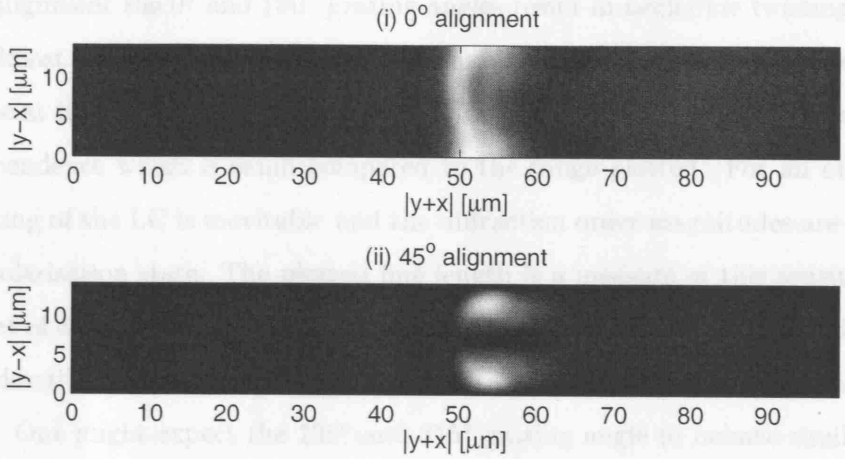

Figure 10-9: Optical reflectance, where a polariser is oriented parallel to the alignment direction with a grating angle of 45° for configuration (a). Black represents the minimum reflectance of 0 and white the maximum, which is different in each case: (i) 1.263 (ii) 0.061.

10.6 Diffraction Orders for all Grating Angles

In order to measure the sensitivity to the input polarisation state, the diffraction patterns have been calculated for a sample of polarisation states that span the complete set of normalized polarisation states (linear, elliptical and circular). For the sake of clarity, only the maximum and minimum magnitude of each diffraction order yielded from this range of incident polarisation states is presented for each pattern of pixel array voltages, shown in Fig. 10-2. The two components of the incident electric field are defined as:

$$E_x = \frac{\cos(\varphi) + i \cdot e \sin(\varphi)}{\sqrt{1+e^2}}, \; E_y = \frac{-\sin(\varphi) + i \cdot e \cos(\varphi)}{\sqrt{1+e^2}},$$

where φ is the angle of the major axis of the polarisation ellipse (the polarisation angle) and e is the ellipticity, which takes the range of $-1 \leq e \leq 1$. Here, $e = 0$ represents linear polarisation and $|e| = 1$ represents circular polarisation. The sign of the ellipticity here is indicative of the sense of the polarisation state, positive representing clockwise and negative anticlockwise polarisations. The complete set of of input polarisation states refers to $-1 \leq e \leq 1$ and $0 \leq \varphi < 2\pi$.

Fig. 10-10 show the magnitude of the +1 and diffraction order at each grating angle, for configuration (a). At each angle two different alignments have been considered, conformal to the pixel grid (0° to x), shown in the upper graph, and at 45°, shown in the lower graph.

With a 0° alignment the 0° and 180° grating angles result in negligible twisting of the LC, providing almost perfect polarisation independent, operation indicated by the presence of a single square at that angle. Diffractive effects (or multiple reflections), do however introduce a slight dependence which is small compared to the range plotted. For all other grating angles twisting of the LC is inevitable and the diffraction order magnitudes are sensitive to the input polarisation state. The plotted line length is a measure of this sensitivity. With an alignment of 45°, the 45° and 225° grating angles result in antisymmetric twisting of the director as described in Section 10.5 and a low sensitivity to the incoming polarisation state is observed. One might expect the 135° and 315° grating angle to behave similarly with a 45° alignment, however due to the pre-tilt, the same antisymmetric twist does not occur. As a result the magnitude of the +1 order depends more strongly on the input polarisation state.

As the ellipticity of the incident wavefront is increased from linear the variation in the +1 order monotonically decreases, tending to zero as the ellipticity approaches one, that of circularly polarised light. The same cannot be said for the maximum and minimum value of the order, for some grating angles. If there is twist of the LC an elliptically polarised incident wavefront tends to maximise or minimise the order. When there is negligible twist of the LC the variation in the +1 order is maximised and minimised by the linear polarisation states.

Fig 10-11 shows the magnitude of the +1 diffraction order at each grating angle, for configuration (b).

The ellipticity of the outgoing wavefront will differ from that of the incident wavefront. For both configuration (a) and (b) the ellipticity of the outgoing wavefront (the +1 diffraction order) is similar. For all grating angles a small change in the ellipticity is achieved which depends on the polarisation state of the incoming wavefront. There are four specific cases where the ellipticity conversion is particularly low, taking a maximum value of ± 0.05. The first two cases arise when both the grating angle and alignment are conformal to the pixel grid (the 0° and 180° grating angles with 0° alignment). The final two cases arise when the grating angle is at 45° to the pixel grid and the alignment is conformal to the grating angle (the 45° and 225° grating angles with 45° alignment), resulting in an antisymmetric twisting of the LC. For the remaining grating angle and alignment combinations the ellipticity is higher, taking a maximum value of ± 0.16. Fig. 10-12 shows the variation in

the ellipticity of the +1 order for all possible grating angles and polarisation angles as the ellipticity of the incident wavefront is varied. The ellipticity conversion is found to increase slightly for incident elliptically polarised states.

The +1 order is high for all grating angles. Approximately 10 dB below this the next largest order, the +2, can be found. It takes a high value due to the increase in gradient from the ideal caused by the extended flyback. If areas of interest can be limited to within the angle of the first diffraction order this is not particularly problematic. The zero order tends to be suppressed well for all grating angles, being on average 20 dB below the +1 order. The magnitude of the orders above the +2 fall off very rapidly, whereas those below the −1 tend to fall off more slowly.

For the oblique grating angles the ragged edge of the pixels with respect to the grating angle will cause light to diffract in the direction perpendicular to the grating angle. Generally the magnitude of the orders associated with this diffraction is low, less than −30 dB for configuration (a) and less than −24 dB for configuration (b). Configuration (a) suppresses these orders better because the LC is less affected by the ragged edge of the pixels due to the smoothing effect of the QWP on the voltage.

Interestingly, when the alignment is conformal to the grating angle (where the twist is antisymmetric) this perpendicular diffraction is maximised. With a low variation in twist, the LC is found better able to tilt, following the ragged pixel edge.

Table 10.3: Maximum & Average Diffraction Order Magnitudes, Config. (*a*)

Diffraction	(i) 0° alignment		(ii) 45° alignment	
Order	Maximum	Average	Maximum	Average
−1	−14.05 dB	−18.82 dB	−13.94 dB	−18.55 dB
0	−17.93 dB	−22.74 dB	−18.14 dB	−22.15 dB
+1	**−0.29** dB	**−1.03** dB	**−0.33** dB	**−1.03** dB
+2	−9.25 dB	−12.95 dB	−8.58 dB	−13.18 dB

Table 10.4: Maximum & Average Diffraction Order Magnitudes, Config. (*b*)

Diffraction	(i) 0° alignment		(ii) 45° alignment	
Order	Maximum	Average	Maximum	Average
−1	−18.13 dB	−22.55 dB	−17.62 dB	−21.94 dB
0	−14.97 dB	−18.86 dB	−16.62 dB	−18.60 dB
+1	**−0.36** dB	**−0.99** dB	**−0.49** dB	**−0.98** dB
+2	−8.46 dB	−12.44 dB	−8.14 dB	−12.77 dB

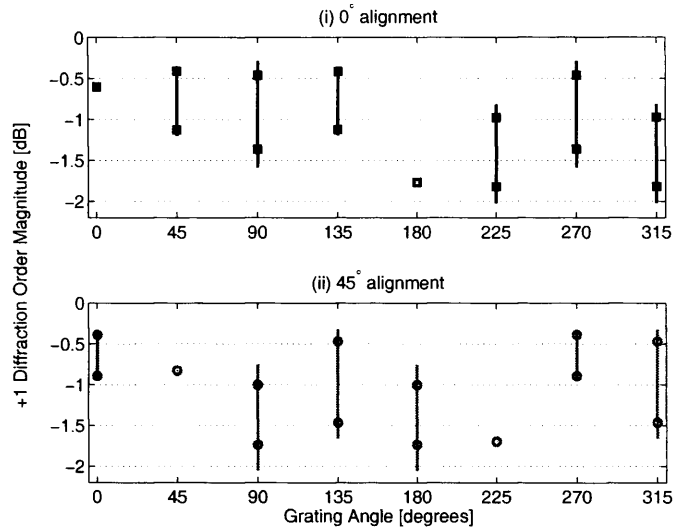

Figure 10-10: +1 Diffraction order magnitude as a function of grating angle for configuration (a). At each grating angle the minimum and maximum magnitude of the diffraction order taken by the complete set of linear input polarisation states is indicated by a marker. The vertical line shows the variation taken by the complete set of (normalised) polarisation states

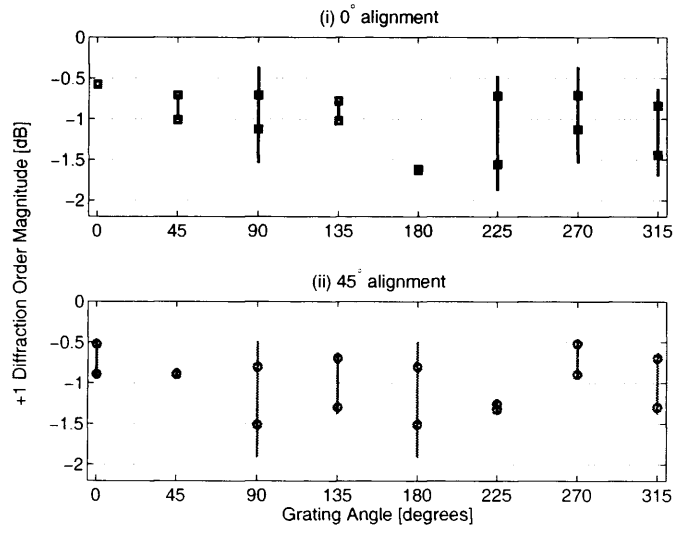

Figure 10-11: +1 Diffraction order magnitude as a function of grating angle for configuration (b)

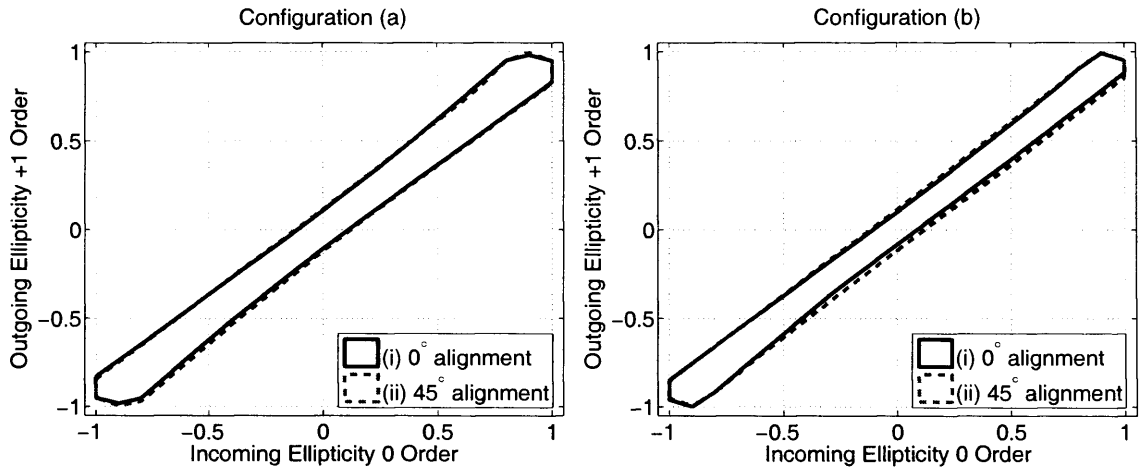

Figure 10-12: Maximum and minimum ellipticity of the +1 diffraction order of the outgoing wavefront across all grating angles and polarisation angles as the ellipticity of the incident wavefront (0 order) is changed

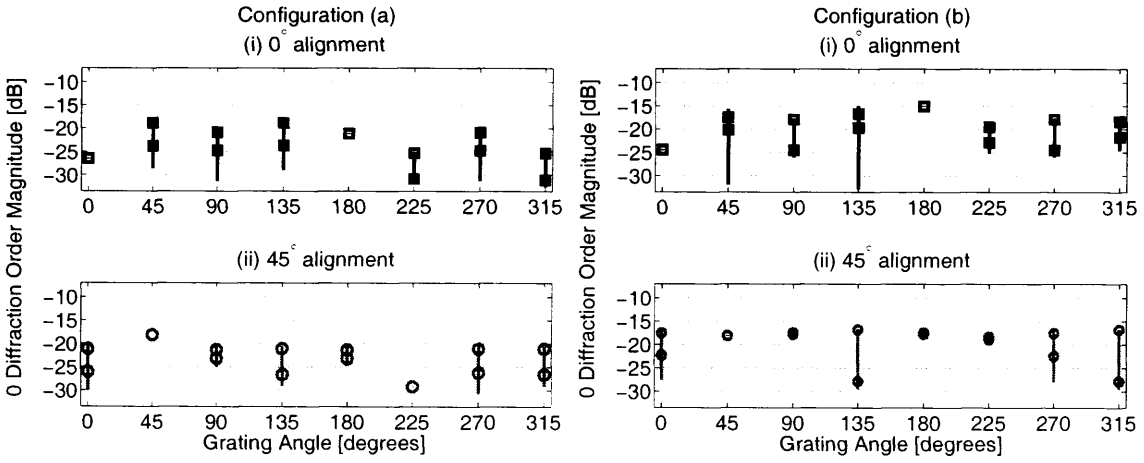

Figure 10-13: 0 diffraction order magnitude as a function of grating angle. The two left hand figures are for configuration (a) and the two right figures for (b)

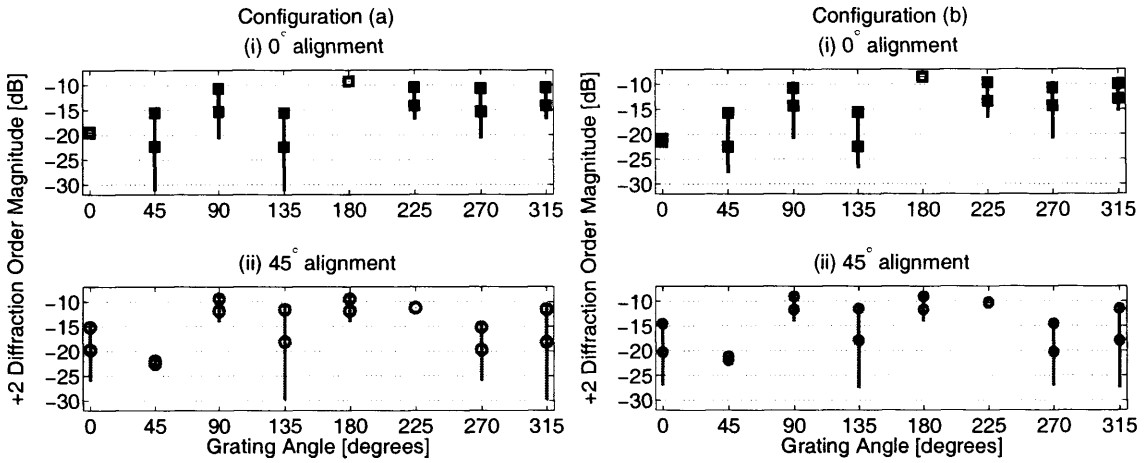

Figure 10-14: +2 diffraction order magnitude. The two left hand figures are for configuration (a) and the two right figures for (b)

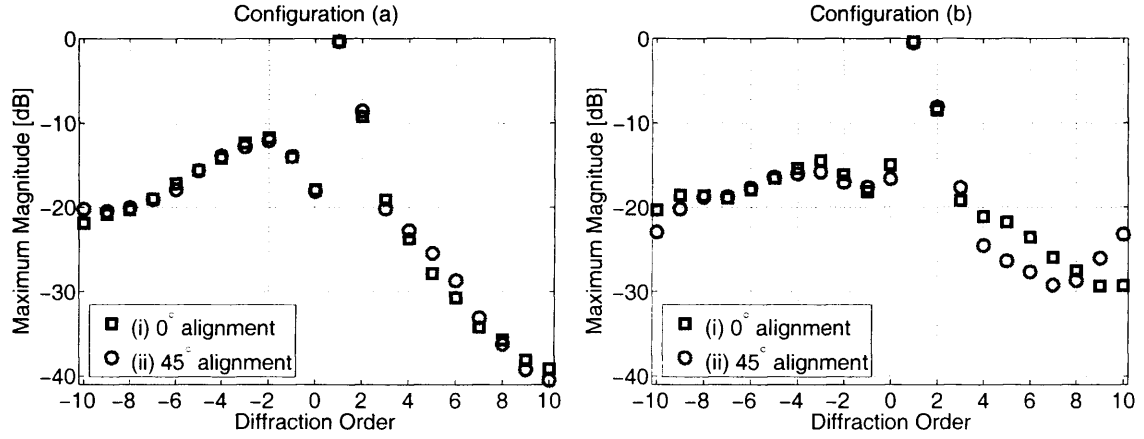

Figure 10-15: The maximum magnitude of each diffraction order taken by the complete set of incident polarisation states and grating angles, both oblique and conformal to the pixel grid

10.7 Discussion

The polarisation state of the incoming wavefront will affect the outgoing wavefront in two ways; (A) the +1 order magnitude will vary with the input polarisation state and (B) the polarisation state of the outgoing wavefront (the +1 order) will differ from the incoming wavefront.

Perhaps (A) is the most important factor. The +1 order magnitude will vary with input polarisation angle, particulary in the case of linear input polarisations. These variations are tiny indeed for the 0° and 180° grating angles, suggesting twist is responsible.

Fig. 10-10 shows the +1 diffraction order magnitude at each grating angle for configuration (a). Both alignments were found to give a similar average magnitude (−1 dB). It is straightforward to pick an alignment that either maximises the +1 order or minimises the polarisation sensitivity for a particular grating angle. As stated in Section 10.4, to minimise the polarisation sensitivity, a 0° alignment is preferable when the grating angle is conformal to the pixel grid and 45° alignment is preferable when the grating angle is at 45° to the pixel grid. Considering all grating angles the preferred alignment is not plainly evident.

To aid in this choice, the polarisation insensitivity can be quantified as the sum of the variation in the +1 diffraction order over all grating angles for the complete set of polarisation states. From Fig. 10-10 this measure indicates that with 45° alignment the +1 order is slightly less sensitive to the incoming polarisation state.

For configuration (b) the electrodes are placed beneath the LC alignment layer and a shorter flyback region results which on average increases the magnitude of the +1 diffraction order, as shown in Fig. 10-11. Again both 0° and 45° alignments give almost the same average magnitude +1 diffraction order. The 45° alignment is found to offer a marginal improvement in polarisation insensitivity (using the same measure introduced above).

The polarisation insensitivity is better for configuration (b), despite the fact that the effective applied voltage across the LC layer is higher, giving rise to more twist. However, a secondary effect of this increased voltage is a narrower flyback. The director lies almost perpendicular to the highest voltage electrode and can twist with ease (there is a low variation in the free energy associated with a change in twist). If the flyback is small then the twisted region is confined to a small space where the director is near vertical and has little influence on the permittivity. The sensitivity of the diffraction orders to the input

polarisation state is then minimal. If the flyback is large, even a small amount of twist can extend into less switched parts of the device, having a significant effect on the permittivity. Despite the increased twisting in configuration (b), the narrower flyback serves to improve the polarisation insensitivity. Using an LC material with a high value of K_{22} (relative to K_{11}) will further improve this, due the reduction in twist.

It was found possible to minimise the variation in the magnitude of the +1 order by increasing the cell thickness above 10 µm. A reduced applied voltage is required to give a 2π optical phase, which results in less twisting of the LC. A disadvantage of having a thick cell is that the fringing fields have a more significant effect, extending the flyback and decreasing the magnitude of the +1 order [32].

For (B) there are two ways the polarisation state can be affected by the device; either by changes to the ellipticity or to the angle of the major axis of the ellipse.

The most significant change to the major axis of the ellipse is due to the QWP, which effectively causes a 90° rotation, in this configuration. This change could be considered as unimportant if all polarisation states experienced the same constant rotation. However, the angle between the input and output major axis is found to vary about 90° (with φ), by less than ±0.06° for the 0° and 180° grating angles, but by as much as ±3° for the other grating angles. Once again, this suggests that the twist of the LC induces this variation.

The ellipticity of the outgoing wavefront (+1 order) changes relative to the incoming wavefront, and depends on the angle of the major axis of the polarisation ellipse, by a maximum value of ±0.16. This polarisation conversion was found to depend on the cell thickness; it increases when the thickness is increased to either 5/4 or 3/2 times the waveplate thickness. By calculating the mean of the maximum change in ellipticity at each grating angle as a function of cell thickness, the first two minima are found when the cell thickness is 9.7 µm and 16.43 µm (twice that of a waveplate).

When evaluating performance it is also important to consider the diffraction orders close to the main beam. Figures 10-13 and 10-14 show the values of the 0 and +2 orders respectively at each grating angle for configurations (a) and (b). It is desirable to minimize these and all orders other than the +1, in order to reduce crosstalk. Therefore, the maximum magnitude of these orders should be low, while the variation with input polarisation state is unimportant. Table 10.3 gives the maximum and average value of the −1, 0, +1 and +2 orders.

Out of these orders it is the 0 order suppression which is most important, and it is generally low for all grating angles. For configuration (a) the 0 order takes a low maximum magnitude of approximately $-18\,\mathrm{dB}$ for both alignments. For configuration (b) this increases to $-15\,\mathrm{dB}$.

The +2 is the second largest diffraction order, which is maximised by choosing an 180° grating angle for both configurations. For (a) this maximum is $-8.6\,\mathrm{dB}$. The gradient of the phase is higher for configuration (b), which further increases this order to $-8.1\,\mathrm{dB}$.

The general characteristics of the phase responses described in Section 10.4 can explain the diffraction patterns shown in Fig. 10-15. Configuration (a) has in general a phase response with a gradient close to $2\pi/100$ for all grating angles and as a result the orders higher than the +1 fall off very rapidly. However, in the case of some grating angles the flyback is elongated, which deflects light into the negative diffraction orders. For configuration (b) the gradient of the phase is further increased from the ideal and oscillations in the phase, due to pixelation, are more evident. Both of these effects serve to slow the rate at which the orders higher than the +1 fall off. The flyback tends to be more abrupt, consequently less light diffracts into the negative orders.

It is possible to increase the voltage of the lowest electrode voltage from zero by about half a volt without having to recalculate the other electrode voltages. With a reduced potential difference across the flyback electrodes the twist is reduced, but the flyback is extended and the phase excursion reduced. It was found that despite the reduction in twist, both the +1 order magnitude and ellipticity (relative to the incident wavefront) were found to vary more. As expected the +1 order suffers an attenuation due the extended flyback.

10.8 Conclusions

The ability of an SLM to steer an incoming wavefront over a range of grating angles both conformal and at 45° to the pixel grid has been analysed. Significant twisting of the LC is induced by the majority of grating angles, reducing the effectiveness of the QWP in providing polarisation insensitive operation, a property it only shows in the absence of twist. The surface alignment was found to have a minor influence on the magnitude of the diffraction orders, but a more noticeable influence on the polarisation insensitivity, which was found best with a 45° alignment.

Two configurations have been considered, the first with electrodes forming the reflector, and second with electrodes positioned beneath the LC alignment layer. When the electrodes form the reflector, smoothing of the applied voltages within the QWP aids in the formation of a linear phase variation, but extends the flyback region. Positioning the electrodes between the LC and the quarter wave layer complicates the manufacturing procedure, but more than halves the driving voltage requirements.

Chapter 11

Diffraction Efficiency for a Phase Chequerboard

11.1 Introduction

In the previous chapter the performance of an SLM was found to be limited by the director field in the fly-back region. These fringing fields and the finite extent of the elastic deformation of the liquid crystal smear the phase transition and induce regions of twist. In this section we focus solely on this fly-back region, by simulating a chequerboard in phase. The effect of altering the pixel pitch on the diffraction efficiency is then evaluated.

For applications such as holography and high definition television a very large number of pixels are required in order to achieve a large area of high resolution [151]. LCOS technology provides a means of delivering high resolution spatial modulation, with high manufacturing yield and cost effectiveness. However, fabrication limitations on the inter-pixel spacing mean that increasing the number of pixels on a given area leads to a smaller pixel size compared to the inter-pixel gap (reduced fill-factor). As the pixel size is reduced, walls can occupy a significant proportion of the device area.

We consider an LCOS configuration where the inter-pixel gap is fixed, while the electrode area is reduced. An alternating pattern of on-off voltages is applied to the pixel array to represent the highest spatial resolution that the system can support. From the calculated director orientation both the phase and intensity of the reflected light is determined. The implications for holographic and image display applications (in terms of the diffraction pattern and the modulation transfer function (MTF) respectively) will be presented.

11.2 Simulation Details

A nematic LCOS device with a pixelated reflector beneath an LC layer and a ground plane forms the basis of all simulations that follow. For both holographic and image display applications a pre-tilt of 2° is chosen to ensure consistent switching. The LC material chosen is Merck E7 and its properties are listed in Table 10.1. Due to the differing wavelengths and modes of operation for each considered application, different applied voltages and cell thickness are required, which will be further detailed in the following sections. The highest possible spatial resolution signal is applied, a chequerboard pattern. A periodic modelling window, oriented at 45° to the pixel grid provides the minimum window area of $2 \times pitch^2$, where the pixel pitch refers to the pixel period including the inter-pixel gap that is held constant at 0.5 µm for all simulations. A constant order vector method has been used to

obtain the director field, and the optical modelling has been performed using the RGM.

11.3 2π Phase Chequerboard Pattern

There are numerous studies of 1D pixel arrays for holographic or beam steering applications [135, 21], but these neglect the complex 3D director fields that arise in real devices. In this section an LCOS device for providing arbitrary phase modulation, using a 2D array of pixels is studied. The advantage in using a nematic LC is that analogue phase levels can be obtained. To achieve good performance without the need for a complex optical configuration, it is desirable to select a cell thickness that provides a phase excursion of 2π. To test the device, simulations have been performed while displaying the highest possible resolution; a 0 to 2π chequerboard in phase. This is the largest phase transition that will occur in a hologram, and it is important that this pattern can be accurately reproduced. Although a 2π chequerboard lacks practical application, it provides a simple means to assess performance. Ideally a propagating wavefront would be unaffected by this phase modulation and power would be confined to the zero diffraction order. However the finite extent of LC deformations, and fringing fields between electrodes, blur the transitions in phase causing deflection into neighbouring diffraction orders.

A planar aligned cell, providing phase modulation, has been simulated and it is assumed that linearly polarised light is input to the device along the direction of the surface director. The issue of polarisation sensitivity is neglected here, therefore the QWP normally positioned between the LC and reflector is omitted. As a result, doubling of the phase excursion is provided by the reflective mode. At the wavelength of 1.55 µm the birefringence of E7 is $\Delta n = 0.189$. Thus, a device thickness in excess of 4.1 µm is required to give a 2π phase excursion.

The potential difference required to give a 2π phase difference can be calculated for a given cell thickness by means of a 1D simulation. Normally the applied voltage is constrained by the driving circuitry, but it is advantageous both in terms of switching times, and minimizing the ratio of the thickness, d, to pixel pitch, to use as thin a cell as possible. A thin cell will require a higher driving voltage to achieve the same phase modulation as a thick cell. Two different cell thicknesses are studied: $d = 5\,\mu\text{m}$ with $3.04V$ applied, and $d = 4.5\,\mu\text{m}$ with $5.39V$ applied.

Fig. 11-1 shows the director and potential distribution at steady-state across a slice through the centre of the 5 µm thick LC cell. Two cases have been considered. Firstly a chequerboard pattern was applied to the cell initially in the relaxed state, yielding the director profile shown in (a). A wall forms above the centre of the ON-pixel on the right hand side, which causes deflection away from the zero diffraction order. Secondly a voltage bias of $1V$ was applied to all electrodes prior to the chequerboard pattern. The effect of this is that now a wall no longer forms when the chequerboard is applied. The resulting director profile is shown in (b).

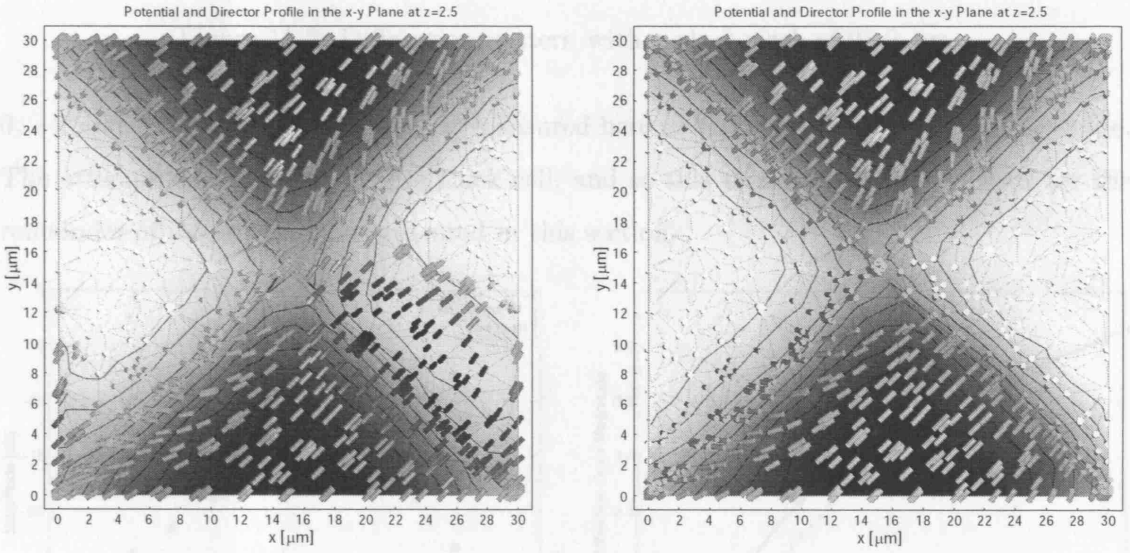

(a) No voltage bias

(b) Voltage bias

Figure 11-1: Director and potential distribution with a pixel pitch of 21.2 µm

From the director profile, the optical transmission through the liquid crystal can be calculated using the RGM, and because this is based on a spectral method, the diffraction pattern is directly available. Fig. 11-2 shows the diffraction pattern for a pixel pitch of 21.2 µm. Diffraction into the higher diffraction orders occurs due to the finite extent of the on-off transitions, and this in turn results in a reduction in zero diffraction order.

Fig. 11-3 shows the diffraction pattern yielded from 4.5 µm and 5.0 µm thick LC cavities, using alignment conformal to the pixel grid and a pixel pitch of 14.14 µm. Taking a diagonal cut across Fig. 11-3 gives the (k, k) diffraction orders, as plotted in Fig. 11-2. The resulting asymmetry of the positive and negative orders is due to the pretilt at the alignment surfaces. A higher voltage is applied for the 4.5 µm thick cell, which increases the transitional region between ON and OFF pixels. The effect of this on the diffraction pattern is to reduce the

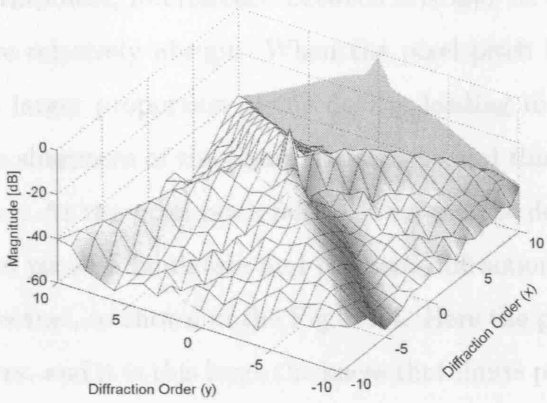

Figure 11-2: Diffraction pattern with a pixel pitch of 21.2 µm

0, −1 and +1 orders. Performance is measured here in terms of the zero order magnitude. The attenuation is less for a 5 µm thick cell, and so this thickness is the one used for the remainder of the simulations presented in this section.

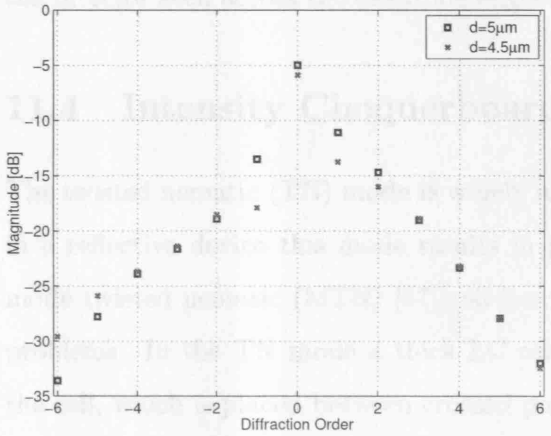

Figure 11-3: Diffraction pattern resulting from 4.5 µm and 5.0 µm thick LC cell with a pixel pitch of 14.14 µm

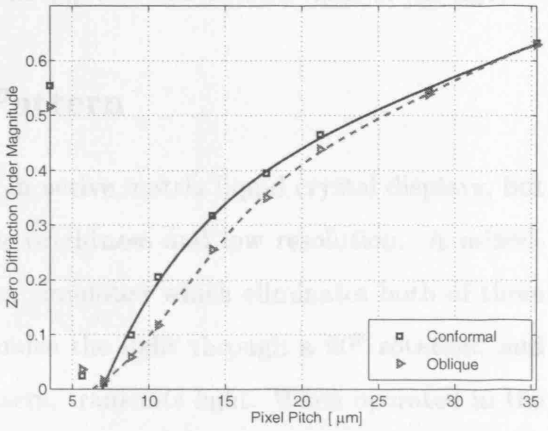

Figure 11-4: Effect of pixel pitch on 0-diffraction order magnitude for alignments both conformal and oblique to the pixel grid

Fig. 11-4 shows the magnitude of the zero diffraction order as the pixel pitch is altered for two different alignments; conformal and oblique (at 45°) to the pixel grid. Although there are two possible conformal alignments, 0° and 90°, both were found to give identical results. Due to the different lengths of the inter-pixel gap and the pixel pitch, and the difficulties this poses for mesh generation, a limited maximum pitch of 35 µm has been simulated. Beyond this length, achieving a good quality mesh is difficult and the number of elements gives rise to a prohibitively large simulation time. When the pixel pitch is large in

comparison to the cell thickness, interference between ON and OFF pixels is low, and the 2π phase transitions are relatively abrupt. When the pixel pitch is decreased, the elastic deformation occupies a larger proportion of the device, leading to a decrease in both the phase excursion and the sharpness of the phase transitions, and this results in a decrease in the zero diffraction order. As the pixel pitch falls below 7 µm the device becomes incapable of describing the desired phase modulation and the zero diffraction order begins to rise as the device become ineffectual, as shown in the Fig. 11-4. Here the pixel pitch is of the same order as the cell thickness, and it is this large thickness that limits performance, not the size of the inter-pixel gap. When the alignment is oblique to the pixel grid, the angle between the director and the pixel edge is consistent across the whole device, and whilst this gives rise to symmetrical regions of twist within the LC, it results in inferior performance to conformal alignment, and the reason for this can be seen in Fig. 11-1(b). Despite an increase in twist in comparison to the oblique case, only with conformal alignment is an abrupt change in the director seen across the electrode edges at the top-left and bottom-right of the figure.

11.4 Intensity Chequerboard Pattern

The twisted nematic (TN) mode is widely used in active matrix liquid crystal displays, but in a reflective device this mode results in poor brightness and low resolution. A mixed-mode twisted nematic (MTN) [57] cell has been simulated which eliminates both of these problems. In the TN mode a thick LC cell guides the light through a 90° rotation, and the cell, which is placed between crossed polarisers, transmits light. When operated in the reflective mode, the necessary inclusion of an analyzer between the cell and mirror reduces the available brightness. Furthermore, the parallax limit on resolution caused by off-axis rays passing through adjacent pixels on forward and reflected paths is exacerbated by the finite thickness of the analyzer. The MTN cell has a smaller cell thickness and so only partial guiding of the light is performed by the 90° twist of the LC. The analyser between the LC cell and the reflector is omitted, and the combined guiding and birefringence effect can be fully exploited.

We consider a common reflective-mode projection system using a polarising beam splitter (PBS). The PBS directs light of one polarisation onto the LC device and selects the orthogonal polarization reflected from the cell, thus acting as a pair of crossed polarisers.

We consider in this case rubbing directions at 20° and 110° to the pixel edges since this gives the maximum reflectivity in the bright state for the cell thickness used [57]. As in the holographic application the pixel voltage is limited by the driving circuitry, but it is beneficial in terms of contrast ratio, to use as high a voltage as possible. Again we test the ability of the device to display the highest possible resolution, a chequerboard pattern, using applied voltages of $0V$ and $5V$.

A single operation wavelength of $\lambda = 0.55\,\mu m$ has been considered, and at this wavelength the material exhibits a birefringence of $\Delta n = 0.2253$. The cell thickness for optimum contrast ratio is given by $d = 0.45\lambda/\Delta n$, where it is necessary to compensate for the effective reduction in birefringence caused by the pre-tilt. A cell thickness of $1.1\,\mu m$ is required, and due to the reduced cross-sectional aspect ratio compared to the holographic application, sharper transitions between on and off pixels are achieved.

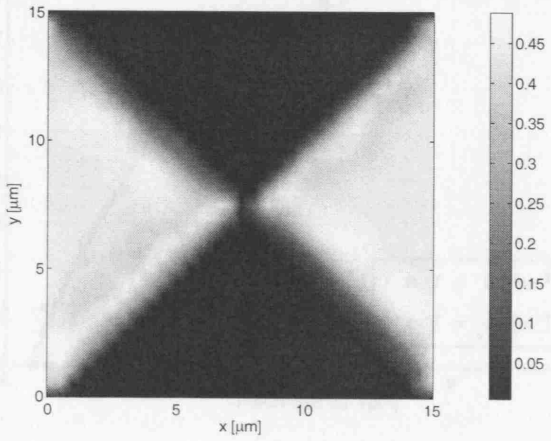

Figure 11-5: MTN cell reflectance for a pixel pitch of 10.6 µm

Fig. 11-5 shows the optical reflectance of a device with a pixel pitch of 10.6 µm and an inter-pixel gap of 0.5 µm. At the centre of the figure, the inter-pixel gap is seen to occupy a significant proportion of the device, but there is a rapid transition between the on and off regions due to the small cell thickness.

The modulation transfer function (MTF) is commonly used as a measure of the performance of lens systems and is defined as the modulation of the image divided by the modulation depth of the object [152]. If we work in terms of intensity, I, then the modulation can be defined as

$$M = \frac{I_{max} - I_{min}}{I_{max} + I_{min}}. \tag{11.1}$$

This definition is used when the stimulus is sinusoidal in nature, but for our purposes it it useful to work in the spatial frequency domain using a definition of the MTF in terms of the power spectrum density (PSD) of the image and the object [152]:

$$PSD_i(f) = MTF^2(f)PSD_o(f), \tag{11.2}$$

where the PSD can be calculated directly from the image as the square of the norm of the two dimensional Fourier transform.

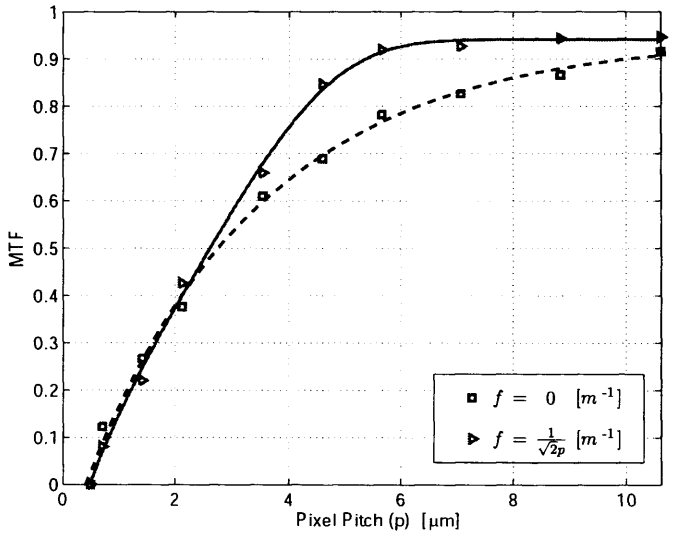

Figure 11-6: Modulation Transfer Function as a function of pixel pitch

The zero (spatial) frequency component of the MTF indicates the mean reflectance over the area of interest. The higher frequency components show the sharpness of the transition between bright and dark states. Fig. 11-6 shows the zero and fundamental frequency components of the MTF as the pixel pitch is altered, and the inter-pixel gap is held constant. The object image chosen for the calculation of the MTF is that of an ideal chequerboard, neglecting the inter-pixel gap. Taking this gap into account would increase the MTF value for low pixel pitches, but would require an estimate of the reflectance within the gap. For small devices the inter-pixel gap takes up an increasing proportion of the device and the MTF reduces for all frequency components. If the LC layer is thicker than the inter-pixel gap, as the pixel pitch approaches the size of this gap, complete switching of

the LC occurs, and the displayed image becomes dark causing the MTF to drop to zero. It is the fundamental frequency which best measures the ability to display the highest resolution images, and this is seen to deteriorate as the pixel pitch falls below 6 µm

11.5 Conclusions

For the holographic application, precise control of potential difference is required to achieve a 2π phase difference between pixels. Any increase or decrease in voltage will alter this phase excursion and have a profound impact on the zero diffraction order magnitude. A thick LC cell is required and so fringing fields, which distort the liquid crystal, blur the phase transitions even when the pixel pitch is relatively large and the size of the inter-pixel gap is insignificant. The use of a nematic LC allows analogue phase levels to be achieved, and for real applications the impact of a given pixel pitch to thickness ratio may be considerably less than for the 'worst case' examined here. In addition, the manufacture of high birefringence LC materials would allow a reduction in cell thickness, and marked improvement in performance. In the image display application maximising the voltage maximises the contrast ratio, and therefore maintains better operation as the pixel size diminishes compared to the holographic application. The MTN cell allows for a very thin LC cell and therefore sharp transitions occur between on and off pixels. Indeed, only as the pixel pitch is reduced below 6 µm does the fundamental frequency component of the MTN fall below 0.9, as the inter-pixel gap begins to take up a significant proportion of the device.

Chapter 12

Bulk Reorientation due to Electrically Induced Disclinations

12.1 Introduction

LCOS devices are capable of supporting high resolutions and are well suited to holographic or beam-steering applications. Ideally, a large number of pixels are desired and it is possible to fabricate very fine structures on the silicon surface, but there will be some limit where the liquid crystal is unable to follow these features. There are two factors that contribute to this limitation, fringing fields between the pixels and the elasticity of the liquid crystal itself. In the previous chapter the limiting pixel size was found that was able to still provide useful phase or intensity modulation. In this chapter we consider even smaller pixel sizes, to determine the director fields that can be obtained as the dimensions approach the CMOS limit and discuss possible applications for such devices. Currently the voltage that can be applied to pixels in an LCOS device is limited to a couple of volts. Can high resolution be used as an alternative to a high voltage to somehow switch the bulk of the liquid crystal? Is it possible to map this high resolution into the liquid crystal?

As the pixels shrink so too does the inter-pixel gap and here the electric field becomes large. Large enough electric fields can potentially cause order melting [16], giving rise to disclinations. In the first section of this chapter the liquid crystal in the inter-pixel gap of an SLM is modelled in the presence of a large electric field strength. The choice of surface alignment will affect whether or not disclinations form and so two cell types have been considered; the planar and hybrid aligned nematic (HAN) cells.

Another effect of increasing the resolution is that the pixels become narrow compared to the cell thickness. The cell thickness is fixed in order to obtain the required optical path length. There are two important effects that will cause such a device to behave differently to a conventional pixel, in which the electrode pitch is in excess of the cell thickness. The electric field does not extend as far into the LC cavity and thus electrically driven reorientation is confined to a small region near the alignment layer. Furthermore, the field will be large in the inter-pixel gap, with the ability to induce order melting. The remainder of the chapter is dedicated to the study of such a device with a high aspect ratio.

Such a device has been studied in the past, with homeotropic anchoring on both upper and lower alignment surfaces with a liquid crystal of positive dielectric anisotropy [33, 153, 154]. In-plane fields in the inter-pixel gap induce, via order melting, a $\pm 1/2$ disclination line pair that separate vertical and horizontal domains. In [33] a fast model to

calculate the director and potential fields was developed and applied to this structure. The reorientation of the liquid crystal remains in the region above the electrode and in the bulk of the device the liquid crystal remains vertically aligned. This behaviour has also been verified experimentally [24]

More recently the study of this device had been continued by R. Ghannam, N. Collings and W.A. Crossland, of the Department of Engineering, University of Cambridge, with whom the work in this chapter has been performed in collaboration. The aim of this work is to design devices and surface alignments in which this surface reorientation can induce switching in the bulk of the device, with or without the use of disclination states.

Of particular interest is the ability to reorient the liquid crystal to give a stable configuration in the bulk supported by disclination lines. This is not only interesting from the point of view of new device types, but for the study of disclination movement. Results are presented for small structures as this makes modelling simpler, but the results are scalable to larger structures with the same aspect ratio, although disclination formation thresholds may differ.

Normally disclinations are formed via thermal processes or by geometrical features. Electrically induced disclinations have not been widely studied and so here we determine the temperature dependence and voltage required for formation and then study the movement of the disclinations taking into account the flow of the liquid crystal.

12.2 Material Properties

All modelling results are produced using the finite element discretisation of the Qian and Sheng equations described in chapter 7 and the material parameters of 5CB (at 26°C) [94, 42, 155, 156, 157].

$a = 0.13 \times 10^6 \cdot (2/3)\,\mathrm{N/m^2{\cdot}K}$, $A = a(T - T^*)$,

$B = -1.6 \times 10^6 \cdot (4/3)\,\mathrm{N/m^2}$, $C = 3.9 \times 10^6 \cdot (4/9)\,\mathrm{N/m^2}$,

$\gamma_1 = 0.0777\,\mathrm{Pa{\cdot}s}$, $\gamma_2 = -0.0848\,\mathrm{Pa{\cdot}s}$,

$\alpha_1 = -0.0060\,\mathrm{Pa{\cdot}s}$, $\alpha_4 = 0.0652\,\mathrm{Pa{\cdot}s}$,

$\alpha_5 = 0.0640\,\mathrm{Pa{\cdot}s}$, $\alpha_6 = -0.0208\,\mathrm{Pa{\cdot}s}$,

$K_{11} = 6.2\,\mathrm{pN}$, $K_{22} = 3.9\,\mathrm{pN}$, $K_{33} = 8.2\,\mathrm{pN}$,

$\varepsilon_\perp = 7.0$, $\Delta\varepsilon = 11.5$, $\Delta n = 0.2$.

The scaling factors multiplying the bulk material constants are due to the Q-tensor definition: $S_0(3\hat{n}\hat{n} - I)/2$ in the uniaxial case, where $\hat{n}$ is the director and S_0 is the equilibrium value of the order parameter. Although the elastic constants and viscosity coefficients depend on the temperature, in this section they are held constant for ease of comparison.

12.3 Order Parameter Variation between ON and OFF pixels

In chapters 10 and 11 the ability of SLM to provide phase modulation for beam steering or holographic applications was estimated in terms of diffraction efficiencies. In these cases the fringing fields between neighbouring pixels were found to limit performance. In this section the behaviour of the liquid crystal in the inter-pixel gap is modelled in more detail than before for a number of different surface alignments. For the time being the study is limited to devices that modulate light intensity and that are suitable for display purposes.

A single inter-pixel gap 0.4 µm wide is positioned at the centre of the modelling window. A continuous ground plane is placed above the upper alignment layer and the two lower electrodes have a length far in excess of that of the inter-pixel gap. Neumann boundary conditions are applied to the sides of the modelling window. In all cases, zero volts is applied to the upper ground plane and to the OFF electrode. 10 V is applied to the ON electrode for 40 µs and then reduced to 5 V. This initial high voltage pulse is applied to encourage disclination formation where possible [16].

To start, a planar aligned cell is considered with a pre-tilt of 2° in the positive z direction. Due to the pre-tilt the director field depends on the sign of the potential difference between the two lower electrodes. Fig. 12-1 shows the steady state director profile with the lower left-hand electrode turned ON and the right-hand electrode turned OFF. In the inter-pixel gap the electric field is high, nevertheless the director field deforms continuously here. Variations in the order parameter are small and no disclinations arise, although a slight increase in the biaxial ordering is observed above the electrodes. Ordering of the liquid crystal is found to peak at the electrode edges.

Reversing the order of the lower electrode voltages gives rise to the director field shown in Fig. 12-2. Shortly after the voltage is applied, fringing fields cause the director to tilt downwards near the left hand edge of the ON electrode, whereas further along the same electrode the pre-tilt causes an upwards tilt. In the midst of these two regions a bend-splay

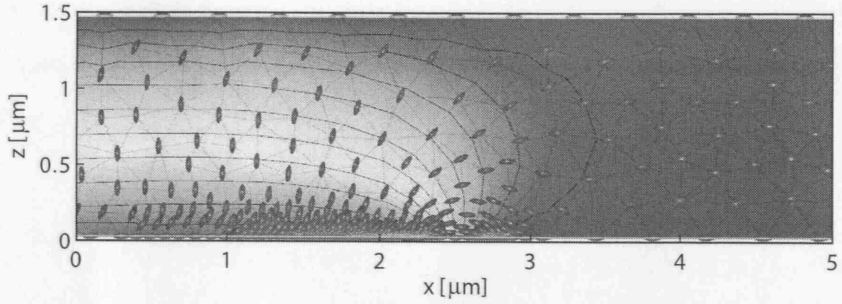

Figure 12-1: Steady state ($\sim 2\,\text{ms}$) director and potential fields arising from ON-OFF pixels in a planar aligned cell. The pre-tilt is 2° in the positive z direction

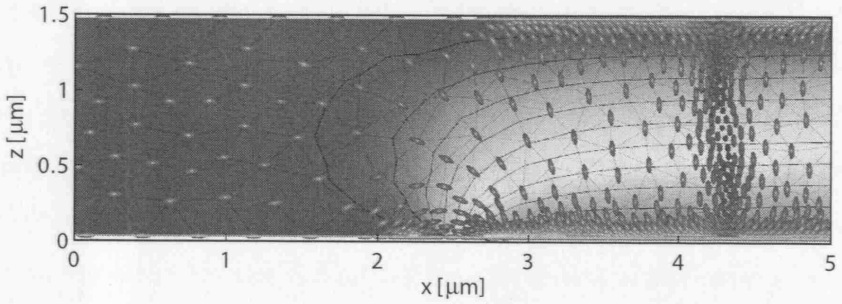

Figure 12-2: Steady state ($\sim 2\,\text{ms}$) director and potential fields arising from OFF-ON pixels in a planar aligned cell. The pre-tilt is 2° in the positive z direction

wall forms which, as time progresses, transforms into a twist wall (since the applied voltage is in excess of twice the Fréedericksz threshold [7, 127]). Since there are two possible directions the director can twist (in and out of the page) and such a wall is found in practice to have kinks. In the inter-pixel gap the director field is once again continuous and no disclination lines are apparent. If the applied voltage is increased much further it is possible to compress the twist wall sufficiently to give rise to a pair of disclination lines [7]. Formation of this wall can be avoided by applying the same voltage to both lower electrodes prior to the OFF-ON pattern.

The planar aligned cell is found to have a continuous director field in the inter-pixel gap which can be well described by a constant order parameter approximation. HAN cells however, behave quite differently as is apparent from the steady-state director field shown in Fig. 12-3.

A pair of disclination lines of strength $\pm 1/2$ form in the LC above the mid-point between the two lower electrodes. A more detailed explanation of this process is described in Section 12.5. These disclination lines then separate; the $+1/2$ disclination moves downwards until

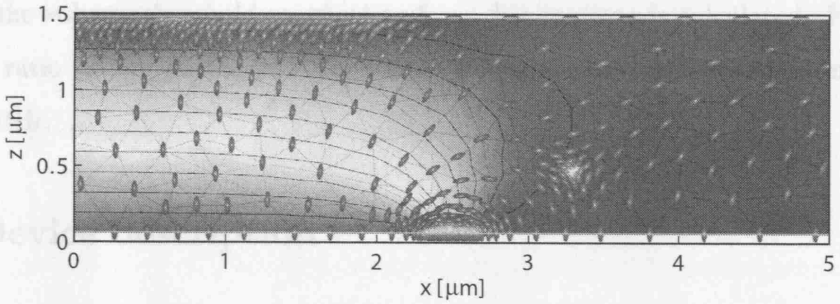

Figure 12-3: Steady state ($\sim$ 10 ms) director and potential fields arising from ON-OFF pixels in a HAN cell

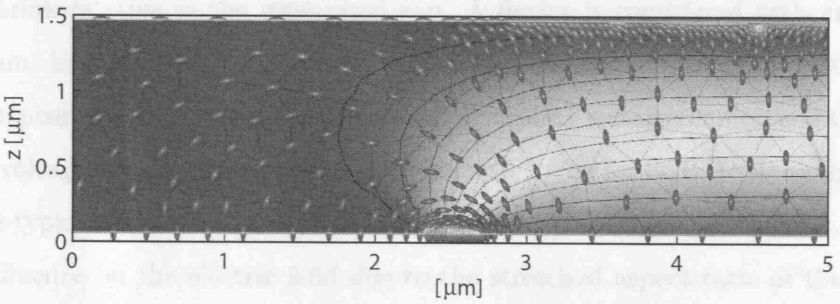

Figure 12-4: Steady state director and potential fields arising from OFF-ON pixels in a HAN cell. $-1/2$ disclination line rises almost vertically and then creeps below the upper alignment surface in the positive x direction, settling at $x = 4.55\,\mu$m after ~ 140 ms!

it is pinned to the lower alignment layer and the $-1/2$ disclination moves upwards and to the right until the steady-state configuration plotted in the figure results.

When the order of the electrode voltages is reversed the disclination lines once again appear, but the $-1/2$ disclination ascends almost vertically until it reaches the upper alignment layer. It then moves slowly beneath the upper alignment layer in the positive x direction, due to the (small) horizontal component of the applied field. After ~ 140 ms the steady-state director field shown in Fig. 12-4 is obtained.

In summary, with a material of positive dielectric anisotropy and with homeotropic anchoring on the lower alignment surfaces the large electric field in the inter-pixel gap is capable of inducing disclinations.

For a negative dielectric anisotropy material and with homeotropic alignment on both alignment surfaces the director field is found to behave quite similarly to the planar cell before (with a positive $\Delta\varepsilon$); the director field is continuous in the inter-pixel gap and with a set of OFF-ON-OFF pixels a bend-splay wall forms above the ON electrode.

In the following sections the reorientation and dynamics of the LC are studied in more

detail and the voltage threshold required to form disclinations is calculated. Furthermore, the aspect ratio of the device is stretched so that the cell thickness is in excess of the electrode pitch.

12.4 Device description

A periodic structure with two in-plane electrodes form the modelling window, which has a period of 1.1 µm and height of 1.5 µm. As the device dimensions diminish the pixel size begins to shrink relative to the inter-pixel gap. A device is considered with an inter-pixel gap of 0.4 µm, in excess of the electrode width of 0.15 µm (a pixel pitch of 0.55 µm). A narrow inter-pixel gap is problematic as even small applied voltages can exceed the dielectric breakdown voltage of either the liquid crystal ($20-40\,\mathrm{V/\mu m}$ for 5CB [158]) or the alignment layers. As is typical of LCOS devices an upper electrode is included which here, if grounded, has little influence on the electric field due to the stretched aspect ratio of the device and can be neglected. However, when a bias voltage is applied to the upper electrode it provides a means to control the tilt of the liquid crystal.

Strong anchoring is assumed, although in reality high fields can break the surface alignment [159] and non-slip boundary conditions are applied for the velocity. Unless otherwise stated a temperature of $(T-T^*) = -2\,\mathrm{K}$ is assumed. Ideally a device is required that works at room temperature (i.e. $(T-T^*) \approx -8\,\mathrm{K}$), however, Landau theory is only valid close to the nematic-isotropic transition. Furthermore, at such low temperatures order parameter changes occur on small length scales near the disclination core in comparison to the container size. This difference in length scales can pose a problem for numerical methods.

Using the finite element method it is possible to concentrate the mesh density about the disclination core, yet elsewhere use a coarser mesh. Even at $(T-T^*) = -2\,\mathrm{K}$ the difference in length scales is large and an adaptation ratio (the ratio of the longest to shortest triangle edge) of $1:100$ is required, which in itself is no problem, provided the disclinations are well isolated. In this device large changes in orientation occur near the electrodes and the mesh can require many elements. To follow the trajectory of disclinations, an adaptive meshing scheme is used with nodes distributed every 1 nm near the disclination core and every 100 nm in the coarsest regions. Such a fine discretisation is required to accurately determine disclination formation thresholds and gives rise to approximately 5000 (second

order) elements.

12.5 Homeotropic alignment - Statics

Homeotropic alignment is applied on the upper and lower alignment surfaces. In order to introduce some bias the surface molecules are oriented at 1° to the surface normal. Initially, when a voltage is applied, the molecules at the midpoint between the two electrodes tend to remain vertical, whilst those in the surrounding regions reorient towards the horizontal. For low applied voltages the vertical region persists and all changes in orientation are limited to a layer above the lower alignment layer.

Increasing the applied voltage further causes the order parameter to drop in this inter-electrode region as the liquid crystal becomes increasingly biaxial. Above a specific value of applied voltage ($\pm 5.6\,\mathrm{V}$ for $(T - T^*) = -2\,\mathrm{K}$) there is an exchange of eigenvalues of the Q-tensor, giving rise to $\pm 1/2$ disclination pairs, as sketched in Fig. 12-5.

Throughout this section this value of voltage will be referred to as the disclination formation threshold and should not be confused with the *Fréedericksz threshold.* A large disclination formation threshold is problematic for several reasons; the large electric field can cause significant drift of ionic impurities in a cycle of the applied voltage waveform, conduction may occur along the alignment layers or dielectric breakdown may occur. Fortunately, the applied voltage need only exceed the disclination formation threshold for a short time ($\sim 20\,\mu\mathrm{s}$ for an applied voltage of $\pm 5.6\,\mathrm{V}$) to induce disclination formation, after which a much reduced voltage is capable of separating the disclinations.

This 'order melting' has been seen observed experimentally in the π cell. The π cell has two topologically distinct states, called the vertical and horizontal states. Switching between the two states is normally achieved through the process of domain growth. In [16] switching from the horizontal to vertical state is achieved through an intermediate locally biaxial state by applying a large voltage.

The applied voltage favours horizontal alignment between the disclination pairs and encourages their separation. The $+1/2$ disclinations move downwards until they reach the lower alignment layer and the $-1/2$ disclinations rise, giving rise to the director profile shown in Fig. 12-6 (a) at steady-state. Fig. 12-6 (b) shows the variation in the order parameter at steady-state, where the drops in order associated with the $\pm 1/2$ disclinations

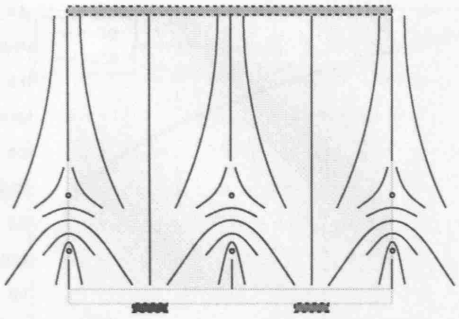

Figure 12-5: Sketch of disclination positions after a voltage is applied. Lines represent director streamlines

are visible at $(x, y) = (0.55, 0.47)$ and $(0.55, 0.02)\,\mu$m, as is the increase in order directly above the electrode edges due to the high electric field. Above the lower alignment layer the liquid crystal is strongly biaxial.

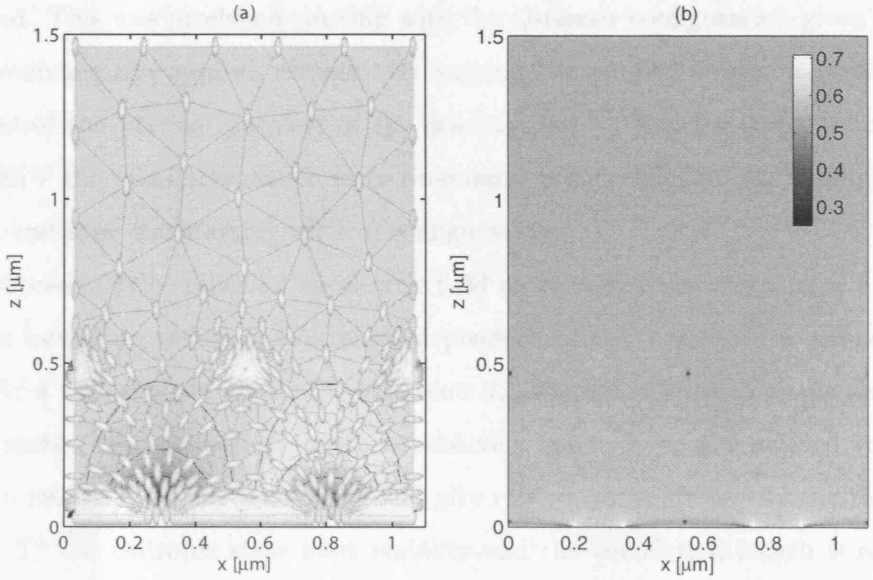

Figure 12-6: (a) Director plot for the homeotropic cell with ± 5.6 V applied. The background colour represents the potential. (b) Plot of the order parameter at steady state ($S_0 = 0.535$).

A parallel can be drawn with growth of horizontal (H) and vertical (V) domains seen in the π cell, which are topologically distinct states and are separated by disclinations lines. In a π cell there is a constant electric field and the disclination velocity is proportional to the applied voltage [122]. However, the use of in-plane electrodes gives rise to an electric field that diminishes with distance within the LC layer, thus the disclinations separate until the force exerted by the electric field matches the elastic attractive forces.

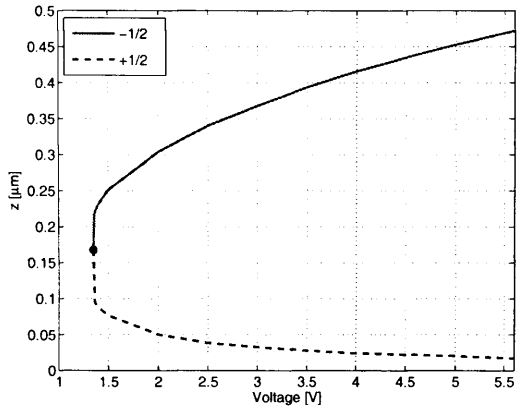

Figure 12-7: Steady-state vertical position of $-1/2$ disclination vs. voltage, as the applied voltage is reduced from ± 5.6 V. Almost temperature invariant, but for the weak dependence of the permittivity on the order parameter

Fig. 12-7 shows the steady-state position of the $\pm 1/2$ disclinations as the applied voltage is varied. This was produced starting with the Q-tensor configuration given by ± 5.6 V and then reducing the applied voltage. By varying the applied field it is possible therefore to control the vertical position of the disclinations. When the applied voltage falls below ± 1.35 V the attractive elastic force overcomes the electric and the disclination lines annihilate, restoring the starting vertical configuration.

The proposed device relies on an electric field to form disclinations and as a result the disclination formation threshold is strongly dependent on the temperature, as shown in Fig 12-8 (a). At a temperature above T^* and below T_c, where both the isotropic and nematic states are stable, the correlation length is relatively large. Even low applied voltages are sufficient to reduce the order parameter and give rise to disclinations. As the temperature falls below T^* the isotropic state loses stability and the correlation length is reduced. A higher voltage is required to reduce the order and induce disclination formation.

For a device that relies on electrically induced disclination formation to be realisable either the temperature needs to be maintained close to T^* (although this has a detrimental effect on the birefringence), or a LC is required with large elastic constants and dielectric anisotropy (giving a larger correlation length). For 5CB both the elastic constants and the dielectric anisotropy are small compared to more recently developed LCs and both of these factors contribute to the high disclination formation threshold.

Fig 12-8 (b) shows the disclination formation threshold as the pixel pitch is varied for two different temperatures. In fact, to produce this plot the width of the structure was

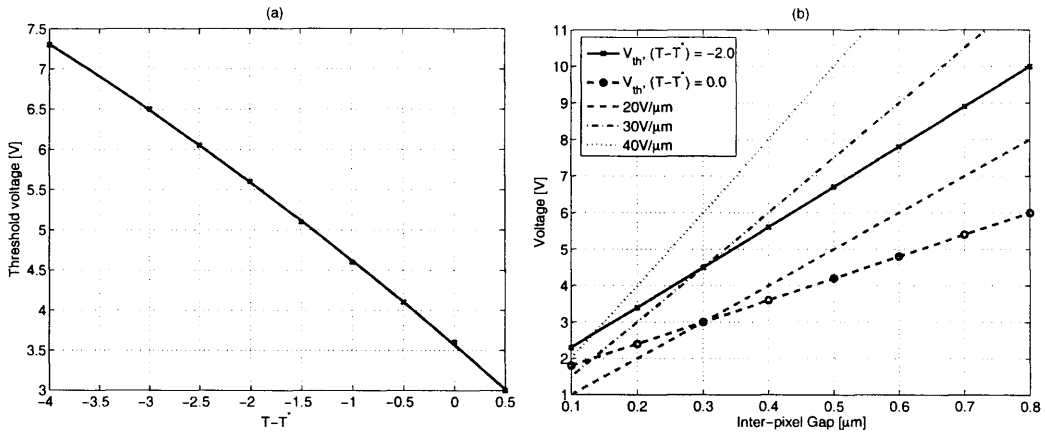

Figure 12-8: Disclination formation threshold in the homeotropically aligned cell as a function of (a) $(T - T^*)$ and (b) pixel pitch.

scaled and thus the threshold is found to depend linearly on the pixel pitch. Also plotted are lines of constant electric field strength, to give an indication of the dielectric breakdown voltage.

For the two temperatures plotted here the electric field required to induce disclination formation decreases as the pixel pitch increases, which improves the feasibility of operation over a wider temperature range for large devices. Next we consider what happens to the position of the disclinations when the pixel pitch is changed. Provided the disclinations have formed, the behaviour of the device depends only on the aspect ratio of the device, not the physical dimensions. The dimensions merely influence the switching speed. Therefore, if the device size is increased by a factor of two, then the $-1/2$ disclinations will move twice the distance with the same applied voltage.

By varying the bias applied to the upper electrode it is possible to control the lateral separation of the $-1/2$ disclinations. With a bias voltage of $5.6V$ applied, the $-1/2$ lines are $\sim 0.2\,\mu\mathrm{m}$ apart.

The same steady state director configuration, as shown in Fig. 12-9, is given by applying this voltage bias from the start of switching or at any time during the switching cycle.

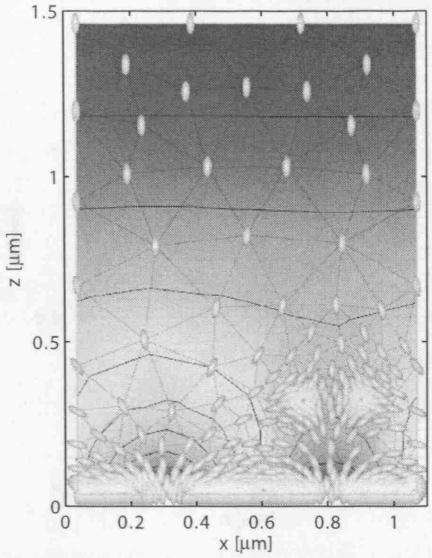

Figure 12-9: Director configuration with homeotropic alignment with ±5.6 V applied with a bias of 5.6 V applied to the upper electrode

12.6 Homeotropic alignment - dynamics and flow

In conventional twisted cells the effect of flow is most evident when a holding voltage is removed, whereby the director can over-tilt before relaxing to a homogeneous state at an accelerated rate (this is known as backflow). With a positive dielectric anisotropy LC and homeotropic alignment backflow is not observed, but the flow accelerates the reorientation of the liquid crystal. Due to the large electric field in the inter-pixel gap it is expected that the electric field driven flow should strongly influence the dynamics.

Fig. 12-10 shows the flow field after applying ±5.6 V for 0.1 ms. At this time the +1/2 disclinations are already stationary above the lower alignment layer and have little influence on the flow field. The −1/2 disclinations continue to rise and the flow field near each disclination is in the positive z-direction and serves to further increase the disclination velocity.

Fig. 12-11 (a) shows the position of the disclinations when a voltage of ±5.6 V is applied, both with and without flow. The flow causes disclination formation to occur 6 µs earlier and accelerates the separation. Both with and without flow the disclinations reach the same steady-state position of $z = 0.47\,\mu\text{m}$ after ~ 2 ms. Fig. 12-11 (b) shows the disclination trajectories when the applied voltage is removed. Confinement alters the

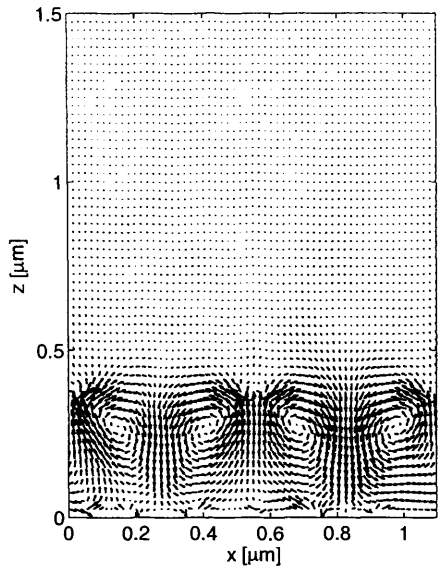

Figure 12-10: Flow field after applying $\pm 5.6\,\mathrm{V}$ for 0.1 ms. Maximum magnitude of the flow is $2.2 \cdot 10^{-4}\mathrm{ms}^{-1}$

behaviour in comparison to the study of isolated disclination pairs [28, 101]. When the voltage is removed, contrary to the behaviour shown by the isolated disclinations, the speed of the $+1/2$ disclinations are not the same as the $-1/2$ disclinations when flow is neglected. The elastic distortion at the alignment layer expels the $+1/2$ disclinations away rapidly. As seen during disclination pair annihilation, flow field preferentially accelerates the $+1/2$ disclination.

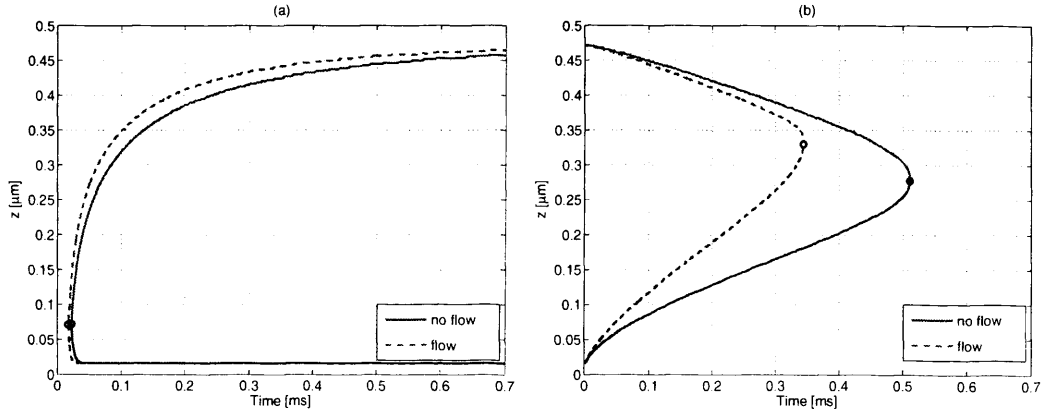

Figure 12-11: Defect trajectory during (a) switching with an applied voltage of $\pm 5.6\,\mathrm{V}$ and (b) relaxation with and without flow

The position where the disclinations annihilate differs to that shown earlier in Fig. 12-7, where the applied voltage was slowly reduced. There the applied voltage pinned the

$+1/2$ disclinations near the alignment layer, whilst the $-1/2$ disclinations descended. If the same voltage is applied to the in-plane electrodes this relaxation process can be further accelerated.

12.7 Planar alignment

The device, as proposed, is of limited practical application; the lower switched region occupies a small proportion of the device and the upper region is almost completely vertically aligned. Does a planar alignment provide more useful results? Directors are aligned in the x-direction with no pre-tilt.

When a voltage is applied, the directors in the inter-pixel gap already lie parallel to the electric field lines and experience little torque. Therefore little reorientation of the LC occurs here. Reorientation of the LC is most prominent above the centre of each electrode. The fringing fields give rise to bend-splay wall $\sim 40\,\text{nm}$ tall in this region. Within a few microseconds the bend-splay wall is compressed by the electric field giving rise to a pair of $\pm 1/2$ disclination lines. This transformation from walls to lines is known as 'pincement'. This process is much faster than the transformation from a bend-splay to a twist wall as was seen in Fig. 12-2).

Due to the narrow electrode widths the potential falls off very rapidly above the electrodes. In fact the electric field is higher here than at the midpoint between the two electrodes and therefore a lower disclination formation threshold of $\pm 3.7\,\text{V}$ is required to give rise to disclinations. The $+1/2$ disclinations are spread along the alignment layer above the electrodes and the $-1/2$ disclinations move upwards, resulting in the director configuration shown in Fig. 12-12(a) at steady-state. In the bulk of the device a planar alignment persists, but the thickness of the bulk (referring to the LC above the disclinations) can be controlled by the applied voltage. Introduction of a small pre-tilt was found to have a minor influence on the resulting director field.

Fig. 12-12(b) shows the steady state director field when a bias voltage of 5.6 V is applied to the upper electrode. The same field is obtained with the initial conditions shown in Fig. 12-12(b) or with a homogeneous planar configuration. The disclinations form above the centre of the electrodes, but the left one rises higher and faster then the right. It moves beyond the left hand edge of the modelling window and wraps around to the right, due to

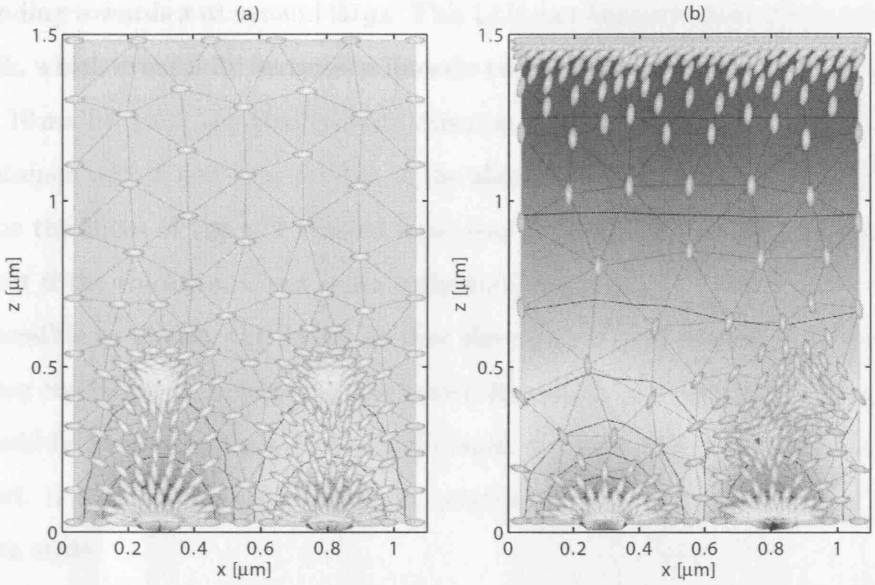

Figure 12-12: Director configuration with planar alignment with ±5.6 V applied. (Takes ~ 2 ms to reach steady-state). (a) with 0 V and (b) with 5.6 V applied to the upper electrode

the periodic boundary condition. Finally the disclination descends until the steady state field plotted in the figure is obtained.

12.8 Alignment along the electrode-edge

With an in-plane alignment, the direction of rubbing is usually at some small angle to electrode edge, ensuring consistent reorientation of the LC. For the purposes of simulation this angle is chosen as 5° (relative to y). The pre-tilt is assumed to be zero. Even low applied voltages (below the disclination formation threshold) are sufficient to rapidly rotate the molecules by almost $\pi/2$ near the lower alignment layer, giving rise to an almost planar alignment (along x) in this region. Reorientation proceeds into the bulk giving rise to a twisted state. By changing the applied voltage the amount of twist can be controlled.

A twist wall forms above each electrode, much like the bend-splay wall seen in Fig 12-2. If the applied voltage is above a disclination formation threshold (±4.2 V) then the twist wall is compressed and gives rise to $\pm 1/2$ disclination lines after a few microseconds. The $+1/2$ disclination lines smear along the alignment layer above the electrodes. The $-1/2$ disclination lines are in fact twist disclinations, which transform into standard disclination lines as they rise under the influence of the electric field. As they rise the layer beneath

twists, tending towards x at around 20 µs. This LC layer beneath them induces reorientation in the bulk, which eventually becomes a linearly twisted layer, but this process is a slow one, taking $\sim$ 10 ms to reach the steady-state director field shown in Fig. 12-13(a). A similar field is obtained with a non-zero pre-tilt at the alignment surfaces. By changing the applied voltage the thickness of the $\pi/2$ twisted layer can be controlled, which could give rise to a useful effect if the thickness is not quite sufficient for guiding.

It is possible to modify the device so that the director field is twisted in the OFF state by changing the rubbing direction of the upper alignment layer only to be along $\hat{x}$. Such a device would be twisted in the off-state and planar in the on-state. Assuming the polarisers are crossed, it is advantageous to use the original in-plane configuration as this gives a better dark state.

Scaling the width of the structure has much the same effect as seen with homeotropic alignment; the disclination formation threshold increases, and the $-1/2$ lines rise to a greater height.

Fig. 12-13(b) shows the director field when a bias voltage of 5.6 V is applied to the upper electrode starting with a homogeneous configuration. It should be pointed out that this field is not obtained using the initial configuration shown in Fig. 12-13(a). Disclinations form as was found before, but the bias voltage causes the left-hand $-1/2$ disclination to rise faster than the right-hand one. The left-hand disclination remains a twist disclination and rises to the upper alignment layer after 1 ms, whereas the right-hand one transforms into the standard (bend-splay) type and settles at $z = 0.2\,\mu$m. Above the right-hand disclination a twist wall forms. It is possible to control the disclination position and the height of the twist wall with a suitable choice of electrode voltages. Such rapid periodic changes in the director field, which can be controlled electrically are of potential interest for photonics applications.

This twist wall is found to form only for low values of pre-tilt at the alignment surfaces. Pre-tilts greater than 0.5° were found to give rise to director fields restricted to lie in the xz plane in the bulk. A low pre-tilt can be achieved using photoalignment; certain materials exhibit an easy direction when illuminated by polarised ultraviolet light. Rubbing is another technique to achieve alignment, but the value of pre-tilt tends to be higher. In conventional cells this pre-tilt is desirable as it prevents the formation of walls and disclinations, however in this device these are the things we wish to promote and control. If a high pre-tilt is unavoidable then using parallel rubbing to give a π cell with the same in-plane electrodes

allows the formation of walls.

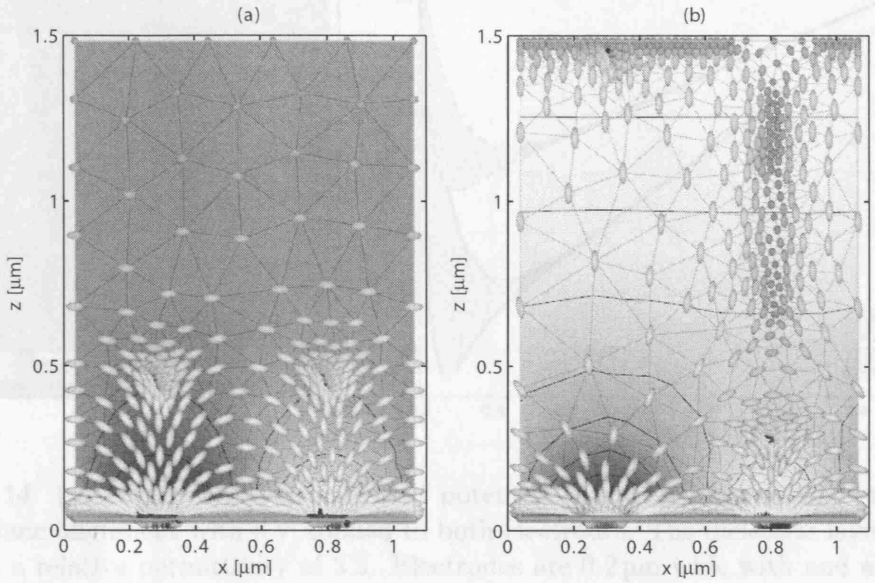

Figure 12-13: Director configuration with IPS alignment with an applied voltage of ±5.6 V. (Takes ∼ 10 ms to reach steady-state) (a) 0 V and (b) 5.6 V applied to the upper electrode

The manufacture of interdigitated electrodes at these length scales is difficult, but a similar switching mechanism can be achieved using a fringing-field style device, as shown in Fig. 12-14. Here, the same potential is applied to the in-plane electrodes which are positioned above a dielectric layer and a ground plane. In such a device short-circuits are much less likely to occur and manufacture is much simpler compared to the interdigitated electrodes of IPS cells.

The upper ground electrode has been omitted and a Neumann boundary condition for the potential is applied in its place. Were this electrode present a voltage of 3.2 V should be applied to limit tilting of the director. To achieve significant reorientation of the LC a thin dielectric layer is required. Consequently even a low applied voltage can exceed dielectric breakdown. A voltage in excess of this breakdown voltage is required to give rise to disclinations. It has been suggested that this theory may overestimate the disclination formation threshold [16]. Therefore, by scaling the structure and with a suitable choice of electrode pitch and width that disclination formation may be possible in practice. For now, however, the disclination free state is considered.

Fig. 12-14 (b) shows the resulting twist though the device for two different applied voltages. Laterally there is a variation in twist taking a maximum value near the electrode

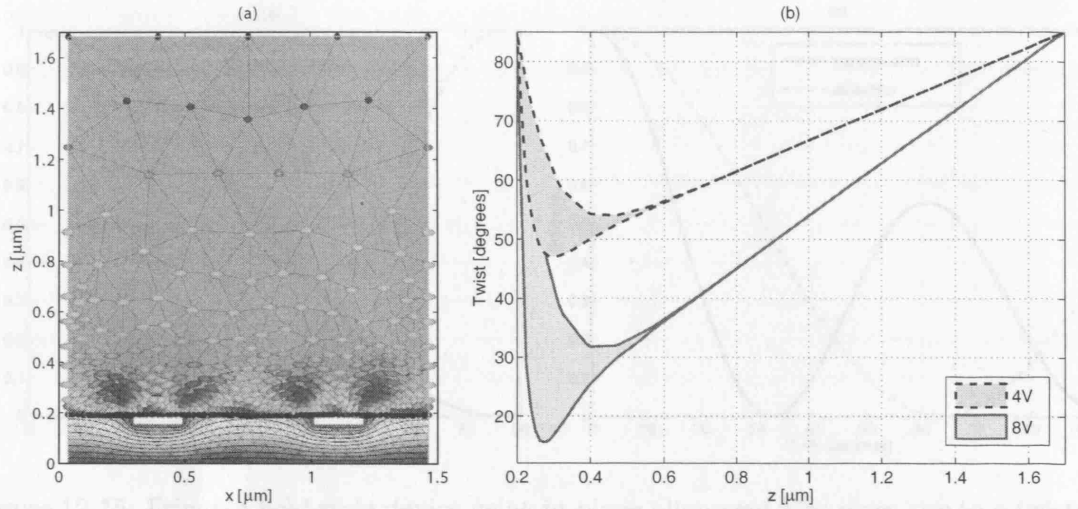

Figure 12-14: (a) Steady state director and potential field in a fringing field style device using in-plane alignment with 8 V applied to both electrodes. The dielectric layer is 0.2 µm thick with a relative permittivity of 3.5. Electrodes are 0.2 µm wide with and a separated by and inter-pixel gap of 0.55 µm. (b) Twist variation through the LC layer. The filled region represents the maximum and minimum lateral variation in twist.

edge and a minimum between the two electrodes. The filled region in the plot indicates the extent of this twist variation for each applied voltage. From $z = 0.6\,\mu\text{m}$ to $z = 1.7\,\mu\text{m}$ the twist variation can be assumed as linear.

It is possible to increase the amount of switching for a given voltage by scaling the device horizontally. This, however, reduces the thickness of the linear twisted region and increases the lateral twist variation.

What are the possible applications for such a device? For display applications a switchable linearly twisted stack is desirable as purely a guiding effect can be used for operation instead of the birefringence effect normally used in planar or IPS cells. As a result the operation would be independent of the wavelength of light, provided that the LC is sufficiently thick. Furthermore, there is little tilting of the director and so a high viewing angle is achieved [160].

Another possible application is as a transflective display. Some transflective pixels are designed to operate in both reflective and transmission simultaneously. Normally the pixel will be divided in two parts, one half optimised for reflection, the other for transmission. Such a design is complicated from a manufacturing point of view.

A device that can be used in the two modes individually would also be desirable. Is it

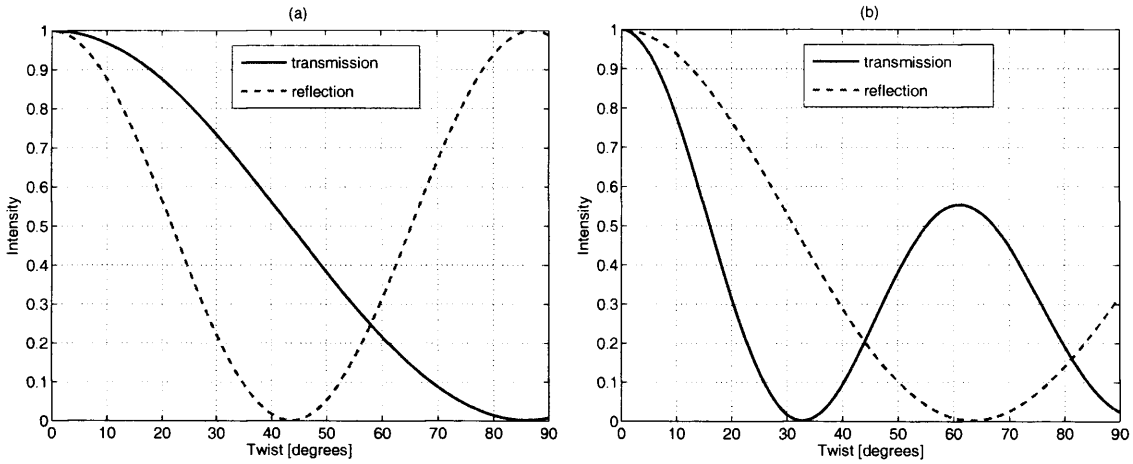

Figure 12-15: Fringing field style device using in-plane alignment also gives rise to a twisted state. (a) Polariser(s) oriented at 45° to the rubbing direction. Mixed mode; birefringence and guiding: $\Delta nd/\lambda = 2.25 + m/2$, where $m \in \mathbb{N}$ (a value of $\Delta nd/\lambda = 5.25$ has been plotted here, 0.63 is the minimum possible value) (b) Polariser(s) oriented along rubbing direction. Partial Guiding $\Delta nd/\lambda = 0.365$

possible to use an LC layer with a variable twist in such a way? Fig. 12-15 shows the optical transmission and reflectance for an LC layer as the total twist is varied. In transmission it is assumed that there is an additional polariser present between the backlight and the reflector that is aligned parallel to the analyser. Two feasible optical configurations are simulated that provide both dark and light states in transmission and reflection; (a) with the polarisers aligned at 45° to surface alignment and (b) with the polarisers parallel to the alignment. For (a) the mode of operation depends on a birefringence and a guiding effect, therefore there are several possible cell thickness that can be used. When the cell is very thin the guiding effect is only partial and so the optimum cell thickness differs somewhat from $\Delta nd/\lambda = 1/4 + m/2$. For (b) partial guiding is the sole mechanism. There is a single optimum LC layer thickness; $\Delta nd/\lambda = 0.365$. Using both configuration (a) and (b) it is possible to obtain both light and dark states in reflection and transmission. The IPS mode of this device is capable of acting as a transflective display.

Both configurations have their advantages and disadvantages. In reflection the twist needs to be controlled between zero and 43° degrees to achieve both light and dark states for (a). In transmission a twist of 86° is required. A lower voltage is required to obtain the 43° twist needed for reflection and it is desirable that this is the low-power mode. Conversely in configuration (b) more twist is required in the reflective mode. Despite this the maximum

twist need never exceed 63° for both modes of operation.

The results presented here are for a normally white mode. In practice the normally black mode is desirable as a better contrast ratio is achievable. To operate in this mode a QWP must be included in the device design and the polariser angles and the optical path length will need to be optimised for this configuration.

12.9 HAN alignment

Two possible HAN configurations with different surface alignments near the interdigitated electrodes have been investigated. If horizontal alignment is chosen near these electrodes switching proceeds much as it did for the planar cell, as shown in Fig. 12-12. Disclination lines form above the centre of each electrode and the $-1/2$ lines move upwards. There is some lateral movement of these disclinations, due to the vertical change in the tilt throughout the structure, but this movement ceases when they are positioned above the electrode edge. The bulk arrangement of molecules remains in the HAN state.

A more interesting device results with vertical alignment next to the interdigitated electrodes. If the applied voltage is below the disclination formation threshold of $\pm 5.6\,\mathrm{V}$, switching is confined to a small region above the lower alignment layer. For voltages above this, disclinations form at the same positions as the homeotropic cell, above the mid-point between the two electrodes. The $-1/2$ disclinations not only move upwards but move laterally too due to the elastic force from the upper alignment layer. Furthermore, the horizontal component of the flow accelerates this lateral motion. As the disclinations continue to rise they also rotate until the situation shown in Fig. 12-16 is reached after $\sim 15\,\mathrm{ms}$. It takes longer to reach steady state than the homeotropic cell as reorientation is driven by the elastic force from the bulk, whereas reorientation was previously only electrically driven. Switching from a HAN to a planar state has occurred in the bulk.

If the applied voltage is then reduced to $\pm 0.8\,\mathrm{V}$, the $+1/2$ disclination lines are expelled upwards from the lower alignment layer and the $-1/2$ lines move downwards. The applied voltage inhibits lateral movement of the disclinations, preventing annihilation, giving rise to the steady-state director profile shown in Fig. 12-17, where the planar aligned region occupies a larger proportion of the cell.

The thickness of the planar region can be controlled by the applied voltage, suggesting

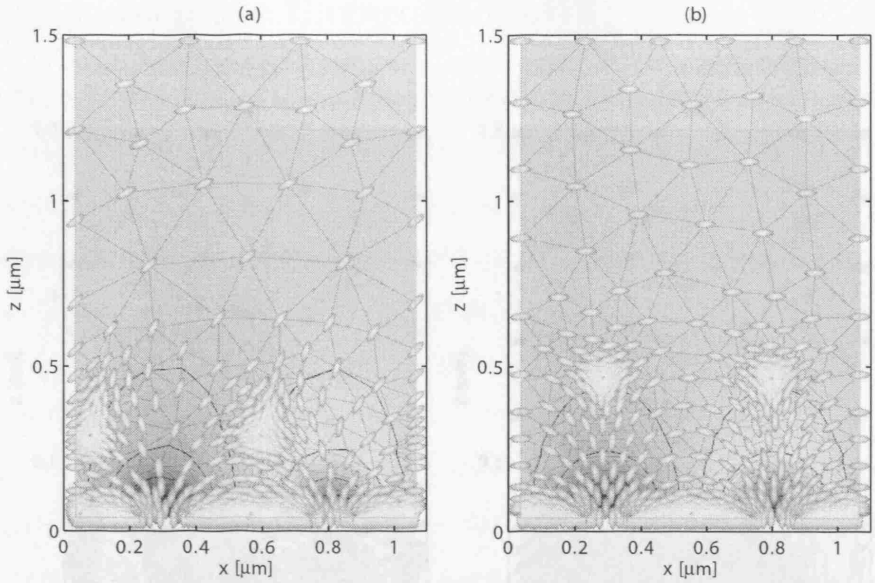

Figure 12-16: Director plot for HAN configuration with homeotropic anchoring on the lower alignment layer, $\pm 5.6\,\mathrm{V}$ applied. (a) shows the director after $50\,\mu\mathrm{s}$ and (b) steady-state reached after $\sim 15\,\mu\mathrm{s}$

a possible application as a variable wave plate.

Fig. 12-18 shows the transmittance of the cell with $\pm 0.8\,\mathrm{V}$ applied calculated using the Jones matrix method and the RGM, which takes into account diffractive effects. The structure is approximately two wavelengths across and so diffractive and refractive effects are expected, and the transmittance is highly sensitive to changes in the wavelength. The transmittance calculated using the GM shows significant guiding.

When the applied voltage is reduced to $\pm 0.7\,\mathrm{V}$ the $\pm 1/2$ lines move until they are almost at the same vertical position and then move laterally before finally annihilating. Previously, with in-plane or homeotropic alignment, a higher voltage was found necessary to prevent annihilation because the $+1/2$ and $-1/2$ lines were in closer proximity.

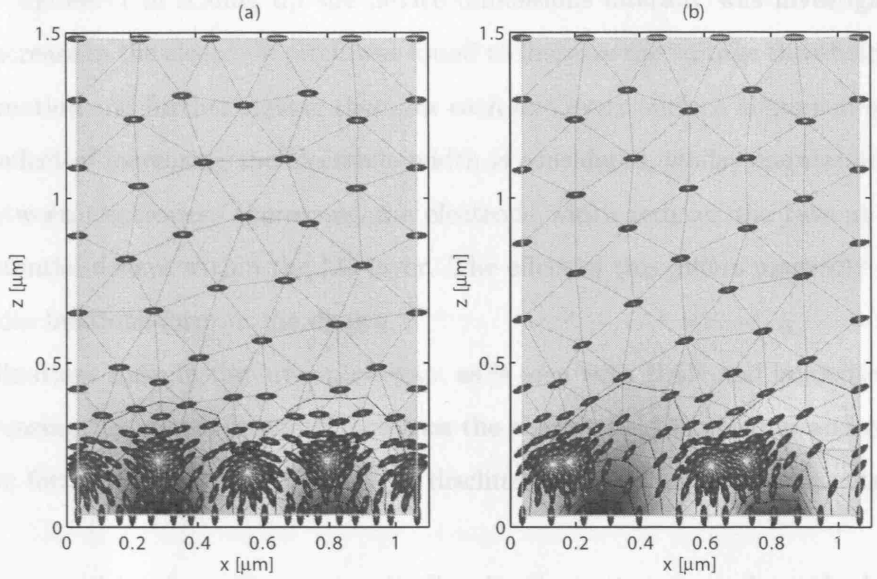

Figure 12-17: Steady-state director plot for HAN configuration with homeotropic anchoring on the lower alignment layer when the applied potential is reduced to (a) $\pm 0.8\,\mathrm{V}$ for $\sim 3\,\mathrm{ms}$ and then again to (b) $\pm 0.7\,\mathrm{V}$, where the director field is shown just prior to annihilation

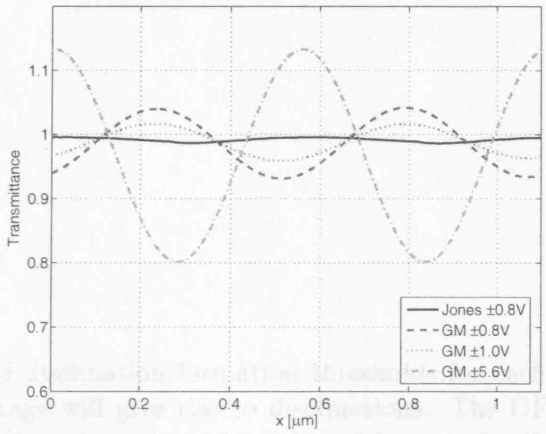

Figure 12-18: Transmittance (one pass) with $\pm 0.8\,\mathrm{V}$ applied calculated using the Jones and Grating methods. Polarisers are ideal and are crossed at $\pm 45°$ to the optic axis. The wavelength is set as $\lambda = 0.55\,\mu\mathrm{m}$

12.10 Increasing the Electrode Width

Previously the effect of scaling up the device dimensions laterally was investigated. This effective increase in the electrode pitch was found to increase the voltage threshold for disclination formation and further elevate them for each and every surface alignment considered. Here, the effect of increasing the electrode width is considered, whilst maintaining the separation between electrodes. Increasing the electrode width reduces the rate at which the electric potential decays within the LC layer. The effect of this differs markedly depending on where disclinations form in the device.

If disclinations form in the inter-pixel gap, as is seen with HAN and homeotropic alignment, increasing the electrode width increases the electric field in the gap and reduces the disclination formation threshold. The $-1/2$ disclinations once formed will rise to a greater height.

For planar and in-plane alignments, disclination formation stems from the LC directly above the electrode centre, induced by the rapid fall-off in voltage. Increasing the electrode width will reduce the electric field above the electrodes, increasing the disclination formation threshold. However, the $-1/2$ disclinations once formed will rise to a greater height for a given voltage.

Table 12.1: Summary of disclination formation thresholds for each alignment type at $T - T^* = 2\,\mathrm{K}$. The ON voltage will give rise to disclinations. The OFF voltage will hold the disclinations. Reducing the voltage from this value with cause the disclinations to annihilate.

Alignment	V_{th} ON	V_{th} OFF
Homeotropic	5.6V	1.35V
Planar	3.7V	1.3V
In-plane	4.2V	1.3V
HAN	5.6V	0.8V

12.11 Conclusions

Two devices have been demonstrated which effectively allow the surface alignment to be electrically switched by in-plane electrodes. The first of these devices uses an in-plane alignment and the off-state is planar. For low voltages the amount of twist in the structure can be controlled by changing the applied voltage. For higher voltages, disclinations are induced and the applied voltage controls the thickness of a $\pi/2$ twisted layer. A simpler design from a manufacturing point of view, that uses fringing-fields to reorient the liquid crystal, is capable of operating in the same way. These devices rely on a stretched aspect ratio, and so long as this is maintained, the results hold true for even large device designs.

The second device is a HAN cell, with homeotropic alignment above interdigitated electrodes. Applying a sufficiently high voltage gives rise to disclinations that support a planar bulk state. The magnitude of the applied voltage controls the thickness of this planar region. Possible applications for these devices are as transflective pixels, variable wave-plates, or photonics applications.

Chapter 13

Bistability due to Electrically Induced Disclinations

13.1 Introduction

Conventional nematic liquid crystal displays have a single stable state in the absence of an applied voltage. A voltage must be applied and held to maintain the switched state, which is topologically identical to the unswitched state. Bistable devices have two stable states in the absence of an applied voltage, which are separated by an energy barrier. This barrier can be overcome by an applied voltage in excess of some threshold and power is only consumed in the transition between states. An advantage of this threshold effect is that a passive matrix addressing scheme may be used, without suffering the same resolution limit as monostable devices. Some mechanism, such as the flexo-electric effect or backflow, is often required to switch between the stable states.

Bistable devices can be formed from cholesteric, ferroelectric and nematic liquid crystals. A review of several nematic bistable devices follows; the bistable twisted nematic display, the surface controlled bistable display and finally the zenithal bistable device.

The two stable states of the bistable twisted nematic display (BTN) twist by 0 and 2π respectively [161]. Parallel rubbing is used with a high pre-tilt and a chiral dopant is added to stabilize the two states. These two states are topologically equivalent. When a voltage is applied the LC reorients vertically. If the voltage is suddenly removed then there will be backflow, giving rise to the twisted state. If the voltage is gradually reduced the flow is inhibited giving the untwisted state. The two states are only metastable however, and tend to nucleate into the topologically distinct (minimum energy) π twisted state.

Another mechanism that allows the transition between two truly stable states (not metastable) is the breaking of the surface alignment [159, 158]. Typically the two stable states are a planar and π state, which are made of near equal energy by introducing a chiral dopant. One of the alignment layers has a high anchoring coefficient and a high pre-tilt, like a conventional cell. The other is treated to give a low anchoring coefficient and no pre-tilt, so that a large voltage is able to break the surface alignment, providing a means to switch between the two stable states. Unfortunately mechanical shock can disrupt the surface alignment and cause unwanted switching between the two states.

The zenithal bistable device (ZBD) [162, 163] uses a grating surface to give bistable alignment. The surface treatment is such that the liquid crystal is homeotropic along the grating and lower alignment surface and usually the device is filled with a positive dielectric

anisotropy material. One of the stable states is free of disclination lines, with very little variation in the director field and the second has disclination lines present at the peaks and troughs of the grating surface. Above the grating the LC bends and splays strongly giving a pseudo-planar alignment [162]. Switching between the two states is achieved by exploiting the flexoelectric effect; whereby the sign of the applied voltage can be toggled to alternate between the two states. The flexoelectric effect arises due to the dipolar nature of most liquid crystals. A splay or bend distortion can create a polarisation, that acts as a macroscopic DC bias.

Factors such as the anchoring strength, the shape of the grating and the grating pitch (p) and depth (d) affect the energy of the two states. For instance if the grating depth is too small then the vertically aligned state is favoured. For both states to be stable, they should be of similar energy. In general this can be achieved using $0.3 < d/p < 1.0$ [162].

The post aligned bistable nematic (PABN) device [164] uses an array of microscopic posts (with a pitch of $\sim 1\,\mu m$) instead of a grating to stabilize two distinct states. No surface treatment is applied to the post surface, in order to give a planar degenerate anchoring. There are two stable states, a planar and a tilted state, referring to the director orientation on the sides of the posts. The PABN device, like the ZBD, relies on the flexoelectric effect to switch between the stable states. Two further examples of bistable devices can be found in [165, 166].

In this chapter a new mechanism to switch between stable states in a nematic liquid crystal is investigated that uses electrically induced disclinations to change the effective alignment on a grating surface.

13.2 Device description

The device is based on a ZBD, but instead of having a continuous electrode below the lower alignment layer, in-plane electrodes are used. Homeotropic alignment is applied on the lower alignment and grating surfaces, giving two stable states. At the lower alignment layer a pre-tilt of 1° relative to the surface normal is used to introduce some bias into the simulations. The first of the stable states is free of disclination lines, where the molecules lie almost vertically through the whole device. The second state has $+1/2$ disclination lines present at the peaks of the grating and $-1/2$ disclination lines at the troughs, giving rise

to a pseudo planar alignment directly below the grating and a HAN state in the bulk, as sketched in Fig. 13-1.

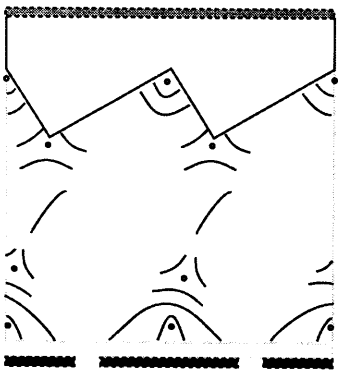

Figure 13-1: Sketch of disclination positions in the stable HAN state with an applied voltage across in-plane electrodes.

In the ZBD the flexoelectric effect was needed to switch between these two stable states. Here we wish to achieve this switching using in-plane fields instead. The most important factor is the choice of a positive or a negative dielectric anisotropy liquid crystal. A bidirectional transition between the two states has so far proved elusive with a positive dielectric anisotropy material (although some preliminary results will be discussed). Thus, a negative dielectric anisotropy is chosen. A disadvantage of this choice is that the magnitude of $\Delta\varepsilon$ tends to be lower for negative than positive dielectric anisotropy materials. For example one such material, Mercks MLC-2039, has a $\Delta\varepsilon$ of -4.1 [167]. Such low values would make the formation of electrically induced disclinations difficult. Fortunately, with the increasing popularity of the VA mode for TV applications, which depend on such materials to deliver high contrast ratios, the development of new materials with strongly negative values of $\Delta\varepsilon$ is an active area of research. It has been suggested that value of $\Delta\varepsilon = -9$ may be obtainable [168].

The modelling window, as sketched in Fig. 13-1, has a 2 µm period and the LC layer is 0.75 µm thick. In-plane electrodes with a pitch of 1 µm and a width of 0.82 µm are positioned below the lower alignment layer with an inter-pixel gap of 0.18 µm. Such a large electrode width is chosen to make the electric field extend to the peak of the grating. The electrodes are laterally offset relative to the grating, with the low voltage electrode centred at $x = 1.06\,\mu\text{m}$. The reason for doing so is best explained after some results have been presented. A 0.7 µm thick dielectric layer is introduced between the grating and the upper

ground electrode to reduce the influence of the upper ground electrode on the electric field when a potential difference is applied across the in-plane electrodes.

The grating is 0.3 µm deep with a period of 1 µm. This gives a d/p of 0.3 which according to [162] is at the lower limit for providing bistable switching. It would be desirable to increase this ratio to move the energies of the two stable state closer, but the size of the in-plane electrodes would have to be reduced too, causing the electric field to drop off more rapidly in the LC layer. In the ZBD the grating shape can be approximated by a smoothed scalene triangle. Here, as a first attempt, an unsmoothed triangle is considered with its first trough positioned at $x = 0.23\,\mu\text{m}$. The shape of the grating will affect the energy of the two stable states, but the calculation of the optimum shape of the grating remains as future work. Strong anchoring is assumed on both the lower alignment layer and the grating, although in reality the anchoring will be weak.

Another possible alignment on the grating surface is planar degenerate anchoring, which would occur if the surface were untreated. Although molecules are free to rotate in the plane parallel to the surface with such an alignment, they tend to lie in the plane of the grooves in the absence of an electric field. Modelling with planar degenerate anchoring remains as future work.

Achieving planar alignment on the triangular grating is difficult in practice, however in theory this alignment demonstrates bistable switching.

The liquid crystal material parameters have been chosen as $K_{11} = K_{33} = 15\,\text{pN}$ and $\Delta\varepsilon = -5.5$ and values of the Landau coefficients are those of 5CB, which were defined in Section 12.2. As the size of the structure is larger than was considered in the previous chapter a higher temperature of $(T - T^*) = 0\,\text{K}$ is used, enlarging the disclination core and reducing the adaption ratio of the mesh. The transition between the stable states will be demonstrated next.

13.3 Vertical to HAN transition

Since the LC has a negative dielectric anisotropy the transition from the vertical to the HAN state is the most straightforward.

Fig. 13-2 shows this vertical state, where the directors lie nearly vertically throughout the device. Only a small drop in order parameter is seen at the peaks and troughs of the

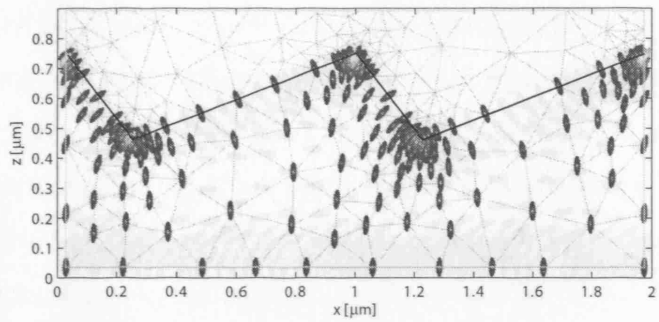

Figure 13-2: Stable vertical state

grating. Applying the same voltage to the in-plane electrodes reorients the liquid crystal in the bulk towards the horizontal. If the applied voltage is large enough the order parameter will begin to drop at the peaks of the grating. This 'order melting' gives rise to a pair of $\pm 1/2$ disclination lines which separate under the influence of the applied voltage, as shown in Fig. 13-3. Here, the flow of the liquid crystal has bee neglected, although in practice the applied voltage should be ramped to avoid possible backflow effects (the study of which remains as future work).

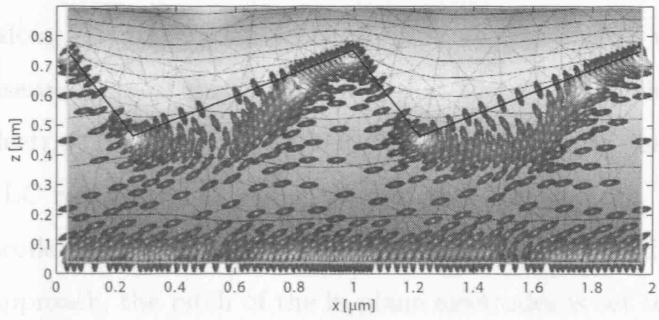

Figure 13-3: Director field after applying a voltage across the cell when in the vertical state. Disclination pairs form at the grating peaks

The $+1/2$ lines are stationary at the peaks, whilst the $-1/2$ lines move in the negative x direction along the grating surface until finally settling at the grating troughs. When the applied voltage is removed the LC relaxes to the HAN state shown in Fig. 13-4.

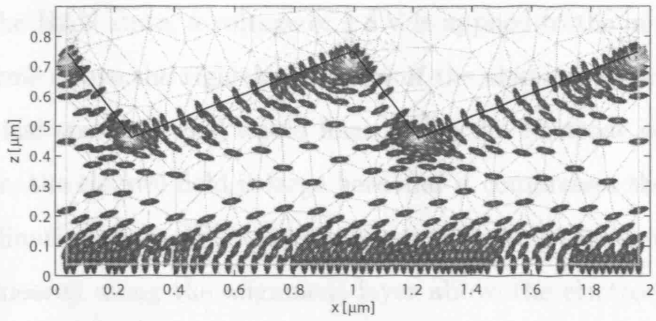

Figure 13-4: Stable HAN state

13.4 HAN to Vertical transition

To switch from the HAN to vertical state an in-plane electric field can be used without relying on the flexoelectric effect. There are two ways in which this in-plane field can be applied.

Firstly, if the electrode pitch is much larger than the grating pitch then the in-plane field in the inter-pixel gap would be large and span many periods of the grating. A large enough voltage would displace the $-1/2$ disclination lines at the grating troughs. These would then move along the grating surface and eventually annihilate with the $+1/2$ lines at the peaks. A disadvantage of this approach is that that in-plane electrodes need to be wide, so that the electric field extends sufficiently far into the LC. In the "deadspace" above the electrodes the LC remains fixed in the HAN state. Furthermore, the presence of the upper ground electrode will have a strong influence on the electric field.

In the second approach, the pitch of the in-plane electrodes is set to match that of the grating. Electrically induced disclinations are used to restore the vertical state by causing them to annihilate with the disclination lines on the grating.

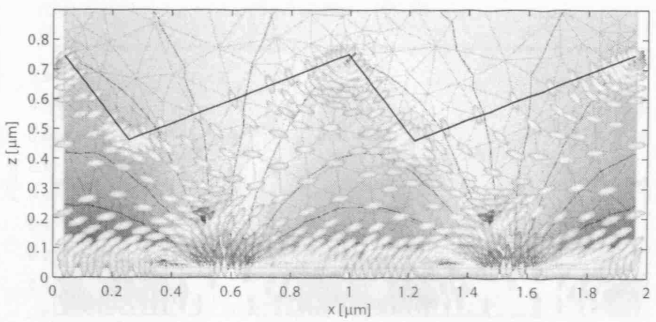

Figure 13-5: HAN state 5 µs after applying an in-plane voltage of ± 8 V

Starting with the HAN state, a voltage of $\pm 8\,\mathrm{V}$ is applied to the in-plane electrodes. A bend-splay wall forms above the right hand edges of the electrodes (were an in-plane field applied to the vertical state the wall would form above the electrode centres). Relative to the electrode centre, the electric field is large here and it compresses the wall giving rise to a pair of $\pm 1/2$ disclinations lines. The $+1/2$ lines move towards the electrode centre as they descend and are smeared along the alignment layer above the electrodes, while the $-1/2$ lines rise. Fig. 13-5 shows the director field $5\,\mu\mathrm{s}$ after applying the voltage.

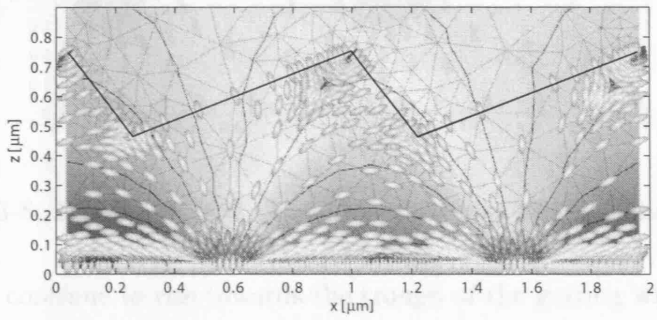

Figure 13-6: HAN state 0.2 ms after applying an in-plane voltage of $\pm 8\,\mathrm{V}$

The $-1/2$ lines move diagonally (upwards and in the positive x direction). Due to the presence of the thick dielectric layer between the ground plane and the grating the electric field extends beyond the peaks of the grating and is sufficient to elevate the $-1/2$ lines to the peaks of the grating, as shown in Fig. 13-7. An important factor in achieving this director field is the lateral displacement of the electrodes. Were the electrodes centred perfectly the horizontal component of the electric field would be low near the grating peaks, limiting the height reached by the $-1/2$ lines. To increase the horizontal component of the electric field the electrodes are displaced laterally so that the grating peaks are closer to the inter-pixel gap.

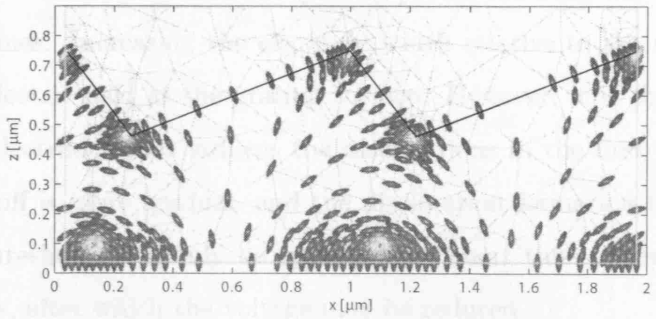

Figure 13-7: Director field $30\,\mu\mathrm{s}$ after removing the in-plane voltage

The electrically induced $-1/2$ lines annihilate with the $+1/2$ lines at the grating peak after the in-plane voltage has been applied for 0.26 ms. Fig. 13-7 shows the director field when the applied voltage is removed after this annihilation. The $+1/2$ lines are rapidly expelled from the lower alignment layer

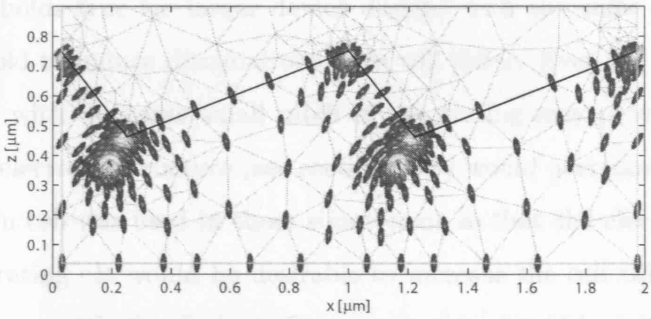

Figure 13-8: Director field 0.42 ms after removing the in-plane voltage

The $+1/2$ lines continue to rise towards the trough of the grating where the $-1/2$ lines are present, as shown in Fig. 13-8. After 0.46 ms the disclinations annihilate to restore the starting vertical state (Fig. 13-2). Switching between the two stable states has been demonstrated.

13.5 Design Considerations

A large voltage was applied as a means to prove feasibility and the actual voltage requirements for disclination formation and for separating the disclinations is yet to be determined. It is desirable to minimise the applied voltage in order to reduce the power consumption and to avoid dielectric breakdown. The device design can be optimised to meet these requirements. It is possible to alter the offset of the electrodes so that the horizontal component of the electric field is maximised near the grating peaks, reducing the voltage required to elevate the $-1/2$ lines. Increasing the electrode width relative to the inter-pixel gap will also increase the electric field at the grating surface. However, it is the electric potential fall-off above the electrodes that induces the disclinations in the first place. With wider electrodes the fall-off is more gradual, and the disclination formation threshold increases. Fortunately this threshold need only be applied for a short time (a few microseconds) to induce disclinations, after which the voltage may be reduced.

When switching from the HAN to the vertical state it may prove advantageous to apply

the same voltage to the lower electrodes before the in-plane voltage. This should shift the position where the bend splay wall forms closer to the electrode edge. Here, the electric field is higher, so a lower voltage is required to induce disclinations.

The device as proposed was made small for the convenience of modelling, but the principle of operation holds true for larger device designs with the same aspect ratio. Only the voltage threshold to induce disclinations lines will differ. Even so, the manufacture of in-plane electrodes with the same small pitch of the grating may prove difficult. Using a fringing field style electrode structure (see section 12.8) would overcome this problem.

A relatively thin cell was used in these simulations so that the electric field extends to the peaks of the grating. It would be desirable to increase the cell thickness to make the two stable states more optically distinct. Once again this should be possible by optimising the lateral offset of the electrodes.

13.6 Positive Dielectric Anisotropy Material

For a material of positive dielectric anisotropy it is the HAN to the vertical transition which is straightforward, requiring the same potential to be applied to the in-plane electrode. To move from the vertical to the HAN state an in-plane voltage can be used to give rise to $\pm 1/2$ disclination line pairs. Somehow the $-1/2$ lines need to be moved to the troughs of the grating and the $+1/2$ lines to the peaks to give the HAN state. Fig. 13-9 shows that the first step is easy enough to achieve by applying a large enough voltage to the in-plane electrodes. Here, the $-1/2$ lines are shown just before they snap to the troughs of the grating. Note that the dimensions of the structure and the electrodes differ from the previous structure. The device has a 2.2 µm period and the LC layer is 1.2 µm thick. The grating is 0.3 µm deep. In-plane electrodes with a pitch of 1.1 µm and a width of 0.3 µm are positioned below the lower alignment layer. The low voltage electrode is centred at $x = 0.48\,\mu\text{m}$.

The second step, trying to move the $+1/2$ lines to the peaks of the grating is not so easy. When the applied voltage is removed the $+1/2$ lines ascend, but are attracted to the $-1/2$ lines at the grating trough and eventually annihilate to restore the vertical state. Fig. 13-10 shows the director field just prior to this annihilation.

A means to somehow laterally separate the $+1/2$ lines from the $-1/2$ lines is required to prevent this annihilation, so that the $-1/2$ lines may ascend to the peaks of the grating.

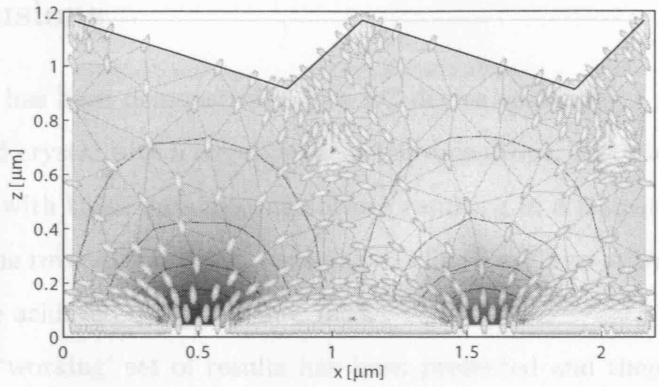

Figure 13-9: Director field 0.6 ms after applying ±6 V to the lower electrodes when in the vertical state (5CB)

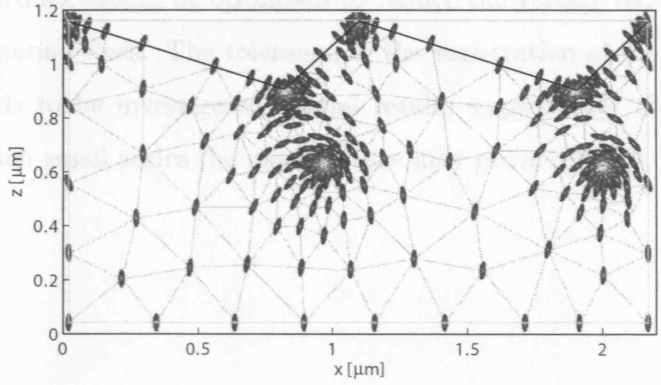

Figure 13-10: Director field 3.4 ms after removing the in-plane voltage

However, with this device design it is difficult to achieve any lateral separation of the electrically induced disclination lines using an in-plane voltage. Only with a large lateral separation would the $+1/2$ escape the range of attraction of the $-1/2$ line on the grating trough.

A possible means to increase this lateral separation would be to apply a bias to the upper electrode at the same time as the in-plane field, as was demonstrated in Fig. 12-9. The bias voltage moves the lines closer together, so a two step procedure is required. First of all a positive bias would be applied to the upper electrode, which would move one of the $-1/2$ lines to a trough. Applying a negative bias to the upper electrode would move the other line to the other trough.

13.7 Conclusions

Bistable switching has been demonstrated in a LC device containing a grating and a standard nematic liquid crystal with a negative dielectric anisotropy. Electrically induced disclinations annihilate with those on a grating surface resulting in a transition from a HAN to a vertical state. The reverse transition, inducing disclinations lines at the peaks and trough of a grating can be achieved using a planar field.

A preliminary 'working' set of results has been presented and there is a great deal of future work to be done. By shaping the grating carefully it should be possible to increase the stability of the two states, by moving their energies close together. The position and lengths of the electrodes should be optimised to reduce the voltage required to induce and separate the disclination lines. The tolerance in the registration of the grating relative to the electrodes needs to be investigated; initial results suggest that the requirements are fairly lax, yet at such small scales the manufacture may prove difficult.

Chapter 14

Conclusions

This thesis is a study of high resolution liquid crystal devices. During the course of the work models have been implemented to calculate the orientation, flow and orientational order of the liquid crystal in these devices and their optical properties have been studied.

The first part of the work detailed the development of continuum theory models for liquid crystal switching. A finite element discretisation of the Oseen-Frank free energy has been developed, with the option of using a tensor or vector representation of the liquid crystal orientation. In this formulation the order parameter is assumed constant. A finite element discretisation of the Qian-Sheng equations has also been implemented and thoroughly tested. This formulation allows for variations in the order parameter and also takes into account the flow of the liquid crystal. Adaptive meshing driven by an error estimate allows significant savings in terms of the number of degrees of freedom and a variable time step is used to model the dynamic behaviour efficiently. The implementation is able to model large containers, which can be of complex shape, whilst still resolving fine features such as disclinations. The three implementations have been compared in situations that arise in common cell types. Comparing constant order parameter implementations, a vector representation of the LC orientation was found to exhibit better (spatial) convergence than a tensor representation.

The second part of the work involved the application of these models to the study of high resolution devices. As the electrode width shrinks, so too does the inter-pixel gap. A high electric field in this gap can be problematic as ionic impurities present in a liquid crystal can drift a significant distance within a cycle of the applied voltage waveform. Even small ion concentrations can have significant influence on the electric field and director orientation in turn. To determine how ions migrate in the inter-pixel gap IPS cells have been studied both experimentally and theoretically. Ions are found to accumulate above electrode edges, hence, wide electrodes are found more resilient to the effects of ion migration.

High resolution liquid crystal devices can be configured electrically to modulate light intensity and or phase and are well suited to holographic or beam-steering applications. Fabrication of such devices is made possible by Liquid Crystal On Silicon (LCOS) technology. In this beam-steering application, an LCOS device has been shown able to provide steering in a number of directions with high efficiency. For most grating orientations the twist of the LC is significant and the diffraction efficiency becomes dependent on the polarisation state of the incident wavefront. Choosing the surface alignment oblique to the pixel grid is found to reduce the polarisation sensitivity.

As the resolution increases there becomes a point where the switching mechanisms used in display devices becomes ineffectual. This limit was found in Chapter 11 for both holographic and image display applications. There becomes an increased need for modelling in order to investigate new switching mechanisms that can be exploited, without the expense of design by fabrication. The final part of the work detailed the search for new switching mechanisms when this limit is exceeded. One of the biggest problems for LCOS devices is that, currently, the supply voltage is limited to a few volts. Using in-plane electrodes and in-plane alignment it is possible to use this limited voltage to reorient a layer of liquid crystal above the electrodes. Elastic forces then do the rest of the work, and the bulk reorients to give a twisted layer. The amount of twist can be modulated by the applied voltage.

For higher applied voltages disclinations can be induced. The high resolution of the electrodes is mapped into the LC layer in the form of disclinations, about which there is a rapid change in permittivity. A device has been demonstrated in which a disclination line supports a twist wall.

These devices are of interest as periodic structures that can be formed containing disclinations and walls may be repositioned by an applied voltage. Rapid periodic changes in the refractive index have many possible interesting applications, such as electromagnetic bandgap structures for microwave and photonics applications and for structured dielectrics.

It has been shown that these electrically induced disclinations can interact with geometrical features present within the liquid crystal layer, such as a triangular grating. A bistable device has been demonstrated, based on the zenithal bistable device (ZBD), that uses electrically induced disclinations to switch between the stable states.

There are several avenues to pursue in continuing the research presented in this thesis: further verification and development of the models and refinement of the proposed device designs.

There is some question as to whether or not the voltage threshold for disclination formation is correctly calculated in the Landau-de Gennes theory. It has been suggested that voltage thresholds are overestimated [16] perhaps because higher order moments of the order parameter are required to represent the biaxial phase prior to disclination formation adequately [34]. This hypothesis could be tested by determining the role these higher order moments play in the intermediate biaxial phase from molecular simulations. If the higher order moments turn out to be important, then either an extension to the current mesoscopic

approach is required, or a hybrid approach, whereby molecular methods are used to describe biaxial regions and the Landau-de Gennes model is used elsewhere.

When studying interfacial properties (for example at the interface between a nematic and an isotropic liquid crystal), even the small density changes between the two regions that result can significantly affect the velocity [82]. It may be necessary to calculate the velocity field using the compressible Navier-Stokes equations. However, for the most part the assumption of incompressibility (as implemented in this work) is valid for a wide range of applications.

Some refinement of proposed device designs is required in each application, and to achieve this the optical properties of each device will need to be studied. The sensitivity to the material properties of the LC and to the uniformity of the surface alignment needs to be evaluated. It would be desirable to manufacture these structures as the measurements would be an ideal means to test the validity of the mesoscopic approaches described in the thesis.

Further optimisation of the device design is necessary to reduce the voltage requirements for disclination formation. In the case of the bistable device it would be desirable to increase the thickness of the proposed device and to improve the stability of the two stable states. The tolerance in the registration between the electrodes and the grating also needs to be investigated. The ability to create, relocate or fix the positions of disclinations electrically in structures containing protrusions (such as a grating surface) may have wider reaching applications besides bistability.

In this work the study of structures containing disclination was limited to two dimensions, but it would be of great interest to study such structures in three dimensions. For instance if a twist wall of finite length could be created by some arrangement of pixel grid voltages, this would have great potential as a photonic band gap structure.

Appendix A

Explicit Expressions

A.1 Optical Modelling - Maxwell's Equations

The full form of the terms appearing in (3.5) can be written as

$$
\begin{aligned}
a_{11} =& \frac{1}{k_0^2} ik_0 \left(\partial_x \frac{\varepsilon_{zx}}{\varepsilon_{zz}} + \frac{\varepsilon_{zx}}{\varepsilon_{zz}} \partial_x \right) \\
a_{12} =& \frac{1}{k_0^2} ik_0 \left(\partial_x \frac{\varepsilon_{zy}}{\varepsilon_{zz}} + \frac{\varepsilon_{zy}}{\varepsilon_{zz}} \partial_x \right) \\
a_{13} =& \frac{1}{k_0^2} \left(\partial_x \frac{1}{\varepsilon_{zz}} \partial_y + \frac{1}{\varepsilon_{zz}} \partial_x \partial_y \right) \\
a_{14} =& -\frac{1}{k_0^2} \left(\partial_x \frac{1}{\varepsilon_{zz}} \partial_x + \frac{1}{\varepsilon_{zz}} \partial_x^2 + k_0^2 \right)
\end{aligned}
$$

$$
\begin{aligned}
a_{21} =& \frac{1}{k_0^2} ik_0 \left(\partial_y \frac{\varepsilon_{zx}}{\varepsilon_{zz}} + \frac{\varepsilon_{zx}}{\varepsilon_{zz}} \partial_y \right) \\
a_{22} =& \frac{1}{k_0^2} ik_0 \left(\partial_y \frac{\varepsilon_{zy}}{\varepsilon_{zz}} + \frac{\varepsilon_{zy}}{\varepsilon_{zz}} \partial_y \right) \\
a_{23} =& \frac{1}{k_0^2} \left(\partial_y \frac{1}{\varepsilon_{zz}} \partial_y + \frac{1}{\varepsilon_{zz}} \partial_y^2 + k_0^2 \right) \\
a_{24} =& -\frac{1}{k_0^2} \left(\partial_y \frac{1}{\varepsilon_{zz}} \partial_x + \frac{1}{\varepsilon_{zz}} \partial_x \partial_y \right)
\end{aligned}
$$

$$
\begin{aligned}
a_{31} =& -\frac{1}{k_0^2} \left(\partial_x \partial_y - k_0^2 \varepsilon_{yx} + k_0^2 \frac{\varepsilon_{zy} \varepsilon_{zx}}{\varepsilon_{zz}} \right) \\
a_{32} =& \frac{1}{k_0^2} \left(\partial_x^2 - k_0^2 \varepsilon_{yy} + k_0^2 \frac{\varepsilon_{yz}^2}{\varepsilon_{zz}} \right) \\
a_{33} =& -\frac{1}{k_0^2} ik_0 \left(\frac{\varepsilon_{zy}}{\varepsilon_{zz}} \partial_y \right) \\
a_{34} =& \frac{1}{k_0^2} ik_0 \left(\frac{\varepsilon_{zy}}{\varepsilon_{zz}} \partial_x \right)
\end{aligned}
$$

$$
\begin{aligned}
a_{41} =& -\frac{1}{k_0^2} \left(\partial_y^2 + k_0^2 \varepsilon_{xx} - k_0^2 \frac{\varepsilon_{zx}^2}{\varepsilon_{zz}} \right) \\
a_{42} =& \frac{1}{k_0^2} \left(\partial_y \partial_x - k_0^2 \varepsilon_{yx} + k_0^2 \frac{\varepsilon_{zy} \varepsilon_{zx}}{\varepsilon_{zz}} \right) \\
a_{43} =& -\frac{1}{k_0^2} ik_0 \left(\frac{\varepsilon_{zx}}{\varepsilon_{zz}} \partial_y \right) \\
a_{44} =& \frac{1}{k_0^2} ik_0 \left(\frac{\varepsilon_{zy}}{\varepsilon_{zx}} \partial_x \right)
\end{aligned}
$$

A.2 Variable Order Parameter Formulation

The full form of the terms appearing in (6.9) can be written as

$$\mathbf{K}_{11} = \int_\Omega \left\{ L_1 \phi^j_{,\alpha} \phi^i_{,\alpha} + L_2 (\phi^j_{,x} \phi^i_{,x} + \phi^j_{,y} \phi^i_{,y} + 4 \phi^j_{,z} \phi^i_{,z})/6 \right\}$$

$$\mathbf{K}_{12} = \int_\Omega \left\{ L_2 (\phi^i_{,y} \phi^j_{,y} - \phi^i_{,x} \phi^j_{,x})/(2\sqrt{3}) \right\}$$

$$\mathbf{K}_{13} = \int_\Omega \left\{ -L_2 (\phi^i_{,y} \phi^j_{,x} + \phi^i_{,x} \phi^j_{,y})/(2\sqrt{3}) \right\}$$

$$\mathbf{K}_{14} = \int_\Omega \left\{ L_2 (2\phi^i_{,z} \phi^j_{,x} - \phi^i_{,x} \phi^j_{,z})/(2\sqrt{3}) \right\}$$

$$\mathbf{K}_{15} = \int_\Omega \left\{ L_2 (2\phi^i_{,z} \phi^j_{,y} - \phi^i_{,y} \phi^j_{,z})/(2\sqrt{3}) \right\}$$

$$\mathbf{K}_{22} = \int_\Omega \left\{ L_1 \phi^j_{,\alpha} \phi^i_{,\alpha} + L_2 (\phi^j_{,x} \phi^i_{,x} + \phi^j_{,y} \phi^i_{,y})/2 \right\}$$

$$\mathbf{K}_{23} = \int_\Omega \left\{ L_2 (\phi^i_{,x} \phi^j_{,y} - \phi^i_{,y} \phi^j_{,x})/2 \right\}$$

$$\mathbf{K}_{24} = \int_\Omega \left\{ L_2 \phi^j_{,z} \phi^i_{,x}/2 \right\}$$

$$\mathbf{K}_{25} = \int_\Omega \left\{ -L_2 \phi^j_{,z} \phi^i_{,y}/2 \right\}$$

$$\mathbf{K}_{33} = \int_\Omega \left\{ L_1 \phi^j_{,\alpha} \phi^i_{,\alpha} + L_2 (\phi^j_{,x} \phi^i_{,x} + \phi^j_{,y} \phi^i_{,y})/2 \right\}$$

$$\mathbf{K}_{34} = \int_\Omega \left\{ L_2 \phi^j_{,z} \phi^i_{,y}/2 \right\}$$

$$\mathbf{K}_{35} = \int_\Omega \left\{ L_2 \phi^j_{,z} \phi^i_{,x}/2 \right\}$$

$$\mathbf{K}_{44} = \int_\Omega \left\{ L_1 \phi^j_{,\alpha} \phi^i_{,\alpha} + L_2 (\phi^j_{,x} \phi^i_{,x} + \phi^j_{,z} \phi^i_{,z})/2 \right\}$$

$$\mathbf{K}_{45} = \int_\Omega \left\{ L_2 \phi^j_{,y} \phi^i_{,x}/2 \right\}$$

$$\mathbf{K}_{55} = \int_\Omega \left\{ L_1 \phi^j_{,\alpha} \phi^i_{,\alpha} + L_2 (\phi^j_{,y} \phi^i_{,y} + \phi^j_{,z} \phi^i_{,z})/2 \right\}$$

$$
\begin{aligned}
R &= q_1^2 + q_2^2 + q_3^2 + q_4^2 + q_5^2 \\
\mathbf{q}_k\mathbf{B}_{k1} &= \int_\Omega \left\{ \phi^i q_1 (A + CR) + \phi^i B (q_1^2 - q_2^2 - q_3^2 + (q_4^2 + q_5^2)/2)/\sqrt{6} \right\} \\
\mathbf{q}_k\mathbf{B}_{k2} &= \int_\Omega \left\{ \phi^i q_2 (A + CR) + \phi^i B (q_4^2 - q_5^2 - 4q_1 q_2/\sqrt{3})/(2\sqrt{2}) \right\} \\
\mathbf{q}_k\mathbf{B}_{k3} &= \int_\Omega \left\{ \phi^i q_3 (A + CR) + \phi^i B (q_4 q_5 - 2q_1 q_3/\sqrt{3})/\sqrt{2} \right\} \\
\mathbf{q}_k\mathbf{B}_{k4} &= \int_\Omega \left\{ \phi^i q_4 (A + CR) + \phi^i B (q_1 q_4/\sqrt{3} + q_2 q_4 + q_3 q_5)/\sqrt{2} \right\} \\
\mathbf{q}_k\mathbf{B}_{k5} &= \int_\Omega \left\{ \phi^i q_5 (A + CR) + \phi^i B (q_1 q_5/\sqrt{3} - q_2 q_5 + q_3 q_4)/\sqrt{2} \right\}
\end{aligned}
$$

$$
\begin{aligned}
g_1 &= \int_\Omega \left\{ \phi^i \varepsilon_0 \Delta\varepsilon (2u_{,z}^2 - u_{,x}^2 - u_{,y}^2)/(3\sqrt{6} S_0) \right\} \\
g_2 &= \int_\Omega \left\{ \phi^i \varepsilon_0 \Delta\varepsilon (u_{,x}^2 - u_{,y}^2)/(3\sqrt{2} S_0) \right\} \\
g_3 &= \int_\Omega \left\{ \phi^i \sqrt{2} \varepsilon_0 \Delta\varepsilon u_{,x} u_{,y}/(3S_0) \right\} \\
g_4 &= \int_\Omega \left\{ \phi^i \sqrt{2} \varepsilon_0 \Delta\varepsilon u_{,x} u_{,z}/(3S_0) \right\} \\
g_5 &= \int_\Omega \left\{ \phi^i \sqrt{2} \varepsilon_0 \Delta\varepsilon u_{,y} u_{,z}/(3S_0) \right\}
\end{aligned}
$$

The terms appearing in (7.5), the rate of change of the dissipated energy with respect to $\dot{q}_i$ can be expanded as

$$
\begin{aligned}
\frac{\partial \mathcal{D}}{\partial \dot{q}_1^i} &= \int_\Omega \left\{ \mu_1 \left(\dot{q}_1 + v_\alpha q_{1,\alpha} - \sqrt{3} q_4 W_{13} - \sqrt{3} q_5 W_{23} \right) o^i + \frac{\mu_2}{2\sqrt{6}} (2v_{3,z} - v_{1,x}) o^i \right\}. \\
\frac{\partial \mathcal{D}}{\partial \dot{q}_2^i} &= \int_\Omega \left\{ \mu_1 \left(\dot{q}_2 + v_\alpha q_{2,\alpha} + q_4 W_{13} - q_5 W_{23} + 2q_3 W_{12} \right) o^i + \frac{\mu_2}{2\sqrt{2}} v_{1,x} o^i \right\}. \\
\frac{\partial \mathcal{D}}{\partial \dot{q}_3^i} &= \int_\Omega \left\{ \mu_1 (\dot{q}_3 + v_\alpha q_{3,\alpha} + q_5 W_{13} + q_4 W_{23} - 2q_2 W_{12}) o^i + \frac{\mu_2}{2\sqrt{2}} v_{2,x} o^i \right\}. \\
\frac{\partial \mathcal{D}}{\partial \dot{q}_4^i} &= \int_\Omega \left\{ \mu_1 \left[\dot{q}_4 + v_\alpha q_{4,\alpha} + (\sqrt{3} q_1 - q_2) W_{13} + q_5 W_{12} - q_3 W_{23} \right] o^i + \frac{\mu_2}{2\sqrt{2}} (v_{3,x} + v_{1,z}) o^i \right\}. \\
\frac{\partial \mathcal{D}}{\partial \dot{q}_5^i} &= \int_\Omega \left\{ \mu_1 \left[\dot{q}_5 + v_\alpha q_{5,\alpha} + (\sqrt{3} q_1 + q_2) W_{23} - q_4 W_{12} - q_3 W_{13} \right] o^i + \frac{\mu_2}{2\sqrt{2}} v_{2,z} o^i \right\}.
\end{aligned}
$$

Appendix B

Implicit Constant Order Vector Formulation

B.1 Implementation

With one elastic constant and a vectorial representation of the liquid crystal orientation, the Euler-Lagrange equation can be found by taking the first order variations in $\mathcal{F}$ as defined in equation (5.1):

$$\delta\mathcal{F} = K\partial_\alpha^2(n_\delta) + \varepsilon_o\Delta\varepsilon n_\mu E_\mu E_\delta.$$

This equation should be supplemented with a term that enforces the unitary length of the director $\hat{n}$:

$$-\delta\mathcal{F} + \lambda\hat{n} = 0, \tag{B.1}$$

which can be solved to give the steady state director field, where λ is a lagrange multiplier. If dynamics are required we must solve

$$-\delta\mathcal{F} + \lambda\hat{n} = \gamma\dot{n}. \tag{B.2}$$

If the time step is small enough it is possible to enforce the constraint by renormalisation alone, and the Lagrange multiplier may be dropped. Here, however, we seek either the steady state solution or consider the case when the time step is large. Since the constraint is non-linear the problem is complicated, and a method such as Newton-Raphson must be applied to obtain a solution.

Taking the approach shown in Appendix B of [77] it is in fact possible to calculate the value of the Lagrange multiplier. Multiplying both sides of (B.1) by $\hat{n}$ gives

$$-\hat{n}\cdot\delta\mathcal{F} + \lambda\hat{n}\cdot\hat{n} = 0,$$

and since $\hat{n}\cdot\hat{n} = 1$

$$\lambda = \hat{n}\cdot\delta\mathcal{F}. \tag{B.3}$$

The Lagrange multiplier may be eliminated from (B.1) and (B.2) using (B.3). For the sake of simplicity the elastic and electric terms are treated separately in the derivation that

follows. Starting with the elastic terms, we take a weighted residual approach and multiply the governing equation by a test function ϕ^p and integrate over the domain Ω:

$$R^p_\delta = K \int_\Omega \left\{ \phi^p \partial^2_\alpha \left(n^j_\delta \phi^j \right) - \phi^p n^j_\lambda \phi^j \partial^2_\alpha (n^k_\lambda \phi^k) n^l_\delta \phi^l \right\},$$

which can be integrated by parts to give

$$R^p_\delta = -K \int_\Omega \left\{ \phi^p_{,\alpha} \phi^j_{,\alpha} n^j_\delta - \partial_\alpha \left(\phi^p \phi^j \phi^l \right) \phi^k_{,\alpha} n^j_\lambda n^k_\lambda n^l_\delta \right\}.$$

For the purposes of simulation, either periodic and Dirichlet boundary conditions are assumed on the boundary. For this reason the surface terms that arise due to this integration have been neglected. If an open boundary condition were required, then these surface terms would need to be calculated. The chain differentiation rule may be applied to the final term in (C.1) to yield

$$R^p_\delta = -K \int_\Omega \left\{ \phi^p_{,\alpha} \phi^j_{,\alpha} n^j_\delta - \left(\phi^p_{,\alpha} \phi^j \phi^l + \phi^p \phi^j_{,\alpha} \phi^l + \phi^p \phi^j \phi^l_{,\alpha} \right) \phi^k_{,\alpha} n^j_\lambda n^k_\lambda n^l_\delta \right\}.$$

A numerical integration scheme allows further simplification of this expression. The integration is changed to a sum over Gauss points. At each point a shape function and its spatial derivative take constant value. The shape functions are decoupled, and the expressions can be simplified. Implementations that use numerical integration offer similar performance to those that use closed forms [64]. Furthermore, the implementation is simpler and less error prone. This simplification, replacing integrals with sums, yields

$$R^p_\delta = -K \sum \left\{ \phi^p_{,\alpha} N_{\delta,\alpha} + \left(\phi^p_{,\alpha} N_\delta + \phi^p N_{\delta,\alpha} \right) N_\lambda N_{\lambda,\alpha} + \phi^p N_{\lambda,\alpha} N_{\lambda,\alpha} N_\delta \right\},$$

where $N_\lambda = n^k_\lambda \phi^k$ and $N_{\lambda,\alpha} = n^k_\lambda \phi^k_{,\alpha}$. Since the equations are non-linear a Jacobian matrix is needed as well as the residual vector in order to apply Newton's method. The contribution to the Jacobian from the elastic terms is given by:

$$\frac{\partial R^p_\delta}{\partial n^i_\mu} = -K \int_\Omega \left\{ \phi^p_{,\alpha} \phi^i_{,\alpha} \delta_{\mu\delta} - \partial_\alpha \left(\phi^p \phi^i \phi^l \right) \phi^k_{,\alpha} n^k_\mu n^l_\delta - \partial_\alpha \left(\phi^p \phi^j \phi^l \right) \phi^i_{,\alpha} n^j_\mu n^l_\delta \right.$$
$$\left. - \partial_\alpha \left(\phi^p \phi^j \phi^i \right) \phi^k_{,\alpha} n^j_\lambda n^k_\lambda \delta_{\mu\delta} \right\}.$$

Taking advantage of the Gauss points once again yields

$$\frac{\partial R^p_\delta}{\partial n^i_\mu} = -K\sum\Big\{\phi^p_{,\alpha}\phi^i_{,\alpha}\delta_{\mu\delta} - \left(\phi^p_{,\alpha}\phi^i N_\delta + \phi^p\phi^i N_{\delta,\alpha} + 2\phi^p\phi^i_{,\alpha}N_\delta\right)N_{\mu,\alpha}$$
$$- \left(\phi^p_{,\alpha}N_\delta + \phi^p N_{\delta,\alpha}\right)\phi^i_{,\alpha}N_\mu$$
$$- \left(\phi^p_{,\alpha}\phi^i N_\lambda N_{\lambda,\alpha} + \phi^p\phi^i N_{\lambda,\alpha}N_{\lambda,\alpha} + 2\phi^p\phi^i_{,\alpha}N_\lambda N_{\lambda,\alpha}\right)\delta_{\mu\delta}\Big\},$$

The electric terms, do not require integration by parts and so discretisation is comparatively simple.

$$R^p_\delta = \varepsilon_o\Delta\varepsilon\int_\Omega\left\{\phi^p n^j_\lambda\phi^j\phi^k_{,\lambda}\phi^l_{,\delta}u^k u^l - \phi^p n^j_\gamma\phi^j n^k_\lambda\phi^k\phi^l_{,\lambda}\phi^m_{,\gamma}u^l u^m n^n_\delta\phi^n\right\}.$$

Introducing $F_{,\lambda} = u^k\frac{\partial\phi^k}{\partial x_\lambda}$ and simplifying assuming the use of Gauss integration

$$R^p_\delta = \varepsilon_o\Delta\varepsilon\sum\left\{\phi^p(N_\lambda F_{,\lambda})F_{,\delta} - \phi^p(N_\lambda F_{,\lambda})^2.N_\delta\right\}.$$

The contribution to the Jacobian matrix from the electric terms is given by

$$\frac{\partial R^p_\delta}{\partial n^i_\mu} = \varepsilon_o\Delta\varepsilon\int_\Omega\Big\{\phi^p\phi^i\phi^k_{,\mu}\phi^l_{,\delta}u^k u^l - 2\phi^p\phi^i n^k_\lambda\phi^k\phi^l_{,\lambda}\phi^m_{,\mu}u^l u^m n^n_\delta\phi^n$$
$$- \phi^p\phi^i n^j_\gamma\phi^j n^k_\lambda\phi^k\phi^l_{,\lambda}\phi^m_{,\gamma}u^l u^m\delta_{\mu\delta}\Big\}$$

or

$$\frac{\partial R^p_\delta}{\partial n^i_\mu} = \varepsilon_o\Delta\varepsilon\sum\left\{\phi^p\phi^i\left[F_{,\mu}F_{,\delta} - 2(N_\lambda F_{,\lambda})F_{,\mu}N_\delta - (N_\lambda F_{,\lambda})^2\delta_{\mu\delta}\right]\right\}.$$

Adding the contributions from the elastic and electric energies completes this formulation giving the Jacobian matrix $\mathbf{J} = \frac{\partial R^p_\delta}{\partial n^i_\mu}$ and the residual vector R^p_δ. The resulting non-linear equations of the form $\mathbf{J}n = -\mathbf{R}$ can then be solved using equation (B.1) for the steady-state case, and (B.2) for the dynamic case.

B.2 Convergence

Using a 1 µm thick planar cell with a 5° pretilt, convergence of this formulation can be tested using the steady state solution given by (B.1). Material parameters were chosen as:

$K = 12.5$ pN, $\varepsilon_\perp = 5.2$ and $\Delta\varepsilon = 13.8$.

Starting from a relaxed state, a voltage of 2.0 V was applied. It was found that convergence was not achieved unless the choice of initial director configuration differed by less than 10° from the final solution. Due to the strongly non-linear nature of the governing equation (strong in the respect that it contains spatial derivatives of the director field) convergence is unlikely unless a good knowledge of the final solution is known.

To rectify this problem Crank-Nicholson time stepping can be used. Due to the highly non-linear nature of the equation the time step must be limited. Such a formulation does not maintain the unitary director length perfectly, and small oscillations occur. Convergence can be improved by normalising the director at each time step. Provided the time step does not exceed some limit convergence is achieved.

Now this formulation will be compared to a simpler formulation that omits the Lagrange multiplier and uses Crank-Nicholson time stepping with renormalisation after each time step. The steady-state mid-plane tilt is compared for a number of different time steps in Table B.1.

Table B.1: Steady State Tilt

Δt	θ_{max} with λ	θ_{max} without λ
$10\mu s$	73.8°	74.4°
$30\mu s$	73.8°	75.4°
$200\mu s$	unstable	80.6°

Without Lagrange multipliers, the resulting system of equations is linear, and a much larger time step can be used. As the time step increases the error in the calculated mid-plane tilt increases.

With Lagrange multipliers the accuracy of the solution is maintained even with relatively large time steps, but since the equations are no longer linear, convergence is not assured for large times steps. Above 30μs the director field was found not to converge to a fixed solution.

Appendix C

The Finite Difference Method

C.1 Adaptive Finite Difference Poisson Solver

The various finite element models described in this thesis have been verified against simpler finite difference approaches. Instead of describing each and every implementation, the discretisation steps are outlined in this Appendix for the Poisson equation model.

For some of the problems considered in this thesis a very fine mesh is required. In traditional finite difference methods the mesh is uniform and the number of degrees of freedom becomes prohibitively large. Here, an adaptive finite difference discretisation is developed that overcomes this problem by allowing the distance between mesh points to vary. The error is $O(h^2)$ in regions where the mesh is uniform and can drop to $O(h)$ where the mesh is adapted.

The Poisson Equation in an anisotropic medium is

$$\nabla \cdot \left(\bar{\bar{\varepsilon}} \cdot \nabla u\right) = -\frac{\rho}{\varepsilon_0}.$$

This can be expanded for a structure oriented in the xz plane as

$$\frac{\partial}{\partial x}\left(\varepsilon_{xx}\frac{\partial u}{\partial x} + \varepsilon_{xz}\frac{\partial u}{\partial z}\right) + \frac{\partial}{\partial z}\left(\varepsilon_{zx}\frac{\partial u}{\partial x} + \varepsilon_{zz}\frac{\partial u}{\partial z}\right) = -\frac{\rho}{\varepsilon_0}, \tag{C.1}$$

$$\frac{\partial g_{xx}}{\partial x} + \frac{\partial g_{xz}}{\partial x} + \frac{\partial g_{zx}}{\partial z} + \frac{\partial g_{zz}}{\partial z} = -\frac{\rho}{\varepsilon_0}. \tag{C.2}$$

In order to discretise this equation a finite difference approach can be taken and as a starting point the derivatives need to be approximated. Formulas for these can be found by considering the Taylor series for a function f at a distance h from a point a.

$$f(a+h) = f(a) + f'(a)h + f''(a)\frac{h^2}{2!} + f'''(a)\frac{h^3}{3!} + \ldots$$
$$f(a-h) = f(a) - f'(a)h + f''(a)\frac{h^2}{2!} - f'''(a)\frac{h^3}{3!} + \ldots$$

When the mesh is uniform these equations can be rearranged to give an approximations of $f'(a)$ and $f''(a)$ in terms of the value of f at two or three mesh points.

$$f'(a) = \frac{f(a+h) - f(a-h)}{2h} + O(h^2). \tag{C.3}$$

$$f''(a) = \frac{f(a+h) - 2f(a) + f(a-h)}{h^2} + O(h^2). \tag{C.4}$$

If the mesh is not uniform then h is no longer constant and changes from node to node. Here, h_{n+1} is the distance between a and its closest neighbour in the positive x direction. h_{n-1} is the distance between a and its closest neighbour in the negative x direction. For our needs only an approximation of the first derivative is required, which is

$$f'(a) = \frac{h_{n-1}^2 f(a+h_{n+1}) + \left(h_{n+1}^2 - h_{n-1}^2\right) f(a) - h_{n+1}^2 f(a-h_{n-1})}{\left(h_{n-1}^2 h_{n+1} + h_{n-1} h_{n+1}^2\right)} + O(h). \qquad \text{(C.5)}$$

With this formula we are in position to discretize (C.2). Each term in g is dealt with separately, starting with g_{zz}.

$$\frac{\partial g_{zz}}{\partial z} = \frac{\partial}{\partial z}\left(\varepsilon_{zz}\frac{\partial u}{\partial z}\right)$$

The derivative of g_{zz} at the node n is written in terms of the value of g_{zz} at $z = a - h_{n+1}/2$, a and $a + h_{n+1}/2$, i.e. at the node itself and at the mid-point between the node and its neighbours. These values are written in shorthand as $g_{zz}^{n-1/2}$, g_{zz}^{n} and $g_{zz}^{n+1/2}$ respectively.

$$\frac{\partial g_{zz}^n}{\partial z} = 2z_s\left(h_{n-1}^2 g_{zz}^{n+1/2} + z_d g_{zz}^n - h_{n+1}^2 g_{zz}^{n-1/2}\right),$$

where

$$z_d = h_{n+1}^2 - h_{n-1}^2 \quad \text{and} \quad z_s = \left(h_{n+1}^2 h_{n-1} + h_{n-1} h_{n-1}^2\right)^{-1}.$$

The next step is to substitute in discretised values for $g_{zz}^{n-1/2}$ and $g_{zz}^{n+1/2}$. These terms require the spatial derivative of u to be calculated at the mid-point between nodes, which can be calculated using (C.3), giving

$$g_{zz}^{n+1/2} = \varepsilon_{zz}^{n+1/2}\frac{u^{n+1} - u^n}{h_{n+1}} \quad \text{and} \quad g_{zz}^{n-1/2} = \varepsilon_{zz}^{n-1/2}\frac{u^n - u^{n-1}}{h_{n-1}}.$$

The value of the permittivity is only available at the mesh points, but we require the value at the midpoints, so averaging is required:

$$\varepsilon_{zz}^{n+1/2} = \frac{1}{2}\left(\varepsilon_{zz}^{n+1} + \varepsilon_{zz}^{n}\right) \quad \text{and} \quad \varepsilon_{zz}^{n-1/2} = \frac{1}{2}\left(\varepsilon_{zz}^{n} + \varepsilon_{zz}^{n-1}\right).$$

The value of g^n_{zz} is obtained using (C.5)

$$g^n_{zz} = z_s \varepsilon^n_{zz} \left(h^2_{n-1} u^{n+1} + z_d u^n - h^2_{n+1} u^{n-1} \right).$$

Combining all these terms gives in full:

$$\begin{aligned}
\frac{\partial g^n_{zz}}{\partial z} &= 2 z_s \frac{h^2_{n-1}}{h_{n+1}} \varepsilon^{n+1/2}_{zz} \left(u^{n+1} - u^n \right) - 2 z_s \frac{h^2_{n+1}}{h_{n-1}} \varepsilon^{n-1/2}_{zz} \left(u^n - u^{n-1} \right) \\
&\quad + 2 z_s^2 z_d \varepsilon^n_{zz} \left(h^2_{n-1} u^{n+1} + z_d u^n - h^2_{n+1} u^{n-1} \right) \\
&= \left(z_s \frac{h^2_{n-1}}{h_{n+1}} \left(\varepsilon^{n+1}_{zz} + \varepsilon^n_{zz} \right) + 2 z_s^2 z_d h^2_{n-1} \varepsilon^n_{zz} \right) u^{n+1} \\
&\quad + \left(-z_s \frac{h^2_{n-1}}{h_{n+1}} \left(\varepsilon^{n+1}_{zz} + \varepsilon^n_{zz} \right) - z_s \frac{h^2_{n+1}}{h_{n-1}} \left(\varepsilon^n_{zz} + \varepsilon^{n-1}_{zz} \right) + 2 z_s^2 z_d^2 \varepsilon^n_{zz} \right) u^n \\
&\quad + \left(z_s \frac{h^2_{n+1}}{h_{n-1}} \left(\varepsilon^n_{zz} + \varepsilon^{n-1}_{zz} \right) - 2 z_s^2 z_d h^2_{n+1} \varepsilon^n_{zz} \right) u^{n-1}.
\end{aligned}$$

A similar result is obtained for $\frac{\partial g^n_{xx}}{\partial x}$ with z substituted for x.

The mixed derivative terms must be dealt with differently. Starting with $\frac{\partial g^n_{zx}}{\partial z}$:

$$\frac{\partial g_{zx}}{\partial z} = \frac{\partial}{\partial z} \left(\varepsilon_{zx} \frac{\partial u}{\partial x} \right)$$

As before this equation is discretised using (C.5), but this time at the nodes themselves, not at the mid-points as before.

$$\frac{\partial g^n_{zx}}{\partial z} = z_s \left(h^2_{n-1} g^{n+1} + z_d g^n - h^2_{n+1} g^{n-1} \right)$$

Repeated application of (C.5) can be used to write g_{zx} in terms of u as follows

$$\begin{aligned}
g^{n+1}_{zx} &= \varepsilon^{n+1,m}_{zx} x_s \left(h^2_{m-1} u^{n+1,m+1} + x_d u^{n+1,m} - h^2_{m+1} u^{n+1,m-1} \right) \\
g^{n-1}_{zx} &= \varepsilon^{n-1,m}_{zx} x_s \left(h^2_{m-1} u^{n-1,m+1} + x_d u^{n-1,m} - h^2_{m+1} u^{n-1,m-1} \right) \\
g^n_{zx} &= \varepsilon^{n,m}_{zx} x_s \left(h^2_{m-1} u^{n,m+1} + x_d u^{n,m} - h^2_{m+1} u^{n,m-1} \right)
\end{aligned}$$

This gives in full:

$$\begin{aligned}\frac{\partial g_{zx}^n}{\partial z} &= h_{n-1}^2 x_s z_s \varepsilon_{zx}^{n+1,m}\left(h_{m-1}^2 u^{n+1,m+1} + x_d u^{n+1,m} - h_{m+1}^2 u^{n+1,m-1}\right)\\ &+ z_d x_s z_s \varepsilon_{zx}^{n,m}\left(h_{m-1}^2 u^{n,m+1} + x_d u^{n,m} - h_{m+1}^2 u^{n,m-1}\right)\\ &- h_{n+1}^2 x_s z_s \varepsilon_{zx}^{n-1,m}\left(h_{m-1}^2 u^{n-1,m+1} + x_d u^{n-1,m} - h_{m+1}^2 u^{n-1,m-1}\right)\end{aligned}$$

Similarly for the other mixed derivative term

$$\frac{\partial g_{xz}^n}{\partial x} = \frac{\partial}{\partial x}\left(\varepsilon_{xz}\frac{\partial u}{\partial z}\right)$$

$$\begin{aligned}\frac{\partial g_{xz}^n}{\partial x} &= h_{m-1}^2 x_s z_s \varepsilon_{xz}^{n,m+1}\left(h_{n-1}^2 u^{n+1,m+1} + z_d u^{n,m+1} - h_{n+1}^2 u^{n-1,m+1}\right)\\ &+ x_d x_s z_s \varepsilon_{xz}^{n,m}\left(h_{n-1}^2 u^{n+1,m} + z_d u^{n,m} - h_{n+1}^2 u^{n-1,m}\right)\\ &- h_{n+1}^2 x_s z_s \varepsilon_{xz}^{n,m-1}\left(h_{n-1}^2 u^{n+1,m-1} + z_d u^{n,m-1} - h_{n+1}^2 u^{n+1,m+1}\right)\end{aligned}$$

Combining both mixed derivative terms to give $(\frac{\partial g_{xz}^n}{\partial x} + \frac{\partial g_{zx}^n}{\partial z})$ and collecting terms in u yields:

$$x_s z_s \begin{bmatrix} -h_{n-1}^2 h_{m+1}^2\left(\varepsilon_{xz}^{n,m-1} + \varepsilon_{xz}^{n+1,m}\right)u^{n+1,m-1} + h_{n-1}^2 x_d\left(\varepsilon_{xz}^{n,m} + \varepsilon_{xz}^{n+1,m}\right)u^{n+1,m} \\ +h_{n-1}^2 h_{m-1}^2\left(\varepsilon_{xz}^{n,m+1} + \varepsilon_{xz}^{n+1,m}\right)u^{n+1.m} - z_d h_{m+1}^2\left(\varepsilon_{xz}^{n,m-1} + \varepsilon_{xz}^{n,m}\right)u^{n.m-1} \\ +2z_d x_d \varepsilon_{xz}^{n,m} u^{n.m} + z_d h_{m-1}^2\left(\varepsilon_{xz}^{n,m+1} + \varepsilon_{xz}^{n,m}\right)u^{n.m+1} \\ +h_{n+1}^2 h_{m+1}^2\left(\varepsilon_{xz}^{n,m-1} + \varepsilon_{xz}^{n-1,m}\right)u^{n-1.m-1} \\ -h_{n+1}^2 x_d\left(\varepsilon_{xz}^{n,m} + \varepsilon_{xz}^{n-1,m}\right)u^{n+1.m} - h_{n+1}^2 h_{m+1}^2\left(\varepsilon_{xz}^{n,m+1} + \varepsilon_{xz}^{n-1,m}\right)u^{n+1,m} \end{bmatrix}$$

Finally (C.2) can be written in terms of u by combining all these terms. giving rise to a system of equations that can be written in matrix form as

$$\mathbf{A}u = \mathbf{b}.$$

Dirichlet boundary conditions are applied resulting in the elimination of rows and columns corresponding to the fixed nodes. Periodic boundary conditions are applied resulting in the addition of the corresponding rows and columns.

C.2 Staggered Grid

In order to perform more detailed verification tests, finite difference implementations were written for both Q-tensor and flow problems. A staggered grid method is used to solve the Navier-Stokes equations for the flow and is detailed in this section. Only an isotropic fluid is considered here for the verification test. In the anisotropic case this method becomes significantly more complex.

A staggered grid method is favoured over traditional FD methods for the Navier-Stokes equations as it provides damping of oscillatory pressure solutions. This method is detailed below, following [169]. In fact this method is equivalent to an FE formulation using bi-quadratic shape functions for the velocity and linear functions for the pressure.

Fig. C-1 shows the positions of the nodes of the grid. The x component of the velocity is defined halfway along the left and right edge of each box and the y component defined halfway along the bottom and top edge of each box. The pressure is defined at the centre of each box.

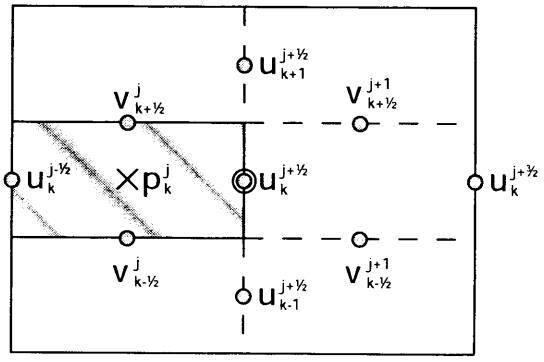

Figure C-1: Staggered Mesh

From the Navier-Stokes equation, neglecting non-linear terms, the x component of the velocity may be written as

$$\left[u_k^{j+\frac{1}{2}}\right]^{n+1} = \left[F_k^{j+\frac{1}{2}}\right]^n - \frac{\Delta t}{\Delta x}\left[p_k^{j+1} - p_k^j\right]^{n+1}. \tag{C.6}$$

where

$$\left[F_k^{j+\frac{1}{2}}\right]^n = \left[u_k^{j+\frac{1}{2}}\right]^n + \frac{\Delta t}{Re}\left[\frac{1}{\Delta x^2}\left(u_k^{j+\frac{3}{2}} - 2u_k^{j+\frac{1}{2}} + u_k^{j-\frac{1}{2}}\right) + \frac{1}{\Delta y^2}\left(u_{k+1}^{j+\frac{1}{2}} - 2u_k^{j+\frac{1}{2}} + u_{k-1}^{j+\frac{1}{2}}\right)\right]^n \tag{C.7}$$

Similarly for the y component of the velocity we have

$$\left[v_{k+\frac{1}{2}}^j\right]^{n+1} = \left[G_{k+\frac{1}{2}}^j\right]^n - \frac{\Delta t}{\Delta y}\left[p_{k+1}^j - p_k^j\right]^{n+1}, \tag{C.8}$$

where

$$\left[G_{k+\frac{1}{2}}^j\right]^n = \left[v_{k+\frac{1}{2}}^j\right]^n + \frac{\Delta t}{Re}\left[\frac{1}{\Delta x^2}\left(v_{k+\frac{1}{2}}^{j+1} - 2v_{k+\frac{1}{2}}^j + v_{k+\frac{1}{2}}^{j-1}\right) + \frac{1}{\Delta y^2}\left(v_{k+\frac{3}{2}}^j - 2v_{k+\frac{1}{2}}^j + v_{k-\frac{1}{2}}^j\right)\right]^n \tag{C.9}$$

Applying the incompressibility condition to the shaded rectangle in Fig. C-1 gives the following expression:

$$\left[D_k^j\right]^{n+1} = \frac{1}{\Delta x}\left[u_k^{j+\frac{1}{2}} - u_k^{j-\frac{1}{2}}\right]^{n+1} + \frac{1}{\Delta y}\left[v_{k+\frac{1}{2}}^j - v_{k-\frac{1}{2}}^j\right]^{n+1} = 0 \tag{C.10}$$

$$\frac{p_k^{j+1} - 2p_k^j + p_k^{j-1}}{\Delta x^2} + \frac{p_{k+1}^j - 2p_k^j + p_{k-1}^j}{\Delta y^2} = \frac{1}{\Delta t}\left[\frac{F_k^{j+\frac{1}{2}} - F_k^{j-\frac{1}{2}}}{\Delta x} + \frac{G_{k+\frac{1}{2}}^j - G_{k-\frac{1}{2}}^j}{\Delta y}\right]^n \tag{C.11}$$

This Poisson equation can then be implicitly solved to yield the pressure solution from which the velocity components can subsequently be calculated using (C.6) and (C.8)

Generalizing this method for anisotropic materials, such as liquid crystals, couples more strongly (C.6) and (C.8). Terms in v are added to (C.6) and terms in u are added to (C.8). Averaging the nodal values of u and v is required to obtain the velocity at the desired locations.

Bibliography

[1] L. Onsager, "The effects of shape on the interaction of colloidal particles," *Ann. N. Y. Acad. Sci.*, vol. 51, pp. 627–659, 1949.

[2] W. Maier and A. Saupe, "Eine einfache molekular-statistische theorie der nematischen kristallinflüssigen zustandes," *Z. Naturforsch*, vol. 13, no. a, pp. 564–556, 1958.

[3] ——, "Eine einfache molekular-statistische theorie der nematischen kristallinflüssigen phase. teil I," *Z. Naturforsch*, vol. 14, no. a, pp. 882–889, 1959.

[4] ——, "Eine einfache molekular-statistische theorie der nematischen kristallinflüssigen phase, teil II," *Z. Naturforsch*, vol. 15, no. a, pp. 287–292, 1960.

[5] L. D. Landau and E. M. Lifshitz, *Statistical physics*, ser. Course of theoretical physics; vol. 5. London: Pergamon, 1958.

[6] L. D. Landau, *Phys. Z. Sowjetunion*, vol. 11, pp. 26–47, 1937.

[7] P. G. de Gennes and J. Prost, *The Physics of Liquid Crystals*, 2nd ed. Clarendon, 1993.

[8] R. C. Jones, "A new calculus for the treatment of optical systems - I. description and discussion of the calculus," *J. Opt. Soc. Am.*, vol. 375, no. 31, pp. 488–493, 1941.

[9] D. W. Berreman, "Optics in stratified and anisotropic media: 4×4-matrix formulation," *J. Opt. Soc. Am.*, vol. 375, no. 62, pp. 502–510, 1972.

[10] M. Nevière and E. Popov, *Light Propagation in Periodic Media: Differential Theory and Design*. New York, USA: Marcel Dekker, Inc., 2003.

[11] O. A. Peverini, D. Olivero, C. Oldano, D. K. G. de Boer, R. Cortie, R. Orta, and R. Tascone, "Reduced-order model technique for the analysis of anisotropic inhomogeneous media: application to liquid-crystal displays," *J. Opt. Soc. Am. A*, vol. 9, no. 19, 2002.

[12] T. Qian and P. Sheng, "Generalized hydrodynamic equations for nematic liquid crystals," *Physical Review E*, vol. 58, no. 6, pp. 7475–7485, 1998.

[13] P. Yeh and C. Gu, *Optics of liquid crystal displays.* New York; Chichester: Wiley, 1999.

[14] http://electromagnetics.biz/Integration.htm, 2006.

[15] P. D. Brimicombe and E. P. Raynes, "The influence of flow on symmetric and asymmetric splay state relaxations," *Liquid Crystals*, vol. 32, no. 10, pp. 1273–1283, 2005.

[16] R. Barberi, F. Ciuchi, G. E. Durand, M. Iovane, D. Sikharulidze, A. M. Sonnet, and E. G. Virga, "Electric field induced order reconstruction in a nematic cell," *Eur Phys J E Soft Matter*, vol. 13, no. 1, pp. 61–71, 2004.

[17] H. Cheng and H. Gao, "Dynamic simulation of pi-cell liquid crystal displays," *Liquid Crystals*, vol. 28, no. 9, pp. 1337–1341, 2001.

[18] C. W. Oseen, "The theory of liquid crystal," *Trans. Faraday Soc.*, vol. 29, pp. 883–898, 1933.

[19] H. Zocher, "The effect of a magnetic field on the nematic state," *Trans. Faraday Soc.*, vol. 29, pp. 945–957, 1933.

[20] F. C. Frank, "On the theory of liquid crystal," *Discuss. Faraday Soc.*, vol. 25, pp. 19–28, 1958.

[21] C. V. Brown, E. E. Kriezis, and S. J. Elston, "Optical diffraction from a liquid crystal phase grating," *J. Appl. Phys.*, vol. 91, no. 6, pp. 3495–3500, 2002.

[22] A. J. Davidson and S. J. Elston, "Three-dimensional beam propagation model for the optical path of light through a nematic liquid crystal," *J. Mod. Optic.*, vol. 53, no. 7, pp. 979–989, 2006.

[23] K. Rokushima and J. Yamakita, "Analysis of anisotropic dielectric gratings," *J. Opt. Soc. Am.*, vol. 73, no. 7, pp. 901–908, 1983.

[24] S. H. Hong, Y. H. Jeong, H. Y. Kim, H. M. Cho, W. G. Lee, and S. H. Lee, "Electro-optic characteristics of 4-domain vertical alignment nematic liquid crystal display with interdigital electrode," *Jounal of Applied Physics*, vol. 87, no. 12, pp. 8259–8263, 2000.

[25] G. R. Luckhurst, R. A. Stephens, and R. W. Phippen, "Computer-simulation studies of anisotropics systems: XIX. mesophases formed by the Gay-Berne model mesogen," vol. 8, pp. 451–464, 1990.

[26] H. Domínguez, E. Velasco, and J. Alejandre, "Stress anisotropy in liquid crystalline phases," *Molecular Physics*, vol. 100, no. 16, pp. 2739–2744, 2002.

[27] M. P. Allen and D. J. Tildesley, *Computer simulation of liquids.* Oxford: Clarendon, 1987.

[28] D. Svenšek and S. Žumer, "Hydrodynamics of pair-annihilating disclination lines in nematic liquid crystals," *Physical Review E*, vol. 66, no. 2 Pt 1, p. 021712, 2002.

[29] C. M. Care, I. Halliday, K. Good, and S. V. Lishchuk, "A generalised lattice Boltzmann algorithm for the flow of nematic liquid crystal with variable order parameter," *Physical Review E*, vol. 67, 2003.

[30] C. Denniston, E. Orlandini, and J. M. Yeomans, "Lattice Boltzmann simulations of liquid crystal hydrodynamics," *Physical Review E Stat Nonlin Soft Matter Phys*, vol. 63, no. 5 Pt 2, p. 056702, 2001.

[31] C. Colpaert, B. Maximus, and H. J. Pauwels, "Study of transient currents in nematic liquid crystals," *Proc. of the SID Research Conference*, pp. 301–304, 1993.

[32] B. Apter, U. Efron, and E. Bahat-Treidel, "On the fringing-field effect in liquid-crystal beam-steering devices," *Appl Opt.*, vol. 43, no. 1, pp. 11–19, 2004.

[33] G. Panasyuk and D. W. Allender, "Approximate description of the three dimensional director and electric field in a liquid crystal display at a high voltage," *Journal of Applied Physics*, vol. 87, no. 2, pp. 649–657, 2000.

[34] J. P. Straley, "Ordered phases of a liquid of biaxial particles," *Phys. Rev. A*, vol. 10, no. 5, pp. 1881–1887, 1974.

[35] S. Chandrasekhar, *Liquid crystals*, ser. Cambridge monographs on physics. Cambridge: Cambridge University Press, 1977.

[36] P. J. Collings and M. Hird, *Introduction to liquid crystals: chemistry and physics*, ser. The liquid crystals book series. London: Taylor & Francis, 1997.

[37] M. J. Stephen and J. P. Straley, "Physics of liquid crystals," *Rev. Mod. Phys.*, vol. 46, pp. 617–704, 1974.

[38] P. W. Anderson, *Basic notions of condensed matter physics.* Menlo Park, Calif.: Benjamin/Cummings Pub. Co., 1983.

[39] E. G. Virga, *Variational theories for liquid crystals*, ser. Applied mathematics and mathematical computation. London: Chapman & Hall, 1994.

[40] B. R. Acharya, A. Primak, and S. Kumar, "Biaxial nematic phase in bent-core thermotropic mesogens," *Phys. Rev. Lett.*, vol. 92, p. 145506, 2004.

[41] A. Sarlah, P. Ziherl, and S. Zumer, "Fluctuations in confined liquid crystals and pretransitional evanescent light scattering," *Mol. Cryst. Liq. Cryst.*, vol. 320, p. 231, 1998.

[42] G. P. Crawford, R. J. Ondris-Crawford, J. W. Doane, and S. Zumer, "Systematic study of orientational wetting and anchoring at a liquid-crystal-surfactant interface," *Physical Review. E. Statistical Physics, Plasmas, Fluids, and Related Interdisciplinary Topics*, vol. 53, no. 4, pp. 3647–3661, 1996.

[43] V. J. Anderson, E. M. Terentjev, S. P. Meeker, J. Crain, and W. C. K. Poon, "Cellular solid behaviour of liquid crystal colloids 1. phase separation and morphology," *Eur. Phys. J. E*, vol. 4, no. 11-20, 2000.

[44] D. Demus, *Handbook of liquid crystals.* Weinheim: Chichester: Wiley-VCH, 1998.

[45] M. V. Kurik and O. D. Lavrentovich, "Defects in liquid crystals: homotopy theory and experimental studies," *Usp. Fiz. Nauk*, vol. 154, pp. 381–431, 1988.

[46] O. D. Lavrentovich, *Defects in liquid crystals: computer simulations, theory, and experiments*, ser. NATO science series. Series II, Mathematics, physics, and chemistry; v. 43. Dordrecht ; London: Kluwer Academic Publishers, 2001.

[47] G. Friedel, *Ann. Phys. (Paris)*, vol. 19, p. 273, 1922.

[48] F. C. Frank, *Discuss. Faraday Soc.*, vol. 25, p. 19, 1978.

[49] I. Dierking, *Textures of liquid crystals*. Weinheim; Cambridge: Wiley-VCH, 2003.

[50] D. Svenšek and S. Žumer, "Instability modes of high-strength disclinations in nematics," *Physical Review E*, vol. 70, no. 6 Pt 1, p. 061707, 2004.

[51] P. Biscari and T. J. Sluckin, "Field-induced motion of nematic disclinations," *SIAM Journal on Applied Mathematics*, vol. 65, no. 6, pp. 2141–2157, 2005.

[52] D. L. Cheung, S. J. Clark, and M. R. Wilson, "Calculation of flexoelectric coefficients for a nematic liquid crystal by atomistic simulation," *J. Chem. Phys.*, vol. 121, pp. 9131–9139, 2004.

[53] A. J. McDonald and S. Hanna, "Atomistic computer simulations of terraced wetting of model 8CB molecules at crystal surfaces," *Mol. Cryst. Liq. Cryst.*, vol. 413, pp. 135–144, 2004.

[54] R. Berardi, M. Ricci, and C. Zannoni, "Ferroelectric and structured phases from polar tapered mesogens," *Ferroelectrics*, vol. 309, pp. 3–13, 2004.

[55] B. J. Berne and P. Pechukas, "Gaussian model potentials for molecular interactions," *J. Chem. Phys.*, vol. 56, pp. 4213–4216, 1972.

[56] J. G. Gay and B. J. Berne, "Modification of the overlap potential to mimic a linear site-site potential," *J. Chem. Phys.*, vol. 74, pp. 3316–3319, 1981.

[57] S.-T. Wu and C.-S. Wu, "Mixed-mode twisted nematic liquid crystal cells for reflective displays," *Applied Physics Letters*, vol. 68, no. 11, pp. 1455–1457, 1996.

[58] A. Lien, "A detailed derivation of extended Jones matrix representation for twisted nematic liquid crystal displays," *Liquid Crystals*, vol. 22, pp. 171–175, 1997.

[59] A. Lien and C.-J. Chen, "A new 2×2 matrix representation for twited nematic liquid crystal displays at oblique incidence," *Jpn. J. Appl. Phys.*, vol. 35, pp. L1200–L1203, 1996.

[60] G. Granet and B. Guizal, "Efficient implementation of the coupled-wave method for metallic lamellar gratings in TM polarization," *J. Opt. Soc. Am. A*, vol. 13, no. 5, p. 1019, 1996.

[61] L. Li, "Formulation and comparison of two recursive matrix algorithms for modeling layered diffraction gratings," *J. Opt. Soc. Am. A*, vol. 13, no. 5, p. 1024, 1996.

[62] K.-J. Bathe, *Finite element procedures in engineering analysis.* London: Prentice Hall, 1996.

[63] H. Kardestuncer and D. H. Norrie, *Finite element handbook.* New York ; London: McGraw-Hill, 1987.

[64] O. C. Zienkiewicz and R. L. Taylor, *The finite element method. Vol. 1, The basis*, 5th ed. Oxford: Butterworth-Heinemann, 2000.

[65] G. R. Cowper, "Gaussian quadrature formulas for triangles," *International Journal of Numerical Methods in Engineering*, vol. 7, pp. 405–408, 1973.

[66] C. W. Clenshaw and A. R. Curtis, "A method for numerical integration on an automatic computer," *Num. Math.*, vol. 2, pp. 197–205, 1960.

[67] A. A. Goldstein, "On steepest descent," *SIAM Journal on Control and Optimization*, vol. 3, pp. 147–151, 1965.

[68] L. Armijo, "Minimization of functions having Lipschitz continuous first partial derivatives," *Pacific Journal of Mathematics*, vol. 16, pp. 1–3, 1966.

[69] K. W. Morton and D. F. Mayers, *Numerical solution of partial differential equations : an introduction.* Cambridge: Cambridge University Press, 1994.

[70] P. M. Gresho, R. L. Sani, and M. S. Engelman, *Incompressible Flow and the Finite Element Method.* Chichester: Wiley, 1998.

[71] B. D. Reddy, *Introductory functional analysis: with applications to boundary value problems and finite elements*, ser. Texts in applied mathematics. New York; London: Springer, 1998.

[72] G. Jeng and A. Wexler, "Self-adjoint variational formulation of problems having non-self-adjoint operators," *IEEE Transactions on Microwave Theory and Techniques*, vol. 26, no. 2, pp. 91– 94, 1978.

[73] N. Schopohl and T. J. Sluckin, "Defect core structure in nematic liquid crystals," *Physical Review Letters*, vol. 59, no. 22, pp. 2582–2584, 1987.

[74] http://www.softeng.cse.clrc.ac.uk/felib3/Docs/html/Intro/intro node55.html, 2006.

[75] F. H. Lin and C. Liu, "Existence of solutions for the Ericksen-Leslie system," *Arch. Rat. Mech. Anal.*, vol. 154, pp. 135–156, 2000.

[76] A. Kilian and S. Hess, "Derivation and application of an algorithm for the numerical calculation of the local orientation of nematic liquid crystals," *Z. Naturforsch*, vol. 44a, pp. 693–703, 1989.

[77] H. Mori, E. C. Gartland, J. R. Kelly, and P. J. Bos, "Multidimensional director modeling using the Q tensor representation in a liquid crystal cell and its application to the π cell with patterned electrodes," *Japanese Journal of Applied Physics*, vol. 38, p. 135, 1999.

[78] A. Rapini and M. Papoular, *J. Phys. (Paris) Colloq.*, vol. 30, pp. C4–54, 1969.

[79] W. Zhao, C.-X. Wu, and M. Iwamoto, "Analysis of weak-anchoring effect in nematic liquid crystals," *Phys. Rev. E*, vol. 62, no. 2, pp. 1481–1484, 2000.

[80] E. Willman, F. A. Fernández, R. James, and S. E. Day, "Phenomenological anisotropic anchoring energy of nematic liquid crystals for the Landau - de Gennes theory," *Submitted to Physical Review E.*

[81] M. C. J. M. Vissenberg, S. Stallinga, and G. Vertogen, "Generalized Landau-de Gennes theory of uniaxial and biaxial nematic liquid crystals," *Phys. Rev. E*, vol. 55, no. 4, pp. 4367–4377, 1997.

[82] C. Denniston and M. O. Robbins, "Mapping molecular models to continuum theories for partially miscible fluids," *Physical Review E Stat Nonlin Soft Matter Phys*, vol. 69, no. 2 Pt 1, p. 021505, 2004.

[83] D. Andrienko, "On the theory and simulation of confined liquid crystals," Ph.D. dissertation, University of Bristol, 2001.

[84] A. Sonnet, A. Kilian, and S. Hess, "Alignment tensor versus director: Description of defects in nematic liquid crystals," *Physical Review E*, vol. 52, no. 1, pp. 718–722, 1995.

[85] T. A. Davis and E. C. Gartland Jr., "Finite element analysis of the Landau–de Gennes minimization problem for liquid crystals," *SIAM Journal on Numerical Analysis*, vol. 35, no. 1, pp. 336–362, 1998.

[86] J. Fukuda, M. Yoneya, and H. Yokoyama, "Nematic liquid crystal around a spherical particle: Investigation of the defect structure and its stability using adaptive mesh refinement," *Eur. Phys. J. E*, vol. 13, pp. 87–98, 2004.

[87] J. R. Shewchuk, "Delaunay refinement algorithms for triangular mesh generation," *Computational Geometry: Theory and Applications*, vol. 22, no. 1-3, pp. 21–74, 2002.

[88] http://gid.cimne.upc.es/, 2006.

[89] P. O. Persson and G. Strang, "A simple mesh generator in MATLAB," *SIAM Review*, vol. 46, no. 2, pp. 329–345, 2004.

[90] C. Johnson and K. Eriksson, "Adaptive finite element methods for parabolic problems I: A linear model problem," *SIAM J. Numer. Anal.*, vol. 28, pp. 43–77, 1991.

[91] O. C. Zienkiewicz and J. Z. Zhu, "Superconvergence and the superconvergent patch recovery," *Finite Elements in Analysis and Design*, vol. 19, no. 1-2, pp. 11–23, 1995.

[92] P. O. Persson, "PDE-based gradient limiting for mesh size functions," in *Proc. of the 13th Int. Meshing Roundtable*, Sandia Nat. Lab, 2004, pp. 377–387.

[93] N. J. Mottram and S. J. Hogan, "Disclination core structure and induced phase changes in nematic liquid crystals," *Philosophical Transactions of the Royal Society*, vol. 355, pp. 2045–2064, 1997.

[94] H. J. Coles, "Laser and electric field induced birefringence studies on the cyanobiphenyl homologues," *Molecular Crystals and Liquid Crystals Letters*, vol. 49, pp. 67–74, 1978.

[95] F. A. Fernández, S. E. Day, P. Trwoga, H. Deng, and R. James, "Three-dimensional dynamic modelling of liquid crystal display cells using finite elements," *Mol. Cryst. Liq. Cryst.*, vol. 375, pp. 291–299, 2002.

[96] P. M. Chaikin and T. C. Lubensky, *Principles of condensed matter physics*. Cambridge: Cambridge University Press, 1995.

[97] D. W. Berreman, "Liquid crystal twist cell dynamics and backflow," *Journal of Applied Physics*, vol. 46, pp. 3746–3751, 1975.

[98] J. L. Ericksen, "Conservation laws for liquid crystals," *Journal of Rheology*, vol. 5, no. 1, pp. 23–34, 1961.

[99] F. M. Leslie, "Some constitutive equations for liquid crystals," *Archive for Rational Mechanics and Analysis*, vol. 28, no. 4, pp. 265–283, 1968.

[100] A. N. Beris and B. J. Edwards, *Thermodynamics of Flowing Systems*. Oxford: Oxford University Press, 1994.

[101] G. Tóth, C. Denniston, and J. M. Yeomans, "Hydrodynamics of topological defects in nematic liquid crystals," *Physical Review Letters*, vol. 88, no. 10, p. 105504, 2002.

[102] D. Marenduzzo, E. Orlandini, and J. M. Yeomans, "Permeative flows in cholesteric liquid crystals," *Phys. Rev. Lett.*, vol. 92, p. 188301, 2004.

[103] J. I. Fukuda, "Effect of hydrodynamic flow on kinetics of nematic-isotropic transition in liquid crystals," *The European Physical Journal B*, vol. 1, pp. 173–177, 1998.

[104] D. J. Acheson, *Elementary fluid dynamics*. Clarendon, 1990.

[105] G. Vertogen and W. H. de Jeu, *Thermotropic liquid crystals, fundamentals*. Berlin: Springer, 1988.

[106] D. Forster, T. Lubensky, P. Martin, J. Swift, and P. Pershan, "Hydrodynamics of liquid crystals," *Phys. Rev. Lett.*, vol. 26, no. 17, pp. 1016–1019, 1971.

[107] A. M. Sonnet, P. L. Maffettone, and E. G. Virga, "Continuum theory for nematic liquid crystals with tensorial order," *Journal of Non-Newtonian Fluid Mechanics*, vol. 119, no. 1-3, pp. 51–59, 2004.

[108] C. M. Care and D. J. Cleaver, "Computer simulation of liquid crystals," *Reports on Progress in Physics*, vol. 68, pp. 2665–2700, 2005.

[109] S. Mkaddem and J. Gartland, E. C., "Fine structure of defects in radial nematic droplets," *Physical Review E Stat Phys Plasmas Fluids Relat Interdiscip Topics*, vol. 62, no. 5B, pp. 6694–6705, 2000.

[110] P. Hood and C. Taylor, "Navier-Stokes equations using mixed interpolation," *Int. Symp. Finite Element Method in Flow. Problems*, pp. 121–132, 1974.

[111] S. J. Tavener, T. Mullin, G. I. Blake, and K. A. Cliffe, "Numerical bifurcation study of electrohydrodynamic convection in nematic liquid crystals," *Physical Review E*, vol. 63, no. 1 Pt 1, p. 011708, 2001.

[112] G. H. Golub and C. F. Van Loan, *Matrix computations*, 3rd ed., ser. Johns Hopkins studies in the mathematical sciences. Baltimore: Johns Hopkins University Press, 1996.

[113] D. Feng and T. H. Pulliam, "Tensor-gmres method for large sparse system of nonlinear equations," *SIAM Journal of Optimization*, vol. 7, no. 3, pp. 757–779, 1997.

[114] E. Cuthill and J. McKee, "Reducing the bandwidth of sparse symmetric matrices," *In Proc. 24th Nat. Conf. ACM*, pp. 157–172, 1969.

[115] S. Turek, "Recent benchmark computations of laminar flow around a cylinder," in *3rd World Conference in Applied Computational Fluid Mechanics*, Freiburg, 1996.

[116] E. Erturk, T. C. Corke, and C. Gokcol, "Numerical solutions of 2-D steady incompressible driven cavity flow at high Reynolds numbers," *International Journal for Numerical Methods in Fluids*, vol. 48, pp. 747–774, 2005.

[117] C. Blanc, D. Svenšek, S. Žumer, and M. Nobili, "Dynamics of nematic liquid crystal disclinations: the role of the backflow," *Phys. Rev. Lett.*, vol. 95, p. 097802, 2005.

[118] J. E. Anderson, P. Watson, and P. J. Bos, "Comparisons of the vector method and tensor method for simulating liquid crystal devices," *Liquid Crystals*, vol. 28, no. 1, pp. 109–115, 2001.

[119] A. Vella, R. Intartaglia, C. Blanc, I. Smalyukh, O. D. Lavrentovich, and M. Nobili, "Electric-field-induced deformation dynamics of a single nematic disclination," *Physical Review E Stat Nonlin Soft Matter Phys*, vol. 71, no. 6 Pt 1, p. 061705, 2005.

[120] Z. Ge, T. X. Wu, X. Zhu, and S. T. Wu, "Reflective liquid-crystal displays with asymmetric incident and exit angles," *J Opt Soc Am A Opt Image Sci Vis*, vol. 22, no. 5, pp. 966–77, 2005.

[121] A. D. Rey and T. Tsuji, "Recent advances in theoretical liquid crystal rheology," *Macromolecular Theory and Simulations*, vol. 7, no. 6, pp. 623 - 639, 1998.

[122] G. Tóth, C. Denniston, and J. M. Yeomans, "Hydrodynamics of domain growth in nematic liquid crystals," *Physical Review E*, vol. 67, no. 5 Pt 1, p. 051705, 2003.

[123] I. Dozov and G. Durand, "Surface controlled nematic bistability," *Liq. Cryst. Today*, vol. 8, pp. 1–7, 1998.

[124] A. M. Figueiredo Neto, P. Martinot-Lagarde, and G. Durand, *J. Physique Lett.* vol. 45, pp. 793–798, 1984.

[125] A. Stieb, G. Baur, and G. Meier, "Alignment inversion walls in nematic liquid crystal layers deformed by an electric field," *J. de Physique*, vol. 36, no. 3, pp. C185–C188, 1975.

[126] P. Schiller and F. Zeitler, "On the theory of domain walls in planar nematic films," *J. Phys. II (France)*, vol. 6, pp. 1175–1182, 1996.

[127] A. de Lózar, W. Schöpf, I. Rehberg, D. Svenšek, and L. Kramer, "Transformation from walls to disclination lines: Statics and dynamics of the pincement transition," *Physical Review E*, vol. 72, no. 5, p. 051713, 2005.

[128] S. Vermael, K. Neyts, C. Desimpel, D. K. G. de Boer, S. E. Day, F. A. Fernández, P. F. Trwoga, and F. Lanowith, "Two-dimensional Monte-Carlo-based ion transport algorithm in liquid crystals," in *Proc. 21st IDRC / the 8th IDW*, Nagoya, Japan, 2001.

[129] A. Sawada, K. Tarumi, and S. Naemura, "Novel characterization method of ions in liquid crystal materials by complex dielectric constant measurements," *Jpn. J. Appl. Phys.*, vol. 38, no. 3A, pp. 1423–1427, 1999.

[130] F. A. Fernández, H. Deng, and S. E. Day, "Dynamic modeling of liquid crystal display cells using a constant charge approach," *IEEE Transactions on Magnetics*, vol. 38, no. 2, part 1, pp. 821–824, 2002.

[131] G. Stojmenovik, "Ion transport and boundary image retention in nematic liquid crystal displays," Ph.D. dissertation, Ghent University, 2005.

[132] H. de Vleeschouwer, A. Verschueren, F. Bougrioa, K. Neyts, G. Stojmenovik, S. Vermael, and H. Pauwels, "Dispersive ion generation in nematic liquid crystal displays," *Jpn. Journal of Applied Physics*, vol. 41, pp. 1489–1494, 2002.

[133] H. Ren, Y. Lin, Y. Fan, and S. T. Wu, "In-plane switching liquid crystal gel for polarization-independent light switch," *Journal of Applied Physics*, vol. 96, no. 7, pp. 3609–3611, 2004.

[134] S. Vermael, G. Stojmenovik, K. Neyts, D. K. G. de Boer, F. A. Fernández, S. E. Day, and R. W. James, "3-dimensional ion transport in liquid crystals," *Japanese Journal of Applied Physics*, vol. 43, no. 7A, pp. 4281–4285, 2004.

[135] P. F. McManamon, E. A. Watson, T. A. Dorschner, and L. J. Barnes, "Applications look at the use of liquid crystal writable gratings for steering passive radiation," *Opt. Eng.*, vol. 32, no. 11, pp. 2657–2664, 1993.

[136] C. M. Titus, J. R. Kelly, E. C. Gartland, S. V. Shiyanovskii, J. Anderson, and P. J. Bos, "Asymmetric transmissive behavior of liquid-crystal diffraction gratings," *Opt. Lett.*, vol. 26, no. 15, pp. 1188–1190, 2001.

[137] X. Wang, D. Wilson, R. Muller, P. Maker, and D. Psaltis, "Liquid-crystal blazed-grating beam deflector," *Appl. Optics*, vol. 39, no. 35, pp. 6545–6555, 2000.

[138] I. G. Manolis, T. D. Wilkinson, M. M. Redmond, and W. A. Crossland, "Reconfigurable multilevel phase holograms for optical switches," *IEEE Photonic. Tech. L.*, vol. 14, no. 6, pp. 801–803, 2002.

[139] K. L. Tan, S. T. Warr, I. G. Manolis, T. D. Wilkinson, M. M. Redmond, W. A. Crossland, R. J. Mears, and B. Robertson, "Dynamic holography for optical interconnections. II. routing holograms with predictable location and intensity of each diffraction order," *J. Opt. Soc. Am. A*, vol. 18, no. 1, pp. 205–215, 2001.

[140] U. Efron, B. Apter, and E. Bahat-Treidel, "Fringing-field effect in liquid-crystal beam-steering devices: an approximate analytical model," *J. Opt. Soc. Am. A*, vol. 21, no. 10, pp. 1996–2008, 2004.

[141] J. Li, S.-T. Wu, S. Brugioni, R. Meucci, and S. Faetti, "Infrared refractive indices of liquid crystals," *J. Appl. Phys.*, vol. 97, no. 7, pp. 073 501–073 501–5, 2005.

[142] R. James, F. A. Fernández, S. E. Day, M. Komarcevic, and W. A. Crossland, "Modelling of high resolution phase spatial light modulators," *Mol. Cryst. Liq. Cryst.*, vol. 422, pp. 209–217, 2004.

[143] J. A. Dobrowolski, L. Li, and J. N. Hilfiker, "Long-wavelength cutoff filters of a new type," *Appl. Optics*, vol. 38, no. 22, pp. 4891–4903, 1999.

[144] W. Gao, A. Khan, P. R. Berger, R. G. Hunsperger, G. Zydzik, H. M. O'Bryan, D. Sivco, and A. Y. Cho, "InGaAs metal-semiconductor-metal photodiodes with transparent cadmium tin oxide Schottky contacts," *Appl. Phys. Lett.*, vol. 65, no. 15, pp. 1930–1932, 1994.

[145] S. Laux, N. Kaiser, A. Zoller, R. Gotzelmann, H. Lauth, and H. Bernitzki, "Room-temperature deposition of indium tin oxide thin films with plasma ion-assisted evaporation," *Thin Solid Films*, vol. 335, no. 1, pp. 1–5, 1998.

[146] J. M. Phillips, R. J. Cava, G. A. Thomas, S. A. Carter, J. Kwo, T. Siegrist, J. J. Krajewski, J. H. Marshall, W. F. Peck, Jr., and D. H. Rapkine, "Zinc-indium-oxide: A high conductivity transparent conducting oxide," *Appl. Phys. Lett.*, vol. 67, no. 15, pp. 2246–2248, 1995.

[147] B. Chiou and J. Tsai, "Antireflective coating for ITO films deposited on glass substrate," *J. Mater. Sci.*, vol. 10, no. 7, pp. 491–495, 1999.

[148] M. Komarčević, W. A. Crossland, T. D. Wilkinson, R. James, F. A. Fernández, and S. E. Day, "Framework for direct numerical optimization of liquid crystal blazed gratings," *to be submitted.*

[149] M. Komarčević, I. G. Manolis, T. D. Wilkinson, and W. A. Crossland, "Polarization effects in reconfigurable liquid crystal phase holograms," *Opt. Commun.*, vol. 244, pp. 105–110, 2005.

[150] M. Bouvier and T. Scharf, "Analysis of nematic-liquid-crystal binary gratings with high spatial frequency," *Opt. Eng.*, vol. 39, no. 8, pp. 2129–2137, 2000.

[151] M. Stanley, "3D electronic holography display system using a 100-megapixel spatial light modulator," *Proceedings of the SPIE; Optical Design and Engineering*, vol. 5249, pp. 297–308, 2004.

[152] E. Levy, D. Peles, M. Opher-Lipson, and S. G. Lipson, "Modulation transfer function of a lens measured with a random target method," *Applied Optics*, vol. 38, no. 4, 1999.

[153] G. Panasyuk and D. W. Allender, "Model for the director and electric field in liquid crystal cells having twist walls or disclination lines," *Journal of Applied Physics*, vol. 91, no. 12, pp. 9603–9612, 2002.

[154] D. Marenduzzo, E. Orlandini, and J. M. Yeomans, "Switching hydrodynamics in multidomain, twisted nematic, liquid-crystal devices," *Europhys. Lett.*, vol. 71, no. 4, pp. 604–610, 2005.

[155] D. Miroshnychenko, N. A. Hill, N. J. Mottram, and J. E. Lydon, "Evolution from a +2 defect to +1/2 defects in a cylindrical geometry," *Molecular Crystals and Liquid Crystals*, vol. 437, pp. 251–267, 2005.

[156] P. G. Cummins, D. A. Dunmur, and D. A. Laidler, "The dielectric properties of nematic 4,4'-n-, pentylcyanobiphenyl," *Molecular Crystals and Liquid Crystals*, vol. 30, pp. 109–123, 1975.

[157] P. P. Karat and N. V. Madhusudana, "Elasticity and orientational order in some 4'-n-alkyl-4-cyanobiphenyls: Part II," *Molecular Crystals and Liquid Crystals*, vol. 40, pp. 239–245, 1977.

[158] D. Stoenescu, D. Gallaire, L. Faget, S. Lamarque-Forget, S. Joly, J.-C. Dubois, P. Martinot-Lagarde, and I. Dozov, "Development of low anchoring strength liquid crystal mixtures for bistable nematic displays," *Proceedings of SPIE, Liquid Crystal Materials, Devices, and Applications*, vol. 6135, 2006.

[159] I. Dozov, M. Nobili, and G. Durand, "Fast bistable nematic display using monostable surface switching," *Applied Physics Letters*, vol. 70, no. 9, pp. 1179–1181, 1997.

[160] Z. Ge, X. Zhu, T. X. Wu, and S. T. Wu, "High transmittance in-plane switching liquid crystal displays," *Journal of Display Technology*, vol. 2, no. 2, pp. 114–120, 2006.

[161] D. W. Berreman and W. R. Heffner, "New bistable cholesteric liquid-crystal display," *Appl. Phys. Lett.*, vol. 37, pp. 109–111, 1980.

[162] G. P. Bryan-Brown, E. L. Wood, C. V. Brown, J. C. Jones, I. C. Sage, and P. Brett, "Grating aligned bistable nematic device," in *Proceedings of SID 97*, vol. 28, Boston, 1997, pp. 37–40.

[163] L. A. Parry-Jones and S. J. Elston, "Flexoelectric switching in a zenithally bistable nematic device," *J. Appl. Phys.*, vol. 97, p. 093515, 2005.

[164] S. Kitson and A. Geisow, "Bistable alignment of nematic liquid crystals around microscopic posts," *Mol. Cryst. Liq. Cryst.*, vol. 153-161, no. 412, pp. 153–161, 2004.

[165] G. V. Prakash, M. Kaczmarek, A. Dyadyusha, J. J. Baumberg, and G. DâĂŹAlessandro, "Control of topological defects in microstructured liquid crystal cells," *Optics Express*, vol. 13, no. 6, pp. 2201–2209, 2005.

[166] A. J. Davidson and N. J. Mottram, "Flexoelectric switching in a bistable nematic device," *Phys. Rev. E*, vol. 65, no. 5, p. 051710, 2002.

[167] Y. Iwata, H. Naito, M. Inoue, H. Ichinose, M. Klasen-Memmer, and K. Tarumi, "Transient current of nematic liquid crystals with negative dielectric anisotropy induced by step-voltage excitation," *Japanese Journal of Applied Physics*, vol. 43, no. 12B, pp. L1588–L1591, 2004.

[168] M. Bremer, M. Klasen-Memmer, D. Pauluth, and K. Tarumi, "Novel liquid-crystal materials with negative dielectric anisotropy for tv application," *Journal of the Society for Information Display*, vol. 14, no. 6, pp. 517–521, 2006.

[169] C. Fletcher, *Computational techniques for fluid dynamics*, 2nd ed. Berlin: Springer, 1991.

List of Publications

[1] E. Willman, F. A. Fernández, R. James, and S. E. Day, "Phenomenological anisotropic anchoring energy of nematic liquid crystals for the Landau - de Gennes theory," *Submitted to Physical Review E.*

[2] R. James, F. A. Fernández, S. E. Day, M. Komarčević, and W. A. Crossland, "Beam steering using an electrically addressed spatial light modulator," *submitted to J. Opt. Soc. Am. A.*

[3] R. James, G. Stojmenovik, C. Desimpel, S. Vermael, F. A. Fernández, S. E. Day, and K. Neyts, "Influence of ion transport on liquid crystal switching," *IEEE Journal of Display Technology*, vol. 2, no. 3, pp. 237–246, 2006.

[4] R. James, E. Willman, F. A. Fernández, and S. E. Day, "Finite-element modeling of liquid-crystal hydrodynamics with a variable degree of order," *IEEE Transactions on Electron Devices*, vol. 53, no. 7, pp. 1575–1582, 2006.

[5] R. James, M. C. Gardner, F. A. Fernández, and S. E. Day, "3D modelling of high resolution devices," *Mol. Cryst. Liq. Cryst.*, vol. 450, pp. 105–118, 2006.

[6] C. Desimpel, J. Beeckman, H. Desmet, K. Neyts, R. James, and F. A. Fernández, "A four-electrode liquid crystal device for 2pi in-plane director rotation," *Journal of Physics D: Applied Physics*, vol. 38, pp. 3976–3984, 2005.

[7] R. James, F. A. Fernández, S. E. Day, M. Komarcevic, and W. A. Crossland, "Modelling of high resolution phase spatial light modulators," *Mol. Cryst. Liq. Cryst.*, vol. 422, pp. 209–217, 2004.

[8] S. Vermael, G. Stojmenovik, K. Neyts, D. K. G. de Boer, F. A. Fernández, S. E. Day, and R. W. James, "3-dimensional ion transport in liquid crystals," *Japanese Journal of Applied Physics*, vol. 43, no. 7A, pp. 4281–4285, 2004.

[9] F. A. Fernández, S. E. Day, P. Trwoga, H. Deng, and R. James, "Three-dimensional dynamic modelling of liquid crystal display cells using finite elements," *Mol. Cryst. Liq. Cryst.*, vol. 375, pp. 291–299, 2002.

List of Conferences

[1] R. James, M. C. Gardner, F. A. Fernández, and S. E. Day, "3D modelling of high resolution devices," in *ECLC 2005 - European Confererence on Liquid Crystals*, Sesto, Italy, 2005.

[2] R. James, F. A. Fernández, S. E. Day, M. Komarčević, and W. A. Crossland, "Effect of pre-twist on the performance of LC diffraction devices," in *British Liquid Crystal Society Annual Meeting*, Manchester, 2004.

[3] R. James, S. Vermael, F. A. Fernández, S. E. Day, and K. Neyts, "Modelling of ion transport in liquid crystal cells," in *SPIE, Optical Design and Engineering*, St. Etienne, France, 2003.

[4] R. James, F. A. Fernández, S. E. Day, M. Komarcevic, and W. A. Crossland, "Modelling of high resolution phase spatial light modulators," in *OLC 2003 - Optics of Liquid Crystals*, Aussois, France, 2003.

[5] R. James, S. Vermael, F. A. Fernández, S. E. Day, and K. Neyts, "Aspects in the modelling of liquid crystal devices," in *British Liquid Crystal Society Annual Meeting*, Cambridge, 2003.